frontiers | Research Topics

Photocatalysis and electrocatalysis for energy conversion

Edited by
Guangzhao Wang, Yue-Yu Zhang, Kezhen Qi,
Changhong Wang and Zhaofu Zhang

Published in
Frontiers in Chemistry

ISSN 1664-8714
ISBN 978-2-83251-394-1
DOI 10.3389/978-2-83251-394-1

About Frontiers

Frontiers is more than just an open access publisher of scholarly articles: it is a pioneering approach to the world of academia, radically improving the way scholarly research is managed. The grand vision of Frontiers is a world where all people have an equal opportunity to seek, share and generate knowledge. Frontiers provides immediate and permanent online open access to all its publications, but this alone is not enough to realize our grand goals.

Frontiers journal series

The Frontiers journal series is a multi-tier and interdisciplinary set of open-access, online journals, promising a paradigm shift from the current review, selection and dissemination processes in academic publishing. All Frontiers journals are driven by researchers for researchers; therefore, they constitute a service to the scholarly community. At the same time, the *Frontiers journal series* operates on a revolutionary invention, the tiered publishing system, initially addressing specific communities of scholars, and gradually climbing up to broader public understanding, thus serving the interests of the lay society, too.

Dedication to quality

Each Frontiers article is a landmark of the highest quality, thanks to genuinely collaborative interactions between authors and review editors, who include some of the world's best academicians. Research must be certified by peers before entering a stream of knowledge that may eventually reach the public - and shape society; therefore, Frontiers only applies the most rigorous and unbiased reviews. Frontiers revolutionizes research publishing by freely delivering the most outstanding research, evaluated with no bias from both the academic and social point of view. By applying the most advanced information technologies, Frontiers is catapulting scholarly publishing into a new generation.

What are Frontiers Research Topics?

Frontiers Research Topics are very popular trademarks of the *Frontiers journals series*: they are collections of at least ten articles, all centered on a particular subject. With their unique mix of varied contributions from Original Research to Review Articles, Frontiers Research Topics unify the most influential researchers, the latest key findings and historical advances in a hot research area.

Find out more on how to host your own Frontiers Research Topic or contribute to one as an author by contacting the Frontiers editorial office: frontiersin.org/about/contact

Photocatalysis and electrocatalysis for energy conversion

Topic editors
Guangzhao Wang — Yangtze Normal University, China
Yue-Yu Zhang — University of Chinese Academy of Sciences, China
Kezhen Qi — Shenyang Normal University, China
Changhong Wang — Tianjin University, China
Zhaofu Zhang — Wuhan University, China

Citation
Wang, G., Zhang, Y.-Y., Qi, K., Wang, C., Zhang, Z., eds. (2023). *Photocatalysis and electrocatalysis for energy conversion*. Lausanne: Frontiers Media SA.
doi: 10.3389/978-2-83251-394-1

The authors declare that the research was conducted in the absence of any commercial or financial relationships that could be construed as a potential conflict of interest.

Table of contents

frontiers | Frontiers in Chemistry

TYPE Editorial
PUBLISHED 09 January 2023
DOI 10.3389/fchem.2022.1128243

OPEN ACCESS

EDITED AND REVIEWED BY
Sam P. De Visser,
The University of Manchester,
United Kingdom

*CORRESPONDENCE
Guangzhao Wang,
✉ wangyan6930@yznu.edu.cn
Changhong Wang,
✉ chwang@hebtu.edu.cn
Kezhen Qi,
✉ qkzh2003@aliyun.com

[†]These authors have contributed equally to this work

SPECIALTY SECTION
This article was submitted to Theoretical and Computational Chemistry, a section of the journal Frontiers in Chemistry

RECEIVED 20 December 2022
ACCEPTED 28 December 2022
PUBLISHED 09 January 2023

CITATION
Wang G, Zhang Z, Zhang Y-Y, Wang C and Qi K (2023), Editorial: Photocatalysis and electrocatalysis for energy conversion.
Front. Chem. 10:1128243.
doi: 10.3389/fchem.2022.1128243

Editorial: Photocatalysis and electrocatalysis for energy conversion

Guangzhao Wang[1*†], Zhaofu Zhang[2,3†], Yue-Yu Zhang[4,5†], Changhong Wang[6*] and Kezhen Qi[7*]

[1]Key Laboratory of Extraordinary Bond Engineering and Advanced Materials Technology of Chongqing, School of Electronic Information Engineering, Yangtze Normal University, Chongqing, China, [2]The Institute of Technological Sciences, Wuhan University, Wuhan, China, [3]University of Cambridge, Cambridge, United Kingtom, [4]Wenzhou Institute, University of Chinese Academy of Sciences, Wenzhou, China, [5]East China University of Science and Technology, Shanghai, China, [6]Hebei Normal University, Shijiazhuang, China, [7]College of Pharmacy, Dali University, Dali, Yunnan, China

KEYWORDS

photocatalysis, electrocatalysis, optoelectronics, energy conversion, pollution treatment

Editorial on the Research Topic
Photocatalysis and electrocatalysis for energy conversion

Introduction

Photocatalysis and electrocatalysis play important roles in solving energy and environmental problems. Photocatalysis can store solar energy into molecular bonds or utilize solar energy to degrade pollutants by leading various chemical reactions with the help of photocatalysts, while electrocatalysis can implement parallel or similar functions and reactions under external voltage. Recently, the applications of photocatalytic and electrocatalytic technologies in energy and environment fields including hydrogen generation, CO_2 reduction, O_2 reduction, and nitrogen fixation have been widely investigated. But the industrial application of photocatalysis and electrocatalysis is still full of challenges, which is mainly limited by the cost and efficiency of current photocatalysts and electrocatalysts. Thus, the design of low-priced and highly efficient photocatalysts and electrocatalysts is still very urgent.

The ideal photocatalysts should possess a long carrier lifetime, a wide light-harvesting region, a strong driving force to carry out oxidation or reduction reaction, while the desired electrocatalysts should utilize very low power energy to drive oxidation or reduction reaction. In this Research Topic "*Photocatalysis and Electrocatalysis for Energy Conversion*," we have collected 10 articles in total, representing the recent advances in both experimental and theoretical investigations on catalysis, photocatalysis, and optoelectronic devices. Below, we give a brief summary and research highlights about these interesting works.

Experimental study on catalysis and photocatalysis

Photocatalytic technology could convert solar energy into chemical energy (or clean renewable energy) and degrade pollutants, which is an effective way to solve the energy crisis and environmental pollution. The potocatlaytic activity for hydrogen production of bulk g-C_3N_4 is mainly restricted by the fast photoinduced carrier recombination rate, poor visible-light harvest ability, and low specific surface area. Gao et al. summarized the strategies of pH modulation, morphology, control, metal or non-metal dopants, metal deposition, heterojunction or homojunction construction, and dye-sensitization to enhance the photocatalytic performance of pristine g-C_3N_4. Sheng et al. prepared two analogous conjugated microporous polymers (CMPs) containing CMP-1 and CMP-2. CMP-1 possesses lower photoexcited carrier recombination than that of CMP-2. Thus, hydrogen production rate of CMP-1 (9,698.53 μmol g^{-1}h $^{-1}$) is about twice of that of CMP-2 (4,727.1 μmol g^{-1}h $^{-1}$). Song et al. prepared a highly efficient Z-scheme g-C_3N_4/Ag/AgBr heterostructure photocatalyst, which exhibits excellent photocatalytic activity for tetracycline hydrochloride degradation. Using phosphate organoamine as the structure guiding agent, Ye et al. synthesized an ISAPO-34/SAPO-18 intergrown zeolite. The active temperature window of copper based catalyst prepared from SAPO-34/SAPO-18 shifts to a lower temperature with the increase of copper content. In addition, the Brønsted acid site decreases obviously because of cooper ion exchange and zeolite structure framework damage.

Theoretical study on catalysis and photocatalysis

First-principles calculations based on density functional theory (DFT) play an increasingly important role in the design of novel catalysts and photocatalysts. Based on DFT theory, Wang et al. predicted that $MoWS_4$ monolayer and bilayer are both indirect bandgap semiconductors. Besides, both $MoWS_4$ monolayer and bilayer show excellent visible-ultraviolet absorption capacity, and their band edge alignments satisfy the requirement for overall water-splitting. Overall, $MoWS_4$ monolayer and bilayer are potential candidates for water-splitting photocatalysts. By utilizing first-principles calculations, Zhang et al. studied the strain effect on the electronic and optical properties of $MoTe_2/PtS_2$ heterostructure. The $MoTe_2/PtS_2$ heterostructure persists the type-II band alignment and the bandgap decreases under external strain. Besides, the compressive strain could tune the band edge positions of $MoTe_2/PtS_2$ heterostructure so as to be suitable for the overall photocatalytic water-splitting at pH 7. Moreover, all the $MoTe_2/PtS_2$ heterostructures show excellent light harvest ability and solar-to-hydrogen efficiency. By calculating and analyzing the electronic and absorptive properties, band edge alignments, Gibbs free energy changes in hydrogen and oxygen evolution reactions, and carrier mobility, Liu et al. predicted ZnO/C_2N heterostructure to be a promising water-splitting photocatalyst. With the aid of first-principles calculations, Zhang et al. predicted that CdO/HfS_2 heterostructure is a potential Z-scheme water-splitting photocatlayst, while Han et al. predicted that Fe@χ_3-borophene is a promising single-atom catalyst for CO oxidation reaction with low energy barrier.

Novel optoelectronic materials

Yuan et al. predicted MoSSe/InS heterostructure to be an indirect bandgap semiconductor with a type-II band alignment. Biaxial strains could effectively tune the bandgaps, band edge positions, and optical property of MoSSe/InS heterostructure. Besides, the visible-ultraviolet light harvest ability of MoSSe/InS heterostructure is obviously improved as compared with MoSSe and InS single-layers. In general, the MoSSe/InS heterostructure possesses potential application in optoelectronic devices.

We hope this Research Topic could guide new ideas for the search and design of highly efficient catalysts and photocatalysts. Finally, we think all the authors, reviewers, and editors who have contributed to this Research Topic.

Author contributions

GW, ZZ, and Y-YZ prepared the first draft, while CW and KQ revised the manuscript.

Funding

This work was supported by the Science and Technology Research Program of Chongqing Municipal Education Commission, China under grant Nos. KJQN202001402 and KJQN202201405.

Conflict of interest

Publisher's note

frontiers in Chemistry

ORIGINAL RESEARCH
published: 22 February 2022
doi: 10.3389/fchem.2022.861838

Type-II Band Alignment and Tunable Optical Absorption in MoSSe/InS van der Waals Heterostructure

X. B. Yuan[1], Y. H. Guo[1], J. L. Wang[1], G. C. Hu[1], J. F. Ren[1,2]* and X. W. Zhao[1]*

[1]School of Physics and Electronics, Shandong Normal University, Jinan, China, [2]Shandong Provincial Engineering and Technical Center of Light Manipulations and Institute of Materials and Clean Energy, Shandong Normal University, Jinan, China

In this work, we study the electronic structure, the effective mass, and the optical properties of the MoSSe/InS van der Waals heterostructures (vdWHs) by first-principles calculations. The results indicate that the MoSSe/InS vdWH is an indirect band gap semiconductor and has type-II band alignment in which the electrons and holes located at the InS and the MoSSe side, respectively. The band edge position, the band gap and the optical absorption of the MoSSe/InS vdWH can be tuned when biaxial strains are applied. In addition, compared with MoSSe and InS monolayers, the optical absorption of the MoSSe/InS vdWH is improved both in the visible and the ultraviolet regions. These findings indicate that the MoSSe/InS vdWHs have potential applications in optoelectronic devices.

Keywords: van der waals heterostructure, first principles calculations, optical absorption, biaxial strain, band edge position

OPEN ACCESS

Edited by:
Guangzhao Wang,
Yangtze Normal University, China

Reviewed by:
Kai Ren,
Nanjing Forestry University, China
Junli Chang,
Southwest University, China

Correspondence:
J. F. Ren
renjf@sdnu.edu.cn
X. W. Zhao
xwzhao@sdnu.edu.cn

Specialty section:
This article was submitted to Theoretical and Computational Chemistry, a section of the journal Frontiers in Chemistry

Received: *25 January 2022*
Accepted: *07 February 2022*
Published: *22 February 2022*

Citation:
Yuan XB, Guo YH, Wang J, Hu GC, Ren J and Zhao XW (2022) Type-II Band Alignment and Tunable Optical Absorption in MoSSe/InS van der Waals Heterostructure. Front. Chem. 10:861838. doi: 10.3389/fchem.2022.861838

INTRODUCTION

With the discovery of graphene in 2004, two-dimensional (2D) materials have been widely studied and applied due to their unique structures and excellent physical and chemical properties (Novoselov et al., 2004). In the past decades, a large number of 2D materials have been emerged, such as transition metal dichalcogenides (TMDCs) (Choi et al., 2017; Qiu et al., 2020), silicene (Fleurence et al., 2012; Wu et al., 2014), group-III monochalcogenides (Huang et al., 2019), Mxenes (Zhou et al., 2021), etc. In order to obtain high-performance devices, the advantages of a single layer 2D material are slightly insufficient, so the van der Waals heterostructures (vdWHs) formed by the van der Waals forces along the vertical superposition of two different 2D materials has been attracted widespread attention (Guo et al., 2021a; Zhao et al., 2021). A variety of vdWHs have been developed, which can be classified into three band alignments, i.e., straddling type-I, staggered type-II, and broken-gap type-III (Özçelik et al., 2016).

The vdWHs not only contain some of the advantages of the isolated monolayers but also produce some other properties (Ren et al., 2021a; Ren et al., 2021b; Ren et al., 2021c; Sun et al., 2022; Shen et al., 2022). For example, Liu *et al.* proposed the MoSSe/g-GeC heterostructure as a promising photovoltaic application material in which visible optical absorption and catalytic activity can be adjusted by strain engineering (Liu et al., 2021). M. M. Obeid and others revealed that GaSe/HfS$_2$ heterostructures have high carrier mobility and can be converted from semiconductor to metal and from indirect band gap to direct band gap when the external electric field is strengthened (Obeid et al., 2020). Zhu *et al.* found that GaN/Zr$_2$CO$_2$ heterostructure has a promising application in tunable high-performance optoelectronic nanodevices due to its large conduction band offset (CBO) and tunable band gap (Zhu et al., 2021). Zhang *et al.* proved that P-GaSe/InS isomorphous heterostructure has excellent performance as a photocatalytic and water splitting material (Zhang et al., 2021).

On the other hand, after Janus MoSSe was successfully synthesized by chemical vapor deposition (CVD) method in 2017 (Lu et al., 2017; Zhang et al., 2017), the unique physical properties of 2D Janus TMDCs due to their mirror asymmetry have been attracted widespread attention. The Janus MoSSe has an easy-to-tune band gap, strong visible optical absorption and suitable band alignment (Yin et al., 2018); Mo atoms are located between S atoms and Se atoms, so an internal electric field is formed, which promotes electron-hole separation and inhibits exciton recombination (Chen et al., 2019). In addition, as a new type of 2D material, Group-III chalcogenides (MX, M = Ga and In, X = S, Se) have been attracted great attention in photoelectric devices due to their wide band gap, high electron mobility, good thermoelectric performance and optical responses (Miao et al., 2016; Xu et al., 2016; Hung et al., 2017). InS has been successfully synthesized experimentally and has a similar structure to InSe (Hollingsworth et al., 2000). Monolayer InS has good optical response characteristics and large band gap. However, InS has some disadvantages in visible optical absorption due to the large indirect band gap, and the separation ability of electron-hole pairs is also weak. Both MoSSe and InS monolayers can be synthesized, so the MoSSe/InS vdWH is also feasible composed experimentally. Therefore, we hope that the MoSSe/InS vdWH has the advantages of the two monolayers.

In this work, based on the first-principles calculations, we mainly study the band edge position, the charge transfer and the optical absorption of the MoSSe/InS vdWH. Effects of biaxial strain on electronic structure and optical properties are also considered. Compared with MoSSe and InS monolayers, the optical absorption of the MoSSe/InS vdWH is improved and can be modulated by biaxial strain. The structure of this paper is as follows: details of the computational methods are provided in **Section 2**, the results and the discussion are shown in **Section 3**, and the conclusion is presented in **Section 4**.

COMPUTATIONAL METHODS

All first-principles calculations are based on density functional theory (DFT) by using Vienna ab initio Simulation Package (VASP) (Kresse and Furthmüller, 1996). The core-ion and valence electron interaction is described by the projector augmented wave (PAW) method, and the general gradient approximation (GGA) in the form of Perdew-Burke-Ernzerhof (PBE) functional is used to calculate the exchange-correlation functional (Blöchl, 1994; Perdew et al., 1996; Kresse and Joubert, 1999). For the plane-wave basis set, the energy cutoff is set to 500 eV. All geometric structures are completely relaxed with the total energy is converged within 1×10^{-6} eV and the Hellmann–Feynman force is less than 0.01 eV $Å^{-1}$. In the empirical correction scheme proposed by Grimme, we use the DFT-D3 method to describe the effect of the interaction between monolayers (Grimme et al., 2010; Grimme et al., 2011). The k-points in the first Brillouin-zone of 4 × 4 × 1 and 8 × 8 × 1 are generated by the Monkhorste Packscheme and they are used for the geometric optimization and the self-consistent calculations, respectively. To avoid the interaction caused by periodic effects, the vacuum layer is set to 20 Å along the Z-axis direction. Since the PBE always underestimates the band gap of the semiconductor, we use hybrid functional (HSE06) to further obtain accurate electronic properties (Heyd et al., 2003). The VASP processing program VASPKIT is used to analyze electronic structure and optical properties (Wang et al., 2021).

RESULTS AND DISCUSSION

Before investigating the MoSSe/InS vdWH, the structural parameters and the electronic characteristics of the MoSSe and InS are studied. The optimized lattice parameters of the MoSSe and InS monolayers are a = b = 3.25 Å and a = b = 3.94 Å respectively. The results are consistent with the previous reported results (Zhu et al., 2021; Hollingsworth et al., 2000; Guo et al., 2021b). Taking into account the lattice mismatch, we constructed a 2 × 2 MoSSe supercell and a $\sqrt{3}\times\sqrt{3}$ InS supercell to form the MoSSe/InS vdWH to achieve a small lattice mismatch value of 4.8%. The calculated electronic band structures of the monolayers by HSE06 functional are plotted in **Figure 1**. We can find that the InS and the MoSSe have indirect band gap and direct band gap, respectively. In **Figure 1A**, the band gap value of InS is 2.48 eV. Its conduction band minimum (CBM) is located at the Γ point, and its valence band maximum (VBM) is located between the Γ point and the M point. As shown in **Figure 1B**, the band gap value of MoSSe is 2.03 eV. Its CBM and VBM are both located at the K point. These results of the MoSSe and InS monolayers are consistent well with previous results (Hollingsworth et al., 2000; Zhu et al., 2021).

For the MoSSe/InS vdWH, after considering the different stacking patterns between the layers, there are six typical stacking configurations, see **Figure 2**. Among them, I-III correspond to the cases when Se atoms are adjacent to InS monolayer, IV-VI correspond to the cases when S atoms are adjacent to InS monolayer. In order to compare the stability of the six configurations, their binding energies are calculated according to the formula: $E_b = E_{total} - E_{MoSSe} - E_{InS}$, where E_{total}, E_{MoSSe}, and E_{InS} are the total energy of the MoSSe/InS vdWH, the energy of the MoSSe monolayer and the energy of the InS monolayer, respectively. The calculated binding energies of the I-VI configurations are −4.078 meV, −4.083 meV, −4.073 meV, −4.057 meV, −4.054 meV, −4.050 meV, respectively. All the six configurations show negative binding energies, which indicate that the MoSSe/InS vdWH is thermodynamically stable. Therefore, the II stacking pattern with the smallest binding energy is considered as the most stable one and it is used in the following calculations.

In order to verify the thermodynamical stability, we perform ab initio molecular dynamics (AIMD) calculations for the MoSSe/InS vdWH at 300 K, as shown in **Figure 3A**. The simulations last for 3 ps with a time step of 0.5 fs. In the calculation of AIMD, the energy fluctuation of the vdWH is very small and the structure has no distortion, indicating that the vdWH has good thermal stability.

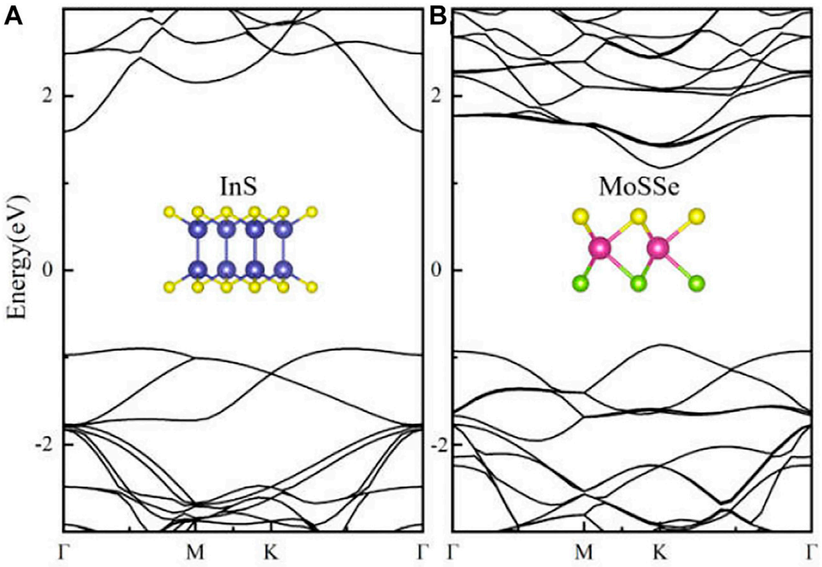

FIGURE 1 | Band structures of **(A)** InS and **(B)** MoSSe monolayers.

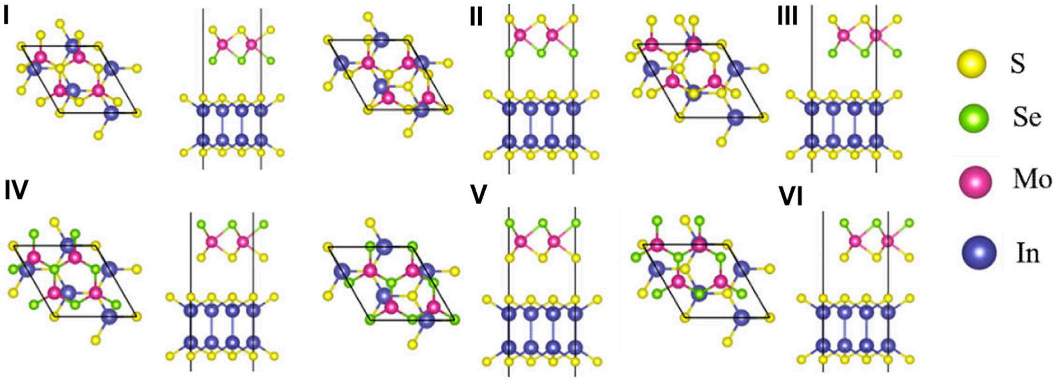

FIGURE 2 | The top and side views of six stacking patterns of the MoSSe/InS vdWHs. The yellow, green, purple and blue balls represent the S, Se, Mo and In atoms, respectively.

Figure 3B shows the projected band structure and the projected density of states (PDOS) of the MoSSe/InS vdWH calculated by HSE06 functional. In **Figure 3B**, it can be seen that the MoSSe/InS vdWH is an indirect band gap semiconductor with a band gap value of 1.67 eV, which is slightly smaller than those of MoSSe and InS monolayers and larger than the redox potential energy of water (1.23 eV). In addition, its CBM and VBM are located at M point and Γ point respectively, and it has type-II band alignment because its CBM and VBM are contributed from InS and MoSSe monolayers respectively. The type-II band alignment can effectively promote the spontaneous separation of electron-hole pairs, making it applicable to various photocatalytic and solar energy conversion devices (Massicotte et al., 2016; Lei et al., 2019). The PDOS also proves our suggestion. It can be seen that the CBM is mainly contributed from the In-p, In-d and S-p orbitals, and the VBM is mainly contributed from the Mo-d orbitals.

As shown in **Figure 4A**, the band decomposition charge densities of CBM and VBM are calculated. CBM and VBM are concentrated in the InS and MoSSe layers respectively, which means that the electrons are located in the InS layer and the holes are located in the MoSSe layer, respectively. In order to further understand the charge transfer mechanism between MoSSe and InS, we calculate the electrostatic potential and the charge density differences of the MoSSe/InS vdWH, as shown in **Figure 4B**. The red dotted line and the blue dotted line represent the vacuum level (E_{vac}) and the Fermi level (E_f), respectively, and Φ is the work function which can be obtained by the difference between Evac and E_f, and its value is 5.51 eV. The charge density difference is in the lower left corner of **Figure 4B**, which is given by $\Delta\rho = \rho_{\mathrm{MoSSe/InS}} - \rho_{MoSSe} - \rho_{InS}$, where $\rho_{MoSSe/InS}$, ρ_{MoSSe} and ρ_{InS} are the total electron densities of the MoSSe/InS vdWH, MoSSe monolayer and InS monolayer, respectively. The

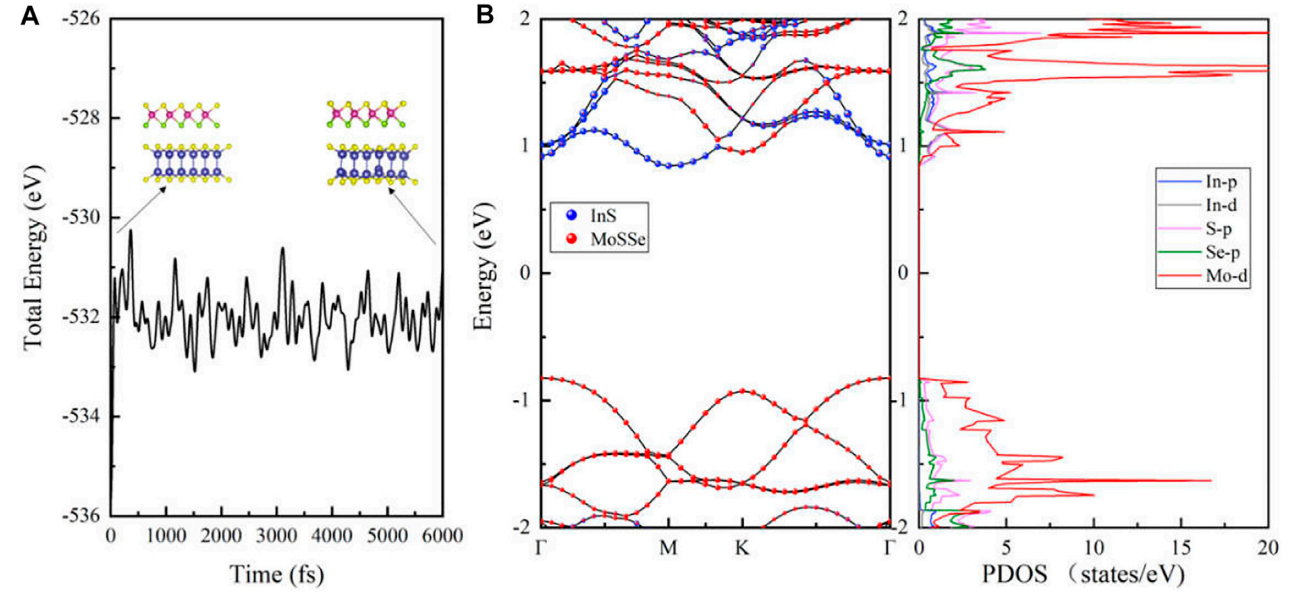

FIGURE 3 | (A) The total energy and the crystal structures calculated from the AIMD of the MoSSe/InSe vdWH. **(B)** The projected band structures and the PDOS of the MoSSe/InS vdWH.

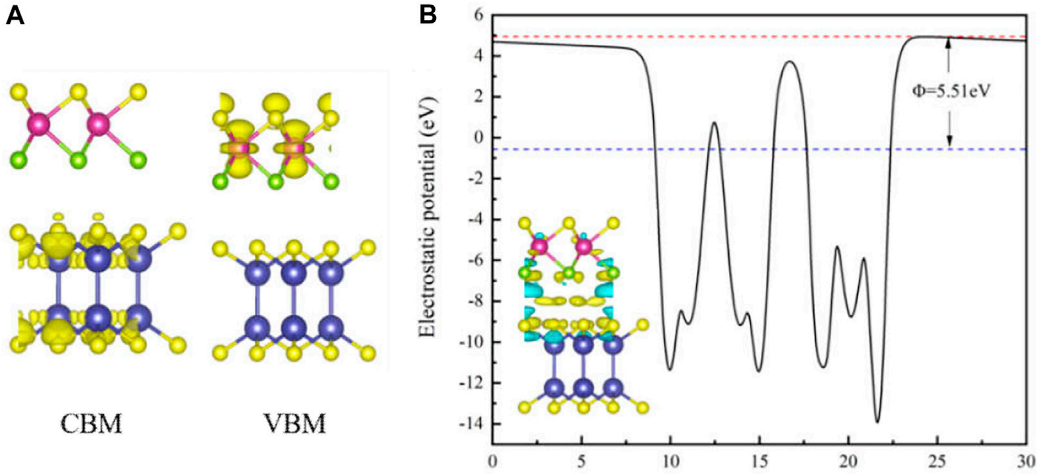

FIGURE 4 | (A) The band decomposition charge densities of CBM and VBM for the MoSSe/InSe vdWH. **(B)** The electrostatic potential and the charge density difference of the MoSSe/InS vdWH.

yellow represents charge accumulation and the blue represents charge depletion. The calculated results show that the electrons are mainly concentrated on the InS side, while the holes are concentrated on the MoSSe side, so the electrons transfer from the MoSSe side to the InS side. We also calculate the effective mass of the electron along different directions according to the formula: $m^* = \pm \hbar^2 (\frac{d^2E_k}{dk^2})^{-1}$. The effective masses of electrons (m_e^*) are 0.569 from K to M point and 0.338 from Γ to M point.

2D materials can withstand greater strain than three-dimensional materials, so biaxial strain is a method that can effectively modulate the electronic structure and the optical properties of 2D materials (Guo et al., 2020; Zhu et al., 2021). In this paper, we study the effect of biaxial strain on the band gap, band edge position and the optical absorption of the MoSSe/InS vdWH. The biaxial strain can be defined as $\varepsilon = (a - a_0)/a_0 \times 100\%$, where a_0 and a are the lattice constants of the strained-free and strained structures, correspondingly. In **Figure 5A**, the blue dashed line marks the redox potentials of H_2O/O_2 (−5.67 eV) and H^+/H_2 (−4.44 eV) of water. It can be seen that both the unstrained and strained band edges of the MoSSe/InS vdWH cross the oxidation potential of H_2O/O_2, so they are suitable for driving oxygen evolution reaction kinetics when pH = 0. In

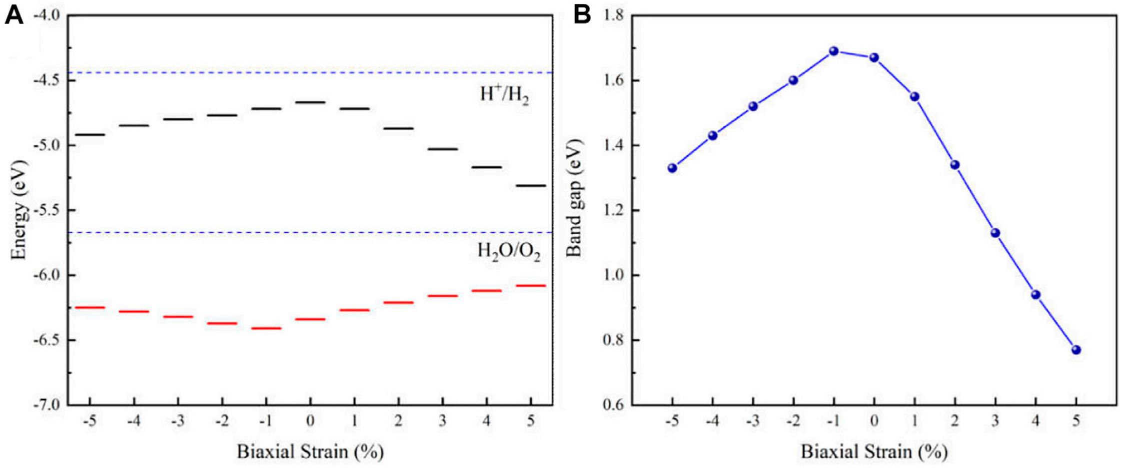

FIGURE 5 | (A) Band edge positions and **(B)** band gap of the MoSSe/InS vdWH under various biaxial strains from −5 to 5%.

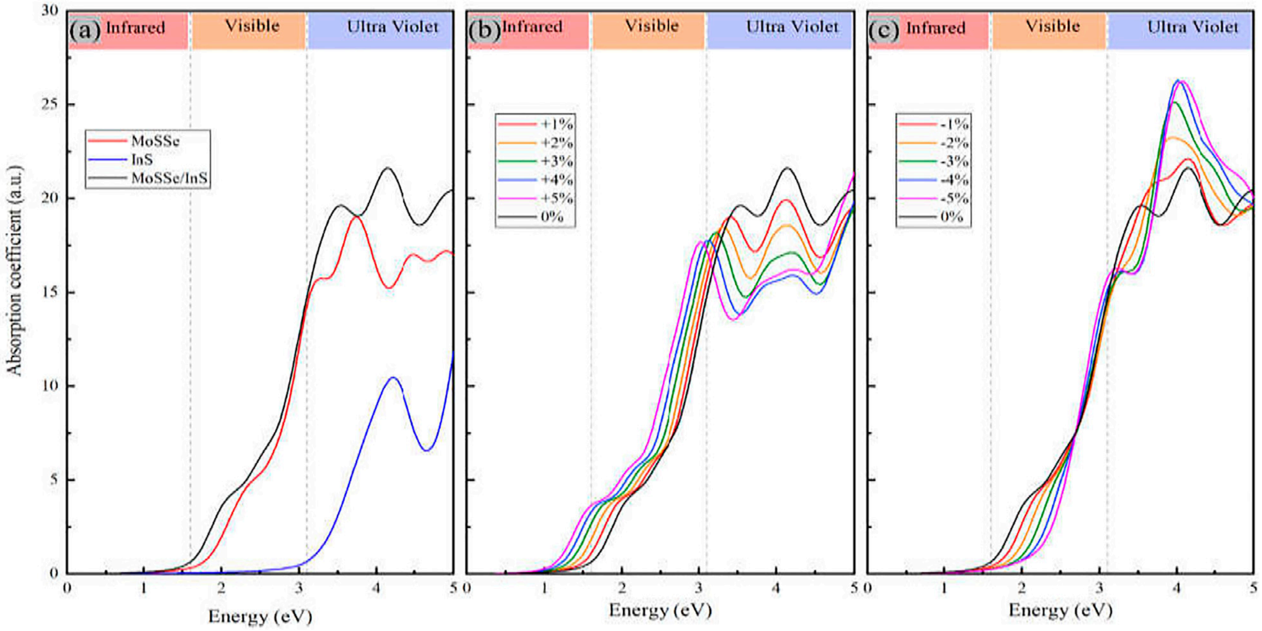

FIGURE 6 | (A) The optical absorption spectra of MoSSe monolayer, InS monolayer and the MoSSe/InS vdWHs, **(B,C)** correspond to the cases with tension strain and compressive strain, respectively.

addition, when the applied pressure and tension increase, the energy levels of the CBM and the VBM move down and up, respectively. **Figure 5B** illustrates that the band gap of the MoSSe/InS vdWH decreases when the tensile strain increase, however, when the compressive strain increases, the band gap firstly reaches to a maximum and then decrease. This tunable band gap has potential applications in devices.

The optical absorption is calculated by the formula,

$$\alpha(\omega) = \frac{\sqrt{2}\omega}{c}\left\{\left[\varepsilon_1^2(\omega) + \varepsilon_2^2(\omega)\right]^{\frac{1}{2}} - \varepsilon_1(\omega)\right\}^{\frac{1}{2}} \tag{1}$$

where ω is the light frequency, $\varepsilon_1(\omega)$ and $\varepsilon_2(\omega)$ represent the real and the imaginary parts of the complex dielectric function, respectively. **Figure 6A** gives the optical absorption spectra of the MoSSe/InS vdWH and the two independent monolayers, and (b) and (c) correspond to the cases under +1%~+5% tension strain and −1%~−5% compressive strain, respectively. As shown in **Figure 6A**, InS has a weaker optical absorption compared with that of the MoSSe. On the other hand, optical absorption of InS in the ultraviolet region is stronger than that in the visible light region. As a good photocatalytic material, MoSSe has a very strong optical absorption. Charge transfer and interlayer coupling promote the overlap of orbitals in the heterostructure, so the MoSSe/InS vdWH exhibits a stronger light absorption capacity compared with MoSSe and InS monolayers. Strain engineering is an important method to modulating the properties of 2D materials. We apply biaxial strain to study the optical properties of the MoSSe/InS vdWH. In **Figure 6B**, it can be found that the optical absorption of the MoSSe/InS vdWH in the visible light region increases when the tension strain increases, while in the ultraviolet region it decreases when the tension strain increases. As shown in **Figure 6C**, when the compressive strain increases, the optical absorption of the MoSSe/InS vdWH exhibits the opposite phenomenon compared with the case when tension strain is applied.

CONCLUSION

In summary, we have explored the electronic structure and the optical properties of the MoSSe/InS vdWH by first-principles calculations. Our results show that the MoSSe/InS vdWH has an indirect band gap with typical type-II band alignment that can effectively promote the spontaneous separation of electron-hole pairs. CBM and VBM are contributed from InS and MoSSe monolayers respectively, and electrons are transferred from the MoSSe layer into the InS layer in MoSSe/InS vdWH. Compared with monolayers, the carrier mobility and the optical absorption of the vdWH are enhanced. After the application of biaxial strain, the position of the band edge is adjusted, and the band gap of the vdWH can also be tuned. In the visible light region, the optical absorption intensity of the MoSSe/InS vdWH increases with the increasing of the tensile strain, and it decreases with the increasing of the compressive strain. Our work shows that the MoSSe/InS vdWH may have potential applications in optoelectronic devices.

DATA AVAILABILITY STATEMENT

The original contributions presented in the study are included in the article/Supplementary Material, further inquiries can be directed to the corresponding authors.

AUTHOR CONTRIBUTIONS

XY and YG did the calculations and wrote the paper, JW collected the references, GH prepared the figures, JR analyzed the data, XZ generated the research idea. All authors read and approved the final manuscript.

FUNDING

This work was supported by the National Natural Science Foundation of China (Grant Nos. 11674197 and 11974215), the Natural Science Foundation of Shandong Province (Grant No. ZR2021MA105), and the Qingchuang Science and Technology Plan of Shandong Province (No. 2019KJJ014).

REFERENCES

Blöchl, P. E. (1994). Projector Augmented-Wave Method. *Phys. Rev. B* 50, 17953–17979. doi:10.1103/physrevb.50.17953

Chen, D., Lei, X., Wang, Y., Zhong, S., Liu, G., Xu, B., et al. (2019). Tunable electronic structures in BP/MoSSe van der Waals heterostructures by external electric field and strain. *Appl. Surf. Sci.* 497, 143809. doi:10.1016/j.apsusc.2019.143809

Choi, W., Choudhary, N., Han, G. H., Park, J., Akinwande, D., and Lee, Y. H. (2017). Recent Development of Two-Dimensional Transition Metal Dichalcogenides and Their Applications. *Mater. Today* 20, 116–130. doi:10.1016/j.mattod.2016.10.002

Fleurence, A., Friedlein, R., Ozaki, T., Kawai, H., Wang, Y., and Yamada-Takamura, Y. (2012). Experimental Evidence for Epitaxial Silicene on Diboride Thin Films. *Phys. Rev. Lett.* 108, 245501. doi:10.1103/physrevlett.108.245501

Grimme, S., Antony, J., Ehrlich, S., and Krieg, H. (2010). A Consistent and Accurate Ab Initio Parametrization of Density Functional Dispersion Correction (DFT-D) for the 94 Elements H-Pu. *J. Chem. Phys.* 132, 154104. doi:10.1063/1.3382344

Grimme, S., Ehrlich, S., and Goerigk, L. (2011). Effect of the Damping Function in Dispersion Corrected Density Functional Theory. *J. Comput. Chem.* 32, 1456–1465. doi:10.1002/jcc.21759

Guo, H., Zhang, Z., Huang, B., Wang, X., Niu, H., Guo, Y., et al. (2020). Theoretical study on the photocatalytic properties of 2D InX(X = S, Se)/transition metal disulfide (MoS2 and WS2) van der Waals heterostructures. *Nanoscale* 12, 20025–20032. doi:10.1039/d0nr04725b

Guo, J. T., Zhao, X. W., Hu, G. C., Ren, J. F., and Yuan, X. B. (2021). Observation and Manipulation of valley Polarization in Two-Dimensional H-Tl2O/CrI3 Heterostructure. *Appl. Surf. Sci.* 558, 149604. doi:10.1016/j.apsusc.2021.149604

Guo, Y. H., Wang, J. L., Hu, G. C., Yuan, X. B., and Ren, J. F. (2021). Strain-tunable electronic and optical properties of novel MoSSe/InSe van der Waals heterostructures. *Phys. Lett. A* 404, 127395. doi:10.1016/j.physleta.2021.127395

Heyd, J., Scuseria, G. E., and Ernzerhof, M. (2003). Hybrid Functionals Based on a Screened Coulomb Potential. *J. Chem. Phys.* 118, 8207–8215. doi:10.1063/1.1564060

Hollingsworth, J. A., Poojary, D. M., Clearfield, A., and Buhro, W. E. (2000). Catalyzed Growth of a Metastable InS Crystal Structure as Colloidal Crystals. *J. Am. Chem. Soc.* 122, 3562–3563. doi:10.1021/ja000106u

Huang, A., Shi, W., and Wang, Z. (2019). Optical Properties and Photocatalytic Applications of Two-Dimensional Janus Group-III Monochalcogenides. *J. Phys. Chem. C* 123, 11388–11396. doi:10.1021/acs.jpcc.8b12450

Hung, N. T., Nugraha, A. R. T., and Saito, R. (2017). Two-dimensional InSe as a Potential Thermoelectric Material. *Appl. Phys. Lett.* 111, 092107. doi:10.1063/1.5001184

Kresse, G., and Furthmüller, J. (1996). Efficient Iterative Schemes Forab Initiototal-Energy Calculations Using a Plane-Wave Basis Set. *Phys. Rev. B* 54, 11169–11186. doi:10.1103/physrevb.54.11169

Kresse, G., and Joubert, D. (1999). From Ultrasoft Pseudopotentials to the Projector Augmented-Wave Method. *Phys. Rev. B* 59, 1758–1775. doi:10.1103/physrevb.59.1758

Lei, C., Ma, Y., Xu, X., Zhang, T., Huang, B., and Dai, Y. (2019). Broken-Gap Type-III Band Alignment in WTe2/HfS2 van der Waals Heterostructure. *J. Phys. Chem. C* 123, 23089–23095. doi:10.1021/acs.jpcc.9b07862

Liu, Y.-L., Shi, Y., and Yang, C.-L. (2021). Two-dimensional MoSSe/g-GeC van der waals heterostructure as promising multifunctional system for solar energy conversion. *Appl. Surf. Sci.* 545, 148952. doi:10.1016/j.apsusc.2021.148952

Lu, A.-Y., Zhu, H., Xiao, J., Chuu, C.-P., Han, Y., Chiu, M.-H., et al. (2017). Janus Monolayers of Transition Metal Dichalcogenides. *Nat. Nanotech* 12, 744–749. doi:10.1038/nnano.2017.100

Massicotte, M., Schmidt, P., Vialla, F., Schädler, K. G., Reserbat-Plantey, A., Watanabe, K., et al. (2016). Picosecond photoresponse in van der Waals heterostructures. *Nat. Nanotech* 11, 42–46. doi:10.1038/nnano.2015.227

Miao, M.-S., Botana, J., Zurek, E., Hu, T., Liu, J., and Yang, W. (2016). Electron Counting and a Large Family of Two-Dimensional Semiconductors. *Chem. Mater.* 28, 1994–1999. doi:10.1021/acs.chemmater.5b03557

Novoselov, K. S., Geim, A. K., Morozov, S. V., Jiang, D., Zhang, Y., Dubonos, S. V., et al. (2004). Electric Field Effect in Atomically Thin Carbon Films. *Science* 306, 666–669. doi:10.1126/science.1102896

Obeid, M. M., Bafekry, A., Ur Rehman, S., and Nguyen, C. V. (2020). A type-II GaSe/HfS2 van der Waals heterostructure as promising photocatalyst with high carrier mobility. *Appl. Surf. Sci.* 534, 147607. doi:10.1016/j.apsusc.2020.147607

Özçelik, V. O., Azadani, J. G., Yang, C., Koester, S. J., and Low, T. (2016). Band Alignment of Two-Dimensional Semiconductors for Designing Heterostructures With Momentum Space Matching. *Phys. Rev. B* 94, 035125. doi:10.1103/PhysRevB.94.035125

Perdew, J. P., Burke, K., and Ernzerhof, M. (1996). Generalized Gradient Approximation Made Simple. *Phys. Rev. Lett.* 77, 3865–3868. doi:10.1103/physrevlett.77.3865

Qiu, B., Zhao, X. W., Hu, G. C., Yue, W. W., Yuan, X. B., and Ren, J. F. (2020). Tuning Optical Properties of Graphene/WSe2 Heterostructure by Introducing Vacancy: First Principles Calculations. *Physica E: Low-dimensional Syst. Nanostructures* 116, 113729. doi:10.1016/j.physe.2019.113729

Ren, K., Zheng, R., Lou, J., Yu, J., Sun, Q., and Li, J. (2021). Ab Initio Calculations for the Electronic, Interfacial and Optical Properties of Two-Dimensional AlN/Zr2CO2 Heterostructure. *Front. Chem.* 9, 796695. doi:10.3389/fchem.2021.796695

Ren, K., Zheng, R., Xu, P., Cheng, D., Huo, W., Yu, J., et al. (2021). Electronic and Optical Properties of Atomic-Scale Heterostructure Based on MXene and MN (M = Al, Ga): A DFT Investigation. *Nanomaterials* 11, 2236. doi:10.3390/nano11092236

Ren, K., Zheng, R., Yu, J., Sun, Q., and Li, J. (2021). Band Bending Mechanism in CdO/Arsenene Heterostructure: A Potential Direct Z-Scheme Photocatalyst. *Front. Chem.* 9, 788813. doi:10.3389/fchem.2021.788813

Shen, Z., Ren, K., Zheng, R., Huang, Z., Cui, Z., Zheng, Z., et al. (2022). The Thermal and Electronic Properties of the Lateral Janus MoSSe/WSSe Heterostructure. *Front. Mater.* 9, 838648. doi:10.3389/fmats.2022.838648

Sun, R. J., Lu, J. J., Zhao, X. W., Hu, G. C., Yuan, X. B., and Ren, J. F. (2022). Robust Valley Polarization Induced by Super-Exchange Effects in HfNX (X= Cl, Br, I)/$FeCl_2$ Two-Dimensional Ferrovalley Heterostructures. *Appl. Phys. Lett.* 120, 063103. doi:10.1063/5.0080466

Wang, V., Xu, N., Liu, J. C., Tang, G., and Geng, W.-T. (2021). VASPKIT: A User-Friendly Interface Facilitating High-Throughput Computing and Analysis Using VASP Code. *Comput. Phys. Commun.* 267, 108033. doi:10.1016/j.cpc.2021.108033

Wu, W., Ao, Z., Wang, T., Li, C., and Li, S. (2014). Electric Field Induced Hydrogenation of Silicene. *Phys. Chem. Chem. Phys.* 16, 16588–16594. doi:10.1039/c4cp01416b

Xu, K., Yin, L., Huang, Y., Shifa, T. A., Chu, J., Wang, F., et al. (2016). Synthesis, Properties and Applications of 2D Layered MIIIXVI(M = Ga, in; X = S, Se, Te) Materials. *Nanoscale* 8, 16802–16818. doi:10.1039/c6nr05976g

Yin, W.-J., Wen, B., Nie, G.-Z., Wei, X.-L., and Liu, L.-M. (2018). Tunable Dipole and Carrier Mobility for a Few Layer Janus MoSSe Structure. *J. Mater. Chem. C* 6, 1693–1700. doi:10.1039/c7tc05225a

Zhang, J., Jia, S., Kholmanov, I., Dong, L., Er, D., Chen, W., et al. (2017). Janus Monolayer Transition-Metal Dichalcogenides. *ACS Nano* 11, 8192–8198. doi:10.1021/acsnano.7b03186

Zhang, W. X., Yin, Y., and He, C. (2021). P Doping Promotes the Spontaneous Visible-Light-Driven Photocatalytic Water Splitting in Isomorphic Type II GaSe/InS Heterostructure. *J. Phys. Chem. Lett.* 12, 7892–7900. doi:10.1021/acs.jpclett.1c02040

Zhao, X. W., Liu, F. J., Ren, J. F., and Qu, F. Y. (2021). Valleytronic and Magneto-Optical Properties of Janus and Conventional TiBrI/CrI3 and Ti X2/CrI3 (X= Br, I) Heterostructures. *Phys. Rev. B.* 104, 085119. doi:10.1103/physrevb.104.085119

Zhou, J., Li, D., Zhao, W., Jing, B., Ao, Z., and An, T. (2021). First-Principles Evaluation of Volatile Organic Compounds Degradation in Z-Scheme Photocatalytic Systems: MXene and Graphitic-CN Heterostructures. *ACS Appl. Mater. Inter.* 13, 23843–23852. doi:10.1021/acsami.1c05617

Zhu, X. T., Xu, Y., Cao, Y., Zhao, Y. Q., Sheng, W., Nie, G.-Z., et al. (2021). Investigation of the Electronic Structure of Two-Dimensional GaN/Zr2CO2 hetero-junction: Type-II Band Alignment with Tunable Bandgap. *Appl. Surf. Sci.* 542, 148505. doi:10.1016/j.apsusc.2020.148505

Conflict of Interest: The authors declare that the research was conducted in the absence of any commercial or financial relationships that could be construed as a potential conflict of interest.

frontiers in Chemistry

ORIGINAL RESEARCH
published: 25 March 2022
doi: 10.3389/fchem.2022.854018

Triazine-Based Conjugated Microporous Polymers With Different Linkage Units for Visible Light–Driven Hydrogen Evolution

Qiannan Sheng*[1]*, Xiujuan Zhong*[1]*, Qianqian Shang*[1]*, YunYun Dong*[1]*, Jinsheng Zhao*[1]*, *Yuchang Du*[2]* *and Yu Xie*[3]

[1]College of Chemistry and Chemical Engineering, Liaocheng University, Liaocheng, China, [2]Key Laboratory of Jiangxi University for Applied Chemistry and Chemical Biology, College of Chemistry and Bioengineering, Yichun University, Yichun, China, [3]College of Environment and Chemical Engineering, Nanchang Hangkong University, Nanchang, China

Conjugated microporous polymers (CMPs), as a kind of two-dimensional material, have attracted extensive attention due to their advantages in visible light–driven photocatalytic splitting of water for hydrogen evolution. However, improving the microstructure and electronic structure of the material to enhance their photocatalytic performance for hydrogen evolution remains a challenge. We designed and reported two analogous CMPs including CMP-1 and CMP-2 that contain triazine and dibenzothiophene-*S*,*S*-dioxide units, which were prepared by Pd-catalyzed Suzuki-Miyaura coupling reaction. The main difference of two CMPs is that the triazine units are connected to benzene unit (CMP-1) or thiophene unit (CMP-2). Both of the CMPs exhibit excellent light capture capability, and compared with CMP-2, CMP-1 has faster separation rates and lower recombination rates for the charge carriers (electron/hole), and then, a higher hydrogen evolution rate was obtained from water decomposition reaction. We find the H_2 production rate of CMP-1 can be up to 9,698.53 μmol $g^{-1}h^{-1}$, which is about twice of that of CMP-2. This work suggests that molecular design is a potent method to optimize the photocatalytic performance toward hydrogen evolution of the CMPs.

Keywords: conjugated microporous polymers, triazine, photocatalytic, hydrogen production, linkage unit

Edited by:
Changhong Wang,
Tianjin University, China

Reviewed by:
Yonggang Xiang,
Huazhong Agricultural University, China
Jayachandran Jayakumar,
National Tsing Hua University, Taiwan

***Correspondence:**
Jinsheng Zhao
j.s.zhao@163.com
Yuchang Du
yuchdu@126.com
Yu Xie
xieyu_121@163.com

Specialty section:
This article was submitted to Catalysis and Photocatalysis, a section of the journal Frontiers in Chemistry

Received: 13 January 2022
Accepted: 23 February 2022
Published: 25 March 2022

Citation:
Sheng Q, Zhong X, Shang Q, Dong Y, Zhao J, Du Y and Xie Y (2022) Triazine-Based Conjugated Microporous Polymers With Different Linkage Units for Visible Light–Driven Hydrogen Evolution.
Front. Chem. 10:854018.
doi: 10.3389/fchem.2022.854018

INTRODUCTION

Hydrogen is a form of clean and high density (120 MJ/kg) energy. If produced efficiently from sunlight-driven photocatalytic splitting of water, then it is anticipated to play an important role in the global effort of realizing carbon neutralization (Fujishima and Honda, 1972; Chen et al., 2010; Linares et al., 2014). In the photocatalytic process, semiconductor catalysts are required to absorb photons and result in the separation and transfer of charge carriers, and the photogenerated electrons are transferred to the protons to produce hydrogen (Turner et al., 2008; Wang et al., 2010; Dincer and Acar, 2015; Shi et al., 2017; Wang L. et al., 2018). Since Fujishima and Honda (1972) found that the decomposition of water into hydrogen and oxygen occurs under the irradiation of light on TiO_2, inorganic semiconductors such as metal oxides and sulfides have been investigated mostly for their photocatalytic ability in water splitting (Chen et al., 2017; Yu et al., 2018; Tsang et al., 2019). However, inorganic catalysts, such as TiO_2 or CdS, are poor light absorbers, susceptible to light corrosion, and often environmentally unfriendly. These limitations have seriously hindered their practical applications and further development (Kudo and Miseki, 2009; Osterloh, 2013; Wang et al., 2019). In recent years, organic polymer catalysts represented by graphitic carbon nitride (GCN) have been well developed, which have the advantages of adjustable energy level and spectral absorption range, environmentally friendly, and the wide availability of raw materials (Dai and Liu, 2020; Jayachandran and Chou, 2020). At present, the pure GCN developed are not competent with the commercial requirements of photocatalytic hydrogen production due to their limited sunlight absorption, high recombination rate of electron/holes, and low photocatalytic activities (Wang et al., 2009; Lin et al., 2016; Cui et al., 2020). Some other types of polymer-based catalysts are also developed over the same period, which are designed and synthesized based on many considerations including the specific active sites (or units), stereo configurations, porous structures, and hydrophilicity (Han et al., 2015; Huang et al., 2015; Yu et al., 2017).

In recent years, certain types of conjugated polymers, such as GCN, conjugated microporous polymers (CMPs) (Wang Z. et al., 2018; Xu et al., 2018; Xiao et al., 2020), linear conjugated porous polymers (CPPs) (Sprick et al., 2018; Bai et al., 2019; Ting et al., 2019), and covalent triazine frameworks (CTFs) (Guo et al., 2019; Huang et al., 2019), have been developed for H_2 evolution. These polymers are adjustable in energy level and spectral absorption range, are environmentally friendly, and can be produced from the widely available raw materials (Dai and Liu, 2020; Jayachandran and Chou, 2020). They can be designed and synthesized to feature specific active sites (or units), stereo configurations, porous structures, hydrophilicity, and dispersibility (Han et al., 2015; Huang et al., 2015; Yu et al., 2017).

Dibenzothiophene-*S*,*S*-dioxide (FSO) has been frequently used as the building unit for the construction of highly active photocatalysts for hydrogen evolution from water splitting because of its aromatic structure, electron deficient character, and its unique function as electron output tentacle (Dai et al., 2018; Zhao et al., 2018). The introduction of the FSO units can help align the energy level for hydrogen evolution and enhance the efficiencies for the separation and transportation of excitons. So far, researchers have synthesized a variety of conjugated polymers containing FSO units, many of which exhibit impressive photocatalytic activities toward hydrogen evolution. Chen et al. found that the CPP P-FSO (**Supplementary Scheme S1**) gives a hydrogen evolution rate (HER) of 8,000 μmol g^{-1} h^{-1} (Lan et al., 2019). Wang et al. reported that the homopolymer of FSO can give a high HER up to 44.2 mmol h^{-1} g^{-1} under visible light irradiation (**Supplementary Scheme S1**) (Shu et al., 2020a). A CMP material S-CMP3 exhibited a HER of 6076 μmol g^{-1} h^{-1} under visible light irradiation (**Supplementary Scheme S1**) (Sprick et al., 2019). Another similar CMP PyDF was also reported, which showed an attractive HER of 18.93 mmol h^{-1} g^{-1} under visible light (**Supplementary Scheme S1**) (Gao et al., 2020). The conjugated polymers containing 1,3,5-triazine unit have been frequently used as photocatalysts, and the nitrogen atoms in the triazine unit have been considered as the active site for the HER reaction because they have lone pair electrons, electron deficient, and hydrophilicity character. Tan et al. prepared some covalent triazine containing frameworks with a D-A_1-A_2 configuration and the highest HER up to 19.3 mmol g^{-1} h^{-1} (Guo et al., 2019). From the study of Jin et al., the polymer CTF-HUST-C1 (**Scheme 1**), a crystalline covalent framework containing triazine unit, gives a HER of 5,100 μmol g^{-1} h^{-1} (Wang et al., 2017).

Therefore, in this work, we synthesized two CMPs, which are constructed from two different triazine derivatives as building units and FSO as linking units, and analyzed their structure and photocatalytic performances. Using triethanolamine (TEOA) as the sacrificial agent and Pt as the co-catalyst, the results showed that CMP-1, a CMP made from benzene rings connecting to a triazine unit, has a HER of 9,699 μmol $g^{-1}h^{-1}$, which is higher than that of CMP-2, an analogous polymer with thiophene unit as the linkage unit.

MATERIALS AND METHODS

Instruments and Reagents

The analytical methods and instruments can be seen in the **Supporting Information** (SI). The reagents and their available sources, and the synthetic procedures for M1 and M3 are also given in SI part.

Synthesis of CMP-1

A 100-ml round bottom flask was charged with 300 mg of M1 (0.6408 mmol), 233.3 mg of M2 (0.4272 mmol), 4 ml of K_2CO_3 (2 M) solution, 16 ml of dioxane, and 37 mg of Pd $(pph_3)_4$ catalyst (5% mol/mol of M1) (**Scheme 1**) (Zhao et al., 2018). The above solution was degassed three times to replace the atmosphere in the flask with nitrogen gas. The flask was heated to reflux in oil bath and be stirred continuously for 48 h. The raw product was cooled down to room temperature and was recovered by filtration, and then, it was washed with ethanol and distilled water successfully and then dried at 100°C under vacuum for 24 h. The crude product was purified by Soxhlet extraction for 24 h, and the solvent used is chloroform, after which the purified product was dried at 80°C overnight. Finally, 229 mg of yellow powder was obtained as CMP-1 with a yield of 78% (Wang Z. et al., 2018).

Synthesis of CMP-2

First, 241 mg of M3 and 300 mg of M1 were added into a round-bottom flask, and then, 4 ml of K_2CO_3 (2 M) solution, 16 ml of dioxane, and 0.037 g of Pd $(pph_3)_4$ were also added subsequently (**Scheme 1**). Second, the mixture was degassed for three times and kept in nitrogen gas environment with the help of a balloon, and the flask was then immersed in an oil bath and was refluxed with magnetic stirring for 48 h (Shu et al., 2020a). After that, the material was obtained by filtration to get a yellow color powder. Last, the sample was dried at 80°C under vacuum for 24 h to get the raw product. The crude product was washed for 24 h with chloroform in a Soxhlet extractor (Shu et al., 2021).

Photocatalytic Hydrogen Production

All the photocatalytic experiments were carried out in a glass-closed gas circulation system with a 100-ml Pyrex glass

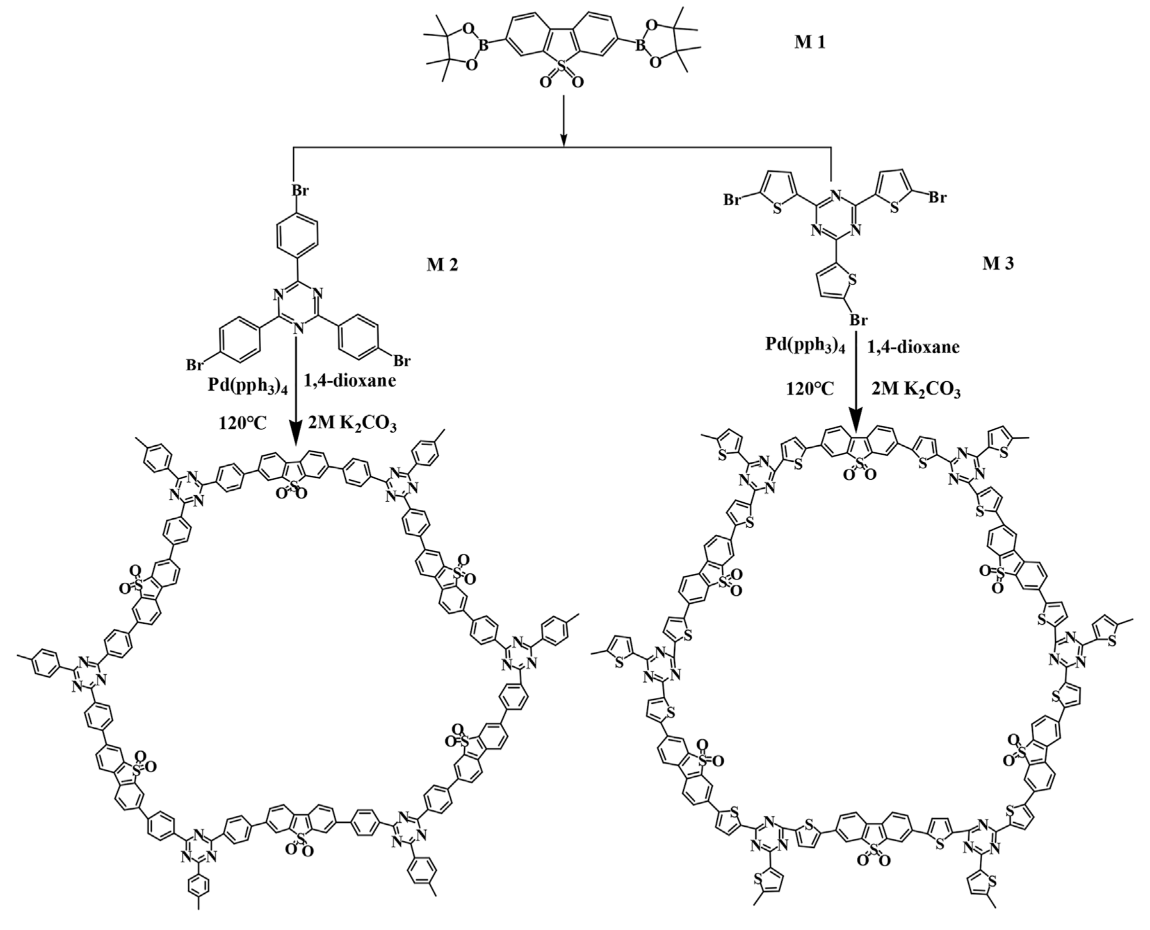

SCHEME 1 | Synthesis of CMP-1 and CMP-2.

reaction vessel as the reactor, and the temperature was maintained at 10°C by a cyclic condensation device. To the above reaction vessel, 20 mg of photocatalyst, 10 ml of TEOA (as sacrificial agent), 10 ml of N-methylpyrrolidone (NMP), and 40 ml of distilled water were added. The catalyst was completely dispersed by ultrasound for 30 min, 24 μl of chloroplatinic acid was added, and then the stirred solution was irradiated with a 300-W Xe lamp (CEL-HXF300) for 3 h to load Pt nanoparticles (3%, w/w) on the catalyst. The Pt-modified photocatalyst can be recovered by filtration and can be used in the following photocatalytic hydrogen evolution experiments. The Xe lamp was equipped with a 420-nm cutoff filter (CEL-UVIRCUT420) to evaluate the visible light–induced photocatalytic activity of the catalysts. Before the light irradiation, the reaction system was pumped for at least 20 min, as far as possible to get rid of the dissolved oxygen in solution, and kept it in a vacuum state. Then, the suspension was stirred for 3 h and irradiated, and the hydrogen evolution was sampled and analyzed every 30 min. The hydrogen produced was detected by gas chromatograph (GC-7920) with a TCD detector. The photocatalysis stability was carried out for five periods with 3 h for one period.

RESULTS AND DISCUSSION

Morphological and Structure Characterization

The microstructures of the CMPs are characterized by scanning electron microscope (SEM) and transmission electron microscope (TEM). According to SEM (**Figures 1A,B**) and TEM (**Figures 1C,D**), the two CMPs have similar morphology and the small particles of them stacked together to form the irregularly shaped aggregation. In addition, the element mapping images (**Figures 1E,F**) are given under SEM by energy-dispersive X-ray spectroscopy (EDS), and it can be seen that four elements C, N, O, and S are evenly distributed in the CMPs. The percentage contents of the four elements are shown in **Supplementary Figure S3**.

Fourier Transform infrared (FT-IR) was used to support the successful preparation of the two CMPs. As shown in **Figure 2A**, a wide peak around 3,430 cm^{-1} is observed, which could be attributed to the characteristic O-H stretching vibration from the trace moisture adsorbed by the CMPs. There are two transmission peaks at 1,505 and 1,370 cm^{-1}, which belong to the stretching vibration of C-N and the in-plane stretching

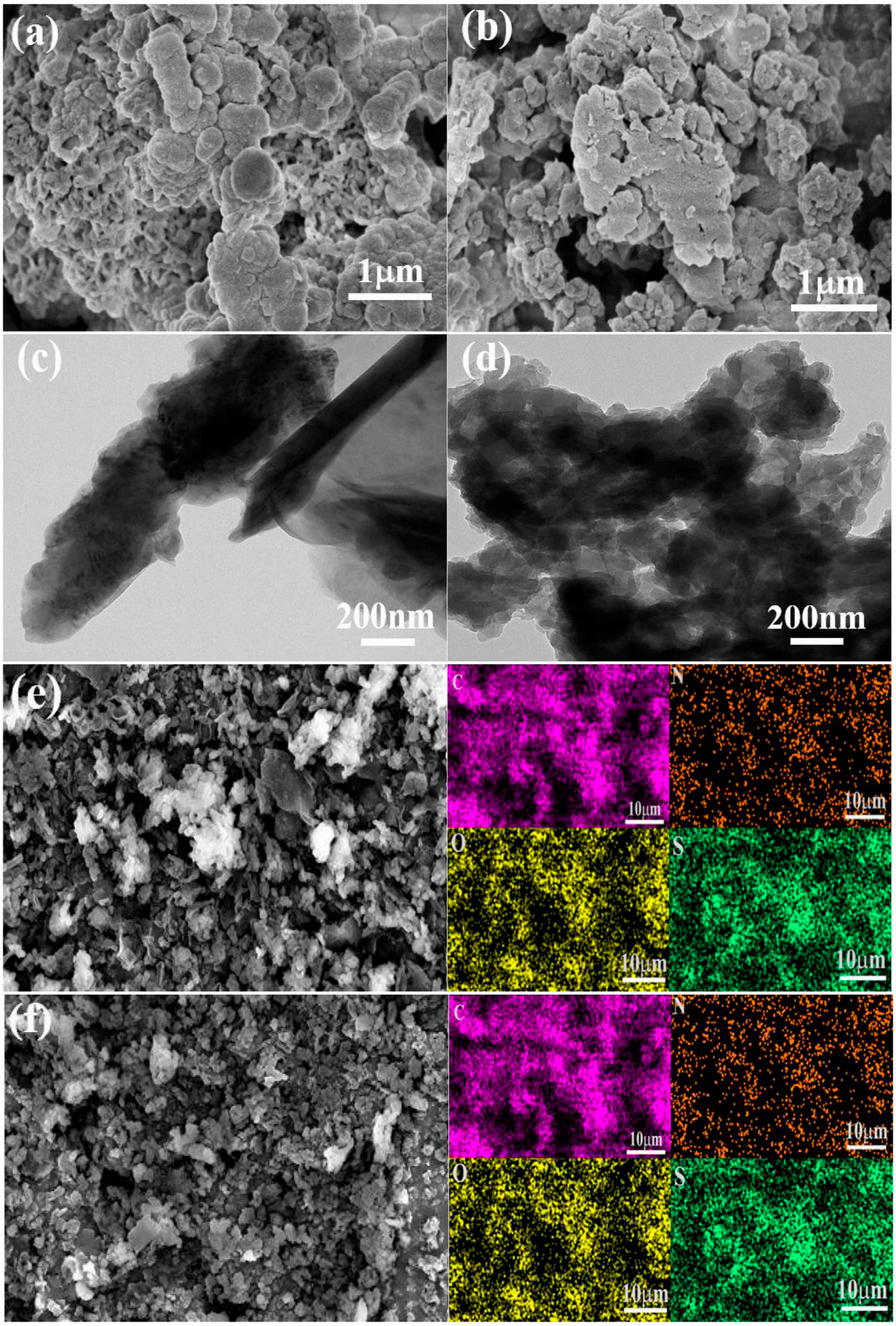

FIGURE 1 | SEM image for CMP-1 **(A)** and CMP-2 **(B)**. TEM image of CMP-1 **(C) and** CMP-2 **(D)**. EDS element mapping images of CMP-1 **(E)** and CMP-2 **(F)**.

vibrations of the triazine ring, respectively (Guo et al., 2019; Gao et al., 2020). The strong peaks at 1,291 and 1,155 cm^{-1} correspond to the characteristic stretching peak of O=S=O group of the FSO unit (Zhang et al., 2020; Shu et al., 2021). The peak at 1,610 cm^{-1} is attributed to skeleton vibrations of aromatic rings. The peak at 788 cm^{-1} is the out-of-plane bending vibration of the C-H bonds, and the peak at 1,028 cm^{-1} is attributed to in-plane bending vibrations of the C-H bonds. The above peaks are the characteristic transmittance peaks shared by the two CMPs, which is also consistent with their similar structures. Different from CMP-1, the CMP-2 exhibits a strong peak at 1,440 cm^{-1}, which belongs to the skeletal vibration of the thiophene unit in

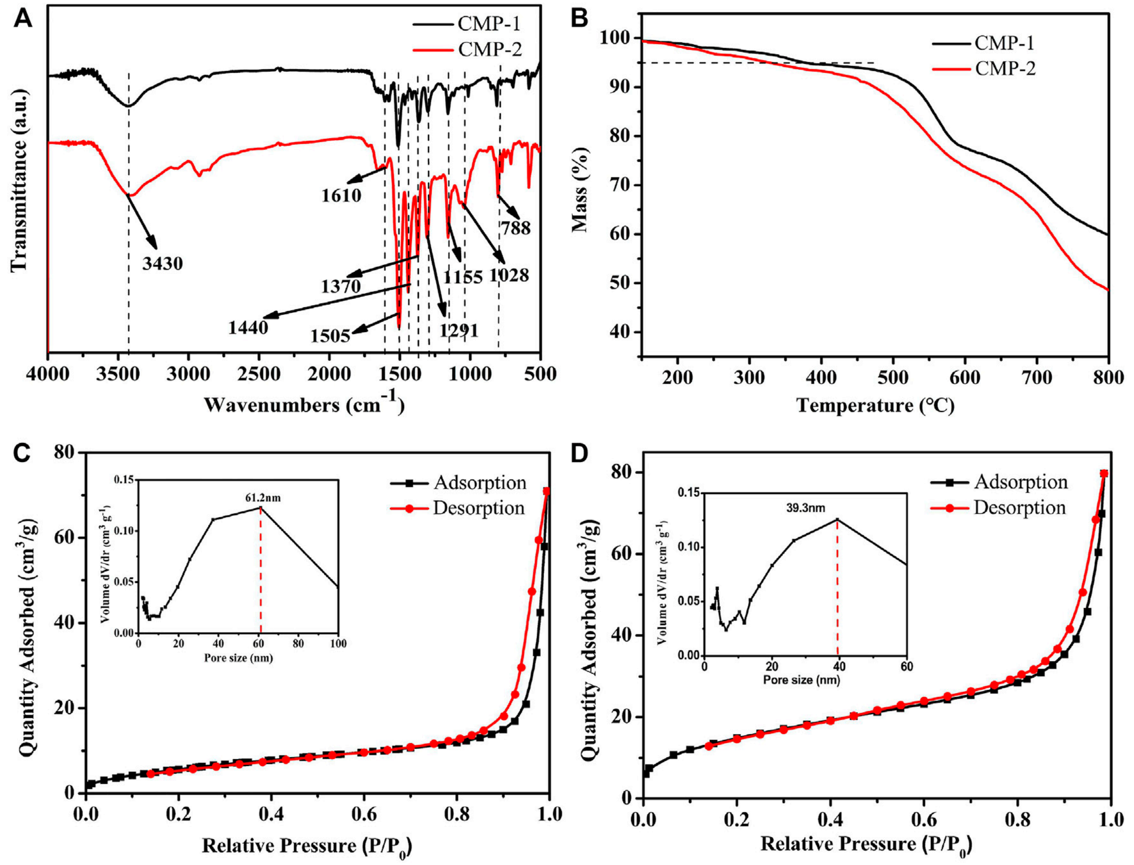

FIGURE 2 | (A) FT-IR spectra of CMPs. **(B)** TGA curves of CMPs. Nitrogen adsorption–desorption isotherms at 77 K and pore size distributions (insets) of **(C)** CMP-1 and **(D)** CMP-2.

CMP-2 (Zhang et al., 2020). From the above analysis, it can be confirmed that the two CMPs are successfully obtained. **Supplementary Figure S4** gives the FT-IR pictures of the CMPs after the photocatalytic reaction, which is identical to that of the as prepared CMPs. The PXRD pattern (**Supplementary Figure S5**) shows that all peaks of the as prepared polymers are broad, indicating the amorphous nature of the materials.

Thermogravimetric analysis (TGA) (**Figure 2B**) was used to analyze the thermal properties of the as prepared CMPs. Because of the rigidity of the polymer skeleton, both of the two CMPs have high initial decomposition temperatures (T_{id}), i.e., 381°C for CMP-1 and 328°C for CMP-2. It is obvious that the T_{id} of CMP-1 is slightly higher than that of CMP-2, although only the benzene unit in CMP-1 was replaced by the thiophene unit in CMP-2. In addition, the characteristics on the surface porosity of the CMPs are also studied. Nitrogen adsorption–desorption experiments were carried out at 77 K; the two polymers showed a similar shape for their isotherms; as shown in **Figures 2C,D**, the two curves are consistent with the type III isotherm. At the low relative pressure region, there is a small amount of absorption, indicating the existence of some micropores. In addition, at the higher P/P0 region (0.85–1.0), the isotherm rises rapidly (likely due to capillary condensation of N_2) and hysteresis was observed for the desorption of N_2. The hysteresis in the desorption curve is due to the elastic deformation or swelling behavior caused by the N_2 adsorption process (Zhou et al., 2019). The Brunner-Emmet-Teller (BET) surface areas of CMP-1 and CMP-2 are 54.77 and 22.92 m^2/g, respectively. In the embedded diagram of **Figures 2C,D**, it can be seen that the pore size distribution of CMP-1 is mainly between 10 and 100 nm and is centered at 61.2 nm, and pore size distribution for CMP-2 is mainly between 10 and 70 nm and is centered at 39.3 nm. In addition, there are few micropores within the CMPs, as shown by the minor peaks at less than 10 nm (Zhang et al., 2020).

X-Ray Photoelectron Spectroscopy (XPS) Analysis

XPS is used to analyze the surface compositions and element states of two CMPs. It can be seen from the survey spectrum (**Figure 3A**), both of two CMPs contain the elements of C, N, O, and S, which is consistent with the above EDS data. **Figures 3B–E** correspond to the XPS spectra of C 1s, N 1s, O 1s, and S 2p, respectively, for CMP-1. After the peak differentiating analysis, three definite peaks can be distinguished from the C 1s spectrum

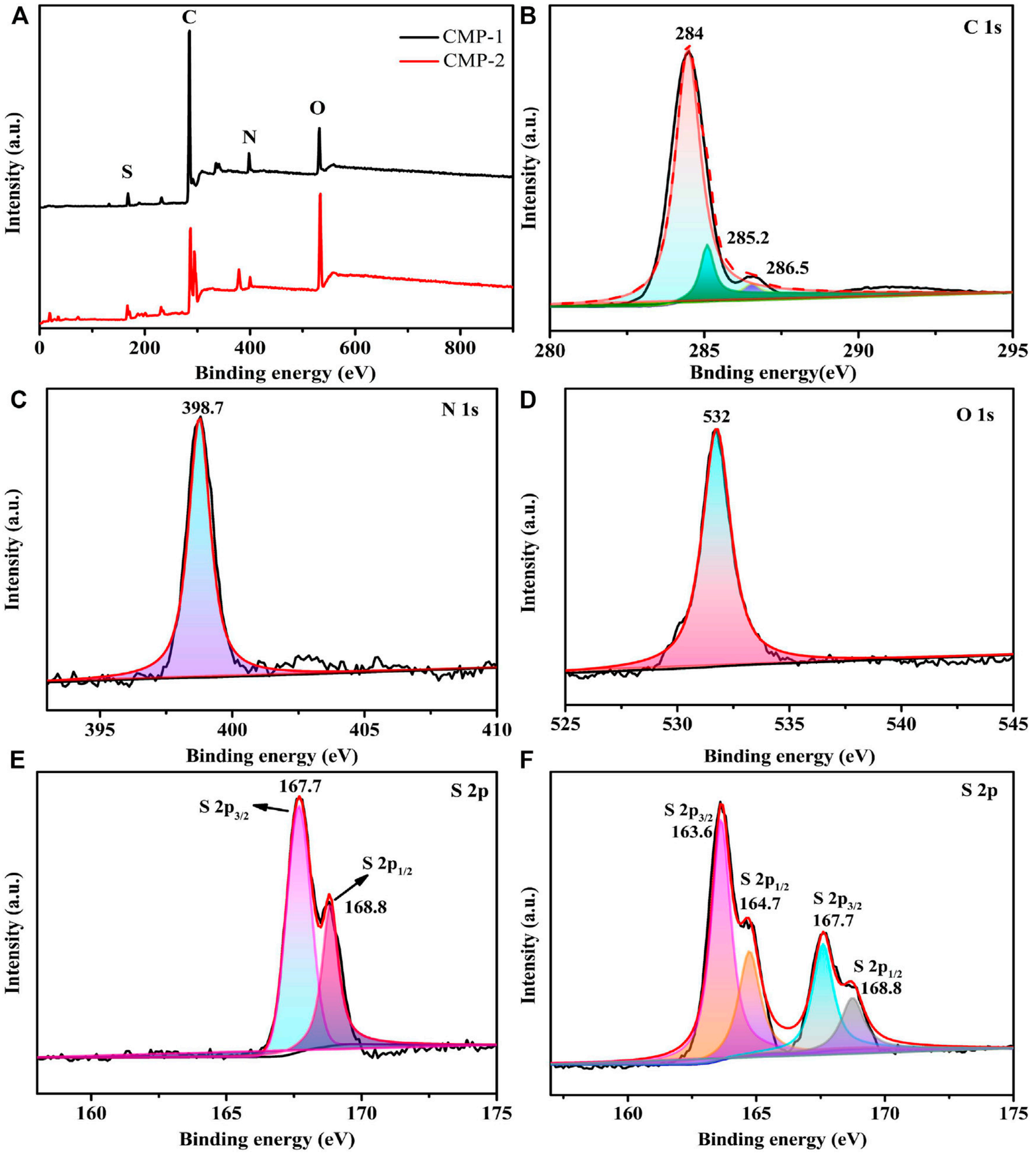

FIGURE 3 | XPS survey spectrum **(A)**; high resolution XPS spectra of C 1s region **(B)**, N 1s region **(C)**, O 1s region **(D)**, and S 2p region of CMP-1 **(E)**; and high resolution XPS spectra of S 2p region of CMP-2 **(F)**.

of CMP-1 (**Figure 3B**), and the binding energies (BEs) are 284.0, 285.2, and 286.5 eV, which belong to the carbon atoms in the C-C/C=C, C=N, and C-S, respectively. For the N 1s spectrum (**Figure 3C**), the peak with a BE value of 398.7 eV belongs to the pyridine nitrogen atom (-C=N-C) in the triazine ring. As shown in **Figure 3D**, the peak with a BE value of 532 eV was identified, which belong to the O 1s of the oxygen atom in the O=S unit within CMP-1. Two distinct peaks are identified in the S 2p spectrum (**Figure 3E**), and their BE values are 167.7 and 168.8 eV, respectively, which correspond to S $2p_{3/2}$ and S $2p_{1/2}$ of the sulfur atom in the O=S=O unit in the CMP-1. The above elements and their corresponding valence states confirmed the formation of CMP-1. The survey scan and the high resolution XPS spectra of the C, N, and O elements of CMP-2 are identical to that of CMP-1, which are consistent with their structural differences, lying in the branched unit, i.e., benzene for CMP-1 and thiophene for CMP-2. To identify the structure of CMP-2, the S 2p spectrum is given in **Figure 3F**; the former two peaks with lower BE values at 163.6 and 164.7 eV correspond to the S $2p_{3/2}$ and the S $2p_{1/2}$ of the sulfur atom in the C-S-C bond of the thiophene unit and the two

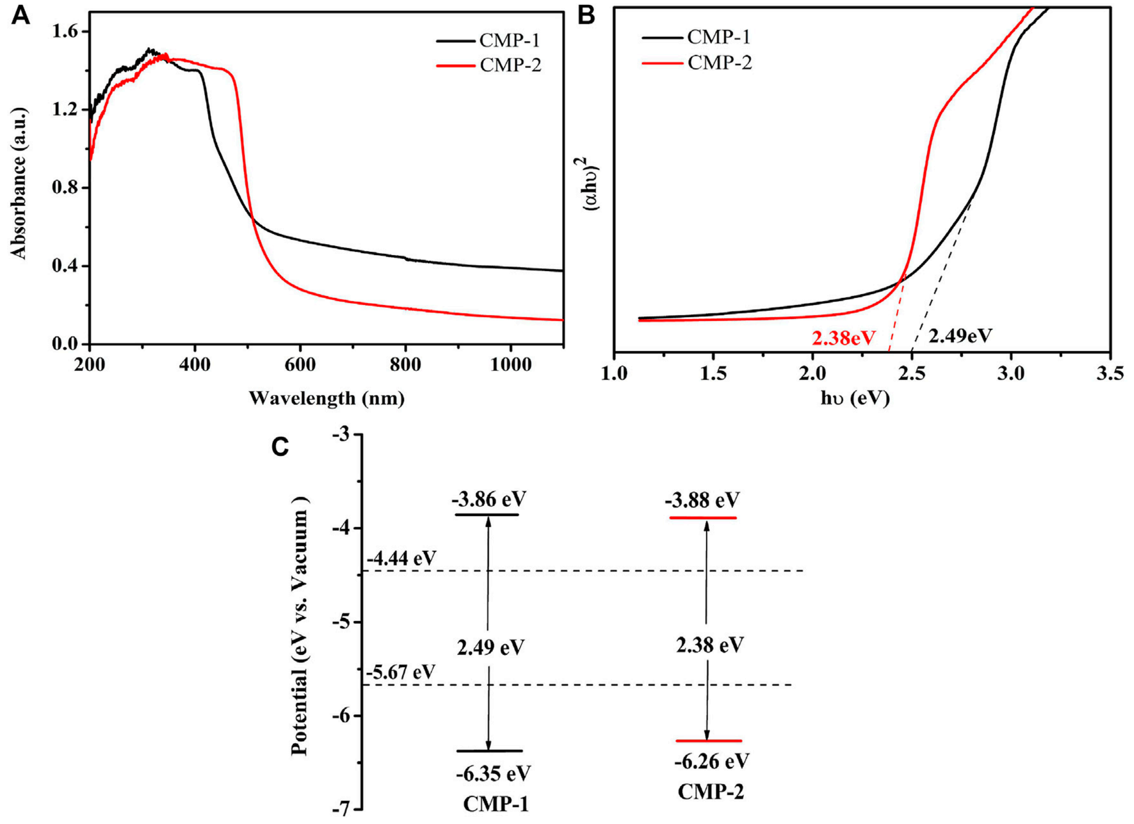

FIGURE 4 | (A) UV-vis absorption spectra of CMP-1 and CMP-2. **(B)** $(\alpha hv)^2$ vs. *hv* curve of CMP-1 and CMP-2. **(C)** The band structure diagram of the CMPs.

latter peaks with higher BE values are found at 167.7 and 168.8 eV, respectively, which correspond to the S $2p_{3/2}$ and the S $2p_{1/2}$ of the sulfur atom in the O=S=O unit. The existence of two valence sulfur atoms is completely consistent with the structure of CMP-2, which confirms the successful preparation of CMP-2 (Shu et al., 2020b).

Band Structure Analysis

For further explore the catalytic performance of the prepared CMPs, the absorbances of them were analyzed by UV-Vis diffuse reflectance spectra (UV-Vis-DRS) (**Figure 4A**). The two CMPs have a wide absorption range, the coverage for CMP-1 is 300–599 nm, which, for CMP-2, is 300–560 nm; both have a strong absorption in the visible range. The following Kubelka–Munk formula was used to draw the Tauc plot (Cui et al., 2020):

$$ahv = A\left(hv - E_g\right)^2 \tag{1}$$

From the Tauc plot as shown in **Figure 4B**, the optical band gaps of the polymers are calculated to be 2.49 and 2.38 eV, respectively, for CMP-1 and CMP-2. The CMPs were also studied by cyclic voltammetry (**Supplementary Figure S6**), the onset reduction potentials ($E_{\text{onset,re}}$) of them were determined, and the lowest unoccupied molecular orbital (LUMO) levels were estimated to draw their band structure diagrams. In addition, the relevant calculations were done using the following formula (Zhang et al., 2020):

$$E_{LUMO} = -e\left[4.8 + \left(E_{onset,re} - 0.5\right)\right] \tag{2}$$

$$E_{HOMO} = E_{LUMO} + E_g \tag{3}$$

In **Eq. 3**, E_g refers to the optical band gaps of the CMPs, the value of 0.5 V is the half wave potential of ferrocene [E (Fc/Fc$^+$) vs. Ag/AgCl], and the $E_{\text{onset,re}}$ values of CMP-1 and CMP-2 are −0.44 and −0.42 V (vs. Ag/AgCl), respectively. The LUMO energy levels of the CMPs are calculated to be −3.86 and −3.88 eV (vs. vacuum), respectively, and the highest occupied molecular orbital (HOMO) levels of two CMPs were calculated to be −6.35 and −6.26 eV, respectively, for COF-1 and COF-2. Then, the band structure diagrams of the polymers are calculated and drawn, as shown in **Figure 4C**. The Mott–Schottky curve of the two CMPs was tested at different frequencies (**Supplementary Figure S7**), both of the materials have a positive slope in the graph regardless of the changes, which is the characteristic of the n-type semiconductors, and the flat band potential (V_{fb}) of CMP-1 and CMP-2 measured from the M-S plots were −0.59, −0.57 V vs. Ag/AgCl, corresponding to −0.38, −0.36 V vs. NHE, respectively, which is equal to the Fermi level (EF) for an n-type semiconductor (Shu et al., 2020b). Meanwhile, the conduction bands (CBs) of the polymers CMP-1 and CMP-2 are calculated to be −0.58 eV (−3.86 eV vs. vacuum) and −0.56 eV

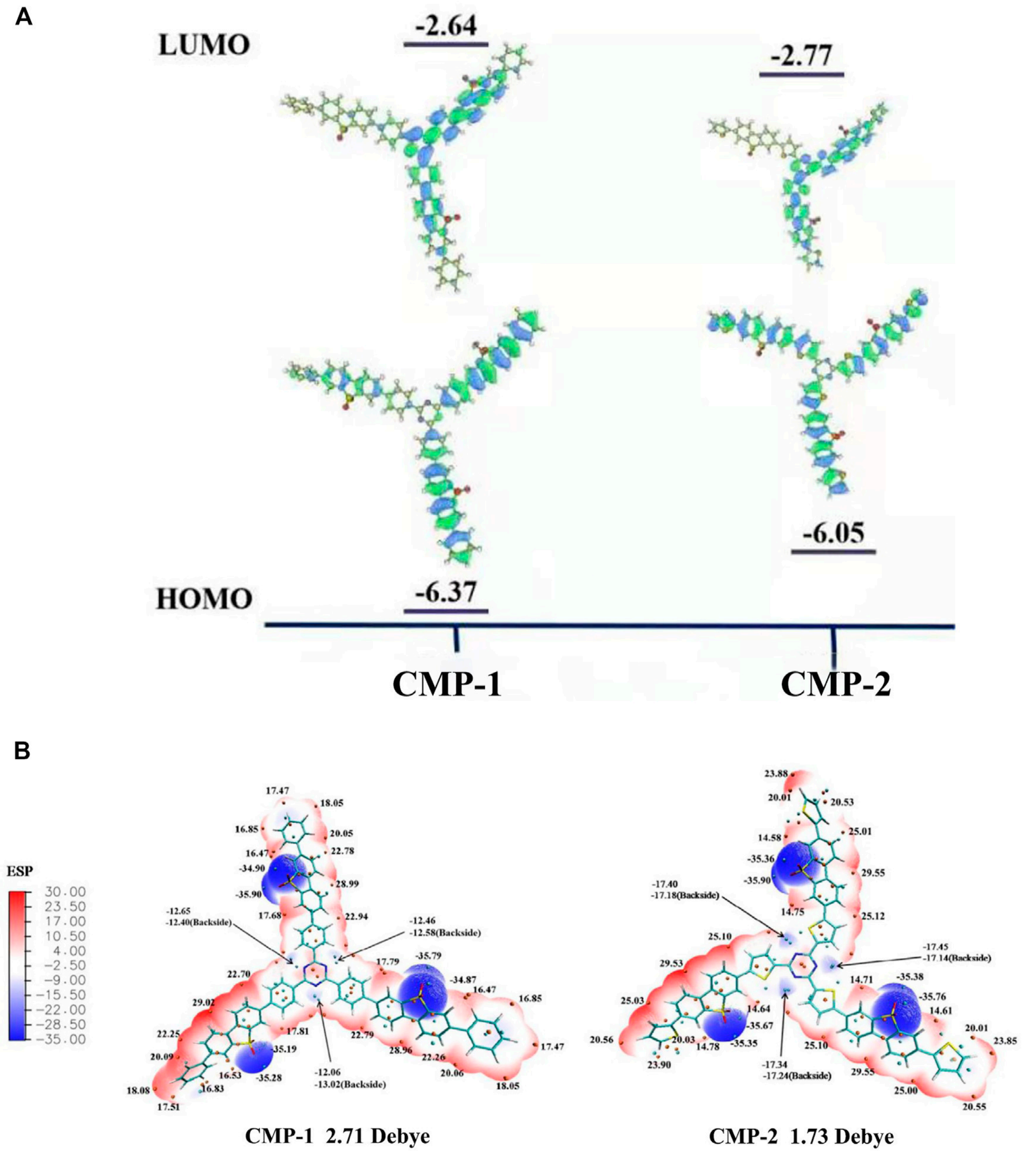

FIGURE 5 | (A) HOMO and LUMO orbits distribution of the polymers from DFT calculation. **(B)** Diagram of molecular dipoles and surface electrostatic potential in CMP-1 and CMP-2.

(−3.88 eV vs. vacuum), respectively. Combined with the band gap value, the valence bands (VBs) of CMP-1 and CMP-2 are calculated to be 1.91 eV (−6.35 eV vs. vacuum) and 1.82 eV (−6.26 eV vs. vacuum), respectively. The HOMO and LUMO data from the Mott–Schottky are consistent with the data from the cyclic voltammetry (CV) results.

Theoretical calculation (density functional theory (DFT)) was conducted on the basic repeated unit of two CMPs to get useful information on their electronic energy levels. For the fragmental unit of CMP-1, the electron density of its HOMO orbital is mainly delocalized over the benzene-FSO-benzene moiety. For the LUMO orbital of CMP-1, its electron density mainly resides on the π* orbital of the triazine-benzene-FSO moiety (**Figure 5A**). CMP-2 has a similar electronic structure as that of CMP-1 (**Figure 5A**). CMP-1 has a slightly higher CB and a lower VB than that CMP-2 (**Figure 5A**), which support the experimental studies of two CMPs. According to the band gap structure discussed above, CMP-1 has both the higher reduction ability and oxidation ability than that of the CMP-2, although the former has a slight narrow light absorption range than the latter one. The intramolecular dipoles of two CMPs could be calculated from the surface

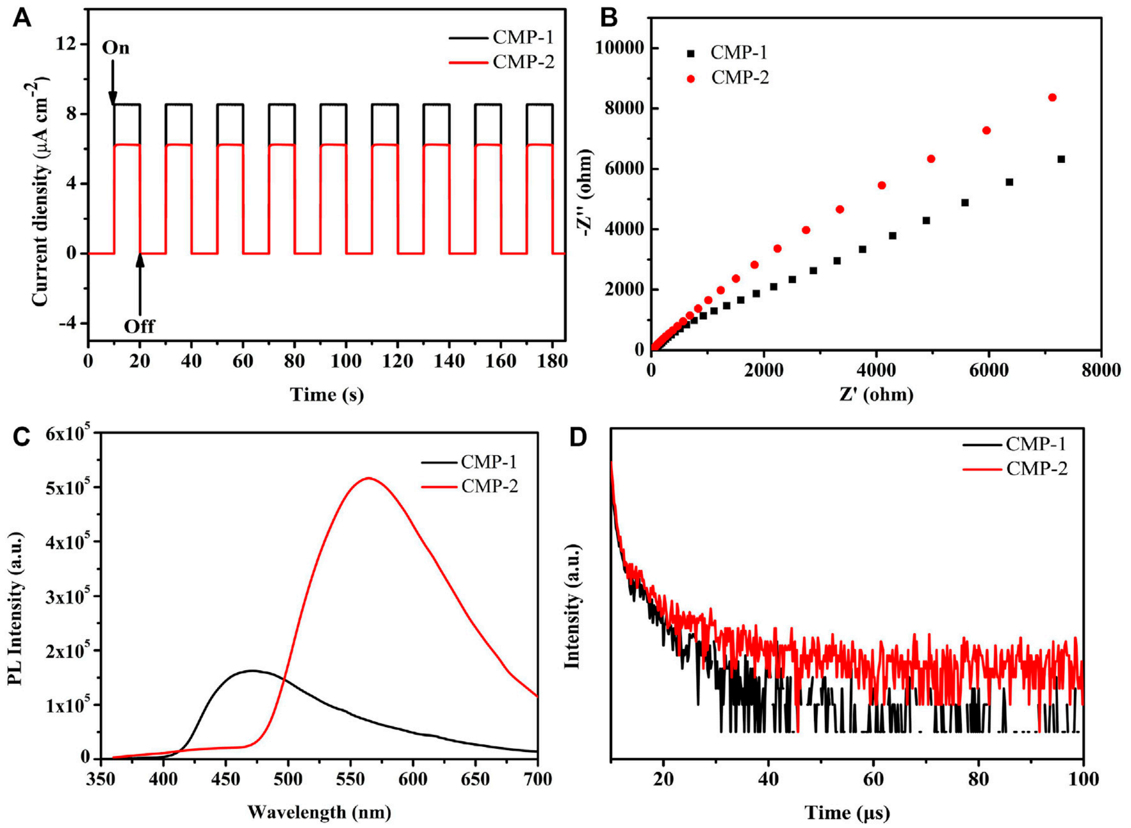

FIGURE 6 | (A) Photocurrent of the CMPs (in 0.5 M Na_2SO_4); **(B)** EIS Nyquist plots of the CMPs; **(C)** PL spectra of the CMPs; **(D)** time-resolved PL spectra of the CMPs.

electrostatic potentials of them (**Figure 5B**), because the CMPs contained both electron donor units (benzene or thiophene) and electron acceptor units (triazine and FSO unit), which contributed to the formation of internal electric field. As calculated, molecular dipoles are 2.71 and 1.73 debye, respectively, for CMP-1 and CMP-2. The increase in molecular dipoles has a positive effect on the separation and transfer of photogenerated carriers, which would result in the higher HER of CMP-1 and CMP-2. The change of the constituent units in the molecular structure would regulate the electronic structures and photocatalytic activities of the catalysts (Ye et al., 2020).

Photo-Induced Charge Carriers and Their Transportation

The photoelectron separation efficiencies of the polymers are also studied. **Figure 6A** shows the transient photocurrents of the two polymers, which were induced by a lamp source equipped with a 420-nm filter and with a biased voltage of 0 V on the photocatalyst-coated ITO electrode. The illumination time and the interval time are 10 s, respectively, and the amplitudes of the photocurrents for both catalysts remained stable levels up to nine cycles of the on-off illumination switch, which indicates that the photocatalysts have stable efficiencies for the separation and generation of the photogenerated carriers (Huang et al., 2015).

Besides, it is clearly shown that CMP-1 has a higher photocurrent response than that of CMP-2 (**Figure 6A**), which suggested that the former catalyst has higher generation/separation efficiencies for the photogenerated carriers than that of the latter catalyst (Huang et al., 2015). The electrochemical impedance spectra (EIS) was also conducted for two catalysts. It is accepted that the smaller radius of the arc, the smaller charge transfer resistance on the electrode surface, suggesting the faster transportation of the surface charge. As shown in **Figure 6B**, the data indicate that CMP-1 has a faster electron transfer process than that of CMP-2 because the semicircular radius of the CMP-1 is somewhat smaller than that of CMP-2 (Han et al., 2015). Photoluminescence spectroscopy was also conducted to compare the recombination rates of the electron/hole charge carriers of the catalysts. As shown in **Figure 6C**, the emission peak positions of the polymers locate at 470 nm for CMP-1 and 565 nm for CMP-2; the blue shift for CMP-1 was due to its wider band gap than that of CMP-2; and, then, the energy required the photon generation of CMP-1 is higher than that of the CMP-2 (Cui et al., 2020). The emission wavelength of CMP-1 is shorter than that of CMP-2, and the emission intensity of CMP-1 is

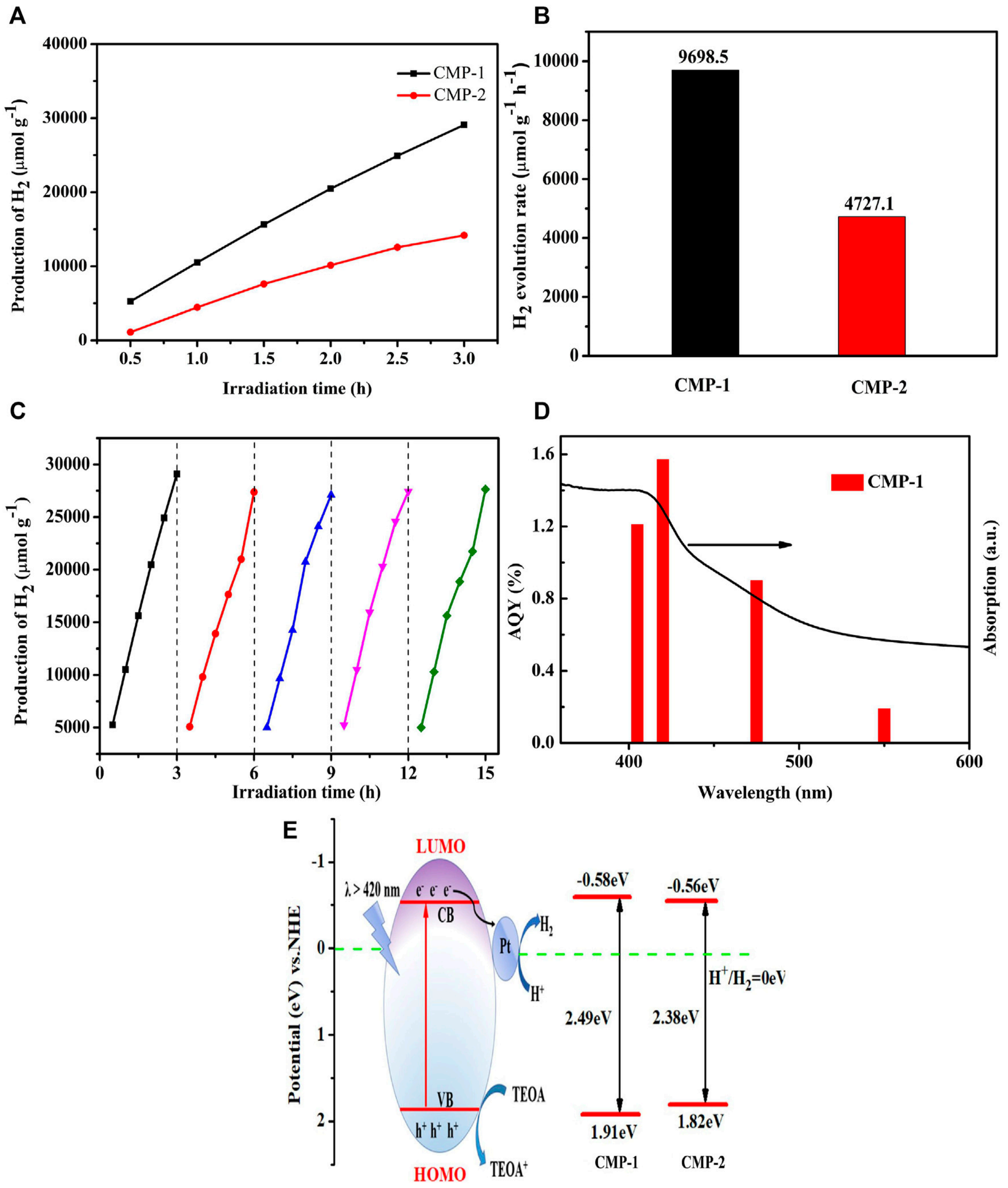

FIGURE 7 | (A) The time-dependent hydrogen production of the CMP materials; **(B)** comparison of photocatalytic H_2 evolution activity of CMP-1 and CMP-2; **(C)** the photocatalytic experiment with CMP-1 over five periods, 3 h for each period; **(D)** wavelength dependent AQY values of CMP-1, and a 300-W Xenon-lamp equipped with series of band-pass filters (405, 420, 455, and 550 nm) is used as light source; **(E)** energy diagram and photocatalytic hydrogen evolution mechanism.

significantly lower than that of CMP-2. The phenomenon reveals that CMP-1 has more sluggish recombination rate of the electron/hole charge carriers than that of CMP-2, which would make CMP-1 have more efficient HER than that of CMP-2 (Jayachandran and Chou, 2020). Time-resolved fluorescence spectroscopy (TRFS) was also conducted for evaluating the recombination rate of the electron/hole couples (**Figure 6D**), and the decay curves of the CMPs can be well fitted by a triple-exponential decay. The fluorescence lifetimes of CMP-1 were calculated to be τ_1 = 0.7990 μs (78.34%) and τ_2 = 6.6269 μs (21.66%), and the data for CMP-2 were calculated to be τ_1 = 0.6284 μs (59.60%) and τ_2 = 7.3962 μs (40.40%). The average lifetime of CMP-1 is 4.86 μs, which is shorter than that of CMP-2 (6.64 μs); this phenomenon indicates that CMP-1 has a higher separation efficiency for charge carriers (or excitons) than that of the CMP-2 (Gao et al., 2020). The fast separation efficiency for

TABLE 1 | The photocatalytic H_2 evolution rate of some CMPs.

Polymer	Optical gap (eV)	Light source[a]	HER (μmol h^{-1} g^{-1})	Cocatalyst	AQY[b] (%)	References
B-BT-1,3,5	2.44	≥420 nm	400	Pt	-	Yang et al. (2016)
L-PyBT	2.23	≥420 nm	1,674	Pt	-	Cheng et al. (2018)
OB-POP-1	2.21	≥420 nm	134	Pt	-	Bi et al. (2017)
OB-POP-2	2.28	≥420 nm	598	Pt	-	Bi et al. (2017)
OB-POP-3	2.14	≥420 nm	908	Pt	2.0	Bi et al. (2017)
OB-POP-4	2.37	≥420 nm	620	Pt	-	Bi et al. (2017)
4-CzPN	2.11	≥420 nm	2,103.2	Pt	6.4	Zhang et al. (2019)
CMP-1	2.49	≥420 nm	9,698.5	Pt	1.57	[this work]
CMP-2	2.38	≥420 nm	4,727.1	Pt	0.11	[this work]

[a] *Xe, Xenon lamp.*

[b] *At 420 nm; HER, hydrogen evolution rate; AQY, apparent quantum yield; TEOA, triethanolamine.*

charge carriers is usually favorable to improve the photocatalytic activity of the catalysts.

Photocatalytic H_2 Production Evolution

The photocatalytic performance of the CMPs was measured using TEOA as the sacrificial agent under the illumination of visible light (≥420 nm), the HERs are recorded every 0.5 h for up to 3 h in five periods, and the resulting data are shown in **Figure 7A**. The average HER (**Figure 7B**) for CMP-1 is 9,698.5 μmol g^{-1} h^{-1} and the value for CMP-2 is about 4,727.1 μmol g^{-1} h^{-1}; the HER for CMP-1 is twice as large as that of CMP-2. In addition; we also conducted the repeated irradiation experiments to study their stability as hydrogen evolution catalysts. As recorded in **Figures 7A,C**, slight decrease in HER was observed for CMP-1 at the second period. From then on and up to the fifth period, nearly no perceptible decline was observed, a reduction by 6% in HER occurs from the first period to the fifth period. The stability in HERs for CMP-2 (**Supplementary Figure S8**) was also measured for five periods and 3 h for each period. Compared with the first period, the HER for the fifth cycle decreased by 41%. This further indicates that the performance of CMP-1 is higher than that of CMP-2 in terms of HER and stability. Among the CMPs reported previously, the two CMPs in this study present fairly decent performance as shown in **Table 1** (Ye et al., 2020; Yang et al., 2016; Cheng et al., 2018; Bi et al., 2017; Zhang et al., 2019). The apparent quantum yield (AQY) values of CMP-1 at four different wavelengths are given in **Figure 7D**, showing the consistence of its photocatalytic activity with its absorption curve. At the wavelength of 420 nm, the AQY value of CMP-1 is 1.57%, and CMP-1 catalyst can work under the broad absorption region between 360 and 600 nm with an AQY value of 0.19% at 550 nm. For comparison, the AQY values of CMP-2 are 0.81% and 0.11%, respectively, at 420 and 550 nm. Detailed control experiments were conducted to understand the indispensable characteristic of catalyst and light irradiation for hydrogen evolution process. In the process of hydrogen evolution experiment, the xenon lamp was turned off randomly, and the hydrogen production stopped increasing. When the light is turned on again, the hydrogen production returned to increasing. In addition, in the other control experiment, the experiment was conducted as the normal hydrogen production conditions except that the photocatalyst was not added in the Pyrex glass bottle, and, in this case, no hydrogen production was detected under the irradiation of the full spectrum light. After the purification process by Soxhlet extraction using chloroform, the residual Pd content of Pd was about 1,021 ppm for CMP-1 and 1,046 ppm for CMP-2. Although the residual Pd catalyst has been considered to play a significant role in the photocatalytic hydrogen production of conjugated polymers, even at ppm level concentrations, and in these studies, the additional Pt nanoparticles are not used as the co-catalyst (Kosco et al., 2018). With the addition of Pt co-catalyst, the residual Pd catalyst will play a very limited role on the hydrogen evolution activity of conjugated polymers.

Photocatalytic Mechanism

On the basis of the discussion, a hydrogen production mechanism (**Figure 7E**) over the present photocatalyst is proposed. The photocatalytic reaction is triggered as the light irradiation initiates the separation of the photogenerated carriers. The photoelectrons in the filled VB of the CMP are driven to the empty CB by the absorbed photons. The photogenerated electrons are captured by the FSO unit, which is considered as the electron-output “tentacle” and then transfers the electrons to the surface of the Pt co-catalyst (Dai et al., 2018). Electrons eventually combine with hydrogen protons in water on the surface of the Pt co-catalyst to produced hydrogen gas. The holes left in the VB are consumed by the oxidation reaction of TEOA (Wang Z. et al., 2018). It is found that CMP-1 has a faster electron/hole separation rate and a lower electron/hole recombination rate than that of CMP-2, although the difference between them only lies in that the benzene unit (as the arm unit) in CMP-1 is replaced by the thiophene unit in CMP-2. A higher LUMO level of CMP-1 allows the Pt Fermi energy to be raised to a higher level when electrons are transferred from the photocatalyst to Pt, thereby leading to a higher HER. Meanwhile, the HOMO of the CMP-1 has a slightly more positive potential than that of CMP-2, indicating that the generated holes in the VB of the CMP-1 have a greater oxidative capacity than that of the CMP-2 (Xiao et al., 2020). The above discussions explained the higher HER of CMP-1 than that of CMP-2.

CONCLUSION

In summary, we reported here the design and synthesis of two CMPs containing benzene (or thiophene) armed triazine and FSO unit. The triazine and FSO-based CMPs offer now choices of robust photocatalysts with broad visible light absorption range and suitable energy level alignments. The benzene-containing CMP-1 has some advantages over the thiophene containing homolog CMP-2, including the lower recombination rate for electron/hole carriers and the higher separation and migration rates for the photogenerated charge carriers. As the bridging unit changes from benzene to thiophene, the HERs of the catalysts alter from 9,698.5 μmol g^{-1} h^{-1} to 4,727.1 μmol g^{-1} h^{-1}. The difference in the catalytic performances obviously originates from the different linker unit employed. In addition, CMP-1 has higher molecular dipoles than that of CMP-2, which may cause a much faster charge mobility in CMP-1 than that in CMP-2. The present study demonstrates that the rational molecular design for CMP materials by selecting ideal bridging units is still one of the effective ways to obtain CMP-based photocatalysts toward hydrogen evolution from water splitting.

DATA AVAILABILITY STATEMENT

The original contributions presented in the study are included in the article/**Supplementary Material**, further inquiries can be directed to the corresponding authors.

AUTHOR CONTRIBUTIONS

QS: Writing—original draft. XZ: Formal analysis. YnD: Methodology. JZ: Writing—review and editing. YcD: Writing—review and editing. YX: Project administration.

FUNDING

The work was financially supported by the National Natural Science Foundation of China (22172069).

SUPPLEMENTARY MATERIAL

The Supplementary Material for this article can be found online at: https://www.frontiersin.org/articles/10.3389/fchem.2022.854018/full#supplementary-material

REFERENCES

Bai, Y., Wilbraham, L., Slater, B. J., Zwijnenburg, M. A., Sprick, R. S., and Cooper, A. I. (2019). Accelerated Discovery of Organic Polymer Photocatalysts for Hydrogen Evolution from Water through the Integration of experiment and Theory. *J. Am. Chem. Soc.* 141, 9063–9071. doi:10.1021/jacs.9b03591

Bi, S., Lan, Z.-A., Paasch, S., Zhang, W., He, Y., Zhang, C., et al. (2017). Substantial Cyano-Substituted Fully Sp2 -Carbon-Linked Framework: Metal-free Approach and Visible-Light-Driven Hydrogen Evolution. *Adv. Funct. Mater.* 27, 1703146. doi:10.1002/adfm.201703146

Chen, S., Takata, T., and Domen, K. (2017). Particulate Photocatalysts for Overall Water Splitting. *Nat. Rev. Mater.* 2, 17050–17066. doi:10.1038/natrevmats.2017.50

Chen, X., Shen, S., Guo, L., and Mao, S. S. (2010). Semiconductor-based Photocatalytic Hydrogen Generation. *Chem. Rev.* 110, 6503–6570. doi:10.1021/cr1001645

Cheng, C., Wang, X., Lin, Y., He, L., Jiang, J.-X., Xu, Y., et al. (2018). The Effect of Molecular Structure and Fluorination on the Properties of Pyrene-Benzothiadiazole-Based Conjugated Polymers for Visible-Light-Driven Hydrogen Evolution. *Polym. Chem.* 9, 4468–4475. doi:10.1039/c8py00722e

Cui, Z., Hu, Y., Zhang, Y., Han, Q., Wang, Y., Zhou, Y., et al. (2020). A New Triazine-Based Conjugated Polymer from Simple Monomers with Stable Photocatalytic Hydrogen Evolution under Visible Light. *Polymer* 211, 123079. doi:10.1016/j.polymer.2020.123079

Dai, C., and Liu, B. (2020). Conjugated Polymers for Visible-Light-Driven Photocatalysis. *Energy Environ. Sci.* 13, 24–52. doi:10.1039/c9ee01935a

Dai, C., Xu, S., Liu, W., Gong, X., Panahandeh-Fard, M., Liu, Z., et al. (2018). Dibenzothiophene-S,S -Dioxide-Based Conjugated Polymers: Highly Efficient Photocatalyts for Hydrogen Production from Water under Visible Light. *Small* 14, 1801839. doi:10.1002/smll.201801839

Dincer, I., and Acar, C. (2015). A Review on Clean Energy Solutions for Better Sustainability. *Int. J. Energ. Res.* 39, 585–606. doi:10.1002/er.3329

Fujishima, A., and Honda, K. (1972). Electrochemical Photolysis of Water at a Semiconductor Electrode. *Nature* 238, 37–38. doi:10.1038/238037a0

Gao, X., Shu, C., Zhang, C., Ma, W., Ren, S.-B., Wang, F., et al. (2020). Substituent Effect of Conjugated Microporous Polymers on the Photocatalytic Hydrogen Evolution Activity. *J. Mater. Chem. A.* 8, 2404–2411. doi:10.1039/c9ta13212k

Guo, L., Niu, Y., Razzaque, S., Tan, B., and Jin, S. (2019). Design of D-A1-A2 Covalent Triazine Frameworks via Copolymerization for Photocatalytic Hydrogen Evolution. *ACS Catal.* 9, 9438–9445. doi:10.1021/acscatal.9b01951

Han, Q., Wang, B., Zhao, Y., Hu, C., and Qu, L. (2015). A Graphitic-C 3 N 4 "Seaweed" Architecture for Enhanced Hydrogen Evolution. *Angew. Chem. Int. Ed.* 54, 11433–11437. doi:10.1002/anie.201504985

Huang, W., He, Q., Hu, Y., and Li, Y. (2019). Molecular Heterostructures of Covalent Triazine Frameworks for Enhanced Photocatalytic Hydrogen Production. *Angew. Chem. Int. Ed.* 58, 8676–8680. doi:10.1002/anie.201900046

Huang, Z. a., Sun, Q., Lv, K., Zhang, Z., Li, M., and Li, B. (2015). Effect of Contact Interface between TiO2 and G-C3n4 on the Photoreactivity of G-C3N4/TiO2 Photocatalyst: (0 0 1) vs (1 0 1) Facets of TiO2. *Appl. Catal. B: Environ.* 164, 420–427. doi:10.1016/j.apcatb.2014.09.043

Jayachandran, J., and Chou, H. (2020). Recent Advances in Visible-Light-Driven Hydrogen Evolution from Water Using Polymer Photocatalysts. *ChemCatChem* 12, 689–704. doi:10.1002/cctc.201901725

Kosco, J., Sachs, M., Godin, R., Kirkus, M., Francas, L., Bidwell, M., et al. (2018). The Effect of Residual Palladium Catalyst Contamination on the Photocatalytic Hydrogen Evolution Activity of Conjugated Polymers. *Adv. Energ. Mater.* 8, 1802181. doi:10.1002/aenm.201802181

Kudo, A., and Miseki, Y. (2009). Heterogeneous Photocatalyst Materials for Water Splitting. *Chem. Soc. Rev.* 38, 253–278. doi:10.1039/b800489g

Lan, Z.-A., Ren, W., Chen, X., Zhang, Y., and Wang, X. (2019). Conjugated Donor-Acceptor Polymer Photocatalysts with Electron-Output "tentacles" for Efficient Hydrogen Evolution. *Appl. Catal. B: Environ.* 245, 596–603. doi:10.1016/j.apcatb.2019.01.010

Lin, L., Ou, H., Zhang, Y., and Wang, X. (2016). Tri-s-triazine-based Crystalline Graphitic Carbon Nitrides for Highly Efficient Hydrogen Evolution Photocatalysis. *ACS Catal.* 6, 3921–3931. doi:10.1021/acscatal.6b00922

Linares, N., Silvestre-Albero, A. M., Serrano, E., Silvestre-Albero, J., and García-Martínez, J. (2014). Mesoporous Materials for Clean Energy Technologies. *Chem. Soc. Rev.* 43, 7681–7717. doi:10.1039/c3cs60435g

Osterloh, F. E. (2013). Inorganic Nanostructures for Photoelectrochemical and Photocatalytic Water Splitting. *Chem. Soc. Rev.* 42, 2294–2320. doi:10.1039/c2cs35266d

Shi, R., Cao, Y., Bao, Y., Zhao, Y., Waterhouse, G. I. N., Fang, Z., et al. (2017). Self-Assembled Au/CdSe Nanocrystal Clusters for Plasmon-Mediated

Photocatalytic Hydrogen Evolution. *Adv. Mater.* 29, 1700803. doi:10.1002/adma.201700803

Shu, C., Han, C., Yang, X., Zhang, C., Chen, Y., Ren, S., et al. (2021). Boosting the Photocatalytic Hydrogen Evolution Activity for D-π-A Conjugated Microporous Polymers by Statistical Copolymerization. *Adv. Mater.* 33, 2008498. doi:10.1002/adma.202008498

Shu, G., Li, Y., Wang, Z., Jiang, J.-X., and Wang, F. (2020a). Poly(dibenzothiophene-S,S-dioxide) with Visible Light-Induced Hydrogen Evolution Rate up to 44.2 Mmol H−1 G−1 Promoted by K2HPO4. *Appl. Catal. B: Environ.* 261, 118230. doi:10.1016/j.apcatb.2019.118230

Shu, G., Wang, Y., Li, Y., Zhang, S., Jiang, J.-X., and Wang, F. (2020b). A High Performance and Low Cost Poly(dibenzothiophene-S,s-dioxide)@TiO2 Composite with Hydrogen Evolution Rate up to 51.5 Mmol H−1 G−1. *J. Mater. Chem. A.* 8, 18292–18301. doi:10.1039/d0ta06159j

Sprick, R. S., Bai, Y., Guilbert, A. A. Y., Zbiri, M., Aitchison, C. M., Wilbraham, L., et al. (2019). Photocatalytic Hydrogen Evolution from Water Using Fluorene and Dibenzothiophene Sulfone-Conjugated Microporous and Linear Polymers. *Chem. Mater.* 31, 305–313. doi:10.1021/acs.chemmater.8b02833

Sprick, R. S., Wilbraham, L., Bai, Y., Guiglion, P., Monti, A., Clowes, R., et al. (2018). Nitrogen Containing Linear Poly(phenylene) Derivatives for Photo-Catalytic Hydrogen Evolution from Water. *Chem. Mater.* 30, 5733–5742. doi:10.1021/acs.chemmater.8b02501

Ting, L., Jayakumar, J., Chang, C. L., Lin, W., Elsayed, M. H., and Chou, H. H. (2019). Effect of Controlling the Number of Fused Rings on Polymer Photocatalysts for Visible-Light-Driven Hydrogen Evolution. *J. Mater. Chem. A.* 7, 40. doi:10.1039/c9ta06425g

Tsang, C. H. A., Li, K., Zeng, Y., Zhao, W., Zhang, T., Zhan, Y., et al. (2019). Titanium Oxide Based Photocatalytic Materials Development and Their Role of in the Air Pollutants Degradation: Overview and Forecast. *Environ. Int.* 125, 200–228. doi:10.1016/j.envint.2019.01.015

Turner, J., Sverdrup, G., Mann, M. K., Maness, P.-C., Kroposki, B., Ghirardi, M., et al. (2008). Renewable Hydrogen Production. *Int. J. Energ. Res.* 32, 379–407. doi:10.1002/er.1372

Wang, K., Yang, L.-M., Wang, X., Guo, L., Cheng, G., Zhang, C., et al. (2017). Covalent Triazine Frameworks via a Low-Temperature Polycondensation Approach. *Angew. Chem. Int. Ed.* 56, 14149–14153. doi:10.1002/anie.201708548

Wang, L., Zhang, Y., Chen, L., Xu, H., and Xiong, Y. (2018). Solar Energy Conversion: 2D Polymers as Emerging Materials for Photocatalytic Overall Water Splitting (Adv. Mater. 48/2018). *Adv. Mater.* 30, 1870369. doi:10.1002/adma.201870369

Wang, P., Xu, S., Chen, F., and Yu, H. (2019). Ni Nanoparticles as Electron-Transfer Mediators and NiS as Interfacial Active Sites for Coordinative Enhancement of H2-Evolution Performance of TiO2. *Chin. J. Catal.* 40, 343–351. doi:10.1016/s1872-2067(18)63157-2

Wang, X., Maeda, K., Chen, X., Takanabe, K., Domen, K., Hou, Y., et al. (2009). Polymer Semiconductors for Artificial Photosynthesis: Hydrogen Evolution by Mesoporous Graphitic Carbon Nitride with Visible Light. *J. Am. Chem. Soc.* 131, 1680–1681. doi:10.1021/ja809307s

Wang, X., Maeda, K., Thomas, A., Takanabe, K., Xin, G., Carlsson, J. M., et al. (2010). A Metal-free Polymeric Photocatalyst for Hydrogen Production from Water under Visible Light. *Nat. Mater.* 8, 271–275. doi:10.1142/9789814317665_0039

Wang, Z., Yang, X., Yang, T., Zhao, Y., Wang, F., Chen, Y., et al. (2018). Dibenzothiophene Dioxide Based Conjugated Microporous Polymers for Visible-Light-Driven Hydrogen Production. *ACS Catal.* 8, 8590–8596. doi:10.1021/acscatal.8b02607

Xiao, W.-J., Wang, Y., Wang, W.-R., Li, J., Wang, J., Xu, Z.-W., et al. (2020). Diketopyrrolopyrrole-Based Donor-Acceptor Conjugated Microporous Polymers for Visible-Light-Driven Photocatalytic Hydrogen Production from Water. *Macromolecules* 53, 2454–2463. doi:10.1021/acs.macromol.9b02488

Xu, Y., Mao, N., Zhang, C., Wang, X., Zeng, J., Chen, Y., et al. (2018). Rational Design of Donor-π-Acceptor Conjugated Microporous Polymers for Photocatalytic Hydrogen Production. *Appl. Catal. B: Environ.* 228, 1–9. doi:10.1016/j.apcatb.2018.01.073

Yang, C., Ma, B. C., Zhang, L., Lin, S., Ghasimi, S., Landfester, K., et al. (2016). Molecular Engineering of Conjugated Polybenzothiadiazoles for Enhanced Hydrogen Production by Photosynthesis. *Angew. Chem.* 128, 9348–9352. doi:10.1002/ange.201603532

Ye, H., Wang, Z., Yu, F., Zhang, S., Kong, K., Gong, X., et al. (2020). Fluorinated Conjugated Poly(benzotriazole)/g-C3n4 Heterojunctions for Significantly Enhancing Photocatalytic H2 Evolution. *Appl. Catal. B: Environ.* 267, 118577. doi:10.1016/j.apcatb.2019.118577

Yu, W., Chen, J., Shang, T., Chen, L., Gu, L., and Peng, T. (2017). Direct Z-Scheme G-C3n4/wo3 Photocatalyst with Atomically Defined junction for H2 Production. *Appl. Catal. B: Environ.* 219, 693–704. doi:10.1016/j.apcatb.2017.08.018

Yu, Y., Yan, W., Wang, X., Li, P., Gao, W., Zou, H., et al. (2018). Surface Engineering for Extremely Enhanced Charge Separation and Photocatalytic Hydrogen Evolution on G-C3 N4. *Adv. Mater.* 30, 1705060. doi:10.1002/adma.201705060

Zhang, G., Ou, W., Wang, J., Xu, Y., Xu, D., Sun, T., et al. (2019). Stable, Carrier Separation Tailorable Conjugated Microporous Polymers as a Platform for Highly Efficient Photocatalytic H2 Evolution. *Appl. Catal. B: Environ.* 245, 114–121. doi:10.1016/j.apcatb.2018.12.007

Zhang, Y., Kong, L., Zhang, Y., Du, H., Zhao, J., Chen, S., et al. (2020). Ultra-low-band gap Thienoisoindigo-Based Ambipolar Type Neutral green Copolymers with ProDOT and Thiophene Units as NIR Electrochromic Materials. *Org. Electro.* 81, 105685. doi:10.1016/j.orgel.2020.105685

Zhao, Y., Ma, W., Xu, Y., Zhang, C., Wang, Q., Yang, T., et al. (2018). Effect of Linking Pattern of Dibenzothiophene-S,s-Dioxide-Containing Conjugated Microporous Polymers on the Photocatalytic Performance. *Macromolecules* 51, 9502–9508. doi:10.1021/acs.macromol.8b02023

Zhou, W., Jia, T., Shi, H., Yu, D., Hong, W., and Chen, X. (2019). Conjugated Polymer Dots/graphitic Carbon Nitride Nanosheet Heterojunctions for Metal-free Hydrogen Evolution Photocatalysis. *J. Mater. Chem. A.* 7, 303–311. doi:10.1039/c8ta09735f

Conflict of Interest: The authors declare that the research was conducted in the absence of any commercial or financial relationships that could be construed as a potential conflict of interest.

frontiers | Frontiers in Chemistry

ORIGINAL RESEARCH
published: 07 April 2022
doi: 10.3389/fchem.2022.879402

First-Principles Calculations of Two-Dimensional CdO/HfS2 Van der Waals Heterostructure: Direct Z-Scheme Photocatalytic Water Splitting

Qiuhua Zhang[1], Kai Ren[2], Ruxing Zheng[2], Zhaoming Huang[3]*, Zongquan An[1]* and Zhen Cui[4]

[1]School of Automobile and Aviation, Wuhu Institute of Technology, Wuhu, China, [2]School of Mechanical and Electronic Engineering, Nanjing Forestry University, Nanjing, China, [3]School of Mechanical Engineering, Wanjiang University of Technology, Ma'anshan, China, [4]School of Automation and Information Engineering, Xi'an University of Technology, Xi'an, China

Using two-dimensional (2D) heterostructure as photocatalyst for water splitting is a popular strategy for the generation of hydrogen. In this investigation, the first-principles calculations are explored to address the electronic performances of the 2D CdO/HfS_2 heterostructure formed by van der Waals (vdW) forces. The CdO/HfS_2 vdW heterostructure has a 1.19 eV indirect bandgap with type-II band alignment. Importantly, the CdO/HfS_2 vdW heterostructure possesses an intrinsic Z-scheme photocatalytic characteristic for water splitting by obtaining decent band edge positions. CdO donates 0.017 electrons to the HfS_2 layer in the heterostructure, inducing a potential drop to further separate the photogenerated electrons and holes across the interface. The CdO/HfS_2 vdW heterostructure also has excellent optical absorption capacity, showing a promising role as a photocatalyst to decompose the water.

Keywords: two-dimensional, CdO/HfS2 heterostructure, Z-scheme, photocatalyst, water splitting

OPEN ACCESS

Edited by:
Guangzhao Wang,
Yangtze Normal University, China

Reviewed by:
Wei Zhang,
Nanjing Forest Police College, China
Biao Wang,
Southwest University, China

Correspondence:
Zhaoming Huang
jimmymacy@163.com
Zongquan An
anzongquan@whit.edu.cn

Specialty section:
This article was submitted to Theoretical and Computational Chemistry,
a section of the journal Frontiers in Chemistry

Received: *19 February 2022*
Accepted: *07 March 2022*
Published: *07 April 2022*

Citation:
Zhang Q, Ren K, Zheng R, Huang Z, An Z and Cui Z (2022) First-Principles Calculations of Two-Dimensional CdO/HfS2 Van der Waals Heterostructure: Direct Z-Scheme Photocatalytic Water Splitting.
Front. Chem. 10:879402.
doi: 10.3389/fchem.2022.879402

INTRODUCTION

After the discovery of graphene in 2004 as a novel two-dimensional (2D) material (Geim and Novoselov, 2007), its outstanding thermal, electronic, and mechanical properties provide remarkable applications in many fields, also promoting the development of the other 2D materials (Cui et al., 2021a; Ren et al., 2021a; Zheng et al., 2021a; Cui et al., 2021b). Acting as popular layered material, transition-metal dichalcogenides (TMDs), expressed by XM_2, where M represents transition-metal atom and X represents chalcogenide atom, is sandwiched by two chalcogenide atoms to form a sandwich structure (Hua Zhang et al., 2018). TMDs materials possess excellent electronic (Mak et al., 2010), thermal (Ren et al., 2022), thermoelectric (Wickramaratne et al., 2014), and optical (Ren et al., 2019a) performances. In recent studies, it has been proved that TMDs materials can be widely used in photocatalyst (Ren et al., 2020a), field-effect transistor (Yu et al., 2017), and photovoltaic devices (Gan et al., 2014). It is worth noting that the TMDs materials also can be prepared by an omnidirectional epitaxy (Xie et al., 2018), physical transport (Huang et al., 2014). Besides, the TMDs materials are also synthesized (Lu et al., 2017), suggesting novel photocatalytic properties (Zheng et al., 2021b; Lou et al., 2021; Zhu et al., 2021; Shao et al., 2022; Shen et al., 2022).

In recent years, using 2D materials as photocatalysts has aroused considerable focus (Wang et al., 2020a; Wang et al., 2020b; Wang et al., 2020c). The photogenerated electrons and holes in excited 2D semiconductors can quickly move to the material surface to participate in a redox reaction, which greatly shortened the photogenerated charge moving path, and a wider reaction area is also provided (Chen et al., 2010). However, the rapid recombination between the photogenerated electrons and holes hinders the reaction efficiency (Ren et al., 2019b). To solve this obstacle, many 2D heterostructures constructed intrinsic type-II band alignment have been investigated as photocatalysts because the lifetime of the photogenerated electrons and holes can be prolonged by separating into different layers. For example, the electronic and optical properties of AlN/Bp heterostructure present type-II band arrangement and have strong light absorption ability, which has great potential in the field of photocatalytic water decomposition (Yang et al., 2017). The experimental results demonstrate that under the condition of light, g-C_3N_4/$Ca_2Nb_2TaO_{10}$ nanocomposite with a mass ratio of 80:20 has the highest hydrogen precipitation efficiency, which is more than 2.8 times that of single-layer g-C_3N_4 (Thaweesak et al., 2017). The nanorod array WO_3/$BiVO_4$ heterostructure was prepared by solvothermal technology. The experiments demonstrate that the photocatalytic performance of the heterostructure is significantly improved compared with the planar WO_3/$BiVO_4$ heterostructure. In particular, the IPCE value at 420 nm of the heterostructure film can be increased from 9.3% to 31% (Su et al., 2011). Similarly, the flower-like structure of $CoNi_2S_4$/Ni_3S_2 heterostructure was synthesized by the hydrothermal method, which shows that the electronic structure is optimized because of the high-intensity coupling between $CoNi_2S_4$ and Ni_3S_2, so as to improve the efficiency of photocatalytic water splitting (Dai et al., 2020). Furthermore, the Z-scheme photocatalyst is popular because of its extraordinary optical carrier moving path, which can provide more efficient photocatalytic performance. For example, the 2D C_7N_6/Sc_2CCl_2 heterostructure possesses ultrafast carrier recombination of about 0.74 ps, suggesting a strong redox capacity for water splitting (Meng et al., 2022). Z-scheme PtS_2/arsenene heterostructure shows a novel high solar-to-hydrogen efficiency of about 49.32% (Ren et al., 2020b). The band bending mechanism in CdO/arsenene was addressed as a potential Z-scheme photocatalyst (Ren et al., 2021b).

More recently, the layered 2D CdO was prepared by the successive ionic layer adsorption and reaction method (Shameem et al., 2017) with outstanding electronic (Zhuang and Hennig, 2013), optical (Wang et al., 2020d), and electromagnetic properties (Zhao et al., 2019), which also can be tuned by the number of layers and stacking order (Hoat et al., 2020). At the same time, the external element doping for CdO can induce magnetic moment behavior (Chaurasiya and Dixit, 2019). In addition, 2D HfS_2 was successfully prepared by the mechanical stripping method, which has attracted extensive attention from researchers (Kanazawa et al., 2016; Wang et al., 2017; Wang et al., 2019). HfS_2 has a decent carrier mobility of 1,800 $cm^2\ v^{-1}\ s^{-1}$ (Obeid et al., 2020). Importantly, HfS_2 can be constructed into type-II heterostructure with other different 2D materials, showing an obvious quantum effect (Mattinen et al., 2019; Obeid et al., 2020). Considering the CdO and HfS_2 monolayers share the same honeycomb structure and excellent physical and chemical properties, the CdO/HfS_2 heterostructure is constructed in this report, using density functional calculations, the electronic properties of the CdO/HfS_2 heterostructure are addressed by type-II band structure. Furthermore, the direct Z-scheme photocatalytic mechanism is also investigated for water splitting. Besides, the interfacial and optical performances of the CdO/HfS_2 heterostructure are studied.

CALCULATION MODELS AND METHODS

In this study, the simulations of the first-principles calculations were performed by the Vienna *ab initio* simulation package (VASP) based on density functional theory (DFT) (Kresse and Furthmüller, 1996a; Kresse and Furthmüller, 1996b). The

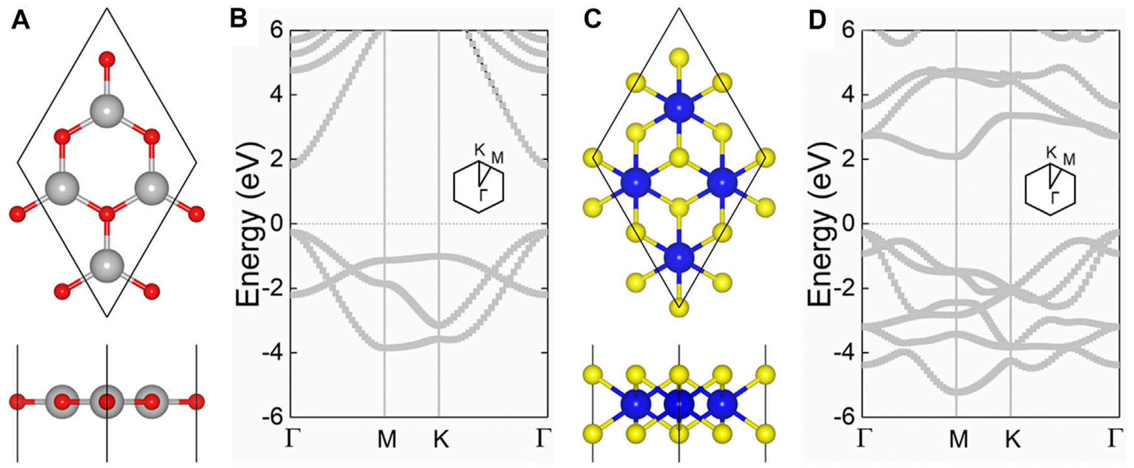

FIGURE 1 | The geometric structures of the **(A)** CdO and **(B)** HfS_2 monolayers; the band structures of the **(C)** CdO and **(D)** HfS_2 monolayers; grey, red, blue, and yellow balls are Cd, O, Hf, and S atoms, the Fermi level is set to 0.

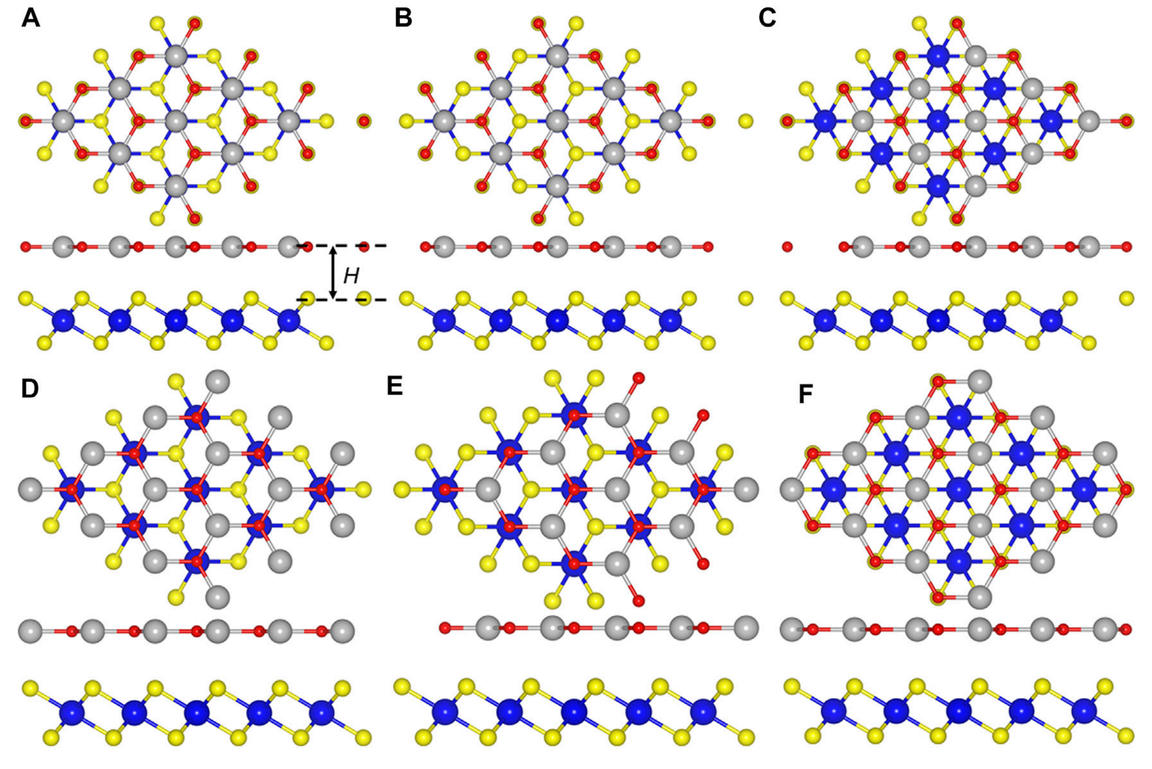

FIGURE 2 | The top and side views of CdO/HfS_2 heterostructure constructed by **(A)** CH-1, **(B)** CH-2, **(C)** CH-3, **(D)** CH-4, **(E)** CH-5, and **(F)** CH-6 configurations.

generalized gradient approximation (GGA) was considered by the projector augmented wave potentials (PAW) using Perdew–Burke–Ernzerhof (PBE) functional for exchange-correlation functional (Perdew et al., 1996; Kresse and Joubert, 1999). The DFT-D3 method was used to describe the dispersion forces using Grimme (2006). Furthermore, the Heyd–Scuseria–Ernzerhof hybrid (HSE06) calculations are explored to obtain the electronic and optical characteristics (Heyd et al., 2003). In the first Brillouin zone, the energy cut-off was used by 550 eV, and the Monkhorst–Pack *k*-point grids were set as 17 × 17 × 1. In addition, 25 Å vacuum space was considered in this investigation. The force and energy were limited within $0.01\ \mathrm{eV}\ \text{Å}^{-1}$ and 0.01 meV, respectively, for convergence.

RESULTS AND DISCUSSION

The hexagonal honeycomb structure of the CdO and HfS_2 monolayers are optimized by the lattice parameters of 3.68 Å and 3.64 Å, respectively, demonstrated by **Figures 1A,C**. One can see that the CdO monolayer possesses a direct bandgap by the conduction band minimum (CBM) sharing the same point of Γ with the valence band maximum (VBM) in **Figure 1B**. While the HfS_2 monolayer has an indirect bandgap with the CBM between the Γ and M, the VBM is found near the Γ point, as shown in **Figure 1D**. Besides, the HSE06 obtained bandgaps of the CdO and HfS_2 monolayers are 2.07 and 2.05 eV, respectively. The results are in good agreement with the previous studies (Wang et al., 2020d; Obeid et al., 2020; Zhang and Ji, 2020).

TABLE 1 | The calculated binding energy (E, eV), bond length (L, Å), and the thickness of interface (H, Å) of the optimized CdO/HfS_2 heterostructure constructed by different stacking styles.

	E	$L_{Hf–S}$	$L_{Cd–O}$	H
CH -1	−38.08	2.58	2.18	3.23
CH -2	−42.29	2.58	2.17	2.97
CH -3	−38.71	2.58	2.18	3.18
CH -4	−41.36	2.57	2.17	3.03
CH -5	−43.93	2.57	2.17	2.86
CH -6	−41.40	2.58	2.18	3.04

The CdO/HfS_2 heterostructure is constructed in a vertical direction expressed by six different representative stacking configurations shown in **Figure 2**. We select the most stable stacking style by calculating the binding energy (E), which is obtained by $E = (E_h—E_{CdO}—E_{HfS2})/S$, where E_h, E_{CdO}, $E_{HfS2,}$ and S represent the energy of the CdO/HfS_2 heterostructure, original CdO, HfS_2 monolayers and the area of the CdO/HfS_2 heterostructure, respectively. Importantly, the obtained lowest binding energy is about $-43.93\ \mathrm{meV}/\text{Å}^{-2}$ for CH-5 configuration, which is smaller than that in graphites of about $-18\ \mathrm{meV}\ \text{Å}^{-2}$, revealing van der Waals (vdW) interactions between the interface of the heterostructure (Chen et al., 2013). Moreover, the following investigations of the CdO/HfS_2 heterostructure are based on such a CH-5 configuration. Besides, the thickness of the interface of the

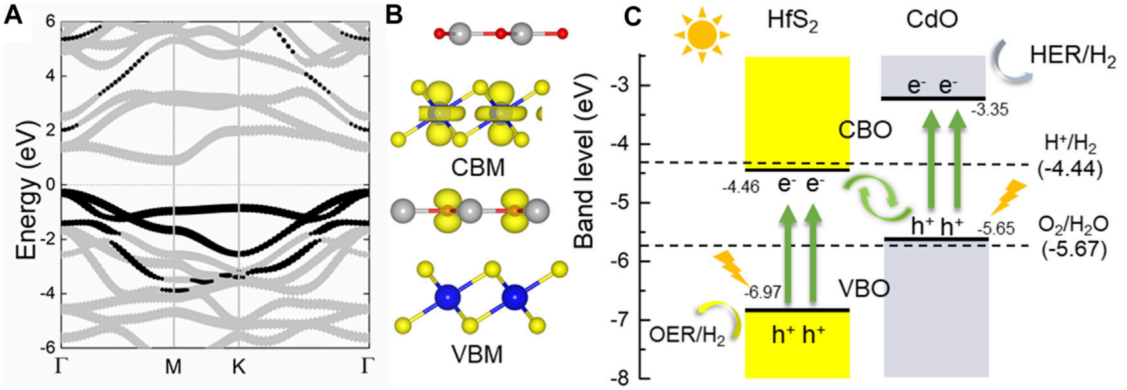

FIGURE 3 | The **(A)** projected band structure, **(B)** band-decomposed charge densities, and **(C)** band alignment of the CdO/HfS$_2$ vdW heterostructure compared with the oxidation and reduction of water splitting at pH 0; the Fermi level is set to 0.

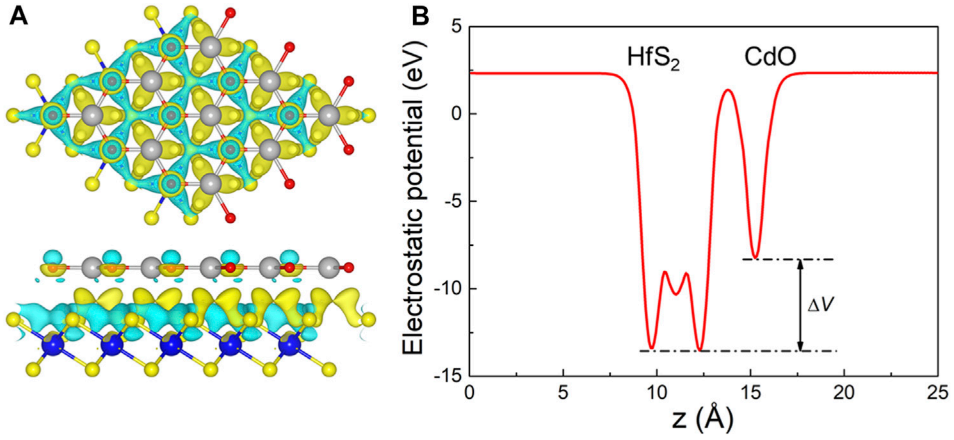

FIGURE 4 | (A) The charge density difference and **(B)** potential drop at the interface of the CdO/HfS$_2$ vdW heterostructure; the yellow and cyan regions mean the gaining and the loss of the electrons, respectively; the isosurface level is used as 10^{-4} |*e*|.

CdO/HfS$_2$ vdW heterostructure, explained by **Figure 2A**, is 2.86 Å, which is comparable with that of other vdW heterostructures such as ZnO/GaN (2.41 Å) (Ren et al., 2020c), BlueP/GeC, and BlueP/SiC (2.99 Å) heterostructures (Ren et al., 2019c) **Table 1**.

Next, the electronic property of the CdO/HfS$_2$ vdW heterostructure is explored by the projected band structure in **Figure 3A** with an indirect bandgap of 1.19 eV. The black and gray marks show the contribution of the band energy from CdO and HfS$_2$ monolayers, respectively. Therefore, the CBM and the VBM of the CdO/HfS$_2$ vdW heterostructure result from the HfS$_2$ and CdO layers, respectively, further proved by the band-decomposed charge densities shown in **Figure 3B**, suggesting a type-II band structure in the heterostructure. This type-II band structure of the CdO/HfS$_2$ vdW heterostructure can induce conduction band offset and valence band offset to further promote the migration of the photogenerated charges, revealed by **Figure 3C**. When the CdO/HfS$_2$ vdW heterostructure is illuminated, the photogenerated electrons will move from VBM of the CdO (or HfS$_2$) to the CBM, resulting in holes at VBM. Some photogenerated electrons (or holes) will be promoted from CBM (or VBM) of the CdO (or HfS$_2$) to the CBM of the HfS$_2$ (or CdO) by the conduction-band offset, CBO (or valence-band offset, VBO). Moreover, the remaining photogenerated electrons at the conduction band of the HfS$_2$ and the photogenerated holes at the valence band of the CdO can make recombination at the interface of the CdO/HfS$_2$ vdW heterostructure because of that specific band energy between the −4.44 and −5.67 eV at pH 0 (Ruiqi Zhang et al., 2018). In contrast, the band edge positions of the CBM and the VBM of the CdO and HfS$_2$ are −3.35 and −6.97 eV, respectively, which are decent for the redox reaction for the water splitting (Xu et al., 2018). This extraordinary flow mode of the photogenerated charge suggests a Z-scheme photocatalytic mechanism in CdO/HfS$_2$ vdW heterostructure, which is also reported by a MoSe$_2$/HfS$_2$ heterostructure (Wang et al., 2019).

When the CdO and HfS$_2$ layers contact, charge density difference ($\Delta\rho$) occurs between the interface of the heterostructure, which is decided by $\Delta\rho = \rho_{\mathrm{h}} - \rho_{\mathrm{CdO}} - \rho_{\mathrm{HfS2}}$,

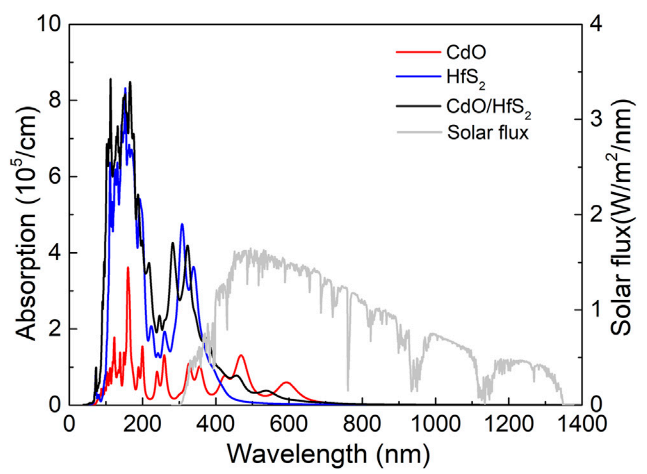

FIGURE 5 | The optical absorption spectrum of the monolayered CdO, HfS_2, and CdO/HfS_2 vdW heterostructure calculated by the HSE06 method.

where ρ_h, ρ_{CdO}, and s_{HfS2} represent the charge density of the CdO/HfS_2 heterostructure, original CdO, and HfS_2 monolayers, respectively. The charge density difference of the CdO/HfS_2 vdW heterostructure is addressed in **Figure 4A**, which shows that the electrons migrate from the CdO layer to the HfS_2 layer. The charge density amount is investigated by Bader-charge analysis (Tang et al., 2009; Sanville et al., 2007) as 0.017 electrons. Besides, the potential drop (ΔV) of the CdO/HfS_2 vdW heterostructure is also obtained in **Figure 4B** by 5.23 eV, which is larger than that of AlN/Zr_2CO_2 (0.66 eV) (Ren et al., 2021c) and Hf_2CO_2/GaN (3.75 eV) (Ren et al., 2021d). It is worth noting that this potential drop is also beneficial in promoting the separation of photogenerated charges (Wang et al., 2018).

Light absorption capacity is essential performance as a photocatalyst for water splitting. The optical absorption properties of the CdO/HfS_2 vdW heterostructure are calculated by $\alpha(\omega) = \frac{\sqrt{2}\omega}{c}\{[\varepsilon_1^2(\omega) + \varepsilon_2^2(\omega)]^{1/2} - \varepsilon_1(\omega)\}^{1/2}$, where α is the absorption coefficient. The angular frequency and the speed of light are expressed by ω and c, respectively. The real and imaginary parts of the dielectric constant are represented by $\varepsilon_1(\omega)$ and $\varepsilon_2(\omega)$, respectively. In **Figure 5**, the HSE06 obtained optical absorption spectra of the monolayered CdO, HfS_2, and CdO/HfS_2 vdW heterostructure are demonstrated by the absorption peaks of $3.56 \times 10^5\ cm^{-1}$, $4.19 \times 10^5\ cm^{-1}$, and $3.51 \times 10^5\ cm^{-1}$ at the wavelength of 342, 323, and 351 nm, respectively, in the ultraviolet region. Importantly, the CdO/HfS_2 vdW heterostructure possesses excellent visible light absorption capacity by the absorption peak of $7.21 \times 10^4\ cm^{-1}$ locating at the wavelength of 465 nm, which is higher than other reported 2D heterostructures as photocatalyst, such as $g\text{-}GaN/Mg(OH)_2$ ($5.33 \times 10^4\ cm^{-1}$) (Ren et al., 2019d) and ZnO/GaN ($4.92 \times 10^4\ cm^{-1}$) (Ren et al., 2020c). Besides, the CdO monolayer also shows a novel absorption peak of $6.01 \times 10^4\ cm^{-1}$ in the visible light spectrum of 591 nm.

CONCLUSION

In this work, the CdO/HfS_2 is constructed by vdW interactions proved by first-principles calculations. The electronic properties of the CdO and HfS_2 monolayers are calculated. In contrast, the CdO/HfS_2 vdW heterostructure possesses a type-II band structure to prevent the recombination of the photogenerated charges. Furthermore, the decent band alignment of the CdO/HfS_2 vdW heterostructure demonstrates a Z-scheme photocatalytic mechanism near the interface. Besides, the CdO/HfS_2 vdW heterostructure shows pronounced visible light absorption performance. These results explain that the CdO/HfS_2 vdW heterostructure can be used as a candidate for an excellent photocatalyst for water splitting.

DATA AVAILABILITY STATEMENT

The raw data supporting the conclusion of this article will be made available by the authors without undue reservation.

AUTHOR CONTRIBUTIONS

Conceptualization, QZ; methodology, KR; software, ZC; validation, ZH; formal analysis, ZA; investigation, KR; resources, KR, original draft preparation, QZ.

FUNDING

This work thanks the excellent top talent cultivation project in colleges and universities in Anhui province (Grant no. gxgnfx2018097), the key projects of natural science research in colleges and universities in Anhui province (Grant no. KJ 2020A0837, KJ 2020A0909), and the sub-project of national double height university scientific research platform construction and upgrading cultivation project (Grant no. Kjcxpt202005).

REFERENCES

Chaurasiya, R., and Dixit, A. (2019). Point Defects Induced Magnetism in CdO Monolayer: A Theoretical Study. *J. Magnetism Magn. Mater.* 469, 279–288. doi:10.1016/j.jmmm.2018.08.076

Chen, X., Shen, S., Guo, L., and Mao, S. S. (2010). Semiconductor-based Photocatalytic Hydrogen Generation. *Chem. Rev.* 110, 6503–6570. doi:10.1021/cr1001645

Chen, X., Tian, F., Persson, C., Duan, W., and Chen, N.-x. (2013). Interlayer Interactions in Graphites. *Sci. Rep.* 3, 3046. doi:10.1038/srep03046

Cui, Z., Luo, Y., Yu, J., and Xu, Y. (2021). Tuning the Electronic Properties of MoSi2N4 by Molecular Doping: A First Principles Investigation. *Physica E: Low-dimensional Syst. Nanostructures* 134, 114873. doi:10.1016/j.physe.2021.114873

Cui, Z., Wang, M., Lyu, N., Zhang, S., Ding, Y., and Bai, K. (2021). Electronic, Magnetism and Optical Properties of Transition Metals Adsorbed Puckered Arsenene. *Superlattices and Microstructures* 152, 106852. doi:10.1016/j.spmi.2021.106852

Dai, W., Ren, K., Zhu, Y.-a., Pan, Y., Yu, J., and Lu, T. (2020). Flower-like CoNi2S4/Ni3S2 Nanosheet Clusters on Nickel Foam as Bifunctional Electrocatalyst for Overall Water Splitting. *J. Alloys Compd.* 844, 156252. doi:10.1016/j.jallcom.2020.156252

Gan, L.-Y., Zhang, Q., Cheng, Y., and Schwingenschlögl, U. (2014). Photovoltaic Heterojunctions of Fullerenes with MoS2 and WS2 Monolayers. *J. Phys. Chem. Lett.* 5, 1445–1449. doi:10.1021/jz500344s

Geim, A. K., and Novoselov, K. S. (2007). The Rise of Graphene. *Nat. Mater* 6, 183–191. doi:10.1038/nmat1849

Grimme, S. (2006). Semiempirical GGA-type Density Functional Constructed with a Long-Range Dispersion Correction. *J. Comput. Chem.* 27, 1787–1799. doi:10.1002/jcc.20495

Heyd, J., Scuseria, G. E., and Ernzerhof, M. (2003). Hybrid Functionals Based on a Screened Coulomb Potential. *J. Chem. Phys.* 118, 8207–8215. doi:10.1063/1.1564060

Hoat, D. M., Naseri, M., Vu, T. V., Rivas-Silva, J. F., Hieu, N. N., and Cocoletzi, G. H. (2020). Structural, Electronic and Optical Properties of CdO Monolayer and Bilayers: Stacking Effect Investigations. *Superlattice. Microst.* 145, 106644. doi:10.1016/j.spmi.2020.106644

Huang, C., Wu, S., Sanchez, A. M., Peters, J. J. P., Beanland, R., Ross, J. S., et al. (2014). Lateral Heterojunctions within Monolayer MoSe2-WSe2 Semiconductors. *Nat. Mater* 13, 1096–1101. doi:10.1038/nmat4064

Hua Zhang, H., Chhowalla, M., and Liu, Z. (2018). 2D Nanomaterials: Graphene and Transition Metal Dichalcogenides. *Chem. Soc. Rev.* 47, 3015–3017. doi:10.1039/c8cs90048e

Kanazawa, T., Amemiya, T., Ishikawa, A., Upadhyaya, V., Tsuruta, K., Tanaka, T., et al. (2016). Few-layer HfS2 Transistors. *Sci. Rep.* 6, 22277. doi:10.1038/srep22277

Kresse, G., and Furthmüller, J. (1996a). Efficiency of Ab-Initio Total Energy Calculations for Metals and Semiconductors Using a Plane-Wave Basis Set. *Comput. Mater. Sci.* 6, 15–50. doi:10.1016/0927-0256(96)00008-0

Kresse, G., and Furthmüller, J. (1996b). Efficient Iterative Schemes Forab Initiototal-Energy Calculations Using a Plane-Wave Basis Set. *Phys. Rev. B* 54, 11169–11186. doi:10.1103/physrevb.54.11169

Kresse, G., and Joubert, D. (1999). From Ultrasoft Pseudopotentials to the Projector Augmented-Wave Method. *Phys. Rev. B* 59, 1758–1775. doi:10.1103/physrevb.59.1758

Lou, J., Ren, K., Huang, Z., Huo, W., Zhu, Z., and Yu, J. (2021). Electronic and Optical Properties of Two-Dimensional Heterostructures Based on Janus XSSe (X = Mo, W) and Mg(OH)$_2$: a First Principles Investigation. *RSC. Adv.* 11, 29576–29584. doi:10.1039/d1ra05521f

Lu, A.-Y., Zhu, H., Xiao, J., Chuu, C.-P., Han, Y., Chiu, M.-H., et al. (2017). Janus Monolayers of Transition Metal Dichalcogenides. *Nat. Nanotech* 12, 744–749. doi:10.1038/nnano.2017.100

Mak, K. F., Lee, C., Hone, J., Shan, J., and Heinz, T. F. (2010). Atomically ThinMoS2: A New Direct-Gap Semiconductor. *Phys. Rev. Lett.* 105, 136805. doi:10.1103/physrevlett.105.136805

Mattinen, M., Popov, G., Vehkamäki, M., King, P. J., Mizohata, K., Jalkanen, P., et al. (2019). Atomic Layer Deposition of Emerging 2D Semiconductors, HfS2 and ZrS2, for Optoelectronics. *Chem. Mater.* 31, 5713–5724. doi:10.1021/acs.chemmater.9b01688

Meng, J., Wang, J., Wang, J., Li, Q., and Yang, J. (2022). C7N6/Sc2CCl2 Weak van der Waals Heterostructure: A Promising Visible-Light-Driven Z-Scheme Water Splitting Photocatalyst with Interface Ultrafast Carrier Recombination. *J. Phys. Chem. Lett.* 13, 1473–1479. doi:10.1021/acs.jpclett.1c04194

Obeid, M. M., Bafekry, A., Ur Rehman, S., and Nguyen, C. V. (2020). A type-II GaSe/HfS2 van der Waals heterostructure as promising photocatalyst with high carrier mobility. *Appl. Surf. Sci.* 534, 147607. doi:10.1016/j.apsusc.2020.147607

Perdew, J. P., Burke, K., and Ernzerhof, M. (1996). Generalized Gradient Approximation Made Simple. *Phys. Rev. Lett.* 77, 3865–3868. doi:10.1103/physrevlett.77.3865

Ren, K., Sun, M., Luo, Y., Wang, S., Yu, J., and Tang, W. (2019). First-principle Study of Electronic and Optical Properties of Two-Dimensional Materials-Based Heterostructures Based on Transition Metal Dichalcogenides and boron Phosphide. *Appl. Surf. Sci.* 476, 70–75. doi:10.1016/j.apsusc.2019.01.005

Ren, K., Luo, Y., Wang, S., Chou, J.-P., Yu, J., Tang, W., et al. (2019). A van der Waals Heterostructure Based on Graphene-like Gallium Nitride and Boron Selenide: A High-Efficiency Photocatalyst for Water Splitting. *ACS Omega* 4, 21689–21697. doi:10.1021/acsomega.9b02143

Ren, K., Ren, C., Luo, Y., Xu, Y., Yu, J., Tang, W., et al. (2019). Using van der Waals heterostructures based on two-dimensional blue phosphorus and XC (X = Ge, Si) for water-splitting photocatalysis: a first-principles study. *Phys. Chem. Chem. Phys.* 21, 9949–9956. doi:10.1039/c8cp07680d

Ren, K., Yu, J., and Tang, W. (2019). A two-dimensional vertical van der Waals heterostructure based on g-GaN and Mg(OH)2 used as a promising photocatalyst for water splitting: A first-principles calculation. *J. Appl. Phys.* 126, 065701. doi:10.1063/1.5099125

Ren, K., Wang, S., Luo, Y., Chou, J.-P., Yu, J., Tang, W., et al. (2020). High-efficiency photocatalyst for water splitting: a Janus MoSSe/XN (X = Ga, Al) van der Waals heterostructure. *J. Phys. D: Appl. Phys.* 53, 185504. doi:10.1088/1361-6463/ab71ad

Ren, K., Tang, W., Sun, M., Cai, Y., Cheng, Y., and Zhang, G. (2020). A direct Z-scheme PtS2/arsenene van der Waals heterostructure with high photocatalytic water splitting efficiency. *Nanoscale* 12, 17281–17289. doi:10.1039/d0nr02286a

Ren, K., Luo, Y., Yu, J., and Tang, W. (2020). Theoretical prediction of two-dimensional ZnO/GaN van der Waals heterostructure as a photocatalyst for water splitting. *Chem. Phys.* 528, 110539. doi:10.1016/j.chemphys.2019.110539

Ren, K., Shu, H., Huo, W., Cui, Z., Yu, J., and Xu, Y. (2021). Mechanical, Electronic and Optical Properties of a Novel B2P6 Monolayer: Ultrahigh Carrier Mobility and strong Optical Absorption. *Phys. Chem. Chem. Phys.* 23, 24915–24921. doi:10.1039/d1cp03838a

Ren, K., Zheng, R., Yu, J., Sun, Q., and Li, J. (2021). Band Bending Mechanism in CdO/Arsenene Heterostructure: A Potential Direct Z-Scheme Photocatalyst. *Front. Chem.* 9, 788813. doi:10.3389/fchem.2021.788813

Ren, K., Zheng, R., Lou, J., Yu, J., Sun, Q., and Li, J. (2021). Ab Initio Calculations for the Electronic, Interfacial and Optical Properties of Two-Dimensional AlN/Zr2CO2 Heterostructure. *Front. Chem.* 9, 796695. doi:10.3389/fchem.2021.796695

Ren, K., Zheng, R., Xu, P., Cheng, D., Huo, W., Yu, J., et al. (2021). Electronic and Optical Properties of Atomic-Scale Heterostructure Based on MXene and MN (M = Al, Ga): A DFT Investigation. *Nanomaterials* 11, 2236. doi:10.3390/nano11092236

Ren, K., Qin, H., Liu, H., Chen, Y., Liu, X., and Zhang, G. (2022). Manipulating Interfacial Thermal Conduction of 2D Janus Heterostructure via a Thermo-Mechanical Coupling. *Adv. Funct. Mater.*, 2110846. doi:10.1002/adfm.202110846

Ruiqi Zhang, R., Zhang, L., Zheng, Q., Gao, P., Zhao, J., and Yang, J. (2018). Direct Z-Scheme Water Splitting Photocatalyst Based on Two-Dimensional Van Der Waals Heterostructures. *J. Phys. Chem. Lett.* 9, 5419–5424. doi:10.1021/acs.jpclett.8b02369

Sanville, E., Kenny, S. D., Smith, R., and Henkelman, G. (2007). Improved Grid-Based Algorithm for Bader Charge Allocation. *J. Comput. Chem.* 28, 899–908. doi:10.1002/jcc.20575

Shameem, A., Devendran, P., Siva, V., Raja, M., Bahadur, S. A., and Manikandan, A. (2017). Preparation and Characterization Studies of Nanostructured CdO Thin Films by SILAR Method for Photocatalytic Applications. *J. Inorg. Organomet. Polym.* 27, 692–699. doi:10.1007/s10904-017-0512-1

Shao, C., Ren, K., Huang, Z., Yang, J., and Cui, Z. (2022). Two-Dimensional PtS2/MoTe2 van der Waals Heterostructure: An Efficient Potential Photocatalyst for Water Splitting. *Front. Chem.* 10, 847319. doi:10.3389/fchem.2022.847319

Shen, Z., Ren, K., Zheng, R., Huang, Z., Cui, Z., Zheng, Z., et al. (2022). The Thermal and Electronic Properties of the Lateral Janus MoSSe/WSSe Heterostructure. *Front. Mater.* 9, 838648. doi:10.3389/fmats.2022.838648

Su, J., Guo, L., Bao, N., and Grimes, C. A. (2011). Nanostructured WO3/BiVO4Heterojunction Films for Efficient Photoelectrochemical Water Splitting. *Nano Lett.* 11, 1928–1933. doi:10.1021/nl2000743

Tang, W., Sanville, E., and Henkelman, G. (2009). A Grid-Based Bader Analysis Algorithm without Lattice Bias. *J. Phys. Condens. Matter* 21, 084204. doi:10.1088/0953-8984/21/8/084204

Thaweesak, S., Lyu, M., Peerakiatkhajohn, P., Butburee, T., Luo, B., Chen, H., et al. (2017). Two-dimensional G-C3N4/Ca2Nb2TaO10 Nanosheet Composites for Efficient Visible Light Photocatalytic Hydrogen Evolution. *Appl. Catal. B: Environ.* 202, 184–190. doi:10.1016/j.apcatb.2016.09.022

Wang, D., Zhang, X., Liu, H., Meng, J., Xia, J., Yin, Z., et al. (2017). Epitaxial Growth of HfS 2 on Sapphire by Chemical Vapor Deposition and Application for Photodetectors. *2d Mater.* 4, 031012. doi:10.1088/2053-1583/aa7ea2

Wang, S., Tian, H., Ren, C., Yu, J., and Sun, M. (2018). Electronic and Optical Properties of Heterostructures Based on Transition Metal Dichalcogenides and Graphene-like Zinc Oxide. *Sci. Rep.* 8, 12009. doi:10.1038/s41598-018-30614-3

Wang, B., Wang, X., Wang, P., Yang, T., Yuan, H., Wang, G., et al. (2019). Bilayer MoSe2/HfS2 Nanocomposite as a Potential Visible-Light-Driven Z-Scheme Photocatalyst. *Nanomaterials* 9, 1706. doi:10.3390/nano9121706

Wang, G., Zhi, Y., Bo, M., Xiao, S., Li, Y., Zhao, W., et al. (2020). 2D Hexagonal Boron Nitride/Cadmium Sulfide Heterostructure as a Promising Water-Splitting Photocatalyst. *Phys. Status Solidi B* 257, 1900431. doi:10.1002/pssb.201900431

Wang, G., Zhang, L., Li, Y., Zhao, W., Kuang, A., Li, Y., et al. (2020). Biaxial Strain Tunable Photocatalytic Properties of 2D ZnO/GeC Heterostructure. *J. Phys. D: Appl. Phys.* 53, 015104. doi:10.1088/1361-6463/ab440e

Wang, G., Li, Z., Wu, W., Guo, H., Chen, C., Yuan, H., et al. (2020). A Two-Dimensional H-Bn/c2n Heterostructure as a Promising Metal-free Photocatalyst for Overall Water-Splitting. *Phys. Chem. Chem. Phys.* 22, 24446–24454. doi:10.1039/d0cp03925j

Wang, G., Gong, L., Li, Z., Wang, B., Zhang, W., Yuan, B., et al. (2020). A Two-Dimensional CdO/CdS Heterostructure Used for Visible Light Photocatalysis. *Phys. Chem. Chem. Phys.* 22, 9587–9592. doi:10.1039/d0cp00876a

Wickramaratne, D., Zahid, F., and Lake, R. K. (2014). Electronic and Thermoelectric Properties of Few-Layer Transition Metal Dichalcogenides. *J. Chem. Phys.* 140, 124710. doi:10.1063/1.4869142

Xie, S., Tu, L., Han, Y., Huang, L., Kang, K., Lao, K. U., et al. (2018). Coherent, Atomically Thin Transition-Metal Dichalcogenide Superlattices with Engineered Strain. *Science* 359, 1131–1136. doi:10.1126/science.aao5360

Xu, Q., Zhang, L., Yu, J., Wageh, S., Al-Ghamdi, A. A., and Jaroniec, M. (2018). Direct Z-Scheme Photocatalysts: Principles, Synthesis, and Applications. *Mater. Today* 21, 1042–1063. doi:10.1016/j.mattod.2018.04.008

Yang, Q., Tan, C.-J., Meng, R.-S., Jiang, J.-K., Liang, Q.-H., Sun, X., et al. (2017). AlN/BP Heterostructure Photocatalyst for Water Splitting. *IEEE Electron. Device Lett.* 38, 145–148. doi:10.1109/led.2016.2633487

Yu, Z., Ong, Z.-Y., Li, S., Xu, J.-B., Zhang, G., Zhang, Y.-W., et al. (2017). Analyzing the Carrier Mobility in Transition-Metal Dichalcogenide MoS2Field-Effect Transistors. *Adv. Funct. Mater.* 27, 1604093. doi:10.1002/adfm.201604093

Zhang, W., and Ji, W. (2020). Two-dimensional van der Waals heterostructure CdO/PtSe2: promising visible light photocatalyst for overall water splitting. *Phys. Chem. Chem. Phys.* 22, 24662–24668. doi:10.1039/d0cp03564e

Zhao, Y., Cui, L., Sun, Y., Zheng, F., and Ke, W. (2019). Ag/CdO NP-Engineered Magnetic Electrochemical Aptasensor for Prostatic Specific Antigen Detection. *ACS Appl. Mater. Inter.* 11, 3474–3481. doi:10.1021/acsami.8b18887

Zheng, Z., Ren, K., Huang, Z., Zhu, Z., Wang, K., Shen, Z., et al. (2021). Remarkably Improved Curie Temperature for Two-Dimensional CrI3 by Gas Molecular Adsorption: a DFT Study. *Semicond. Sci. Technol.* 36, 075015. doi:10.1088/1361-6641/ac01a2

Zheng, R., Ren, K., Yu, J., Zhu, Z., and Sun, Q. (2021). "Type-II Heterostructure Based on Two-Dimensional Arsenene and PtS$_2$ with Novel Light Absorption Performance," in *Third International Conference on Optoelectronic Science and Materials (ICOSM 2021)* (Hefei: SPIE), 182–186.

Zhu, Z., Ren, K., Shu, H., Cui, Z., Huang, Z., Yu, J., et al. (2021). First-Principles Study of Electronic and Optical Properties of Two-Dimensional WSSe/BSe van der Waals Heterostructure with High Solar-to-Hydrogen Efficiency. *Catalysts* 11, 991. doi:10.3390/catal11080991

Zhuang, H. L., and Hennig, R. G. (2013). Computational Identification of Single-Layer CdO for Electronic and Optical Applications. *Appl. Phys. Lett.* 103, 212102. doi:10.1063/1.4831972

Conflict of Interest: The authors declare that the research was conducted in the absence of any commercial or financial relationships that could be construed as a potential conflict of interest.

frontiers | Frontiers in Chemistry

ORIGINAL RESEARCH
published: 25 July 2022
doi: 10.3389/fchem.2022.934048

The First-Principles Study of External Strain Tuning the Electronic and Optical Properties of the 2D $MoTe_2$/PtS_2 van der Waals Heterostructure

Li Zhang[1], Kai Ren[2,3], Haiyan Cheng[4], Zhen Cui[5] and Jianping Li[6]*

[1]Department of Application & Engineering, Zhejiang Institute of Economics and Trade, Hangzhou, China, [2]School of Mechanical and Electronic Engineering, Nanjing Forestry University, Nanjing, China, [3]School of Mechanical Engineering, Wanjiang University of Technology, Maanshan, China, [4]School of Foreign Languages, Zhejiang University of Finance & Economics Dongfang College, Zhejiang, China, [5]School of Automation and Information Engineering, Xi'an University of Technology, Xi'an, China, [6]School of Automotive & Transportation Engineering, Shenzhen Polytechnic, Shenzhen, China

Two-dimensional van der Waals (vdW) heterostructures reveal novel properties due to their unique interface, which have attracted extensive focus. In this work, the first-principles methods are explored to investigate the electronic and the optical abilities of the heterostructure constructed by monolayered $MoTe_2$ and PtS_2. Then, the external biaxial strain is employed on the $MoTe_2$/PtS_2 heterostructure, which can persist in the intrinsic type-II band structure and decrease the bandgap. In particular, the $MoTe_2$/PtS_2 vdW heterostructure exhibits a suitable band edge energy for the redox reaction for water splitting at pH 0, while it is also desirable for that at pH 7 under decent compressive stress. More importantly, the $MoTe_2$/PtS_2 vdW heterostructure shows a classy solar-to-hydrogen efficiency, and the light absorption properties can further be enhanced by the strain. Our results showed an effective theoretical strategy to tune the electronic and optical performances of the 2D heterostructure, which can be used in energy conversion such as the automotive battery system.

Keywords: vdW heterostructures, first-principles method, $MoTe_2$/PtS_2, strain, solar-to-hydrogen efficiency

Edited by:
Guangzhao Wang,
Yangtze Normal University, China

Reviewed by:
San-Dong Guo,
Xi'an University of Posts and Telecommunications, China
Sake Wang,
Jinling Institute of Technology, China

Correspondence:
Jianping Li
szyljp0170@szpt.edu.cn

Specialty section:
This article was submitted to Theoretical and Computational Chemistry, a section of the journal Frontiers in Chemistry

Received: *02 May 2022*
Accepted: *24 May 2022*
Published: *25 July 2022*

Citation:
Zhang L, Ren K, Cheng H, Cui Z and Li J (2022) The First-Principles Study of External Strain Tuning the Electronic and Optical Properties of the 2D $MoTe_2$/PtS_2 van der Waals Heterostructure. Front. Chem. 10:934048. doi: 10.3389/fchem.2022.934048

INTRODUCTION

Graphene shows unique electronic and thermal performances after being prepared as a two-dimensional (2D) material (Geim and Novoselov, 2007), which has also attracted other layered materials (Cui et al., 2021a; Cui et al., 2021b; Ren et al., 2022a; Wang et al., 2022a). However, its zero bandgap restricts the applications as electronic switch and other devices. Therefore, 2D semiconducting materials include transition metal dichalcogenides (TMDs) (Shen et al., 2022), phosphorene, and MXenes. MoS_2 possesses excellent electronic and photoelectric properties similar to or even more advantageous than graphene in some aspects (Butler et al., 2013; Zhang et al., 2018). After the successful synthesis of graphene and MoS_2, more and more 2D materials have been found and synthesized. Its direct bandgap is about ~1.8 eV (Wickramaratne et al., 2014), which can be widely used in transistors, optoelectronics, and photocatalysts (Radisavljevic et al., 2011; Qiu et al., 2013; Ma et al., 2020). Black phosphorene has intrinsic direct bandgap and high carrier mobility (Li et al., 2014). Due to the anisotropic structure, black phosphorene shows remarkable anisotropic electronic, mechanical, and thermal properties. All these excellent properties endow its application in high-performance photovoltaic (Liu et al., 2017), spin-filter devices (You et al., 2016), thermal rectifiers (Ren et al., 2020a), field-effect transistors (Hong et al., 2014), etc.

To expand the family of 2D materials, tremendous investigations have been conducted to predict the structure and properties of these layered materials (Sun et al., 2020; Sun and Schwingenschlögl, 2020; Sun et al., 2021; Sun and Schwingenschlögl, 2021). In addition, the formation of the van der Waals (vdW) heterostructure by different 2D materials is also a popular strategy to extend the applications of the 2D materials (Wang et al., 2022b). The vdW interactions in the heterostructure result in novel interfacial performances, which can improve the electronic (Ren et al., 2021a), optical (Ren et al., 2019a), and catalytic (Wang et al., 2018a; Wang et al., 2020a; Wang et al., 2020b) characteristics. Furthermore, such excellent properties of the heterostructure can even be tuned by the electric field (Sun et al., 2017a), strain (Ren et al., 2019b; Wang et al., 2020c; Wang et al., 2020d), stacking (Ren et al., 2022b), doping (Ren et al., 2022c),and defect (Sun et al., 2017b). When applied, the external strain is an effective tactic; for example, the band structure of the MXene/blue phosphorene vdW heterostructure can result in the transformation from type-I to type-II by the strain (Guo et al., 2017). The external strain also possesses a significant influence on the layer distance, which further decides the interfacial performances (Guo et al., 2020). Under the strain, the evolution of Schottky barriers of the GaN/graphene heterostructure can be converted from the n-Schottky to Ohmic type (Deng and Wang, 2019). Recently, the TMD materials of MoTe$_2$ and PtS$_2$ monolayers have been prepared experimentally (Qu et al., 2017; Zhao et al., 2019). The MoTe$_2$ and PtS$_2$ monolayers present the novel electronic (Qu et al., 2017; Sajjad et al., 2018) and thermoelectric (Shi et al., 2017) properties, which have been widely studied. The 2D MoTe$_2$ can be obtained from mechanically exfoliated bulk crystals (Chang et al., 2016), which have potential usages in electronics, such as inverters and amplifiers, and in logic and digital circuits. Moreover, the electronic property of MoTe$_2$ is sensitive to atomic doping (Kanoun, 2018), suggesting tunable electronic and optical performances. The PtS$_2$ monolayer also presents tunable properties by the strain (Liu et al., 2018) and electric field (Nguyen et al., 2019). In addition, the PtS$_2$ monolayer is reported to be formed as a vdW heterostructure such as PtS$_2$/arsenene (Ren et al., 2020b), PtS$_2$/InSe (Nguyen et al., 2019), and HfS$_2$/PtS$_2$ (Colibaba et al., 2019). Furthermore, the MoTe$_2$ and PtS$_2$ monolayers share a honeycomb hexagonal structure with a small lattice mismatch, explaining the advantage to be formed as a heterostructure. Therefore, the MoTe$_2$ and PtS$_2$ monolayers have been decided to be used for constructing the heterostructure in this work. The first-principles calculations are developed to investigate the band structure of the MoTe$_2$/PtS$_2$ (MP) heterostructure. Importantly, the tunable electronic, charge density, potential, light absorption ability, and the solar-to-hydrogen efficiency (STH) by the external biaxial strain are addressed.

COMPUTATIONAL METHODS

In this investigation, the Vienna *ab initio* simulation software package (VASP) was used to find the first-principles simulations by the density functional theory (DFT) (Kresse and Furthmüller, 1996a; Kresse and Furthmüller, 1996b). In the generalized gradient approximation (GGA), the projector augmented wave (PAW) potentials were used with the Perdew–Burke–Ernzerhof (PBE) functional to describe the core electrons and the exchange–correlation functional (Perdew et al., 1996; Kresse and Joubert, 1999). The cut-off energy was used by 550 eV, and the Monkhorst–Pack *k*-point was 15 × 15 × 1 in the calculations. Furthermore, the Heyd–Scuseria–Ernzerhof hybrid method was adopted to calculate the electronic and optical properties (Heyd et al., 2005). The weak dispersion forces were described by the DFT-D3 method proposed by Grimme et al. (2010). Due to the ignorable effect of the spin–orbit coupling (SOC) on the electronic properties of the studied system, shown in **Supplementary Figure S1**, the SOC is not employed in the calculations. The vacuum thickness was set as 25 Å to prohibit the interaction adjacent layers. Besides, the convergence criterion of the force in the simulations was 0.01 eV Å^{-1}, while the energy was controlled in 0.01 meV.

RESULTS AND DISCUSSION

The lattice parameters of the MoTe$_2$ and PtS$_2$ monolayers are optimized as 3.564 and 3.529 Å, respectively, showing a low lattice mismatch of about 0.1%, which are suitable to be constructed as a heterostructure. **Supplementary Figure S2** shows the band structures of the pristine MoTe$_2$ and PtS$_2$ monolayers calculated using the HSE06 functional with the indirect and direct bandgaps of 1.22 and 2.60 eV, respectively, demonstrating an agreement with the previous reports (Shao et al., 2022). Then, the MP heterostructure is constructed by considering six different highly symmetrical structures, as shown in **Supplementary Figure S3**. By calculating the binding energy, the most stable stacking configuration is decided, as shown in **Figure 1A**, that the Mo atoms are located on top of the upper S atoms, while the Te atoms are set on top of the lower S atoms. The MoTe$_2$/PtS$_2$ heterostructure is built by vdW forces because of the weak binding energy of about −28.10 meV Å^{-2} (Ren et al., 2022b), which is lower than that in graphites (about −18 meV Å^{-2}) (Chen et al., 2013). The projected band structure of the MP vdW heterostructure is obtained in **Figure 1B**, suggesting an indirect bandgap of about 1.26 eV. The CBM and the VBM of the MP vdW heterostructure result from the PtS$_2$ and MoTe$_2$ monolayers, respectively, showing a type-II band alignment, which can separate the photogenerated electrons and holes using as a photocatalyst for water splitting (Ren et al., 2021b). In detail, when the MP vdW heterostructure obtains the energy from the light, the photogenerated electrons will move to the conduction band of the MoTe$_2$ and PtS$_2$ monolayers, as shown in **Figure 1C**, resulting in photogenerated holes staying at the valence band. Then, the conduction band offset (CBO) can promote the photogenerated electrons from MoTe$_2$ to PtS$_2$ at the conduction band, while the photogenerated holes will be transferred from PtS$_2$ to MoTe$_2$ at the valence band. Thus, the photogenerated charges in the MP vdW heterostructure are prevented from recombination.

Next, the external biaxial strain is applied in the MP vdW heterostructure to explore its effect on the electronic structure.

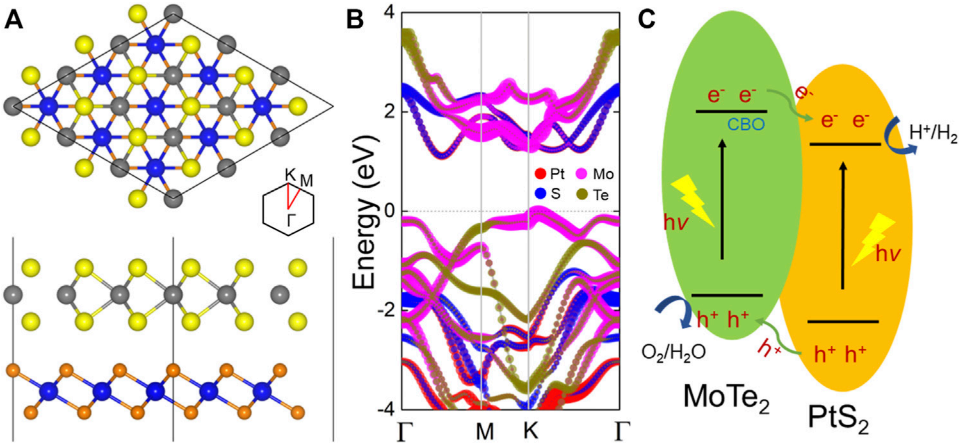

FIGURE 1 | (A) Geometric and **(B)** band structure of the MP heterostructure with the lowest binding energy. **(C)** Photogenerated charge migration path in the MP vdW heterostructure. The yellow, gray, orange, and blue spheres represent the Te, Mo, S, and Pt atoms, respectively. The Fermi level is decided as 0 shown by the gray dashed line.

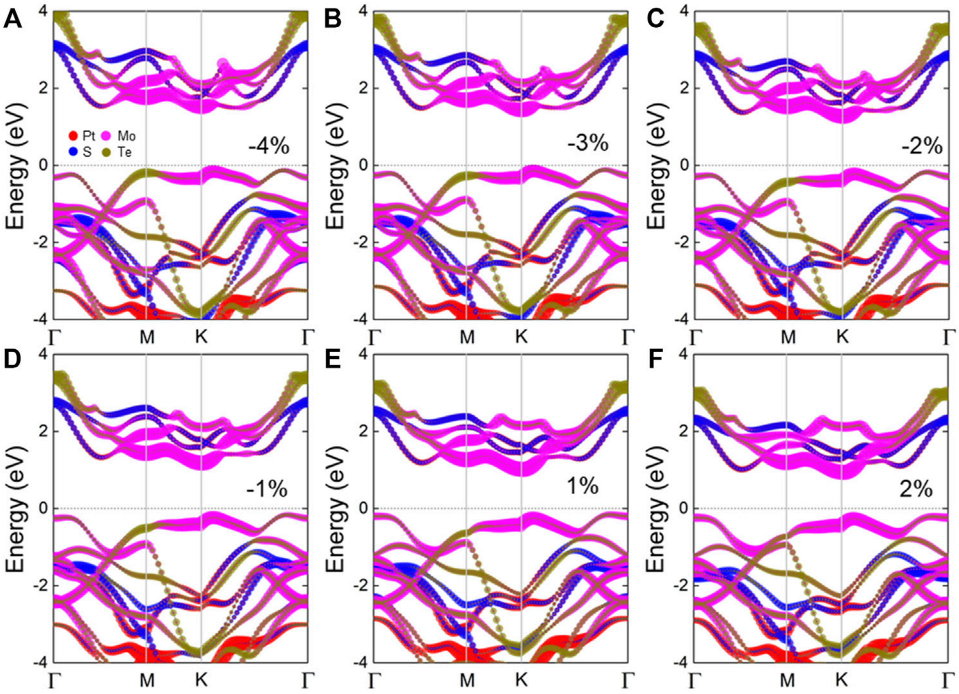

FIGURE 2 | Band structures of the MP vdW heterostructure under the external strains of **(A)** –4%, **(B)** –3%, **(C)** –2%, **(D)** –1%, **(E)** 1%, and **(F)** 2%.

In **Figure 2**, the projected band structure of the MP vdW heterostructure under the external biaxial strain from –4 to 2% is obtained, where negative and positive values represent pressure and tension, respectively. One can see that the type-II band structure is retained in the MP vdW heterostructure with that strain, which still can separate the photogenerated electrons and holes, while the bandgap decreased from 1.454 to 1.150 eV by the external biaxial strain from –4 to 2%, as shown in **Figure 3A**. In addition, the binding energy (E_b) is also investigated, which is decided by

$$E_b = E_H - E_M - E_P, \quad (1)$$

where E_H, E_M, and E_P represent the total energy of the MP vdW heterostructure, pristine MoTe$_2$, and PtS$_2$, respectively. The calculated binding energy change of the MP vdW heterostructure applied by different external biaxial strains is demonstrated by **Figure 3B**, which shows the stability of the MP

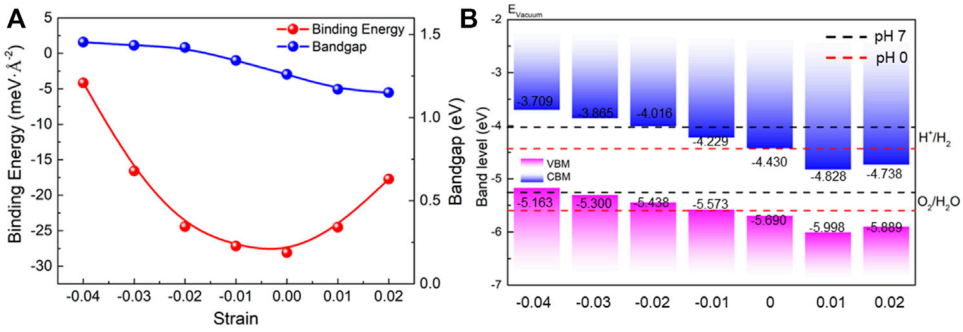

FIGURE 3 | (A) Band alignment of the MP vdW heterostructure by the external strain comparing the energy potential of the redox reaction at pH values 0 and 7. **(B)** Binding energy and the bandgap difference of the MP vdW heterostructure tuned by the external strain.

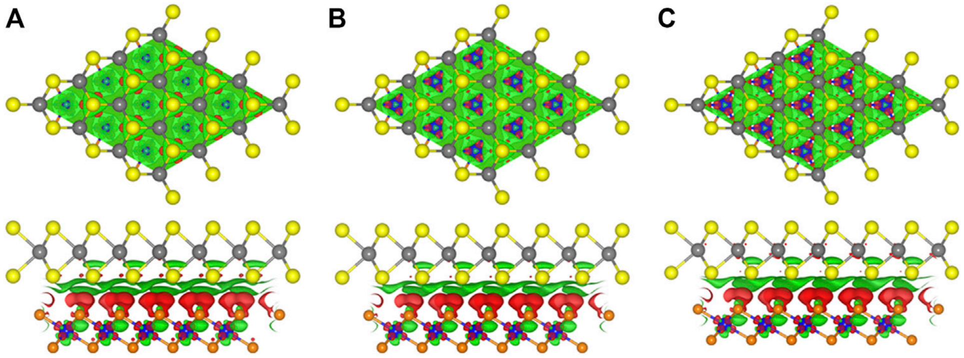

FIGURE 4 | Isosurface of the charge density difference of the MP vdW heterostructure under the strains of **(A)** –4%, **(B)** –2%, and **(C)** 2%; red and green marks demonstrate the losing and gaining of electrons, respectively. The isosurface parameter is 0.001 |e|.

vdW heterostructure, and the lowest binding energy of the MP vdW heterostructure is the unstressed state.

The band edge positions of the MP vdW heterostructure under different strains are also calculated by the HSE06 functional, demonstrated in **Figure 3B**. The potential energy values of the oxidation and reduction reactions for water splitting are −5.67 eV and −4.44 eV, respectively, at pH 0. The energy of the redox potential can be decided by the pH level with: $E = -4.44\,\text{eV} + \text{pH} \times 0.059\,\text{eV}$ for the reduction reaction, while the potential of the oxidation is obtained by $E = -5.67\,\text{eV} + \text{pH} \times 0.059\,\text{eV}$. Thus, the calculated potentials of the oxidation and reduction reactions at pH 0 are −5.26 eV and −4.03 eV, respectively, at pH 7. As a decent photocatalyst, the band edge positions of the CBM (or VBM) of the heterostructure should be higher (or lower) than the potential of the reduction (or oxidation) for water splitting (Ren et al., 2021c). In **Figure 3B**, one can see that the MP vdW heterostructure possesses suitable band edge positions to promote the redox reaction at pH 7 for water splitting by the external biaxial strains of −3% and −2%, while the MP vdW heterostructure can be used as a promising photocatalyst for water splitting at pH 0 without the external strain.

The charge density difference ($\Delta\rho$) of the MP vdW heterostructure tuned by the strain is also investigated, which is calculated as follows:

$$\Delta\rho = \rho H - \rho M - \rho P, \tag{2}$$

where ρ_H, $\rho_{M,}$ and ρ_P are used as the charge densities of the MP vdW heterostructure, pristine MoTe$_2$, and PtS$_2$, respectively. Under these strains, the PtS$_2$ layer still gains the electrons from the MoTe$_2$ layer, and the charge density difference between the interface of the MP vdW heterostructure under −4%, −2%, and 2% is demonstrated in **Figures 4A–C**, respectively. In addition, the quantitative analysis of the charge transfer in the MP vdW heterostructure is explored by the Bader charge method (Sanville et al., 2007). The calculated charge transfers between the interface of the MP vdW heterostructure under −4%, −2%, and 2% are 0.0463 |e|, 0.0475 |e|, and 0.052 |e|, respectively.

The charge density difference between the interface of the MoTe$_2$ and PtS$_2$ monolayers can induce a potential drop. The potential energy of the MoTe$_2$ and PtS$_2$ in the heterostructure by the different strains is investigated in **Figure 5**, showing that the strain can increase the potential energy of the MoTe$_2$ and PtS$_2$ from pressure to tension. The potential drop across the interface of the MP vdW heterostructure is obtained as 4.962, 4.720, 4.672, and 4.500 eV by the external biaxial strains of −4%, −2%, −0%, and 2%, respectively, which demonstrates the decreased charge density difference. It is worth emphasizing that such a potential

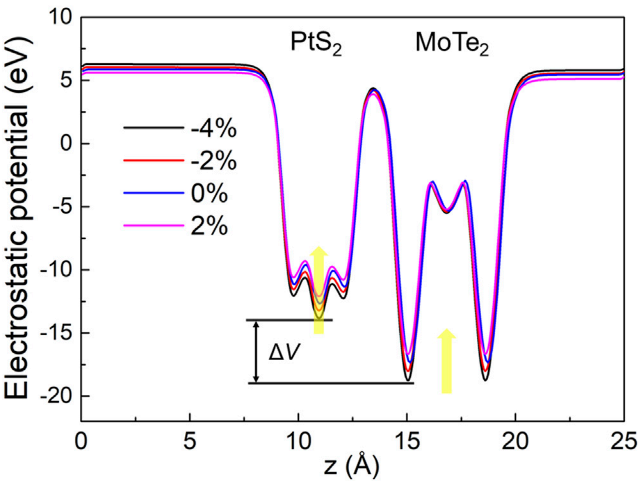

FIGURE 5 | Potential drop of the MP vdW heterostructure across the interface by different external strains.

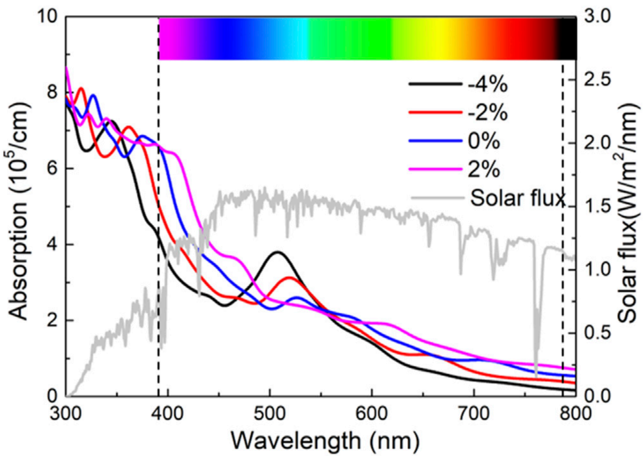

FIGURE 6 | Calculated optical absorption of the MP vdW heterostructure under the external strain.

drop in the MP vdW heterostructure can also provide a critical boost for the separation of the photogenerated electrons and holes.

We also studied the light absorption coefficient (α) of the MP vdW heterostructure by external strain using the HSE06 method, which is calculated as follows:

$$\alpha(\omega) = \frac{\sqrt{2}\omega}{c}\left\{\left[\varepsilon_1^2(\omega) + \varepsilon_2^2(\omega)\right]^{1/2} - \varepsilon_1(\omega)\right\}^{1/2}, \tag{3}$$

where ω is the angular frequency, and c is the speed of light. The real and imaginary parts are represented by $\varepsilon_1(\omega)$ and $\varepsilon_2(\omega)$, respectively. Moreover, $\varepsilon_1(\omega)$ and $\varepsilon_2(\omega)$ can be obtained as follows:

$$\varepsilon_2(q \to O_{\hat{u}}, \hbar\omega) = \frac{2e^2\pi}{\Omega\varepsilon_0}\sum_{k,v,c}\left|\langle\Psi_k^c|\hat{u}\cdot r|\Psi_k^v\rangle\right|^2 \times \delta\left(E_k^c - E_k^v - E\right), \tag{4}$$

$$\varepsilon(\omega) = \varepsilon_1(\omega) + i\varepsilon_2(\omega), \tag{5}$$

where Ψ_k, E_k, and $\hat{u}$ are the wave function, energy, and unit vector of the electric field of the incident light, respectively. The superscripts (v and c) in Ψ_k and E_k are labeled as the conduction bands and valence bands, respectively. The calculated light absorption performance of the strained MP vdW heterostructure is explained by **Figure 6** marked by a visible spectrum (Wang et al., 2018b). Evidently, applying the external compressive stress can improve the light absorption capacity at the absorption wavelength ranging from 480 to 550 nm. In detail, the light absorption peaks of the MP vdW heterostructure are obtained as $3.79 \times 10^5\ \mathrm{cm}^{-1}$, $3.13 \times 10^5\ \mathrm{cm}^{-1}$, and $2.60 \times 10^5\ \mathrm{cm}^{-1}$ locating the wavelength at 509 nm, 519, and 527 nm, respectively, by the strains of −0.04, −0.02, and 0, while the light absorption performance of the MP vdW heterostructure can be enhanced by tensile stress when the absorption wavelength exceeds 550 nm. Furthermore, these obtained absorption performances are also higher than those of other 2D heterostructures, such as CdO/HfS_2 ($3.51 \times 10^5\ \mathrm{cm}^{-1}$) (Zhang et al., 2022), arsenene/$PtSe_2$ ($2.23 \times 10^5\ \mathrm{cm}^{-1}$) (Zheng et al., 2021), and MoSSe/GaN ($2.74 \times 10^5\ \mathrm{cm}^{-1}$) (Ren et al., 2020c).

Furthermore, the solar-to-hydrogen efficiency of the MP vdW heterostructure is calculated by $\eta_{\mathrm{STH}} = \eta_{\mathrm{abs}} \times \eta_{\mathrm{cu}}$ (Fu et al., 2018), where η_{abs} is the efficiency of light absorption, and η_{cu} demonstrates carrier utilization. As for the light absorption, it can be decided by

$$\eta_{\mathrm{abs}} = \frac{\int_{E_g}^{\infty} P(\hbar\omega)\mathrm{d}(\hbar\omega)}{\int_0^{\infty} P(\hbar\omega)\mathrm{d}(\hbar\omega)}, \tag{6}$$

where E_g means the bandgap of the studied material. $\hbar\omega$ is used to explain the photon energy, while the AM1.5G solar energy flux is $P(\hbar\omega)$. The carrier utilization is obtained by

$$\eta_{\mathrm{cu}} = \frac{\Delta G\int_{E}^{\infty}\frac{P(\hbar\omega)}{\hbar\omega}\mathrm{d}(\hbar\omega)}{\int_{E_g}^{\infty} P(\hbar\omega)\mathrm{d}(\hbar\omega)}. \tag{7}$$

To describe the potential difference in water splitting, ΔG is used by 1.23 eV here. Importantly, the photon energy of E is calculated by

$$E = \begin{cases} E_g, \ (\chi(\mathrm{H_2}) \ge 0.2, \chi(\mathrm{O_2}) \ge 0.6), \\ E_g + 0.2 - \chi(\mathrm{H_2}), \ (\chi(\mathrm{H_2}) < 0.2, \chi(\mathrm{O_2}) \ge 0.6), \\ E_g + 0.6 - \chi(\mathrm{O_2}), \ (\chi(\mathrm{H_2}) \ge 0.2, \chi(\mathrm{O_2}) < 0.6), \\ E_g + 0.8 - \chi(\mathrm{H_2}) - \chi(\mathrm{O_2}), \ (\chi(\mathrm{H_2}) < 0.2, \chi(\mathrm{O_2}) < 0.6). \end{cases} \tag{8}$$

The overpotential for the reduction and oxidation reactions for water splitting is explained by $\chi(\mathrm{H_2})$ and $\chi(\mathrm{O_2})$, respectively. In addition, previous experimental investigations provide the necessary overpotentials for the reduction and oxidation reactions as 0.2 and 0.6 eV (Fu et al., 2018), respectively. The efficiencies of light absorption of the MP vdW heterostructure

TABLE 1 | Energy conversion efficiency of light absorption, carrier utilization, and the solar-to-hydrogen efficiency of the MP vdW heterostructure under the external strain.

Strain	η_{abs} (%)	η_{cu} (%)	η_{STH} (%)
–0.03	89.44	33.66	30.10
–0.02	89.80	30.11	30.11
0	93.26	30.10	30.10

under the strains of –0.03, –0.02, and 0 are calculated by 89.44, 89.80, and 93.26%, respectively. Furthermore, the carrier utilization of the MP vdW heterostructure is 33.66, 33.53, and 32.28%, respectively, by the strains of –0.03, –0.02, and 0. Thus, the solar-to-hydrogen efficiencies are obtained as 30.10, 30.11, and 30.10%, respectively, at pH values 7, 7, and 0, as shown in **Table. 1**, which is higher than other 2D heterostructures such as CdO/arsenene (about 11.67%) (Ren et al., 2021b) and GaS/arsenene (about 25.46%) (Li et al., 2021).

CONCLUSION

In this work, the first-principles method is employed to investigate the electronic and optical performances of the MP vdW heterostructure. The external strain is also applied on the MP vdW heterostructure, and the results show that the MP vdW heterostructure maintains the type-II band alignment and decreased bandgap. In addition, the external compressive stress can tune the MP vdW heterostructure as a potential for water splitting at pH 7 because of the decent band edge positions. The strain also has a significant influence on the interfacial properties of the MP vdW heterostructure. Furthermore, the MP vdW heterostructure possesses excellent light absorption capacity and light conversion efficiency, which can also be enhanced by the strain. The results show that the MP vdW heterostructure possesses potential energy conversion used in the automotive battery system.

DATA AVAILABILITY STATEMENT

The raw data supporting the conclusions of this article will be made available by the authors, without undue reservation.

AUTHOR CONTRIBUTIONS

All the authors listed have made a substantial, direct, and intellectual contribution to the work and approved it for publication.

ACKNOWLEDGMENTS

The author LZ thanks the Zhejiang Provincial Natural Science Foundation of China (Grant No. LZY21E060002).

SUPPLEMENTARY MATERIAL

The Supplementary Material for this article can be found online at: https://www.frontiersin.org/articles/10.3389/fchem.2022.934048/full#supplementary-material

REFERENCES

Butler, S. Z., Hollen, S. M., Cao, L., Cui, Y., Gupta, J. A., Gutiérrez, H. R., et al. (2013). Progress, Challenges, and Opportunities in Two-Dimensional Materials beyond Graphene. *ACS Nano* 7, 2898–2926. doi:10.1021/nn400280c

Chang, Y.-M., Lin, C.-Y., Lin, Y.-F., and Tsukagoshi, K. (2016). Two-Dimensional MoTe$_2$ Materials: From Synthesis, Identification, and Charge Transport to Electronics Applications. *Jpn. J. Appl. Phys.* 55, 1102A1101. doi:10.7567/jjap.55.1102a1

Chen, X., Tian, F., Persson, C., Duan, W., and Chen, N.-x. (2013). Interlayer Interactions in Graphites. *Sci. Rep.* 3, 3046. doi:10.1038/srep03046

Colibaba, S. A., Körbel, S., Motta, C., El-Mellouhi, F., and Sanvito, S. (2019). Interlayer dielectric function of a type-II van der Waals semiconductor: The HfS2/PtS2 heterobilayer. *Phys. Rev. Mater.* 3, 124002. doi:10.1103/physrevmaterials.3.124002

Cui, Z., Luo, Y., Yu, J., and Xu, Y. (2021). Tuning the Electronic Properties of MoSi2N4 by Molecular Doping: A First Principles Investigation. *Phys. E Low-dimensional Syst. Nanostructures* 134, 114873. doi:10.1016/j.physe.2021.114873

Cui, Z., Wang, M., Lyu, N., Zhang, S., Ding, Y., and Bai, K. (2021). Electronic, Magnetism and Optical Properties of Transition Metals Adsorbed Puckered Arsenene. *Superlattices Microstruct.* 152, 106852. doi:10.1016/j.spmi.2021.106852

Deng, Z., and Wang, X. (2019). Strain Engineering on the Electronic States of Two-Dimensional GaN/graphene Heterostructure. *RSC Adv.* 9, 26024–26029. doi:10.1039/c9ra03175h

Fu, C.-F., Sun, J., Luo, Q., Li, X., Hu, W., and Yang, J. (2018). Intrinsic Electric Fields in Two-Dimensional Materials Boost the Solar-To-Hydrogen Efficiency for Photocatalytic Water Splitting. *Nano Lett.* 18, 6312–6317. doi:10.1021/acs.nanolett.8b02561

Geim, A. K., and Novoselov, K. S. (2007). The Rise of Graphene. *Nat. Mater* 6, 183–191. doi:10.1038/nmat1849

Grimme, S., Antony, J., Ehrlich, S., and Krieg, H. (2010). A Consistent and Accurate Ab Initio Parametrization of Density Functional Dispersion Correction (DFT-D) for the 94 Elements H-Pu. *J. Chem. Phys.* 132, 154104. doi:10.1063/1.3382344

Guo, W., Ge, X., Sun, S., Xie, Y., and Ye, X. (2020). The strain effect on the electronic properties of the MoSSe/WSSe van der Waals heterostructure: a first-principles study. *Phys. Chem. Chem. Phys.* 22, 4946–4956. doi:10.1039/d0cp00403k

Guo, Z., Miao, N., Zhou, J., Sa, B., and Sun, Z. (2017). Strain-mediated type-I/type-II transition in MXene/Blue phosphorene van der Waals heterostructures for flexible optical/electronic devices. *J. Mat. Chem. C* 5, 978–984. doi:10.1039/c6tc04349f

Heyd, J., Peralta, J. E., Scuseria, G. E., and Martin, R. L. (2005). Energy Band Gaps and Lattice Parameters Evaluated with the Heyd-Scuseria-Ernzerhof Screened Hybrid Functional. *J. Chem. Phys.* 123, 174101. doi:10.1063/1.2085170

Hong, T., Chamlagain, B., Lin, W., Chuang, H.-J., Pan, M., Zhou, Z., et al. (2014). Polarized Photocurrent Response in Black Phosphorus Field-Effect Transistors. *Nanoscale* 6, 8978–8983. doi:10.1039/c4nr02164a

Kanoun, M. B. (2018). Tuning Magnetic Properties of Two-Dimensional MoTe2 Monolayer by Doping 3d Transition Metals: Insights from First Principles Calculations. *J. Alloys Compd.* 748, 938–942. doi:10.1016/j.jallcom.2018.03.132

Kresse, G., and Furthmüller, J. (1996). Efficiency of Ab-Initio Total Energy Calculations for Metals and Semiconductors Using a Plane-Wave Basis Set. *Comput. Mater. Sci.* 6, 15–50. doi:10.1016/0927-0256(96)00008-0

Kresse, G., and Furthmüller, J. (1996). Efficient Iterative Schemes Forab Initiototal-Energy Calculations Using a Plane-Wave Basis Set. *Phys. Rev. B* 54, 11169–11186. doi:10.1103/physrevb.54.11169

Kresse, G., and Joubert, D. (1999). From Ultrasoft Pseudopotentials to the Projector Augmented-Wave Method. *Phys. Rev. B* 59, 1758–1775. doi:10.1103/physrevb.59.1758

Li, J., Huang, Z., Ke, W., Yu, J., Ren, K., and Dong, Z. (2021). High solar-to-hydrogen efficiency in Arsenene/GaX (X = S, Se) van der Waals heterostructure for photocatalytic water splitting. *J. Alloys Compd.* 866, 158774. doi:10.1016/j.jallcom.2021.158774

Li, L., Yu, Y., Ye, G. J., Ge, Q., Ou, X., Wu, H., et al. (2014). Black Phosphorus Field-Effect Transistors. *Nat. Nanotech* 9, 372–377. doi:10.1038/nnano.2014.35

Liu, G., Gan, Y., Quhe, R., and Lu, P. (2018). Strain Dependent Electronic and Optical Properties of PtS2 Monolayer. *Chem. Phys. Lett.* 709, 65–70. doi:10.1016/j.cplett.2018.08.029

Liu, Y., Cai, Y., Zhang, G., Zhang, Y.-W., and Ang, K.-W. (2017). Al-Doped Black Phosphorus P-N Homojunction Diode for High Performance Photovoltaic. *Adv. Funct. Mat.* 27, 1604638. doi:10.1002/adfm.201604638

Ma, L., Xu, Y., Zheng, J., and Dai, X. (2020). Ecodesign Method of Intelligent Boom Sprayer Based on Preferable Brownfield Process. *J. Clean. Prod.* 268, 122206. doi:10.1016/j.jclepro.2020.122206

Nguyen, C. V., Bui, H. D., Nguyen, T. D., and Pham, K. D. (2019). Controlling electronic properties of PtS2/InSe van der Waals heterostructure via external electric field and vertical strain. *Chem. Phys. Lett.* 724, 1–7. doi:10.1016/j.cplett.2019.03.048

Perdew, J. P., Burke, K., and Ernzerhof, M. (1996). Generalized Gradient Approximation Made Simple. *Phys. Rev. Lett.* 77, 3865–3868. doi:10.1103/physrevlett.77.3865

Qiu, D. Y., da Jornada, F. H., and Louie, S. G. (2013). Optical Spectrum ofMoS2: Many-Body Effects and Diversity of Exciton States. *Phys. Rev. Lett.* 111, 216805. doi:10.1103/physrevlett.111.216805

Qu, D., Liu, X., Huang, M., Lee, C., Ahmed, F., Kim, H., et al. (2017). Carrier-Type Modulation and Mobility Improvement of Thin MoTe2. *Adv. Mat.* 29, 1606433. doi:10.1002/adma.201606433

Radisavljevic, B., Radenovic, A., Brivio, J., Giacometti, V., and Kis, A. (2011). Single-layer MoS2 Transistors. *Nat. Nanotech* 6, 147–150. doi:10.1038/nnano.2010.279

Ren, K., Liu, X., Chen, S., Cheng, Y., Tang, W., and Zhang, G. (2020). Remarkable Reduction of Interfacial Thermal Resistance in Nanophononic Heterostructures. *Adv. Funct. Mat.* 30, 2004003. doi:10.1002/adfm.202004003

Ren, K., Luo, Y., Wang, S., Chou, J.-P., Yu, J., Tang, W., et al. (2019). A van der Waals Heterostructure Based on Graphene-like Gallium Nitride and Boron Selenide: A High-Efficiency Photocatalyst for Water Splitting. *ACS Omega* 4, 21689–21697. doi:10.1021/acsomega.9b02143

Ren, K., Qin, H., Liu, H., Chen, Y., Liu, X., and Zhang, G. (2022). Manipulating Interfacial Thermal Conduction of 2D Janus Heterostructure via a Thermo-Mechanical Coupling. *Adv. Funct. Mater.* 32, 2110846. doi:10.1002/adfm.202110846

Ren, K., Shu, H., Huo, W., Cui, Z., and Xu, Y. (2022c). Tuning Electronic, Magnetic and Catalytic Behaviors of Biphenylene Network by Atomic Doping. *Nanotechnology* 33, 345701.

Ren, K., Shu, H., Huo, W., Cui, Z., Yu, J., and Xu, Y. (2021). Mechanical, Electronic and Optical Properties of a Novel B2P6 Monolayer: Ultrahigh Carrier Mobility and Strong Optical Absorption. *Phys. Chem. Chem. Phys.* 23, 24915–24921. doi:10.1039/d1cp03838a

Ren, K., Sun, M., Luo, Y., Wang, S., Yu, J., and Tang, W. (2019). First-principle Study of Electronic and Optical Properties of Two-Dimensional Materials-Based Heterostructures Based on Transition Metal Dichalcogenides and Boron Phosphide. *Appl. Surf. Sci.* 476, 70–75. doi:10.1016/j.apsusc.2019.01.005

Ren, K., Tang, W., Sun, M., Cai, Y., Cheng, Y., and Zhang, G. (2020). A direct Z-scheme PtS2/arsenene van der Waals heterostructure with high photocatalytic water splitting efficiency. *Nanoscale* 12, 17281–17289. doi:10.1039/d0nr02286e

Ren, K., Wang, S., Luo, Y., Chou, J.-P., Yu, J., Tang, W., et al. (2020). High-efficiency photocatalyst for water splitting: a Janus MoSSe/XN (X = Ga, Al) van der Waals heterostructure. *J. Phys. D. Appl. Phys.* 53, 185504. doi:10.1088/1361-6463/ab71ad

Ren, K., Zheng, R., Xu, P., Cheng, D., Huo, W., Yu, J., et al. (2021). Electronic and Optical Properties of Atomic-Scale Heterostructure Based on MXene and MN (M = Al, Ga): A DFT Investigation. *Nanomaterials* 11, 2236. doi:10.3390/nano11092236

Ren, K., Zheng, R., Yu, J., Sun, Q., and Li, J. (2021). Band Bending Mechanism in CdO/Arsenene Heterostructure: A Potential Direct Z-Scheme Photocatalyst. *Front. Chem.* 9, 788813. doi:10.3389/fchem.2021.788813

Ren, K., Zhu, Z., Wang, K., Huo, W., and Cui, Z. (2022). Stacking-Mediated Type-I/Type-II Transition in Two-Dimensional MoTe2/PtS2 Heterostructure: A First-Principles Simulation. *Crystals* 12, 425. doi:10.3390/cryst12030425

Sajjad, M., Singh, N., and Schwingenschlögl, U. (2018). Strongly Bound Excitons in Monolayer PtS2 and PtSe2. *Appl. Phys. Lett.* 112, 043101. doi:10.1063/1.5010881

Sanville, E., Kenny, S. D., Smith, R., and Henkelman, G. (2007). Improved Grid-Based Algorithm for Bader Charge Allocation. *J. Comput. Chem.* 28, 899–908. doi:10.1002/jcc.20575

Shao, C., Ren, K., Huang, Z., Yang, J., and Cui, Z. (2022). Two-Dimensional PtS2/MoTe2 van der Waals Heterostructure: An Efficient Potential Photocatalyst for Water Splitting. *Front. Chem.* 10, 847319. doi:10.3389/fchem.2022.847319

Shen, Z., Ren, K., Zheng, R., Huang, Z., Cui, Z., Zheng, Z., et al. (2022). The Thermal and Electronic Properties of the Lateral Janus MoSSe/WSSe Heterostructure. *Front. Mat.* 9, 838648. doi:10.3389/fmats.2022.838648

Shi, D., Wang, G., Li, C., Shen, X., and Nie, Q. (2017). Preparation and Thermoelectric Properties of MoTe 2 Thin Films by Magnetron Co-sputtering. *Vacuum* 138, 101–104. doi:10.1016/j.vacuum.2017.01.030

Sun, M., Chou, J.-P., Ren, Q., Zhao, Y., Yu, J., and Tang, W. (2017). Tunable Schottky barrier in van der Waals heterostructures of graphene and g-GaN. *Appl. Phys. Lett.* 110, 173105. doi:10.1063/1.4982690

Sun, M., Chou, J.-P., Yu, J., and Tang, W. (2017). Effects of Structural Imperfection on the Electronic Properties of graphene/WSe2 Heterostructures. *J. Mat. Chem. C* 5, 10383–10390. doi:10.1039/c7tc03131a

Sun, M., Luo, Y., Yan, Y., and Schwingenschlögl, U. (2021). Ultrahigh Carrier Mobility in the Two-Dimensional Semiconductors B8Si4, B8Ge4, and B8Sn4. *Chem. Mat.* 33, 6475–6483. doi:10.1021/acs.chemmater.1c01824

Sun, M., and Schwingenschlögl, U. (2020). δ-CS: A Direct-Band-Gap Semiconductor Combining Auxeticity, Ferroelasticity, and Potential for High-Efficiency Solar Cells. *Phys. Rev. Appl.* 14, 044015. doi:10.1103/physrevapplied.14.044015

Sun, M., and Schwingenschlögl, U. (2021). Structure Prototype Outperforming MXenes in Stability and Performance in Metal-Ion Batteries: A High Throughput Study. *Adv. Energy Mat.* 11, 2003633. doi:10.1002/aenm.202003633

Sun, M., Yan, Y., and Schwingenschlögl, U. (2020). Beryllene: A Promising Anode Material for Na- and K-Ion Batteries with Ultrafast Charge/Discharge and High Specific Capacity. *J. Phys. Chem. Lett.* 11, 9051–9056. doi:10.1021/acs.jpclett.0c02426

Wang, G.-Z., Chang, J.-L., Tang, W., Xie, W., and Ang, Y. S. (2022b). 2D Materials and Heterostructures for Photocatalytic Water-Splitting: A Theoretical Perspective. *J. Phys. Phys. D. Appl. Phys.* 55, 293002.

Wang, G., Chang, J., Tang, W., Xie, W., and Ang, Y. S. (2022a). 2D Materials and Heterostructures for Photocatalytic Water-Splitting: a Theoretical Perspective. *J. Phys. D. Appl. Phys.* 55, 293002. doi:10.1088/1361-6463/ac5771

Wang, G., Gong, L., Li, Z., Wang, B., Zhang, W., Yuan, B., et al. (2020). A Two-Dimensional CdO/CdS Heterostructure Used for Visible Light Photocatalysis. *Phys. Chem. Chem. Phys.* 22, 9587–9592. doi:10.1039/d0cp00876a

Wang, G., Zhang, L., Li, Y., Zhao, W., Kuang, A., Li, Y., et al. (2020). Biaxial Strain Tunable Photocatalytic Properties of 2D ZnO/GeC Heterostructure. *J. Phys. D. Appl. Phys.* 53, 015104. doi:10.1088/1361-6463/ab440e

Wang, G., Zhi, Y., Bo, M., Xiao, S., Li, Y., Zhao, W., et al. (2020). 2D Hexagonal Boron Nitride/Cadmium Sulfide Heterostructure as a Promising Water-Splitting Photocatalyst. *Phys. Status Solidi B* 257, 1900431. doi:10.1002/pssb.201900431

Wang, S., Ren, C., Tian, H., Yu, J., and Sun, M. (2018). MoS2/ZnO van der Waals heterostructure as a high-efficiency water splitting photocatalyst: a first-principles study. *Phys. Chem. Chem. Phys.* 20, 13394–13399. doi:10.1039/c8cp00808f

Wang, S., Tian, H., Ren, C., Yu, J., and Sun, M. (2018). Electronic and Optical Properties of Heterostructures Based on Transition Metal Dichalcogenides and Graphene-like Zinc Oxide. *Sci. Rep.* 8, 12009. doi:10.1038/s41598-018-30614-3

Wang, S., Ukhtary, M. S., and Saito, R. (2020). Strain Effect on Circularly Polarized Electroluminescence in Transition Metal Dichalcogenides. *Phys. Rev. Res.* 2, 033340. doi:10.1103/physrevresearch.2.033340

Wickramaratne, D., Zahid, F., and Lake, R. K. (2014). Electronic and Thermoelectric Properties of Few-Layer Transition Metal Dichalcogenides. *J. Chem. Phys.* 140, 124710. doi:10.1063/1.4869142

You, B., Wang, X., Zheng, Z., and Mi, W. (2016). Black phosphorene/monolayer transition-metal dichalcogenides as two dimensional van der Waals heterostructures: a first-principles study. *Phys. Chem. Chem. Phys.* 18, 7381–7388. doi:10.1039/c5cp07585h

Zhang, H., Chhowalla, M., and Liu, Z. (2018). 2D Nanomaterials: Graphene and Transition Metal Dichalcogenides. *Chem. Soc. Rev.* 47, 3015–3017. doi:10.1039/c8cs90048e

Zhang, Q., Ren, K., Zheng, R., Huang, Z., An, Z., and Cui, Z. (2022). First-Principles Calculations of Two-Dimensional CdO/HfS2 Van der Waals Heterostructure: Direct Z-Scheme Photocatalytic Water Splitting. *Front. Chem.* 10, 879402. doi:10.3389/fchem.2022.879402

Zhao, D., Xie, S., Wang, Y., Zhu, H., Chen, L., Sun, Q., et al. (2019). Synthesis of Large-Scale Few-Layer PtS2 Films by Chemical Vapor Deposition. *AIP Adv.* 9, 025225. doi:10.1063/1.5086447

Zheng, R., Ren, K., Yu, J., Zhu, Z., and Sun, Q. (2021). Type-II Heterostructure Based on two-Dimensional Arsenene and PtS$_2$ With Novel Light Absorption Performance. Third International Conference on Optoelectronic Science and Materials (ICOSM 2021), Hefei, China, December 9, 2021 (SPIE), 182–186.

Conflict of Interest: The authors declare that the research was conducted in the absence of any commercial or financial relationships that could be construed as a potential conflict of interest.

frontiers | Frontiers in Chemistry

TYPE Original Research
PUBLISHED 25 August 2022
DOI 10.3389/fchem.2022.1003027

OPEN ACCESS

EDITED BY
Guangzhao Wang,
Yangtze Normal University, China

REVIEWED BY
Junli Chang,
Southwest University, China
Liu Xuefei,
Guizhou Normal University, China

*CORRESPONDENCE
Zishuang Cheng,
czs19950627@163.com
Chuntao Chang,
changct@dgut.edu.cn

SPECIALTY SECTION
This article was submitted to Theoretical and Computational Chemistry, a section of the journal Frontiers in Chemistry

RECEIVED 25 July 2022
ACCEPTED 03 August 2022
PUBLISHED 25 August 2022

CITATION
Wang F, Cheng Z, Zhang X, Xie C, Liu F, Chang C and Liu G (2022), A novel two-dimensional transition metal dichalcogenide as water splitting photocatalyst with excellent performances.
Front. Chem. 10:1003027.
doi: 10.3389/fchem.2022.1003027

A novel two-dimensional transition metal dichalcogenide as water splitting photocatalyst with excellent performances

Fang Wang[1,2], Zishuang Cheng[1,3]*, Xiaoming Zhang[3], Chunxiao Xie[1,4], Fucai Liu[2], Chuntao Chang[1]* and Guodong Liu[3]

[1]School of Mechanical Engineering, Neutron Scattering Technical Engineering Research Center, Dongguan University of Technology, Dongguan, China, [2]School of Optoelectronic Science and Engineering, University of Electronic Science and Technology of China, Chengdu, China, [3]School of Materials Science and Engineering, Hebei University of Technology, Tianjin, China, [4]Guangdong-Taiwan College of Industrial Science & Technology, Dongguan University of Technology, Dongguan, China

With the rising demand for renewable energy, photocatalysts are considered the most promising solution to harness solar energy, and the search for photocatalysts with excellent performances remains an urgent task. Here, based on density functional theory (DFT), the photocatalytic properties of $MoWS_4$ are systematically investigated. The $MoWS_4$ monolayer and bilayer are demonstrated as semiconductors with indirect band gaps of 2.01 and 1.48 eV. Moreover, they exhibit high and anisotropic light absorption coefficients of up to ~10^5 cm^{-1} in the visible-ultraviolet region. The intrinsic band edge positions could fully satisfy the redox potentials of water without any external adjustment. The electron mobility of $MoWS_4$ monolayer is 557 cm^2 $V^{-1}s^{-1}$, which is seven times higher than MoS_2 monolayer. Hence, $MoWS_4$ can be regarded as a promising 2D photocatalyst candidate for water splitting.

KEYWORDS

two-dimensional materials, transition metal dichalcogenides, water splitting photocatalyst, high mobility, density functional theory

Introduction

With the depletion of fossil energy and the increasing pollution of the natural environment, the demands for renewable energy become critical and urgent for sustainable development of global economy. In 1972, Fujishima and Honda discovered that TiO_2 can split water to produce hydrogen and oxygen in the presence of sunlight, making photocatalysis one of the most noteworthy solutions to harness solar energy (Fujishima and Honda, 1972). Afterwards, great efforts have been made to develop effective photocatalysts, including transition metal oxides, sulfides, nitrides, and so forth (Tsuji et al., 2005; Suntivich et al., 2011; Han et al., 2018). However, the low quantum efficiency derived from charge recombination on the surface and in the bulk of these

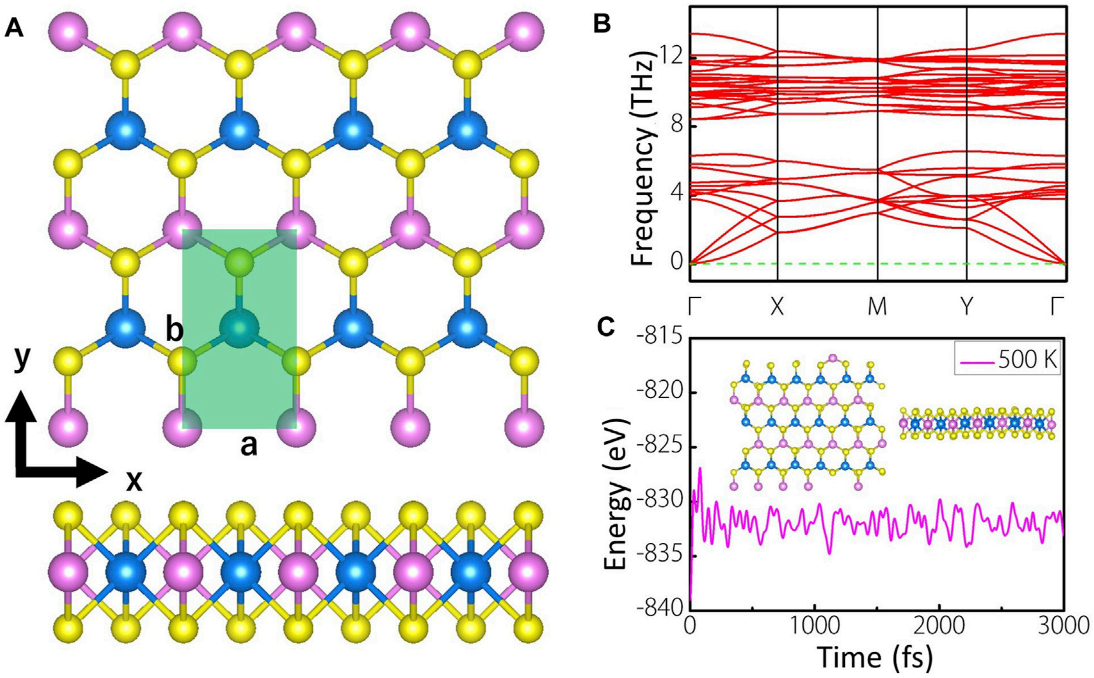

FIGURE 1
(A) Top and side views of $MoWS_4$ monolayer. The pink, blue, and yellow balls represent Mo, W, and S atoms, respectively. The light green area is the unit cell of $MoWS_4$ monolayer **(B)** Phonon spectra of $MoWS_4$ monolayer **(C)** Evolution of the total energy and a snapshot of $MoWS_4$ monolayer after a 3,000 fs AIMD simulations in vacuum at 500K

photocatalysts could not meet the criteria of favorable photocatalyst for sunlight driven water splitting (Fujishima et al., 2000).

Due to the interesting structures and corresponding electronic properties, two-dimensional (2D) materials have been widely used in various fields and also provide new research directions for efficient photocatalysis (Singh et al., 2015). In recent years, 2D photocatalysts showed the greater advantages over their bulk phase counterparts in terms of photocatalytic performance. For example, Both SnS_2 monolayer and ZnSe nanosheet exhibited higher photocurrent density than their bulk materials (Sun et al., 2012a; Sun et al., 2012b). In addition, various 2D materials have also been theoretically and experimentally demonstrated to be used as photocatalysts for water splitting, such as 2D transition metal dichalcogenides, g-C_3N_4, phosphorene, and so on (Wang et al., 2009; Zhuang and Hennig, 2013a; Rahman et al., 2016; Phuc et al., 2018; Zhang et al., 2022). However, few of these photocatalysts can simultaneously satisfy high visible light absorption, high carrier mobility and perfect band edge positions. For instance, MoS_2 monolayer showed lower carrier mobility, and $MoTe_2$ monolayer can't perfectly meet the redox potential of water (Wang et al., 2009; Zhuang and Hennig, 2013a; Cai et al., 2014; Rahman et al., 2016; Zhang et al., 2022). Both GaS and GaSe monolayers demonstrated low visible light absorption due to the large band gaps (Zhuang and Hennig, 2013b). Therefore, it is still a challenge to develop water splitting photocatalysts with excellent performances.

In this work, based on the first-principles calculations, we propose a novel 2D transition metal dichalcogenide namely $MoWS_4$ and systemically investigate its photocatalytic properties. Firstly, the stability of $MoWS_4$ monolayer is confirmed by calculating its phonon spectra and ab initio molecular dynamics (AIMD) simulations. Secondly, we calculate the band structures of $MoWS_4$ monolayer and bilayer, and show their semiconductive characteristic. Then, relevant photocatalytic properties are systematically investigated. It is found that $MoWS_4$ monolayer and bilayer can nicely meet the redox potentials without strain engineering, and their light absorption coefficients reach ~10^5 cm^{-1} in the visible-ultraviolet region. Moreover, the electronic mobility of $MoWS_4$ monolayer is as high as 557 cm^2 $V^{-1}s^{-1}$.

Computational details

For geometric and electronic structures, all calculations are performed by using the Vienna ab into simulation package (VASP) based on density functional theory (DFT) (Kresse and Furthmuller, 1996). We choose the generalized gradient

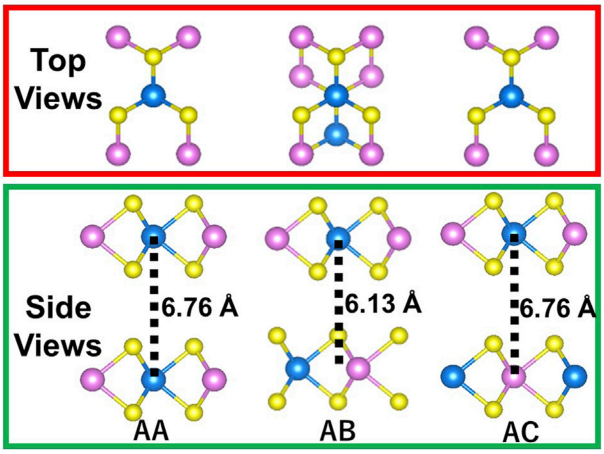

FIGURE 2
Top and side views of $MoWS_4$ bilayer with three stacking patterns (AA, AB, and AC).

approximation (GGA) of the Perdew–Burke–Ernzerhof (PBE) functional as the exchange-correlation functional to perform these calculations (Perdew et al., 1996). For the 2D monolayer structure, the vacuum layer thickness is set as about 20 Å to avoid layer-to-layer effects. The kinetic energy cutoff is set as 500 eV. The Brillouin zone is regulated with 10 × 6 × 1. During the calculations, the DFT-D2 method with Grimme correction is used to describe the long-range van der Waals interactions (Grimme, 2006). Besides, all atoms are fully relaxed, and the energy and force convergence criteria are set as 10^{-6} eV and 0.01 eV $Å^{-1}$, respectively. Except for PBE functional, to obtain the more accurate results, the HSE06 functional is also adopted to calculate the band structures and the band edge positions (Deák et al., 2010). To identify structural stability of $MoWS_4$ monolayer, its phonon spectra are calculated by using the PHONOPY code (Gonze and Lee, 1997). A 6 × 3 supercell structure of $MoWS_4$ monolayer is used in ab initio molecular dynamics (AIMD) simulations (NVT ensemble), which is carried out for 3 ps with a time step of 1 fs at 500 K (Cimas et al., 2014).

The optical properties can be defined by the complex dielectric function (frequency) for characterization:

$$\varepsilon(\omega) = \varepsilon_1(\omega) + i\varepsilon_2(\omega) \tag{1}$$

where $\varepsilon_1(\omega)$ and $\varepsilon_2(\omega)$ represent the real and imaginary parts, respectively. Based on the Kramers–Kronig transformation (Kuzmenko, 2005), the real part $[\varepsilon_1(\omega)]$ can be expressed as follows:

$$\varepsilon_1(\omega) = 1 + \left(\frac{2}{\pi}\right) p \int_0^{\infty} d\omega' \frac{(\omega')^2 \varepsilon_2(\omega)}{(\omega')^2 - (\omega)^2} \tag{2}$$

where p is the integral principal value. In addition, the imaginary part $[\varepsilon_2(\omega)]$ can be described as (Saha et al., 2000):

$$\varepsilon_2(\omega) = \frac{4\pi e^2}{m^2\omega^2} \sum_{i,f} \int \frac{2d^3k}{(2\pi)^3} \left|\langle ik|P|fk\rangle\right|^2 F_i^k\left(1 - F_f^k\right)\delta\left(E_f^k - E_i^k - E\right) \tag{3}$$

where ω, E, F, P, $||ik\rangle$, and $|fk\rangle$ represent the incident photon frequency, the incident photon energy, the Fermi function, the transition matrix, the CB state and VB state, respectively. Finally, the absorption coefficient $[\alpha(\omega)]$ can be calculated by (Cheng et al., 2022a):

$$\alpha(\omega) = \frac{\sqrt{2}\omega}{c}\left[\sqrt{\varepsilon_1^2(\omega) + \varepsilon_2^2(\omega)} - \varepsilon_1(\omega)\right]^{1/2} \tag{4}$$

where c denotes the speed of light in vacuum.

The carrier mobility is calculated by the following formula (Qiao et al., 2014):

$$\mu = \frac{e\hbar^3 C_{2D}}{k_B T m_e^* m_d E_d^2} \tag{5}$$

where C_{2D} is the elastic modulus, which can be expressed by $C_{2D} = \frac{1}{S_0}\frac{\partial^2 E}{\partial \delta^2}$, here E is the total energy of monolayer after deformation, S_0 is the lattice area of monolayer under equilibrium and δ is the uniaxial strain. Besides, k_B is the Boltzmann constant, T is the temperature. m_e^* is the effective mass along the transport direction and m_d is the average effective mass determined by $m_d = \sqrt{m_x^* m_y^*}$. E_d represents the deformation potential constant, which is expressed by $E_d = \frac{\partial E_{edge}}{\partial \delta}$, here E_{edge} represents the shift of the band edge position with respect to the uniaxial strain δ.

Results and discussions

Crystal structures, stability, and electronic properties

Figure 1A shows the top and side views of 4 × 2 supercell of $MoWS_4$ monolayer, which has a space group of *Pmm2*. The light green area is the unit cell of $MoWS_4$ monolayer, which contains four atoms. The pink, blue, and yellow balls represent Mo, W, and S atoms, respectively. $MoWS_4$ monolayer is a honeycomb structure from the top view, while sandwich structure from the side view, which is very similar to the structure of MoS_2 monolayer (Kan et al., 2014). After fully geometric optimization, the lattice constants are a = 3.188 Å and b = 5.526 Å with a layer thickness of 3.119 Å.

To confirm the stability of $MoWS_4$ monolayer, the formation energy (E_{form}), defined as: $E_{form} = [E_{MoWS_4} - E_{Mo} - E_W - 4E_S]/6$, is calculated, where E_{MoWS_4} presents the total energy of the unit cell of $MoWS_4$ monolayer, and E_{Mo}, E_W, and E_S present the energies of each Mo, W, and S atom in itself bulk phase, respectively. The calculated formation energy of $MoWS_4$ monolayer is −1.1 eV/atom (<0),

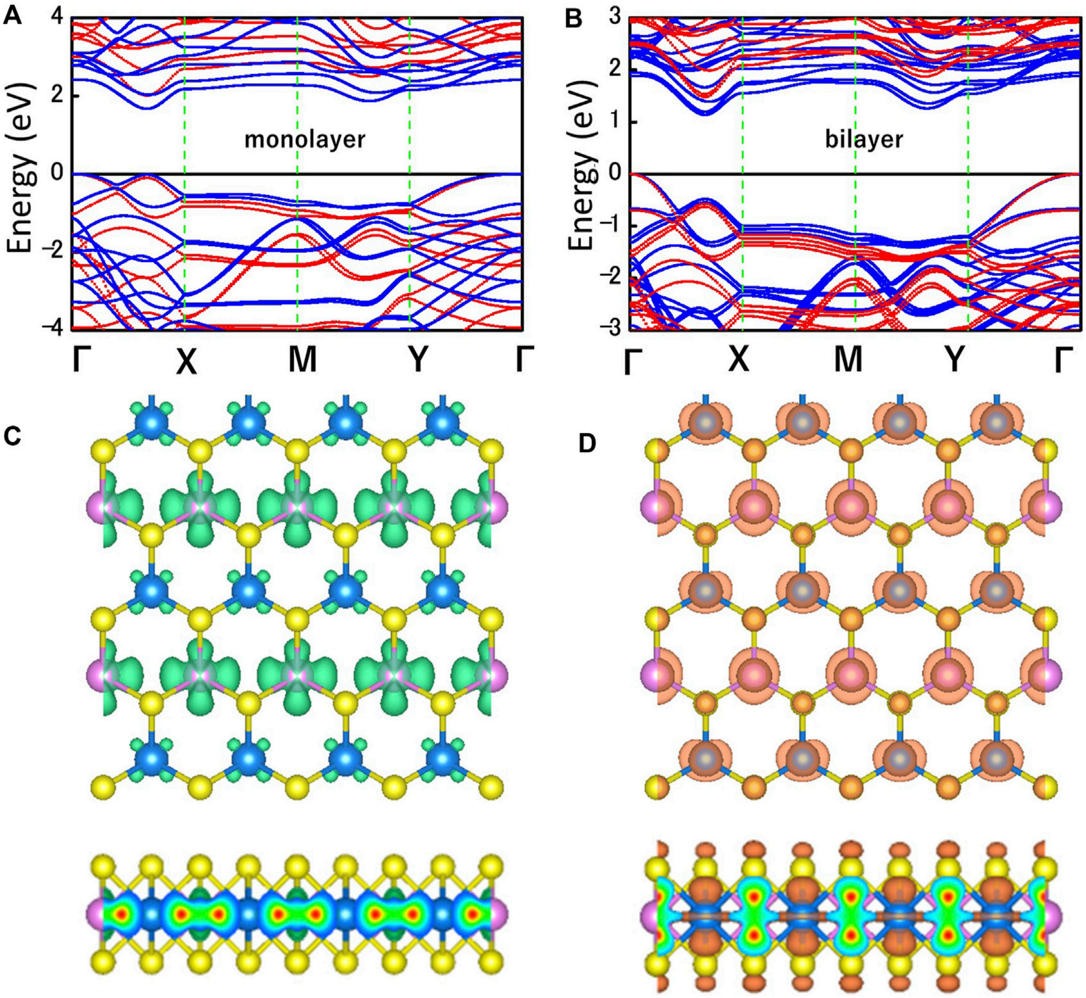

FIGURE 3
Band structures of **(A)** $MoWS_4$ monolayer and **(B)** $MoWS_4$ bilayer. The red and blue represent the HSE06 functional and PBE functional, respectively. Top and side views of the charge density at the **(C)** CBM, and **(D)** VBM. The isosurface value is set as 0.012 e $Å^{-3}$.

implying the procedure of synthesizing $MoWS_4$ monolayer is exothermic and favorable. Besides, the dynamic and thermal stabilities of $MoWS_4$ monolayer are further investigated. As shown in Figure 1B, the calculated phonon spectra exhibit no imaginary frequency, indicating high dynamic stability of $MoWS_4$ monolayer. The thermal stability is further studied *via* AIMD calculations. As illustrated in Figure 1C, the total energy of the $MoWS_4$ monolayer remains essentially stable and no deformation occurs in its final structure. These results suggest that $MoWS_4$ monolayer exhibits good dynamic and thermal stability, which deduces the possibility of experimental synthesis of $MoWS_4$ monolayer.

Figure 2 shows the top and side views of $MoWS_4$ bilayer. Three stacking patterns (AA, AB, and AC) are considered in the bilayer structures of $MoWS_4$. The results of the calculated total energy are −94.2727 eV, −94.4175 eV, and −94.2726 eV for AA, AB, and AC stacking patterns, respectively. AA and AC stacking structures have the same layer spacing of 6.76 Å, and AB stacking has a spacing of 6.13 Å. Obviously, the AB stacking structure is most stable energetically.

Figures 3A,B shows the electronic band structures of $MoWS_4$ monolayer and bilayer obtained by using the PBE functional (blue) and the HSE06 functional (red). The Fermi level and the high symmetry path are set as 0 eV and *Γ-X-M-Y-Γ*, respectively. The $MoWS_4$ monolayer and bilayer are indirect band gap semiconductors and their band gaps calculated by HSE06/PBE functional are 2.01/1.67 eV and 1.48/1.14 eV, respectively. The band gaps obtained by the HSE06 functional are larger than that obtained by the PBE functional since the PBE functional tends to underestimate the band gap. Figures 3C,D shows the maps of charge density for MoW_4 monolayer at the conduction band minimum (CBM) and the valence band maximum (VBM), and it

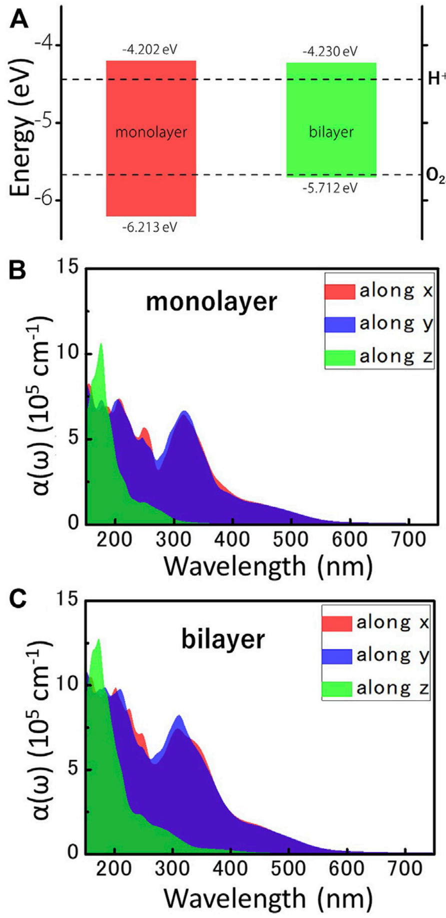

FIGURE 4
(A) The locations of VBM and CBM of $MoWS_4$ monolayer and bilayer, which are obtained by the HSE06 functional. The redox potentials of water splitting at pH = 0 are shown for comparison. All the energy levels are based on the vacuum level, and the vacuum level is set as 0 eV. The optical absorption coefficients for the different directions of **(B)** $MoWS_4$ monolayer and **(C)** $MoWS_4$ bilayer.

can be concluded that the CBM is mainly contributed by the Mo atoms, whereas the VBM comes from a combination of Mo, W, and S atoms.

Photocatalytic water splitting and optical properties

Considering the excellent semiconductor properties of $MoWS_4$ monolayer and bilayer, we systematically study their feasibility as photocatalysts for water splitting. It is well known that a photocatalytic candidate should meet the following conditions: Firstly, its band gap should exceed the free energy of water splitting (1.23 eV). Obviously, the band gaps of $MoWS_4$ monolayer and bilayer both exceed 1.23 eV; Secondly, its band edges must cross the redox potentials of water. The CBM energy should be higher than the reduction potential of H^+/H_2 (−4.44 eV), and the VBM energy should be lower than the oxidation potential of O_2/H_2O (−5.67 eV) (Abe, 2010; Sun et al., 2019; Cheng et al., 2022b). For 2D materials, the band edges with respect to the vacuum level ($E^{Vac}_{CBM/VBM}$) can be obtained by: $E^{Vac}_{CBM/VBM} = E^{DFT}_{CBM/VBM} - V_{vacuum}$, where $E^{DFT}_{CBM/VBM}$ represents the value of CBM/VBM obtain by DFT and V_{vacuum} represents the electrostatic potential in the vacuum region. We plot the map of band edges relative to the vacuum level of $MoWS_4$ monolayer and bilayer in Figure 4A, and find that the band edge positions of $MoWS_4$ monolayer and bilayer can perfectly satisfy the redox potential for the water splitting reaction at pH = 0. Specifically, the band edges of CBM/VBM for $MoWS_4$ monolayer and bilayer are −4.202/−6.213 eV and −4.230/−5.712 eV, respectively. Thus, the results suggest that the $MoWS_4$ monolayer and bilayer can be promising candidates for water splitting photocatalysts.

Besides, efficient light absorption is also an important feature for water splitting photocatalysts. Figures 4B,C shows the light absorption spectra of the $MoWS_4$ monolayer and bilayer within the visible-ultraviolet light range. The result can be summarized as follows: 1) Their light absorption coefficients in the ultraviolet light range are higher than visible light region (up to ~10^6 cm^{-1}); 2) Their light absorption coefficients of $MoWS_4$ bilayer overall are higher than that of $MoWS_4$ monolayer; 3) Their light absorption coefficients are significantly anisotropic: that is higher in the z direction, but have a wider range of light absorption spectra in the x and y directions. It is known that the high light absorption coefficients can guarantee the effective use of solar energy, which is very favorable for water splitting photocatalysts (Zhao et al., 2018; Fan et al., 2021). Therefore, both $MoWS_4$ monolayer and bilayer can be promising potential candidates as photocatalysts.

Strain engineering and high carrier mobility

We further investigate the effect of strain engineering on the photocatalytic performance of $MoWS_4$ monolayer. Figure 5 shows the band structures of $MoWS_4$ monolayer under the in-plane biaxial strain from −2 to 2%. Its band gap increases when compressive strain increases or tensile strain decreases, and its band gap varies in the range of 1.508–2.378 eV. In addition, when it is subjected to compressive strain, the indirect bandgap changes to be a direct bandgap; while when it is subjected to tensile strain, it remains an indirect bandgap semiconductor. As illustrated in Figure 6, we study the changes of its band edge positions under the applied in-plane biaxial strain. All of VBM positions are lower than the oxidation potential of O_2/H_2O under the −2~2% in-plane biaxial strain, which indicates that $MoWS_4$ monolayer always serves as a potential photocatalyst to generate

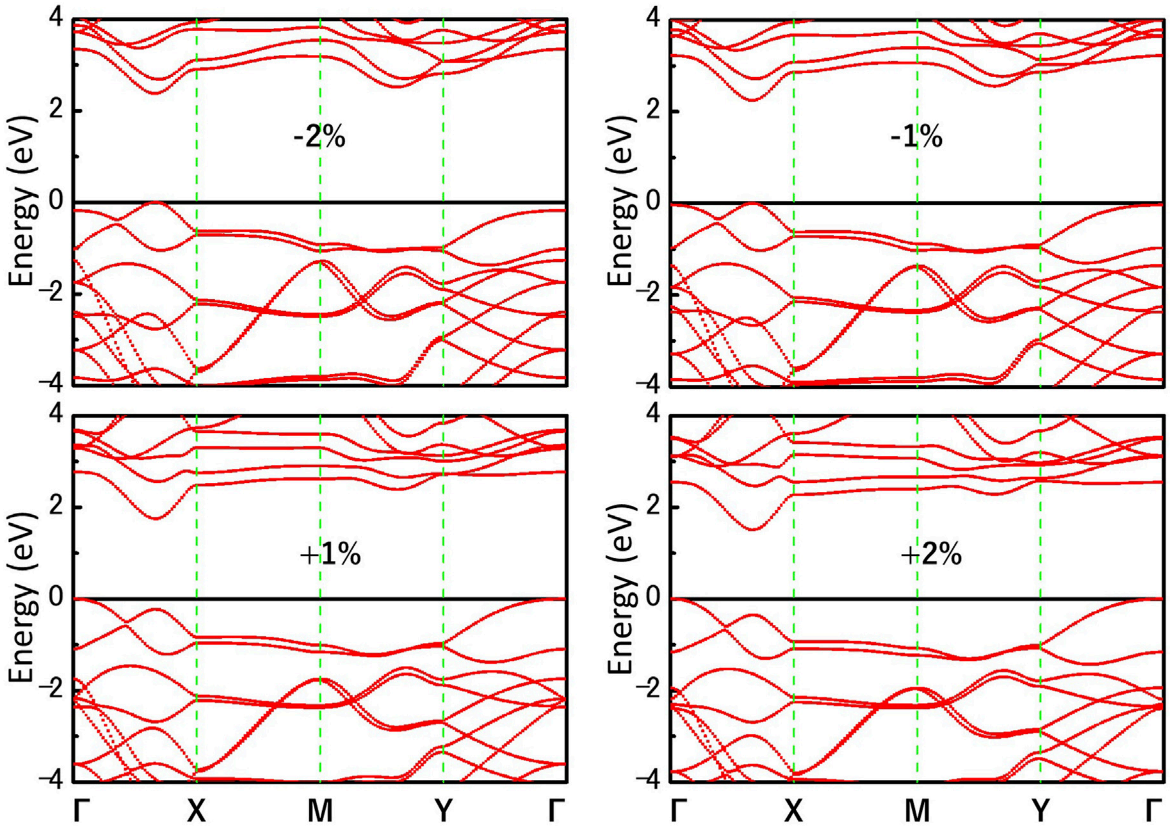

FIGURE 5
Band structures of $MoWS_4$ monolayer under the biaxial strain from −2 to 2% are calculated by HSE06 functional.

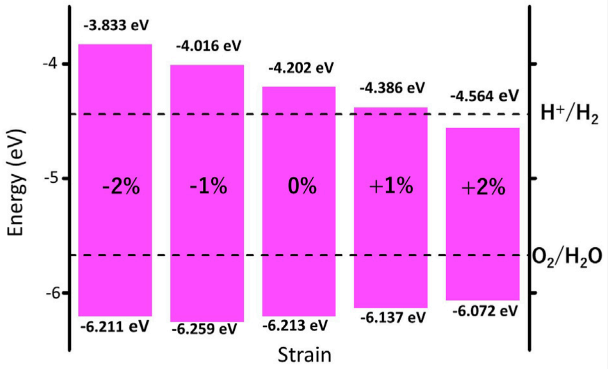

FIGURE 6
Strain effects on band edge positions of $MoWS_4$ monolayer with respect to the vacuum level (0 eV). The redox potentials of water splitting at pH = 0 are shown for comparison.

oxygen. Besides, when the applied tensile strain reaches 2%, its CBM positions become lower than the reduction potential of H^+/H_2. Thus, excessive tensile strain will lead to its inability to produce hydrogen. In general, compressive strain does not cause $MoWS_4$ monolayer to deviate from the basic requirements for water splitting photocatalyst, but tensile strain can easily affect its hydrogen production performance.

As we know, the fast carrier migration capability is necessary for high performance photocatalysts. Thus, the PBE functional is used to calculate the carrier mobility of $MoWS_4$ monolayer according to Eq. 5. Subsequently, we calculate its carrier effective masses (m^*), in-plane stiffness (C_{2D}) and deformation potential constants (E_d). Therein, to obtain E_d of $MoWS_4$ monolayer, the linear fitting maps of band edge positions are plotted as the function of the applied uniaxial strain δ along the x and y directions (Bardeen and Shockley, 1950; Zhang et al., 2021a), as illustrated in Figure 7 and the result is summarized in Table 1. It is notable that the values of E_d have a small difference along the x and y directions, which shows that the scattering ability of its carriers in different directions is also similar. In addition, the carrier effective masses of $MoWS_4$ monolayer have a small difference along the x and y directions. The electron effective masses of $MoWS_4$ monolayer are much lower than its hole effective masses ($m_e = 0.377m_0$ and $0.374m_0$ along the x and y directions), which are smaller than that of many 2D photocatalytic materials, such as Penta-PdSSe ($m_e = 2.16m_0$),

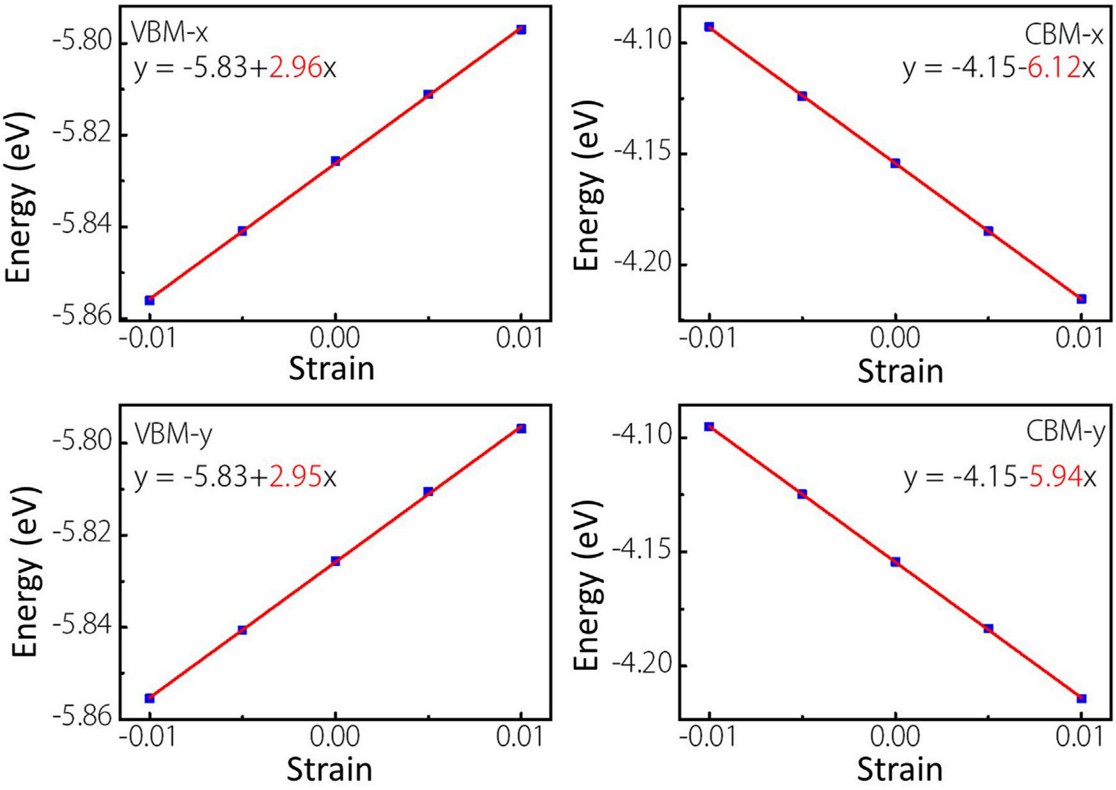

FIGURE 7
Linear fitting maps of VBM and CBM locations of $MoWS_4$ monolayer under the strain along *x* and *y* directions.

TABLE 1 Carrier effective masses m^*, In-plane stiffness C_{2D}, Deformation potential constants E_d, and carrier mobility μ for $MoWS_4$ monolayer along the *x* and *y* directions.

Materials	Direction	Carrier type	m^* (m_0)	C_{2D} (N/m)	E_d (eV)	μ ($cm^2V^{-1}s^{-1}$)
$MoWS_4$	*X*	Electron	0.377	131.86	6.12	529
		Hole	2.927	131.86	2.96	38
	Y	Electron	0.374	129.5	5.94	557
		Hole	2.857	129.5	2.95	38

Penta-$PdSe_2$ (m_e = 1.88m_0), δ-SnS (m_e = 1.01m_0), SnP_3 (m_e = 0.9m_0) (Long et al., 2018; Sun et al., 2018; Zhang et al., 2021b; Xiao et al., 2021). The smaller carrier effective masses benefit the transfer rate of photogenerated carriers in the photocatalytic process. What's more, the calculated electron mobility along *x* and *y* directions are 529 $cm^2V^{-1}s^{-1}$ and 557 $cm^2V^{-1}s^{-1}$, respectively, whereas the calculated hole mobility along *x* and *y* directions are both 38 $cm^2 V^{-1}s^{-1}$. The reason for this difference is that the hole effective mass is much larger than the electron effective mass. More importantly, as shown in Figure 8, the electron mobility of $MoWS_4$ monolayer can significantly exceed that of many other 2D photocatalytic materials such as MoS_2 (μ_e = 72.16 $cm^2 V^{-1} s^{-1}$, μ_h = 200.52 $cm^2 V^{-1} s^{-1}$), Penta-PdS_2 (μ_e = 40.97 $cm^2 V^{-1} s^{-1}$, μ_h = 339.25 $cm^2 V^{-1} s^{-1}$), Penta-$PdSe_2$ (μ_e = 29.40 $cm^2 V^{-1} s^{-1}$, μ_h = 534.55 $cm^2 V^{-1} s^{-1}$), SnP_2S_6 monolayer (μ_e = 148.48 $cm^2 V^{-1} s^{-1}$, μ_h = 143.12 $cm^2 V^{-1} s^{-1}$), As_2S_3 monolayer (μ_e = 253.11 $cm^2 V^{-1} s^{-1}$, μ_h = 10.85 $cm^2 V^{-1} s^{-1}$) (Cai et al., 2014; Wang et al., 2015; Long et al., 2018; Jing et al., 2019; Liu et al., 2021). It is well known that materials with high carrier mobility can effectively reduce their photogenerated electron and hole recombination rates and increase the participation rate in redox reactions, which are beneficial for

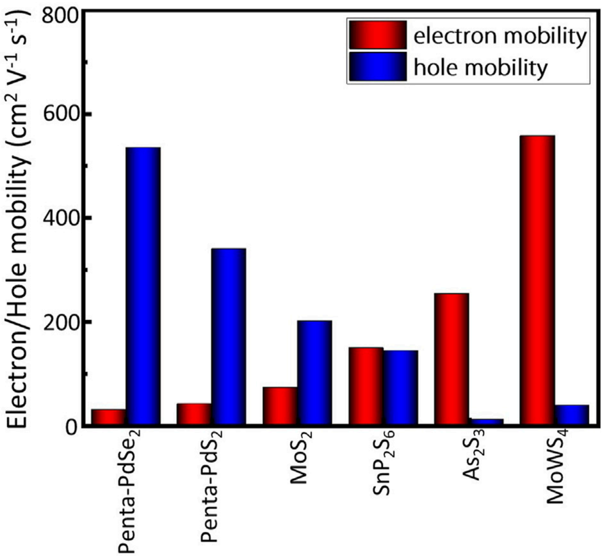

FIGURE 8
Carrier mobility of $MoWS_4$ compared with other typical 2D photocatalysts.

photocatalytic processes. Thus, our results suggest that $MoWS_4$ monolayer is a promising 2D photocatalyst candidate for water splitting.

Conclusion

Based on the first-principles calculations, we systematically investigate photocatalytic properties of two-dimensional $MoWS_4$. It is found that both the $MoWS_4$ monolayer and bilayer are semiconductors with indirect band gaps and show high and anisotropic light absorption coefficients in the visible-ultraviolet range. The band edge positions of the materials can satisfy the redox potentials perfectly and the electron mobility of $MoWS_4$ monolayer is up to 557 cm^2 V^{-1} s^{-1}, which outperforms many other 2D photocatalytic materials, such as MoS_2 monolayer, Penta-PdS_2, Penta-$PdSe_2$, and SnP_2S_6 monolayer. These results indicate that $MoWS_4$ can be a promising photocatalyst for water splitting with outstanding performances.

Data availability statement

The original contributions presented in the study are included in the article/Supplementary Material, further inquiries can be directed to the corresponding authors.

Author contributions

FW: Methodology, Investigation, Writing-original draft. ZC: Conceptualization, Investigation, Methodology, Writing—original draft. XZ: Investigation, Writing-original draft. CX: Validation, Resources. FL: Data curation, Validation. CC: Conceptualization, Writing—original draft, Supervision, Funding acquisition. GL: Validation, Data curation, Supervision.

Funding

The authors are grateful for support from the National Natural Science Foundation of China (52101192 and 51871056), Foundation for Basic and Applied Basic Research-Joint Foundation of Dongguan-Guangdong Province (2020A1515111109), and Department of Education of Guangdong in China (2018KZDXM069 and 2021 KCXTD050).

Conflict of interest

The authors declare that the research was conducted in the absence of any commercial or financial relationships that could be construed as a potential conflict of interest.

Publisher's note

References

Abe, R. (2010). Recent progress on photocatalytic and photoelectrochemical water splitting under visible light irradiation. *J. Photochem. Photobiol. C Photochem. Rev.* 11, 179–209. doi:10.1016/j.jphotochemrev.2011.02.003

Bardeen, J., and Shockley, W. (1950). Deformation potentials and mobilities in non-polar crystals. *Phys. Rev.* 80, 72–80. doi:10.1103/physrev.80.72

Cai, Y. Q., Zhang, G., and Zhang, Y. W. (2014). Polarity-reversed robust carrier mobility in monolayer MoS_2 nanoribbons. *J. Am. Chem. Soc.* 136, 6269–6275. doi:10.1021/ja4109787

Cheng, Z. S., Zhang, X. M., Zhang, H., Liu, H. Y., Dai, X. F., Liu, G. D., et al. (2022). Binary pentagonal auxetic materials for photocatalysis and energy storage with outstanding performances. *Nanoscale* 14, 2041–2051. doi:10.1039/d1nr08368f

Cheng, Z. S., Zhang, X. M., Zhang, H., Liu, H. Y., Dai, X. F., Liu, G. D., et al. (2022). Two-dimensional auxetic pentagonal materials as water splitting photocatalysts with excellent performances. *J. Mat. Sci.* 57, 7667–7679. doi:10.1007/s10853-022-07130-x

Cimas, Á., Tielens, F., Sulpizi, M., Gaigeot, M. P., and Costa, D. (2014). The amorphous silica-liquid water interface studied by *ab initio* molecular dynamics (AIMD): Local organization in global disorder. *J. Phys. Condens. Matter* 26, 244106. doi:10.1088/0953-8984/26/24/244106

Deák, P., Aradi, B., Frauenheim, T., Janzén, E., and Gali, A. (2010). Accurate defect levels obtained from the HSE06 range-separated hybrid functional. *Phys. Rev. B* 81, 153203. doi:10.1103/physrevb.81.153203

Fan, Y. S., Xi, X. L., Liu, Y. S., Nie, Z. R., Zhao, L. Y., and Zhang, Q. H. (2021). Regulation of morphology and visible light-driven photocatalysis of WO_3 nanostructures by changing pH. *Rare Met.* 40, 1738–1745. doi:10.1007/s12598-020-01490-6

Fujishima, A., and Honda, K. (1972). Electrochemical photolysis of water at a semiconductor electrode. *Nature* 238, 37–38. doi:10.1038/238037a0

Fujishima, A., Rao, T. N., and Tryk, D. A. (2000). Titanium dioxide photocatalysis. *J. Photochem. Photobiol. C Photochem. Rev.* 1, 1–21. doi:10.1016/s1389-5567(00)00002-2

Gonze, X., and Lee, C. Y. (1997). Dynamical matrices, born effective charges, dielectric permittivity tensors, and interatomic force constants from density-functional perturbation theory. *Phys. Rev. B* 55, 10355–10368. doi:10.1103/physrevb.55.10355

Grimme, S. (2006). Semiempirical GGA-type density functional constructed with a long-range dispersion correction. *J. Comput. Chem.* 27, 1787–1799. doi:10.1002/jcc.20495

Han, N., Liu, P. Y., Jiang, J., Ai, L. H., Shao, Z. P., and Liu, S. M. (2018). Recent advances in nanostructured metal nitrides for water splitting. *J. Mat. Chem. A* 6, 19912–19933. doi:10.1039/c8ta06529b

Jing, Y., Zhou, Z. P., Zhang, J., Huang, C. B., Li, Y. F., and Wang, F. (2019). SnP_2S_6 monolayer: A promising 2D semiconductor for photocatalytic water splitting. *Phys. Chem. Chem. Phys.* 21, 21064–21069. doi:10.1039/c9cp04143e

Kan, M., Wang, J. Y., Li, X. W., Zhang, S. H., Li, Y. W., Kawazoe, Y., et al. (2014). Structures and phase transition of a MoS_2 monolayer. *J. Phys. Chem. C* 118, 1515–1522. doi:10.1021/jp4076355

Kresse, G., and Furthmuller, J. (1996). Efficient iterative schemes for *ab initio* total-energy calculations using a plane-wave basis set. *Phys. Rev. B* 54, 11169–11186. doi:10.1103/physrevb.54.11169

Kuzmenko, A. B. (2005). Kramers-Kronig constrained variational analysis of optical spectra. *Rev. Sci. Instrum.* 76, 083108. doi:10.1063/1.1979470

Liu, X. F., Zhang, Z. F., Ding, Z., Lv, B., Luo, Z. J., Wang, J. S., et al. (2021). Highly anisotropic electronic and mechanical properties of monolayer and bilayer As_2S_3. *Appl. Surf. Sci.* 542, 148665. doi:10.1016/j.apsusc.2020.148665

Long, C., Liang, Y., Jin, H., Huang, B. B., and Dai, Y. (2018). $PdSe_2$: Flexible two-dimensional transition metal dichalcogenides monolayer for water splitting photocatalyst with extremely low recombination rate. *ACS Appl. Energy Mat.* 2, 513–520. doi:10.1021/acsaem.8b01521

Perdew, J. P., Burke, K., and Ernzerhof, M. (1996). Generalized gradient approximation made simple. *Phys. Rev. Lett.* 77, 3865–3868. doi:10.1103/physrevlett.77.3865

Phuc, H. V., Hieu, N. N., Hoi, B. D., Hieu, N. V., Thu, T. V., Hung, N. M., et al. (2018). Tuning the electronic properties, effective mass and carrier mobility of MoS_2 monolayer by strain engineering: First-principle calculations. *J. Electron. Mat.* 47, 730–736. doi:10.1007/s11664-017-5843-8

Qiao, J. S., Kong, X. H., Hu, Z. X., Yang, F., and Ji, W. (2014). High-mobility transport anisotropy and linear dichroism in few-layer black phosphorus. *Nat. Commun.* 5, 4475–4477. doi:10.1038/ncomms5475

Rahman, M. Z., Kwong, C. W., Davey, K., and Qiao, S. Z. (2016). 2D phosphorene as a water splitting photocatalyst: Fundamentals to applications. *Energy Environ. Sci.* 9, 709–728. doi:10.1039/c5ee03732h

Saha, S., Sinha, T. P., and Mookerjee, A. (2000). Electronic structure, chemical bonding, and optical properties of paraelectric $BaTiO_3$. *Phys. Rev. B* 62, 8828–8834. doi:10.1103/physrevb.62.8828

Singh, A. K., Mathew, K., Zhuang, H. L., and Hennig, R. G. (2015). Computational screening of 2D materials for photocatalysis. *J. Phys. Chem. Lett.* 6, 1087–1098. doi:10.1021/jz502646d

Sun, Y. F., Cheng, H., Gao, S., Sun, Z. H., Li, Q. H., Liu, Q., et al. (2012). Freestanding tin disulfide single-layers realizing efficient visible-light water splitting. *Angew. Chem. Int. Ed. Engl.* 51, 8857–8861. doi:10.1002/ange.201204675

Sun, Y. F., Sun, Z. H., Gao, S., Cheng, H., Liu, Q. H., Piao, J. Y., et al. (2012). Fabrication of flexible and freestanding zinc chalcogenide single layers. *Nat. Commun.* 3, 1057–7. doi:10.1038/ncomms2066

Sun, S. S., Meng, F. C., Wang, H. Y., Wang, H., and Ni, Y. X. (2018). Novel two-dimensional semiconductor SnP_3: High stability, tunable bandgaps and high carrier mobility explored using first-principles calculations. *J. Mat. Chem. A* 6, 11890–11897. doi:10.1039/c8ta02494d

Sun, S. S., Meng, F. C., Xu, Y. F., He, J., Ni, Y. X., and Wang, H. Y. (2019). Flexible, auxetic and strain-tunable two dimensional penta-X_2C family as water splitting photocatalysts with high carrier mobility. *J. Mat. Chem. A* 7, 7791–7799. doi:10.1039/c8ta12405a

Suntivich, J., May, K. J., Gasteiger, H. A., Goodenough, J. B., and Yang, S. H. (2011). A perovskite oxide optimized for oxygen evolution catalysis from molecular orbital principles. *Science* 334, 1383–1385. doi:10.1126/science.1212858

Tsuji, I., Kato, H., and Kudo, A. (2005). Visible-light-induced H_2 evolution from an aqueous solution containing sulfide and sulfite over a ZnS-$CuInS_2$-$AgInS_2$ solid-solution photocatalyst. *Angew. Chem. Int. Ed. Engl.* 117, 3631–3634. doi:10.1002/ange.200500314

Wang, X. C., Maeda, K., Thomas, A., Takanabe, K., Xin, G., Carlsson, J. M., et al. (2009). A metal-free polymeric photocatalyst for hydrogen production from water under visible light. *Nat. Mat.* 8, 76–80. doi:10.1038/nmat2317

Wang, Y., Li, Y., and Chen, Z. F. (2015). Not your familiar two dimensional transition metal disulfide: Structural and electronic properties of the PdS_2 monolayer. *J. Mat. Chem. C* 3, 9603–9608. doi:10.1039/c5tc01345c

Xiao, F., Lei, W., Wang, W., Xu, L. L., Zhang, S. L., and Ming, X. (2021). Pentagonal two-dimensional noble-metal dichalcogenide PdSSe for photocatalytic water splitting with pronounced optical absorption and ultrahigh anisotropic carrier mobility. *J. Mat. Chem. C* 9, 7753–7764. doi:10.1039/d1tc01245b

Zhang, W., Chai, C. C., Fan, Q. Y., Sun, M. L., Song, Y. X., Yang, Y. T., et al. (2021). Two-dimensional tetrahex-GeC_2: A material with tunable electronic and optical properties combined with ultrahigh carrier mobility. *ACS Appl. Mat. Interfaces* 13, 14489–14496. doi:10.1021/acsami.0c23017

Zhang, Q., Wang, X., and Yang, S. L. (2021). δ-SnS: An emerging bidirectional auxetic direct semiconductor with desirable carrier mobility and high-performance catalytic behavior toward the water-splitting reaction. *ACS Appl. Mat. Interfaces* 13, 31934–31946. doi:10.1021/acsami.1c03650

Zhang, Y. F., Wei, J. M., Liu, T. Y., Zhong, Z., Luo, Z. J., Xiao, W. J., et al. (2022). Tunable properties of ZnSe/graphene heterostructure as a promising candidate for photo/electro-catalyst applications. *Appl. Surf. Sci.* 574, 151679. doi:10.1016/j.apsusc.2021.151679

Zhao, P., Ma, Y. D., Lv, X. S., Li, M. M., Huang, B. B., and Dai, Y. (2018). Two-dimensional III_2-VI_3 materials: Promising photocatalysts for overall water splitting under infrared light spectrum. *Nano Energy* 51, 533–538. doi:10.1016/j.nanoen.2018.07.010

Zhuang, H. L., and Hennig, R. G. (2013). Computational search for single-layer transition-metal dichalcogenide photocatalysts. *J. Phys. Chem. C* 117, 20440–20445. doi:10.1021/jp405808a

Zhuang, H. L., and Hennig, R. G. (2013). Single-layer group-III monochalcogenide photocatalysts for water splitting. *Chem. Mat.* 25, 3232–3238. doi:10.1021/cm401661x

frontiers | Frontiers in Chemistry

TYPE Original Research
PUBLISHED 13 September 2022
DOI 10.3389/fchem.2022.1008332

Fe@χ_3-borophene as a promising catalyst for CO oxidation reaction: A first-principles study

Jian-Wei Han[1], Wei-Yue Bian[1], Yue-Yu Zhang[1,2]* and Meng Zhang[1]*

[1]School of Physics, East China University of Science and Technology, Shanghai, China, [2]Wenzhou Institute, University of Chinese Academy of Sciences, Wenzhou, Zhejiang, China

A novel single-atom catalyst of Fe adsorbed on χ_3-borophene has been proposed as a potential catalyst for CO oxidation reaction (COOR). Quantitative pictures have been provided of both the stability of Fe@χ_3-borophene and various kinetic reaction pathways using first-principles calculations. Strong adsorption energy of -3.19 eV and large diffusion potential of 3.51 eV indicates that Fe@χ_3-borophene is highly stable. By exploring reaction mechanisms for COOR, both Eley-Ridel (E-R) and trimolecule E-R (TER) were identified as possible reaction paths. Low reaction barriers with 0.49 eV of E-R and 0.57 eV of TER suggest that Fe@χ_3-borophene is a very promising catalyst for COOR. Charge transfer between the χ_3-borophene and CO, O_2 and CO_2 gas molecules plays a key role in lowering the energy barrier during the reactions. Our results propose that Fe@χ_3-borophene can be a good candidate of single-atom catalyst for COOR with both high stability and catalytic activity.

KEYWORDS

CO oxidation reaction, borophene, first-principles study, catalytic activity, reaction mechanism

Introduction

The CO oxidation reaction (COOR) is a simple yet fundamental reaction to reveal the intrinsic mechanism of multiphase catalytic conversion reactions and to test the reactivity of new catalysts (Alavi et al., 1998). The conversion of CO to non-toxic gases at room temperature has attracted considerable attention in recent years due to the seriously growing environmental problems and energy shortages (Ernst and Zibrak, 1998; Prockop and Chichkova, 2007). In the past few years, many studies have been focusing on the mechanism of COOR using noble metal nanoparticles and alloys as catalysts such as Pd (Kalita and Deka, 2009), Ag (Kim et al., 2010), Pt (Zhang and Hu, 2001), Au (Lopez and Nørskov, 2002) and others. However, due to the high cost and scarcity of these metals, they have never been commercialized. Therefore, it is crucial to find suitable catalytic methods and catalysts for COOR to improve the catalytic effect and reduce the cost.

A new class of heterogeneous catalysis emerges in the past decade by supporting metal nanoparticles on a surface. Among these systems, single-atom catalysts (SACs) on two-

OPEN ACCESS

EDITED BY
Jamie Platts,
Cardiff University, United Kingdom

REVIEWED BY
Quanguo Jiang,
Hohai University, China
Xueling Lei,
Jiangxi Normal University, China

*CORRESPONDENCE
Yue-Yu Zhang,
yueyu.zhang@foxmail.com
Meng Zhang,
mzhang@ecust.edu.cn

SPECIALTY SECTION
This article was submitted to Theoretical and Computational Chemistry, a section of the journal Frontiers in Chemistry

RECEIVED 31 July 2022
ACCEPTED 24 August 2022
PUBLISHED 13 September 2022

CITATION
Han J-W, Bian W-Y, Zhang Y-Y and Zhang M (2022), Fe@χ_3-borophene as a promising catalyst for CO oxidation reaction: A first-principles study.
Front. Chem. 10:1008332.
doi: 10.3389/fchem.2022.1008332

dimensional substrates has been a popular research topic since the single-atom catalyst Pt_1/FeO_x was first reported to be synthesized in 2009 by Zhang et al. (Qiao et al., 2011). The advantages of SACs include clear active sites, high utilization of metals, high-efficiency in catalytic performance, wide applicability and so on (Yang et al., 2013; Liu et al., 2018; Wang et al., 2018). A fundamental understanding of the reaction pathways on SACs can not only further guide the experimentalist to find more efficient catalysts but also provide valuable theoretical research ideas for COOR.

Due to the outstanding stability and large surface area, graphene has become a promising candidate for anchoring SACs since its discovery in 2004 (Wang et al., 2012). Up to now, the COOR of the noble metal [Au (Lu et al., 2009), Cu (Song et al., 2011), Pt (Tang et al., 2013)], and other transition metal atoms (Pd (Jia et al., 2014), Mo (Tang et al., 2015)) adsorbed or doped on the surface of graphene has been studied successively. In these systems, the reaction path based on Langmuir–Hinshelwood (L-H) mechanism (Lu et al., 2009), Eley-Ridel (E-R) mechanism (Tang et al., 2017) and trimolecule E-R (TER) mechanism (Zhang et al., 2015) has been confirmed. Recently, an increasing amount of efforts has been devoted to finding catalysis for SACs based on other two-dimensional materials, such as graphyne (Wu et al., 2015), MoS_2 (Du et al., 2015), and hexagonal boron nitride monolayer (h-BN) (Lin et al., 2013; Liu et al., 2014), or to modify graphene to change some of the carbon atoms to N and other atoms (Zhang et al., 2016; Liu et al., 2017), thereby changing the catalytic environment of single metal to achieve better catalytic performance.

As a neighbor of carbon, borophene has attracted increasing interest since it was synthesized recently on a silver substrate under ultrahigh-vacuum with four phases including 2-Pmmn, β_{12}, χ_3, and honeycomb phases (Tang and Ismail-Beigi, 2007; Yang et al., 2008; Mannix et al., 2015). Borophene has complex bonding mechanisms and multiple coordination capabilities (Wang et al., 2019). Particularly, the adsorption of metal atoms with electron-donating properties is expected to occur more likely on borophene than on graphene because of the electron deficient property of boron atoms (Liu et al., 2013). Due to the unique physical and chemical properties, borophene has pronounced potential applications in the service of SACs as the substrate. Based on density functional theory, nitrogen reduction reaction (Liu et al., 2019a; Zhu et al., 2019), hydrogen evolution reaction (Xu et al., 2020a), oxygen evolution/reduction reaction (Xu et al., 2021) and electrocatalytic CO_2 reduction (Shen et al., 2018; Zhang et al., 2020) about SACs have been extensively studied on different phases of borophene, and promising catalytic results have been obtained, indicating that borophene has great research potential for applications in the field of SACs.

However, these previous studies on the application of borophene on SACs mainly focus on electrocatalysis. Besides, most of these works are about α-borophene and β-borophene phase which are considered as the thermodynamically most stable phase based on the density functional theory simulation (Wu et al., 2012). As far as we know, there are few studies about COOR of SACs on borophene, especially there is a lack of research on the catalytic performance of the other phases of borophene. Here, the χ_3-borophene has been selected to investigate the SACs, which was successfully synthesized by Feng's team in 2016 under ultra-high vacuum conditions (Feng et al., 2016). Fe cation has been reported with good catalytic activity for many reactions in the gas phase, while other cations such as Ti^+, Zr^+, V^+, Nb^+, Cr^+ have no such activity (Staley, 1981). In spite of extensive investigations in SACs on two dimensional materials, the transition metal atoms with unfilled d electrons and robust magnetic properties are an interesting and challenging topic in catalysis. In this paper, the COOR of Fe atoms adsorbed on χ_3-borophene are systematically investigated using density functional theory to explore the COOR effect. We believe that the results of this paper will provide new ideas for the catalytic properties of borophene and the study of COOR.

Computational details

The first-principles calculations were carried out using the $DMol^3$ package (Delley, 1990) embedded in Material Studio. Here we used χ_3-borophene as substrate and a (2 × 4) supercell was built for simulation, which contains total 64 boron atoms. The Perdew–Burke–Ernzerhof (PBE) functional was used as the exchange-correlation functional under the generalized gradient approximation (GGA) (Perdew et al., 1996). The electronic eigenfunctions were expanded in terms of localized atomic orbital DNP (Delley, 1990) basis set, and the core treatment used was DFT semicore pseudopotentials (DSPPs) (Delley, 2002), which replaced the core electrons with individual effective potentials. The real-space cutoff radius was set to 4. 7 Å to ensure high-quality results. In the process of geometric optimization, the energy convergence value was 1.0×10^{-5} Ha/atom, the maximum stress convergence value was 0.02 Ha/Å, the maximum displacement convergence value was 0.005 Å, and the threshold of self consistent-field (SCF) density convergence was 1.0×10^{-6} Ha. The K point of the Brillouin zone was selected as 2 × 2 × 1 under the Monkhorst-Pack method (Monkhorst and Pack, 1976). The K point set for PDOS calculation which is 4 × 4 × 1 here in the Fe@χ_3-borophene system. The vacuum layer between χ_3-borophene layers was set to 20 Å to ensure that there was no interaction between layers. Van der Waals interaction was described by DFT + D2 method throughout all calculations (Grimme, 2006). Mulliken's net charge analysis has been applied to count charge transfer between the adsorbate atoms and the substrate (Mulliken, 1955). The transition states (TSs) were searched by the linear both synchronous transit (LST) and

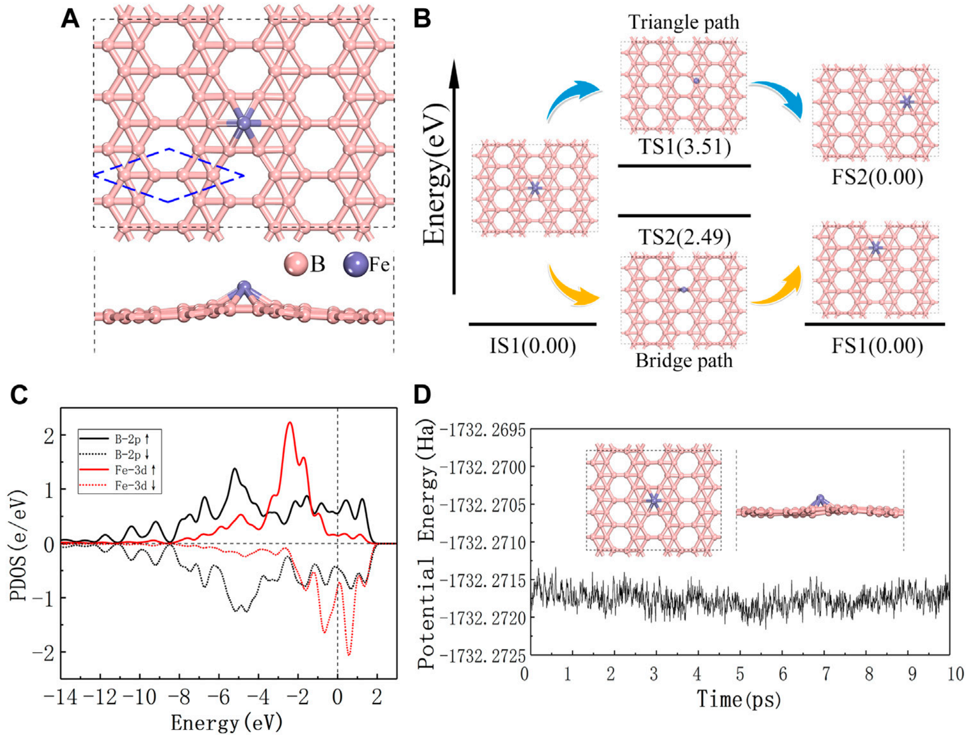

FIGURE 1
(A) Top and side views of the most stable configurations of single Fe atom adsorbed on χ_3-borophene, the blue dashed line is the primitive cell of χ_3-borophene. **(B)** The energy profile for Fe atom diffusion on χ_3-borophene surface with the configurations involved. **(C)** The spin polarized partial density of states for Fe atom and the 6 B atoms around it, the vertical dashed line at 0 eV is the Fermi level. **(D)** *Ab-initio* molecular dynamics calculation of Fe@χ_3-borophene at 300 K, the trajectory length is 10 ps, the inserted figure shows the structure of the system after 10 ps?

quadratic synchronous transit (QST) protocol. We first performed LST, and then repeated conjugate gradient minimization and QST maximization until the TS was found (Halgren and Lipscomb, 1977). To check the dynamic stability of the substrate, we ran the *ab-initio* molecular dynamics simulation using the NVT ensemble.

The adsorption energy E_{ads} of the adsorbent on the substrate is defined as:

$$E_{ads} = E_{adsorbate/substrate} - E_{adsorbate} - E_{substrate} \quad (1)$$

where $E_{adsorbate/substrate}$ is the total energy of the system, $E_{adsorbate}$ is the energy of the ground state of the adsorbate, and $E_{substrate}$ is the energy of the substrate. In order to include the influence of temperature, the change in Gibbs free energy (ΔG) of reaction path is calculated according to

$$\Delta G = \Delta E + \Delta E_{ZPE} - T\Delta S \quad (2)$$

where ΔE and ΔE_{ZPE} are the difference between total energy at 0 K and the zero-point vibration energy, respectively. ΔS is the change of entropy, defined as $\Delta S = \Delta S_{trans} + \Delta S_{rot} + \Delta S_{vib}$, where ΔS_{trans}, ΔS_{rot}, and ΔS_{vib} represent the contribution of translation, rotation, and vibration modes, respectively.

According to the transition state theory, the time required for each step of the reaction can be estimated by the Arrhenius law (Arrhenius, 1889):

$$\tau = \frac{1}{\nu e^{\left(\frac{-E_a}{\kappa_B T}\right)}} \quad (3)$$

where E_a is the energy barrier of the reaction, T is the temperature (K), ν is the attempt frequency, and here the value we use is 10^{12} Hz, which is the same value used in similar systems (Xu et al., 2016; Xu et al., 2018), and κ_B is the Boltzmann constant.

Results and discussion

Structural stability of Fe@χ_3-borophene

The thermodynamic stability of Fe@χ_3-borophene is first studied before we further investigate the catalytic activity of this system for COOR. The atomic model of Fe@χ_3-borophene include a single Fe atom adsorbed on χ_3-borophene. The initial adsorption sites of a single Fe atom in the Fe@χ_3-borophene are first placed at top-site, bridge-site or triangle-site and then optimized, as depicted in Figure 1A and Supplementary Figure S1. The result of geometric optimization shows that the heart-site is the most favorable site for Fe atom adsorption on χ_3-borophene with an adsorption energy of -3.19 eV. The distance between the Fe atom at the heart-site and the adjacent B atom is 2.067 Å and the protruding height between the Fe atom and the χ_3-borophene plane is 1.381 Å.

The diffusion behavior of Fe atoms on the χ_3-borophene surface is studied by evaluating the energy barrier between one heart-site to a neighboring one. Two diffusion paths are identified as the Bridge path and the Triangle path and shown in Figure 1B. The calculated energy barriers of the Bridge path and Triangle path are 2.49 and 3.51 eV, respectively. Therefore, the Bridge path should be preferred as the diffusion path. Higher diffusion energy barrier is shown for Fe@χ_3-borophene than those reported on graphene (Li et al., 2010), so that Fe atom is less favorable to migrate on χ_3-borophene.

To study the self-aggregation of Fe on χ_3-borophene, the structures and energies of nFe (n = 1–4) and Fe_n (n = 1–4) clusters adsorbed on the surface of both graphene and χ_3-borophene (as shown in Supplementary Figures S2 and S3) are calculated for comparison. It can be seen from Supplementary Figures S2 and S3 that the total energy of isolated Fe atoms is significantly lower than that of Fe clusters on χ_3-borophene, indicating that the structure of isolated Fe atoms anchored on χ_3-borophene's heart-site is favorited, while Fe tends to form clusters spontaneously on graphene. Thus, we could avoid the problem of self-aggregation of Fe atoms by choosing χ_3-borophene as substrate.

The spin polarized partial density of states (PDOS) for Fe@χ_3-borophene has been studied to further understand the interaction between Fe atom and χ_3-borophene. PDOS in Figure 1C shows both the 3d-orbital of the guest Fe and the 2p-orbital of the host B atoms cross the Fermi level, showing the metallic characteristics of the Fe atom adsorbed on χ_3-borophene system as demonstrated in the pure χ_3-borophene (Feng et al., 2016). The superposition of one sharp peak originates from the d orbital of the adsorbed Fe atom and the p orbital of substrate B atoms span from -8.0 to 2.0 eV near the Fermi level. The strong hybridization shown in PDOS verifies the strong interaction between the guest Fe and host borophene and results in the high stability of the structure. We find that the shapes of the PDOS not only in d state of Fe atom but also in p state of borophene are quite different (see Figure 1C). Fe@χ_3-borophene carries a large magnetic moment of 3.0 μ_B, which is similar to the results obtained from the calculations with Fe adsorbed on different 2d borophene polymorphs (Alvarez-Quiceno et al., 2017; Liu et al., 2019b). Mulliken population analysis shows that the total magnetic moment of the clusters is mainly localized on the Fe atom. The χ_3-borophene substrate provides a small contribution to the magnetic moments, as shown in Figure 1C. This can be ascribed to the internal charge transfer from the Fe to the B atoms. Due to the electron deficiency of χ_3-borophene, the Fe atom is positively charged, donating about 1.34 e to the substrate. According to literatures (Lu et al., 2009), charge transfers not only contribute to the stability of the system, but also provide activity for subsequent catalytic reactions.

The stability of Fe@χ_3-borophene under room temperature is confirmed by *ab-initio* molecular dynamics calculation (Figure 1D). Within the employed simulation time of 10 ps at 300 K, no structural change is detected, while the instantaneous values of the potential energy fluctuate slightly due to thermal fluctuations. Thus, the lowest energy structure of Fe@χ3-borophene is expected to be stable at room temperature.

Adsorption properties of CO, O_2 and CO_2 on Fe@χ_3-borophene

In order to understand the specific reaction path of COOR on the surface of Fe@χ_3-borophene, it is important to further study the adsorption and co-adsorption properties of various gas molecules including CO, O_2 and CO_2 involved in COOR on Fe@χ_3-borophene. The most stable adsorption configurations of various gas molecules absorbed on Fe@χ_3-borophene are shown in Figure 2 and Supplementary Figure S4. Their adsorption energies, charge transfers and magnetic moments are listed in Table 1.

The most favorable adsorption sites for CO and O_2 are shown in Figures 2A,C, respectively. Both the CO and O_2 molecules adsorb on top of the Fe atom as they approach the Fe@χ_3-borophene. For CO, the lowest energy adsorption model is that the CO molecule is located vertically above the Fe@χ_3-borophene, where Fe, C, O atoms form a line and the C atom is bonded with the Fe atom. The bond length of CO* (1.167 Å) is slightly larger than that of gaseous CO (1.129 Å) and the distance between Fe and C is 1.766 Å ("*" represents the adsorption state). The most stable adsorption position for O_2* is the horizontal configuration, where two O atoms are adsorbed on the Fe@χ_3-borophene and form an inverted triangle with the Fe atom. The bond length of O_2* increases significantly from 1.208 Å to 1.381 Å compared to the gas phase and the bond length of O and Fe is 1.847 Å. The lowest energy adsorption positions for other gas molecules or combinations of gas molecules including 2CO, CO + O_2, CO_3, CO_2 and 2CO_2 are drawn in Supplementary Figure S4.

The PDOS for CO-Fe@χ_3-borophene is shown in Figure 2B. After the CO molecule is absorbed, the 3d spin-up and spin-down lines of Fe atom in the graph are almost identical in shape. A CO molecule adsorbed on the Fe@χ_3-borophene is found to exhibit no magnetic moment, which means the magnetic moment of 3.0 μ_B in the substrate is completely quenched. The 5σ orbital has similar energy levels to 1π orbital for the

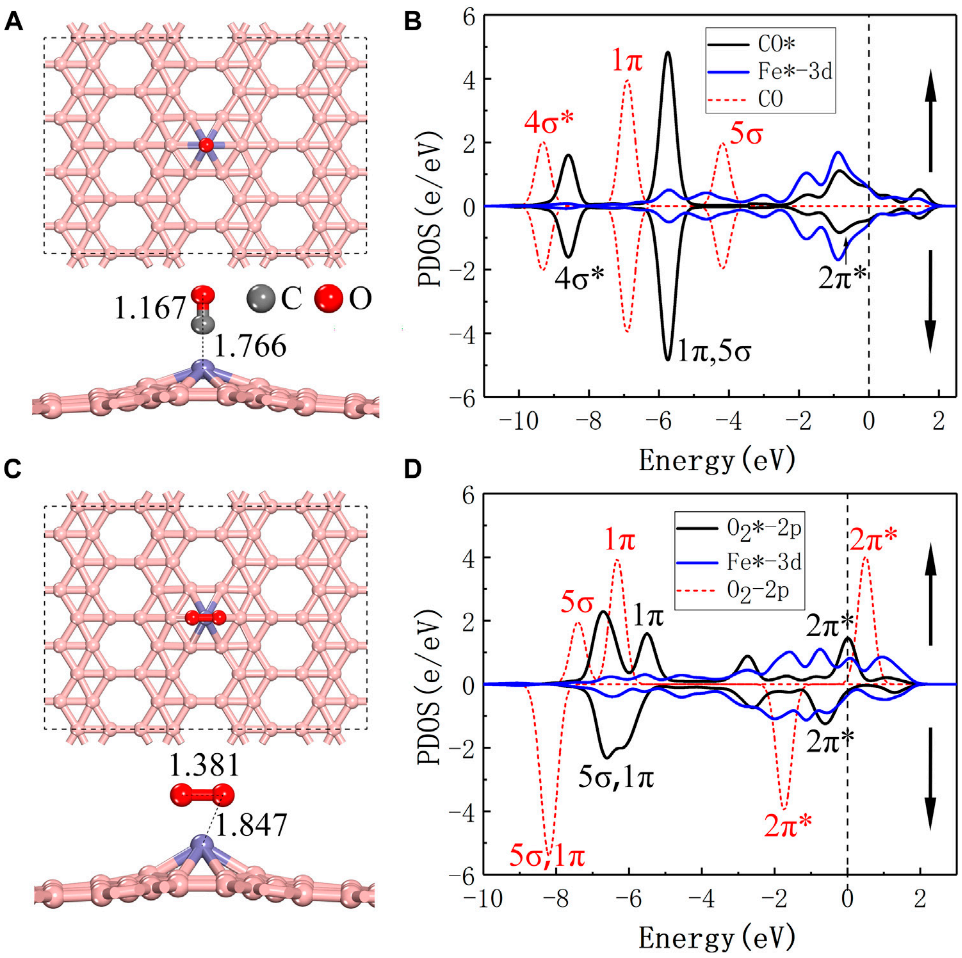

FIGURE 2
(A,C) are top and side views of the most stable configurations of CO/O_2 adsorbed on Fe@χ_3-borophene, respectively. **(B,D)** are the spin polarized partial density of states for the CO/O_2 and Fe after adsorbed on Fe@χ_3-borophene. The vertical dashed line at 0 eV is the Fermi level and the red dashed line is the PDOS for CO and O_2 in the gas phase.

TABLE 1 The related parameters of gas molecules absorbed on Fe@χ_3-borophene: adsorption energy (E_{ads}), charge transfer between the Fe atom and the χ_3-borophene (Δq_1), charge transfer between gas molecules and Fe@χ_3-borophene (Δq_2), magnetic moment of the system.

System	E_{ads} (eV)	Δq_1 (e)	Δq_2 (e)	*Moment* (μ_B)
CO_2	-0.30	1.37	-0.02	3.0
$2CO_2$	-0.59	1.38	0.02	3.0
O_2	-2.16	1.29	-0.56	2.0
CO	-2.44	0.94	-0.24	0.0
CO + O_2	-3.15	1.14	-0.62	0.0
2CO	-4.29	0.95	-0.28	0.0
CO_3	-5.24	1.31	-0.98	0.0

adsorbed CO molecule. The 2π* orbitals of CO are filled and have an obvious hybrid effect with the 3d orbitals of Fe atom, leading to a reduction in the energy of the system (Jiang et al., 2018; Jiang et al., 2020; Jiang et al., 2021). For O_2-Fe@χ_3-borophene, the empty 2π* anti-bond orbital is occupied, which results in a longer bond length of O-O bond as Figure 2D shows. Due to the presence of the anti-bond orbital, O_2 is activated and the energy required to open the O-O bond is thus reduced, which is helpful to the subsequent catalytic reaction. The PDOS also demonstrates that the 2π* orbital of O_2 has a strong hybridization with the 3d-orbital of Fe, thus making the system more stable.

The value of the adsorption energy of the individual CO and O_2 molecules on Fe@χ_3-borophene are -2.44 eV and -2.21 eV, respectively. These large absolute values of the adsorption energy

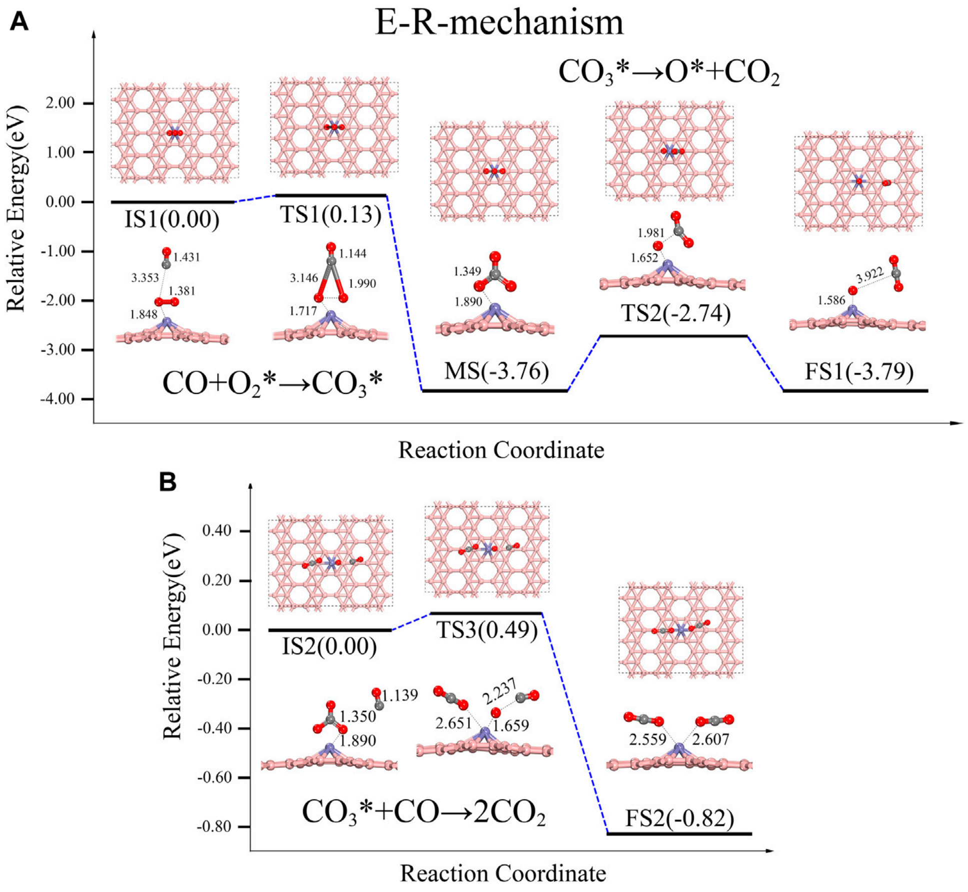

FIGURE 3
Energy distribution diagram under the E-R path and its corresponding structure diagram, the rate-determining step is IS2-FS2, turning over an energy barrier of 0.49 eV.

suggest that there are strong interactions between CO/O_2 and Fe@χ3-borophene. The strong interaction between the gas molecules and borophene substrate is a prerequisite for the subsequent catalytic reaction of COOR. It should be noted that the difference between the adsorption energies of CO and O_2 molecules is only 0.23 eV. As a result, either CO or O_2 molecules can be absorbed firstly on the substrate. If a single CO is absorbed at the first time, the adsorption state of 2CO* will be formed when another CO approaches, as shown in Supplementary Figure S4A, where 2 C atoms are simultaneously bonded to Fe with the adsorption energy of -4.29 eV. We also simulate the structure of the classical co-adsorbed state of CO + O_2* when a CO molecule is first absorbed and then an O_2 molecule approaches (Supplementary Figure S4B). In this case, a Fe atom is bonded with two O atoms and a C atom at the same time with the adsorption energy of -3.15 eV. Since the adsorption energy of the CO + O_2* is 1.14 eV smaller than the case of 2CO*, the CO + O_2* is more difficult to occur. Another possible adsorption pathway is that a single O_2 is first adsorbed on the substrate. In this case, an intermediate state of CO_3* will easily form when CO approaches the system with a large adsorption energy of -5.24 eV, which is 2.09 eV more negative than the case of CO + O_2*, so that the CO + O_2* is unlikely to form in this case either. Furthermore, the adsorption energies of one or two CO_2 molecules are -0.33 eV and -0.59 eV respectively, which is quite small compared to that of the other gas molecules. Only -0.02 e and 0.02 e are transferred between CO_2 and the substrate, indicating that CO_2 is physically adsorbed on the substrate by van der Waals interactions, and can be separated from the substrate very easily.

Reaction mechanism of CO oxidation on Fe@χ_3-borophene

According to the adsorption energy calculations of different gas molecules, the possible paths for COOR on the Fe@χ_3-borophene are summed up as follows.

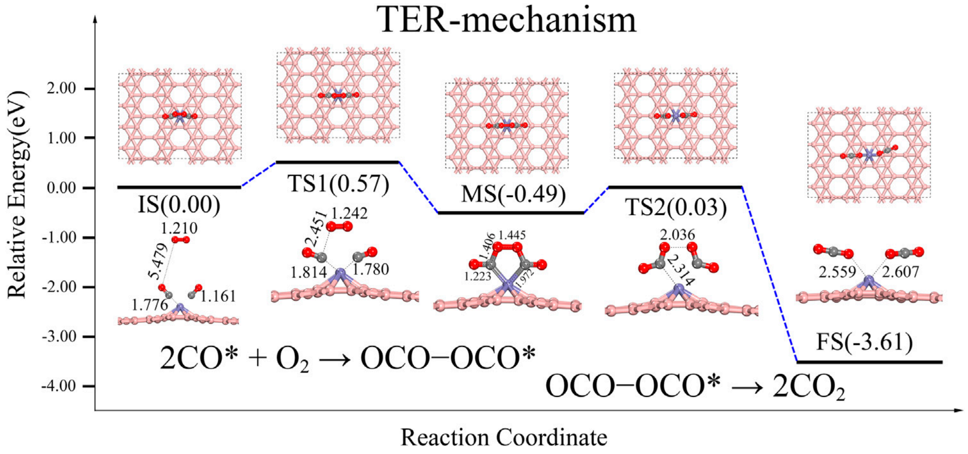

FIGURE 4
Energy distribution diagram under TER path and its corresponding structure diagram, the rate-determining step is IS-MS2 turning over an energy barrier of about 0.57 eV.

E-R:

$$O_2^* + CO \rightarrow CO_3^*$$
$$CO_3^* \rightarrow O^* + CO_2 \; or \; CO_3^* + CO \rightarrow 2CO_2$$

TER:

$$2CO^* + O_2 \rightarrow OCO - OCO^*$$
$$OCO - OCO^* \rightarrow 2CO_2$$

where "*" represents the adsorption state.

1) E-R reaction

The E-R reaction path is shown in Figure 3. We place the CO molecule above the O_2-Fe@χ_3-borophene as the initial state (IS), representing the CO in the gas phase. In the first step of the reaction path, CO molecule combines with O_2* to form an intermediate state (MS) CO_3*. The energy barrier for this step is only 0.13 eV, and this reaction releases a large amount of heat (3.76 eV). In the conventional E-R reaction, the next step is the decomposition of CO_3* into O* and CO_2 (see Figure 3A). We simulate this reaction and find that the reaction barrier for CO_3* to form CO_2 by breaking the C-O bond directly requires 1.02 eV, which indicates that this step is unlikely to occur. However, there is another possible path for CO_3* to decompose with lower energy barrier. Chen's team found that the direct separation of CO_3* requires 1.34 eV, while the path to form $2CO_2$ via another CO only needs to cross an energy barrier of 0.15 eV (Chen et al., 2020) when they studied the COOR on the 3Si-graphene-Ni. According to Chen's result, here we also investigated the reaction path of forming $2CO_2$ by adding a second CO molecule in our system and the reaction pathway is shown in Figure 3B, where the reaction barrier is found to be reduced. In this reaction path way, the gas phase CO suspended around the CO_3* is used as the IS. When the second CO molecule approaches, one of the C-O bonds in CO_3* breaks. As a result, a CO_2 is subsequently detached and the remaining single O atom combines with the CO molecule to form the final state (FS) $2CO_2$*. This reaction requires climbing an energy barrier of 0.49 eV and gives off 0.82 eV of heat as shown in Figure 3B, which is nearly half of the energy barrier of 1.02 eV for direct decomposition, indicating that the presence of gas-phase CO does effectively facilitate the dissociation of CO_3*.

2) TER reaction

From the adsorption energies discussed above, it is apparent that two CO molecules are more likely to be adsorbed on Fe@χ_3-borophene due to its ~1.14 eV greater adsorption energy than that of the CO + O_2*. Figure 4 shows that the TER reaction path, which starts from the IS of the reaction with the gas-phase O_2 physiosorbed on 2CO-Fe@χ3-borophene. The two co-adsorbed CO effectively activate the gas-phase O_2 to cross an energy barrier of about 0.57 eV. The product is an OCO-Fe-OCO* intermediate state releasing an energy of 0.49 eV. This OCO-Fe-OCO* intermediate state has a pentagonal structure, which is similar to the OCO-Pt-OCO* intermediate state reported by the Zhang team in the TER path on Pt/NG (Zhang et al., 2015). During the reaction, it is found that two oxygen atoms in O_2 will approach the 2 C atoms of the CO molecules progressively and eventually form bonds to the C atom with a bond length of 1.406 Å.

The second step of the reaction path is that the intermediate state of OCO-Fe-OCO* proceeds to the final state of $2CO_2$*. It can be seen from Figure 4 that the MS needs to cross an energy

TABLE 2 The relevant parameters of each basic reaction path: the energy released by the reaction ($E_{reaction}$), the energy barrier required for the reaction ($E_{barrier}$), the charge transfer between reactants and substrates (Δq_1), the charge obtained by χ_3-borophene (Δq_2), the charge loss of Fe atom (Δq_3), the magnetic moment of the system (Moment), the distance between Fe atom and the χ_3-borophene surface ($d_{Fe\text{-}bor}$).

Reaction mechanisms	**ER-step**						**TER-step**				
	IS1	**TS1**	**MS**	**IS2**	**TS3**	**FS2**	**IS**	**TS1**	**MS**	**TS2**	**FS**
$E_{reaction}$ (eV)		3.89			0.82			0.49		3.12	
$E_{barrier}$ (eV)		0.13			0.49			0.57		0.52	
Δq_1 (e)	−0.54	−0.84	−0.97	−0.97	−0.44	−0.02	−0.28	−0.39	−0.74	−0.68	−0.02
Δq_2 (e)	−0.75	−0.60	−0.34	−0.32	−0.82	−1.36	−0.67	−0.65	−0.29	−0.54	−1.36
Δq_3 (e)	1.29	1.44	1.31	1.29	1.23	1.38	0.95	1.04	1.03	1.22	1.38
Moment (μ_B)	2.0	1.8	0.0	0.0	0.7	3.0	2.0	1.8	0.0	2.1	3.0
$d_{Fe\text{-}bor}$ (Å)	1.403	1.384	1.371	1.371	1.377	1.381	1.378	1.373	1.368	1.372	1.381

barrier of about 0.52 eV to form two CO_2, which is almost the same as the energy barrier of 0.57 eV required from IS to MS. The breaking of the O-O bond and C-Fe bond releases about 3.12 eV of heat. The O-O bond grows from 1.352 Å to 2.036 Å, and finally breaks completely, while the C-Fe bond grows from 1.973 Å to 2.314 Å, and finally breaks completely. The final product $2CO_2$ is physically adsorbed on the system and can be easily dissociated to allow the cycle to continue.

3) Discussion of catalytic results and electronic properties

Here we summarize the rate-determining steps (RDS) of both reactions described above. The important parameters of each reaction are listed in Table 2. In the E-R reaction, the RDS is2-FS2, climbing an energy barrier of about 0.49 eV, which is less than the energy barrier needed for the E-R reaction on Fe-SV-graphene (Li et al., 2010; Xu et al., 2020b). The RDS in the TER reaction is IS-MS, requiring an energy barrier of about 0.57 eV.

We analyze the electronic structural property of the system to provide deeper understanding for the reaction. As can be seen from the charge transfer between reactants and substrates (Δq_1) in Table 2, the adsorbate will gain the largest number of electrons from the fe@χ_3-borophene when O_2 needs to be activated in both E-R and TER processes, with 0.97 e and 0.74 e obtained for the MS state in the E-R and TER reactions, respectively. Most of the obtained electrons will occupy the 2π* anti-bonding orbital of O_2, leading to a longer bond length of O_2, which makes subsequent catalytic reactions easier. In addition, it can be found from Δq_2 which denotes the charge obtained by the χ_3-borophene that it always gets electrons during the whole reaction process, and the number of electrons gained decreases significantly when the reaction requires a large number of electrons to activate O_2, with 0.34 e and 0.29 e obtained for the MS state in the E-R and TER reactions, respectively. It is not difficult to find that χ_3-borophene plays an important role in both donating and obtaining electrons in the whole reaction. Finally, it can be observed by the charge loss of Fe atom (Δq_3) that the charge transfer of Fe atom is not very large in the E-R reaction. One possible reason is that Fe plays the role of a transport medium during the charge transfer process. Due to the strong electron deficiency of χ_3-borophene, when a single Fe atom is adsorbed on the surface of χ_3-borophene, the Fe atom will lose 1.34 e, and these electrons will be temporarily stored in the χ_3-borophene. When O_2 requires electrons to be activated in the subsequent catalytic process, charge transfer occurs from χ_3-borophene to O_2, so as to provide electrons to active the catalytic reaction. Therefore, not only does the Fe atom that directly interacts with the gas molecules play an important role in catalysis, but also the χ_3-borophene as the substrate is the key to the catalytic reaction.

It is widely known that the analysis of the electronic state of the reaction path is of great significance for understanding the COOR process. It can be seen from Table 2 that no matter whether it is the E-R reaction or the TER reaction, the magnetic moments of the system undergo a process from presence to disappearance, and finally regain. O_2 in the gas phase has a triplet state, resulting in a total magnetic moment of 2.0 μ_B when O_2 is initially adsorbed. As the reaction processes, charge transfer occurs between the adsorbate, Fe atom and the χ_3-borophene, to promote the annihilation of the magnetic moment. Finally, the formation of CO_2 brings the overall magnetic moment back to the original 3.0 μ_B of Fe@χ_3-borophene.

During the COOR catalytic reaction, the distance between the Fe atom and the χ_3-borophene surface is slightly changed. The initial distance is 1.381 Å after the geometry optimization. In the catalytic reaction, the distance of the Fe atom from the χ_3-borophene surface varies as shown in Table 2. The distances show a pattern of first getting smaller and then larger.

The influence of temperature

In order to get a more realistic picture of the catalytic reaction, it is important to consider the effect of temperature. According to Peng team’s research, χ_3-borophene remains thermodynamically stable at 1000 K (Peng et al., 2017), thus we plot the change of

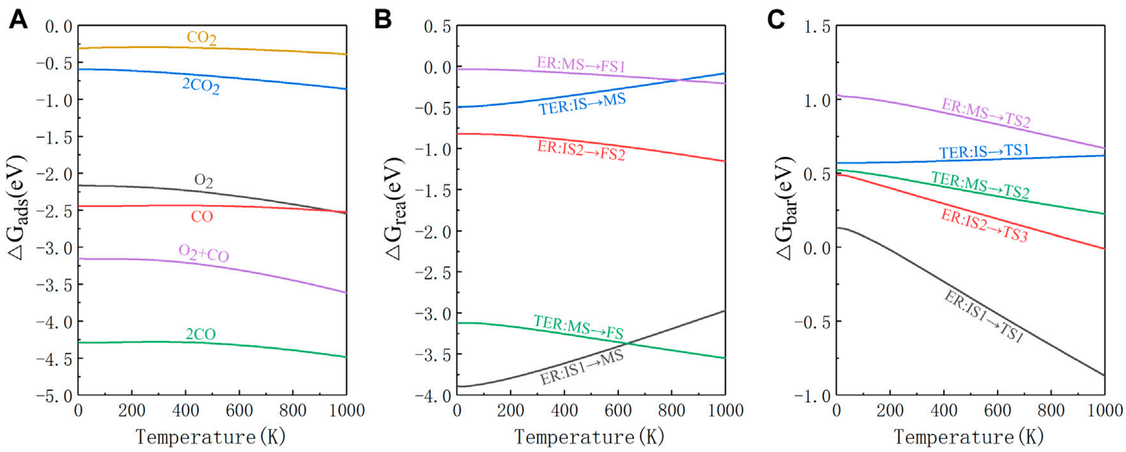

FIGURE 5
The change in Gibbs free energy of each reaction path at 0–1000 K. **(A)** The gas molecules adsorption energy. **(B)** The energy released by the reaction. **(C)** The energy barrier required for the reaction.

TABLE 3 Time required for each step of the reaction path in E-R and TER reaction at 200 K, 298.15 K, 400 K, 500 K.

Reaction step Reaction time	E-R-step			TER-step	
	IS1-MS	MS-FS1	IS2-FS2	IS-MS	MS-FS
τ (s)/200 K	3.42×10^{-13}	5.64×10^{12}	9.88×10^{-1}	3.11×10^{2}	9.88×10^{-1}
τ (s)/298.15 K	8.72×10^{-15}	1.04×10^{4}	3.14×10^{-5}	6.04×10^{-3}	3.14×10^{-5}
τ (s)/400 K	1.17×10^{-15}	2.97×10^{-1}	1.47×10^{-7}	2.30×10^{-5}	1.47×10^{-7}
τ (s)/500 K	3.59×10^{-16}	6.07×10^{-4}	6.34×10^{-9}	8.78×10^{-7}	6.34×10^{-9}

adsorption energy, reaction energy, and energy barrier for the whole system at 0–1000 K as shown in Figure 5. As can be seen from Figure 5A, when the temperature ranges from 0 to 300 K, the value of adsorption energy is almost the same compared to the adsorption energy at 0 K. When the temperature is greater than 300 K, the absolute value of the adsorption energy increases, but the order of the adsorption energy values does not change. The absolute value of the adsorption energy of O_2+CO* is still about 1 eV lower than 2CO*, so the L-H reaction will not occur, indicating that the reaction path we obtained at 0 K is unchanged. The changes in the Gibbs free energy of the E-R and TER reactions are all negative, so all steps are exothermic as depicted in Figure 5B. Finally in Figure 5C we find that as the temperature reaches 200 K, the reaction energy barrier of IS1→TS1 in the E-R reaction becomes negative. It indicates that CO_3* is more likely to form spontaneously under the influence of temperature. The energy barrier of MS→TS2 is always greater than IS2→TS3 in the E-R reaction, so the E-R reaction still requires a second external CO to participate in the presence of temperature. The energy barrier of IS→TS1 in the TER reaction increases slightly with temperature, but the value of the energy barrier is not large, and the reaction can still proceed. Overall, the RDS of each reaction step does not change with the presence of temperature and most of the reaction energy barriers decrease significantly with the increasing temperature.

Reaction rate

Table 3 shows the specific time required for each step of the reaction process obtained by the Arrhenius law. In the E-R reaction, it can be seen that the time required for IS1-MS is very short at any temperature, which is consistent with the low energy barrier. In addition, the time required for IS2-FS2 is much less than that for MS-FS1, which means that the direct dissociation of CO_3* is very difficult and the second CO is always required in the actual reaction. In the TER reaction, when the temperature is 200 K, the time taken by IS-MS is about 3.11×10^2 s, thus the reaction is not easy to occur. However, the entire TER reaction can proceed normally at higher temperature. In summary, the reaction rate of the E-R reaction is fast at any temperature, while the TER reaction is more suitable when temperature is above 200 K.

Conclusion

The DFT calculations have been performed to investigate the mechanism of CO oxidation on Fe@χ_3-borophene. In this work we have ensured the stability of the system with formation energy calculation, diffusion path calculation and *Ab-Initio* molecular dynamics simulation. Two possible reaction paths have been identified by absorption energy comparisons and their energy barriers have been calculated. The results show that the COOR on the Fe@χ_3-borophene substrate has good catalytic performance. Further electronic structure analysis indicates that charge transfers between χ_3-borophene and CO, O_2 and CO_2 molecules are the major cause of both the low energy barrier and magnetic moment difference. First-principles study of Fe@ χ_3-borophene as a catalyst for COOR provides new possibilities and ideas for the COOR, and proposes new opportunities for the application of borophene in the field of heterogeneous catalysis.

Data availability statement

The original contributions presented in the study are included in the article/Supplementary Material, further inquiries can be directed to the corresponding authors.

Author contributions

MZ, Y-YZ, and J-WH designed the research and wrote the paper. J-WH and W-YB carried out the simulation. All authors entered the discussion and commented on the manuscript.

Funding

This project is supported by the Startup Grant of Wenzhou Institute and Oujiang Laboratory (WIUCASQD2021014 and WIUCASQD2022025). Calculations are performed at the super computer center in School of Physics, East China University of Science and Technology.

Conflict of interest

Publisher's note

Supplementary material

The Supplementary Material for this article can be found online at: https://www.frontiersin.org/articles/10.3389/fchem.2022.1008332/full#supplementary-material

References

Alavi, A., Hu, P., Deutsch, T., Silvestrelli, P. L., and Hutter, J. (1998). CO oxidation on Pt(111): An*Ab Initio*Density functional theory study. *Phys. Rev. Lett.* 80 (16), 3650–3653. doi:10.1103/physrevlett.80.3650

Alvarez-Quiceno, J. C., Schleder, G. R., Marinho, E., Jr, and Fazzio, A. (2017). Adsorption of 3*d*, 4*d*, and 5*d*transition metal atoms onβ_{12}—Borophene. *J. Phys. Condens. Matter* 29 (30), 305302. doi:10.1088/1361-648x/aa75f0

Arrhenius, S. (1889). Über die Reaktionsgeschwindigkeit bei der Inversion von Rohrzucker durch Säuren. *Z. fur Phys. Chem.* 4, 226–248. doi:10.1515/zpch-1889-0416

Chen, W., Zhao, G., Wu, B., Tang, Y., Teng, D., and Dai, X. (2020). Theoretical study on the catalytic properties of single-atom catalyst stabilised on silicon-doped graphene sheets. *Mol. Phys.* 118 (7), e1652368. doi:10.1080/00268976.2019.1652368

Delley, B. (1990). An all-electron numerical method for solving the local density functional for polyatomic molecules. *J. Chem. Phys.* 92 (1), 508–517. doi:10.1063/1.458452

Delley, B. (2002). Hardness conserving semilocal pseudopotentials. *Phys. Rev. B* 66 (15), 155125. doi:10.1103/physrevb.66.155125

Du, C., Lin, H., Lin, B., Ma, Z., Hou, T., Tang, J., et al. (2015). MoS_2 supported single platinum atoms and their superior catalytic activity for CO oxidation: A density functional theory study[J]. *J. Mat. Chem. A Mat.* 3 (46), 23113–23119. doi:10.1039/c5ta05084g

Ernst, A., and Zibrak, J. D. (1998). Carbon monoxide poisoning. *N. Engl. J. Med. Overseas. Ed.* 339 (22), 1603–1608. doi:10.1056/nejm199811263392206

Feng, B., Zhang, J., Zhong, Q., Li, W., Li, S., Li, H., et al. (2016). Experimental realization of two-dimensional boron sheets. *Nat. Chem.* 8 (6), 563–568. doi:10.1038/nchem.2491

Grimme, S. (2006). Semiempirical GGA-type density functional constructed with a long-range dispersion correction. *J. Comput. Chem.* 27 (15), 1787–1799. doi:10.1002/jcc.20495

Halgren, T. A., and Lipscomb, W. N. (1977). The synchronous-transit method for determining reaction pathways and locating molecular transition states. *Chem. Phys. Lett.* 49 (2), 225–232. doi:10.1016/0009-2614(77)80574-5

Jia, T. T., Lu, C. H., Zhang, Y. F., and Chen, W. K. (2014). A comparative study of CO catalytic oxidation on Pd-anchored graphene oxide and Pd-embedded vacancy graphene[J]. *J. nanoparticle Res.* 16 (2), 1–11. doi:10.1007/s11051-013-2206-0

Jiang, Q., Huang, M., Qian, Y., Miao, Y., and Ao, Z. (2021). Excellent sulfur and water resistance for CO oxidation on Pt single-atom-catalyst supported by defective graphene: The effect of vacancy type. *Appl. Surf. Sci.* 566, 150624. doi:10.1016/j.apsusc.2021.150624

Jiang, Q., Zhang, J., Ao, Z., Huang, H., He, H., and Wu, Y. (2018). First principles study on the CO oxidation on Mn-embedded divacancy graphene. *Front. Chem.* 6, 187. doi:10.3389/fchem.2018.00187

Jiang, Q., Zhang, J., Huang, H., Wu, Y., and Ao, Z. (2020). A novel single-atom catalyst for CO oxidation in humid environmental conditions: Ni-Embedded divacancy graphene. *J. Mat. Chem. A Mat.* 8 (1), 287–295. doi:10.1039/c9ta08525d

Kalita, B., and Deka, R. C. (2009). Reaction intermediates of CO oxidation on gas phase Pd_4 clusters: A density functional study. *J. Am. Chem. Soc.* 131 (37), 13252–13254. doi:10.1021/ja904119b

Kim, H. Y., Han, S. S., Ryu, J. H., and Lee, H. M. (2010). Balance in adsorption energy of reactants steers CO oxidation mechanism of Ag13 and Ag12Pd1 nanoparticles: Association mechanism versus carbonate-mediated mechanism. *J. Phys. Chem. C* 114 (7), 3156–3160. doi:10.1021/jp9111553

Li, Y., Zhou, Z., Yu, G., Chen, W., and Chen, Z. (2010). CO catalytic oxidation on iron-embedded graphene: Computational quest for low-cost nanocatalysts. *J. Phys. Chem. C* 114 (14), 6250–6254. doi:10.1021/jp911535v

Lin, S., Ye, X., Johnson, R. S., and Guo, H. (2013). First-principles investigations of metal (Cu, Ag, Au, Pt, Rh, Pd, Fe, Co, and Ir) doped hexagonal boron nitride nanosheets: Stability and catalysis of CO oxidation. *J. Phys. Chem. C* 117 (33), 17319–17326. doi:10.1021/jp4055445

Liu, C., Li, Q., Zhang, J., Jin, Y., MacFarlane, D. R., and Sun, C. (2019). Conversion of dinitrogen to ammonia on Ru atoms supported on boron sheets: A DFT study. *J. Mat. Chem. A Mat.* 7 (9), 4771–4776. doi:10.1039/c8ta08219g

Liu, H., Gao, J., and Zhao, J. (2013). From boron cluster to two-dimensional boron sheet on Cu (111) surface: Growth mechanism and hole formation[J]. *Sci. Rep.* 3 (1), 1–9. doi:10.1038/srep03238

Liu, J. C., Tang, Y., Wang, Y. G., Zhang, T., and Li, J. (2018). Theoretical understanding of the stability of single-atom catalysts. *Natl. Sci. Rev.* 5 (5), 638–641. doi:10.1093/nsr/nwy094

Liu, J. H., Yang, L. M., and Ganz, E. (2019). Efficient electrocatalytic reduction of carbon dioxide by metal-doped β_{12}-borophene monolayers. *RSC Adv.* 9 (47), 27710–27719. doi:10.1039/c9ra04135d

Liu, X., Duan, T., Sui, Y., Meng, C., and Han, Y. (2014). Copper atoms embedded in hexagonal boron nitride as potential catalysts for CO oxidation: A first-principles investigation. *RSC Adv.* 4 (73), 38750–38760. doi:10.1039/c4ra06436d

Liu, Z., He, T., Liu, K., Chen, W., and Tang, Y. (2017). Structural, electronic and catalytic performances of single-atom Fe stabilized by divacancy-nitrogen-doped graphene. *RSC Adv.* 7 (13), 7920–7928. doi:10.1039/c6ra28387j

Lopez, N., and Nørskov, J. K. (2002). Catalytic CO oxidation by a gold Nanoparticle: A density functional study. *J. Am. Chem. Soc.* 124 (38), 11262–11263. doi:10.1021/ja026998a

Lu, Y. H., Zhou, M., Zhang, C., and Feng, Y. P. (2009). Metal-embedded graphene: A possible catalyst with high activity. *J. Phys. Chem. C* 113 (47), 20156–20160. doi:10.1021/jp908829m

Mannix, A. J., Zhou, X. F., Kiraly, B., Wood, J. D., Alducin, D., Myers, B. D., et al. (2015). Synthesis of borophenes: Anisotropic, two-dimensional boron polymorphs. *Science* 350 (6267), 1513–1516. doi:10.1126/science.aad1080

Monkhorst, H. J., and Pack, J. D. (1976). Special points for Brillouin-zone integrations. *Phys. Rev. B* 13 (12), 5188–5192. doi:10.1103/physrevb.13.5188

Mulliken, R. S. (1955). Atomic Dipole moment corrected Hirshfeld population method[J]. *J. Chem. Phys.* 1833, 23. doi:10.1142/S0219633612500113

Peng, B., Zhang, H., Shao, H., Ning, Z., Xu, Y., Ni, G., et al. (2017). Stability and strength of atomically thin borophene from first principles calculations. *Mater. Res. Lett.* 5 (6), 399–407. doi:10.1080/21663831.2017.1298539

Perdew, J. P., Burke, K., and Ernzerhof, M. (1996). Generalized gradient approximation made simple. *Phys. Rev. Lett.* 77 (18), 3865–3868. doi:10.1103/physrevlett.77.3865

Prockop, L. D., and Chichkova, R. I. (2007). Carbon monoxide intoxication: An updated review. *J. neurological Sci.* 262 (1-2), 122–130. doi:10.1016/j.jns.2007.06.037

Qiao, B., Wang, A., Yang, X., Allard, L. F., Jiang, Z., Cui, Y., et al. (2011). Single-atom catalysis of CO oxidation using Pt1/FeOx. *Nat. Chem.* 3 (8), 634–641. doi:10.1038/nchem.1095

Shen, H., Li, Y., and Sun, Q. (2018). Cu atomic chains supported on β-borophene sheets for effective CO_2 electroreduction[J]. *Nanoscale* 10 (23), 11064–11071. doi:10.1039/c8nr01855c

Song, E. H., Wen, Z., and Jiang, Q. (2011). CO catalytic oxidation on copper-embedded graphene. *J. Phys. Chem. C* 115 (9), 3678–3683. doi:10.1021/jp108978c

Staley, R. H. (1981). Gas-phase oxidation catalysis by transition-metal cations[J]. *J. Am. Chem. Soc.* 103 (5), 1286–1287.

Tang, H., and Ismail-Beigi, S. (2007). Novel precursors for boron nanotubes: The competition of two-center and three-center bonding in boron sheets. *Phys. Rev. Lett.* 99 (11), 115501. doi:10.1103/physrevlett.99.115501

Tang, Y., Chen, W., Shen, Z., Chang, S., Zhao, M., and Dai, X. (2017). Nitrogen coordinated silicon-doped graphene as a potential alternative metal-free catalyst for CO oxidation. *Carbon* 111, 448–458. doi:10.1016/j.carbon.2016.10.028

Tang, Y., Pan, L., Chen, W., Li, C., Shen, Z., and Dai, X. (2015). Reaction mechanisms for CO catalytic oxidation on monodisperse Mo atom-embedded graphene. *Appl. Phys. A* 119 (2), 475–485. doi:10.1007/s00339-015-9093-4

Tang, Y., Yang, Z., Dai, X., Ma, D., and Fu, Z. (2013). Formation, stabilities, and electronic and catalytic performance of platinum catalyst supported on non-metal-doped graphene. *J. Phys. Chem. C* 117 (10), 5258–5268. doi:10.1021/jp400202e

Wang, A., Li, J., and Zhang, T. (2018). Heterogeneous single-atom catalysis. *Nat. Rev. Chem.* 2 (6), 65–81. doi:10.1038/s41570-018-0010-1

Wang, H., Wang, Q., Cheng, Y., Li, K., Yao, Y., Zhang, Q., et al. (2012). Doping monolayer graphene with single atom substitutions. *Nano Lett.* 12 (1), 141–144. doi:10.1021/nl2031629

Wang, Z. Q., Lü, T. Y., Wang, H. Q., and Zheng, J. C. (2019). Review of borophene and its potential applications[J]. *Front. Phys.* 14 (3), 1–20. doi:10.1007/s11467-019-0884-5

Wu, P., Du, P., Zhang, H., and Cai, C. (2015). Graphyne-supported single Fe atom catalysts for CO oxidation. *Phys. Chem. Chem. Phys.* 17 (2), 1441–1449. doi:10.1039/c4cp04181j

Wu, X., Dai, J., Zhao, Y., Zhuo, Z., Yang, J., and Zeng, X. C. (2012). Two-dimensional boron monolayer sheets. *ACS Nano* 6 (8), 7443–7453. doi:10.1021/nn302696v

Xu, L., Yang, L. M., and Ganz, E. (2018). Mn–graphene single-atom catalyst evaluated for CO oxidation by computational screening[J]. *Theor. Chem. Accounts* 137 (7), 1–13. doi:10.1007/s00214-018-2270-8

Xu, X., Hou, X., Lu, J., Zhang, P., Xiao, B., and Mi, J. (2020). Metal-doped two-dimensional borophene nanosheets for the carbon dioxide electrochemical reduction reaction. *J. Phys. Chem. C* 124 (44), 24156–24163. doi:10.1021/acs.jpcc.0c05998

Xu, X., Si, R., Dong, Y., Fu, K., Guo, Y., He, Y., et al. (2021). Borophene–supported single transition metal atoms as potential oxygen evolution/reduction electrocatalysts: A density functional theory study[J]. *J. Mol. Model.* 27 (3), 1–10. doi:10.1007/s00894-021-04693-5

Xu, X. Y., Li, J., Xu, H., and Zhao, C. (2016). DFT investigation of Ni-doped graphene: Catalytic ability to CO oxidation. *New J. Chem.* 40 (11), 9361–9369. doi:10.1039/c6nj00924g

Xu, X. Y., Xu, H., Guo, H., and Zhao, C. (2020). Mechanism investigations on CO oxidation catalyzed by Fe-doped graphene: A theoretical study. *Appl. Surf. Sci.* 523, 146496. doi:10.1016/j.apsusc.2020.146496

Yang, X., Ding, Y., and Ni, J. (2008). *Ab initio*prediction of stable boron sheets and boron nanotubes: Structure, stability, and electronic properties. *Phys. Rev. B* 77 (4), 041402. doi:10.1103/physrevb.77.041402

Yang, X. F., Wang, A., Qiao, B., Li, J., Liu, J., and Zhang, T. (2013). Single-atom catalysts: A new frontier in heterogeneous catalysis. *Acc. Chem. Res.* 46 (8), 1740–1748. doi:10.1021/ar300361m

Zhang, C. J., and Hu, P. (2001). CO oxidation on Pd(100) and Pd(111): A comparative study of reaction pathways and reactivity at low and medium coverages. *J. Am. Chem. Soc.* 123 (6), 1166–1172. doi:10.1021/ja002432f

Zhang, P., Xu, X., Song, E., Hou, X., Yang, X., Mi, J., et al. (2020). Transition metal-doped α-borophene as potential oxygen and hydrogen evolution electrocatalyst: A density functional theory study. *Catal. Commun.* 144, 106090. doi:10.1016/j.catcom.2020.106090

Zhang, X., Lu, Z., Xu, G., Wang, T., Ma, D., Yang, Z., et al. (2015). Single Pt atom stabilized on nitrogen doped graphene: CO oxidation readily occurs via the tri-molecular eley–rideal mechanism. *Phys. Chem. Chem. Phys.* 17 (30), 20006–20013. doi:10.1039/c5cp01922b

Zhang, X., Lu, Z., and Yang, Z. (2016). Single non-noble-metal cobalt atom stabilized by pyridinic vacancy graphene: An efficient catalyst for CO oxidation. *J. Mol. Catal. A Chem.* 417, 28–35. doi:10.1016/j.molcata.2016.03.008

Zhu, H. R., Hu, Y. L., Wei, S. H., and Hua, D. Y. (2019). Single-metal atom anchored on boron monolayer (β_{12}) as an electrocatalyst for nitrogen reduction into ammonia at ambient conditions: A first-principles study. *J. Phys. Chem. C* 123 (7), 4274–4281. doi:10.1021/acs.jpcc.8b11696

frontiers | Frontiers in Chemistry

TYPE Original Research
PUBLISHED 19 October 2022
DOI 10.3389/fchem.2022.1048437

EDITED BY
Guangzhao Wang,
Yangtze Normal University, China

REVIEWED BY
Shuyuan Xiao,
Nanchang University, China
Kai Ren,
Nanjing Forestry University, China

*CORRESPONDENCE
Yong Tang,
20202127@huanghuai.edu.cn

SPECIALTY SECTION
This article was submitted to Theoretical and Computational Chemistry, a section of the journal Frontiers in Chemistry

RECEIVED 19 September 2022
ACCEPTED 29 September 2022
PUBLISHED 19 October 2022

CITATION
Liu M, Tang Y, Yao H, Bai L, Song J and Ma B (2022), Theoretical study on photocatalytic performance of ZnO/C_2N heterostructure towards high efficiency water splitting.
Front. Chem. 10:1048437.
doi: 10.3389/fchem.2022.1048437

Theoretical study on photocatalytic performance of ZnO/C_2N heterostructure towards high efficiency water splitting

Meiping Liu[1,2], Yong Tang[2,3]*, Haizi Yao[3], Liuyang Bai[3], Jun Song[3] and Benyuan Ma[3]

[1]Henan Key Laboratory of Smart Lighting, Huanghuai University, Zhumadian, Henan, China, [2]School of Materials Science and Engineering, Xiangtan University, Xiangtan, Hunan, China, [3]School of Energy Engineering, Huanghuai University, Zhumadian, Henan, China

The construction of van der Waals heterostructures offers effective boosting of the photocatalytic performance of two-dimensional materials. In this study, which uses the first-principles method, the electronic and absorptive properties of an emerging ZnO/C_2N heterostructure are systematically explored to determine the structure's photocatalytic potential. The results demonstrate that ZnO and C_2N form a type-II band alignment heterostructure with a reduced band gap, and hence superior absorption in the visible region. Furthermore, the band edge positions of a ZnO/C_2N heterostructure meet the requirements for spontaneous water splitting. The ZnO/C_2N heterostructure is known to possess considerably improved carrier mobility, which is advantageous in the separation and migration of carriers. The Gibbs free energy calculation confirms the high catalytic activity of the ZnO/C_2N heterostructure for water-splitting reactions. All the aforementioned properties, including band gap, band edge positions, and optical absorption, can be directly tuned using biaxial lateral strain. A suitable band gap, decent band edge positions, high catalytic activity, and superior carrier mobility thus identify a ZnO/C_2N heterostructure as a prominent potential photocatalyst for water splitting.

KEYWORDS
ZnO/C_2N heterostructure, first-principles method, type-II band alignment, water splitting, carrier mobility, strain

Introduction

The splitting of water into hydrogen (H_2) and oxygen (O_2) under the action of a photocatalyst has attracted extensive interest for its potential in tackling crises of energy and environmental pollution. Apart from the two basic requirements for band gap and band-edge positions, (Fujishima and Honda, 1972), excellent light absorption, low carrier recombination, and considerable carrier mobility are also necessary for a superior photocatalyst (Li et al., 2016). Extensive experimental and theoretical studies have been conducted to explore efficient novel photocatalysts.

In recent years, emerging two-dimensional (2D) materials have opened up a colorful stage for the design of new photocatalysts (Fan et al., 2021; Ren et al., 2022a; Qin et al., 2022). Notably, the naturally high surface area of 2D materials can provide more active sites for catalytic reactions (Ganguly et al., 2019). Furthermore, 2D materials shorten the migration distance of photogenerated carriers, thereby reducing the recombination of an electron–hole pair (Fan et al., 2021). A large number of 2D materials have been developed for photocatalysis, such as transition-metal dichalcogenide (Voiry et al., 2016), MXene (Cheng et al., 2019), carbonitrides (Wang et al., 2009), and others (Roger et al., 2017). In 2015, Mohammed et al. synthesized a new 2D multifunctional material C_2N with a band gap of 1.96eV (Mahmood et al., 2015). The C_2N monolayer possesses phonon modes close to those of graphenes (Sahin, 2015), indicating its fine thermal stability. Many facts confirm the highly tunable photocatalytic ability of monolayered C_2N for water splitting (Xu et al., 2015; Ashwin Kishore and Ravindran, 2017). However, the rapid recombination of photogenerated carriers is still a serious issue for the use of the C_2N monolayer in water splitting (Xu et al., 2015).

Some engineering processes have been proposed to improve the photocatalytic performance of monolayer C_2N for water splitting, including doping (Du et al., 2016), defects (Zhang et al., 2018), atomic adsorption (Kishore et al., 2019; Zhang et al., 2022), and strain (Guan et al., 2015). More recently, nascent van der Waals (vdW) heterostructures (Ye et al., 2019; Zhao et al., 2021; Wang et al., 2022) have also been widely considered as a means of promoting the photocatalytic water-splitting performance of the C_2N monolayer. The vdW heterostructure, composed of different 2D components, can maintain the excellent properties of those components, while some novel properties may be generated due to the interlayer coupling effects (Novoselov et al., 2016). Notably, the electron–hole pair, separated on the constituent monolayers, can substantially reduce the recombination rate of carriers, which is indeed favorable for photocatalytic water splitting (Deng et al., 2016; Novoselov et al., 2016). Kumar found that the carrier mobilities of the C_2N/WS_2 heterostructure with photocatalytic potential are efficiently enhanced (Kumar et al., 2018). Theoretical studies reveal that the $C_2N/GaTe$, $C_2N/InTe$, and $C_2N/InSe$ heterostructures are all suitable for photocatalysis, while their photocatalytic properties are sensitive to strain (Wang et al., 2019; Wang X. et al., 2020). The vdW heterostructures, such as the C_2N/Janus monochalcogenides (Ma et al., 2021), CdS/C_2N (Luo et al., 2017), and h-BN/C_2N (Wang G. et al., 2020), are also predicted to have excellent photocatalytic performance. Recently, the novel ZnO/C_2N heterostructure with a direct band gap of 2.0 eV has been reported, and its optoelectronic properties can be tuned with vertical strain and an external electric field (Song et al., 2021). Monolayered ZnO with its graphene-like structure is a 2D photocatalytic material with high carrier mobility. However, its large band gap (~3.3 eV) (Ren et al., 2020) leads to poor absorption, limiting its photocatalytic application. Perhaps the ZnO/C_2N heterostructure formed by two photocatalysts has more prominent carrier mobility and photocatalytic performance, but this remains unknown thus far.

In this work, theoretical work is conducted to comprehensively explore the electronic structure, carrier mobility, hydrogen evolution reaction (HER), and absorption properties of the ZnO/C_2N heterostructure, as well as the effect of lateral strain on these properties. All the results confirm the substantial application potential of a ZnO/C_2N heterostructure in photocatalysis for water splitting.

Computational methods

All calculations are implemented with the Vienna Ab-initio Simulation Package (VASP), based on the projected augmented wave method (PAW) (Kresse and Furthmüller, 1996a; Kresse and Furthmüller, 1996b). The generalized gradient approximation within the Perdew–Burke–Ernzerhof scheme (GGA-PBE) is used to describe the exchange-correlation functional (Perdew et al., 1996), while the DFT-D3 correction method (Grimme et al., 2010) is utilized to describe the vdW interaction between the two monolayers. The Heyd–Scuseria–Ernzerh hybrid functional (HSE06) (Heyd et al., 2003) is also adopted to determine the band gap of the ZnO/C_2N heterostructure and its pristine components. The lattice constants and atomic positions of pristine ZnO and C_2N monolayers are fully relaxed using the 6 × 6 × 1 and 15 × 15 × 1 *G*-centered Monkhorst–Pack (Monkhorst and Pack, 1976) *k*-mesh scheme to simplify the Brillouin zone, while a 3 × 3 × 1 *k*-mesh sampling is chosen for the ZnO/C_2N heterostructure. All ion relaxation processes interrupt the process until the force per atom is less than 0.01 eV/Å and the energy convergence criterion of 10^{-5} eV is set. The plane wave cutoff of 450 eV is used throughout this work, and a 20 Å vacuum toward the *z*-direction is applied to shield interaction between neighboring layers. VASPKIT and VESTA are used for visualization (Momma and Izumi, 2011; Wang et al., 2021).

Results and discussions

The geometric structures of ZnO and C_2N monolayers are shown in Supplementary Figures S1A–C. Their lattice parameters are found to be 3.29 Å and 8.32 Å, respectively, which is consistent with previous reports (Mahmood et al., 2015; Lee et al., 2016). Both monolayers are direct band gap semiconductors, as the band structures are presented in

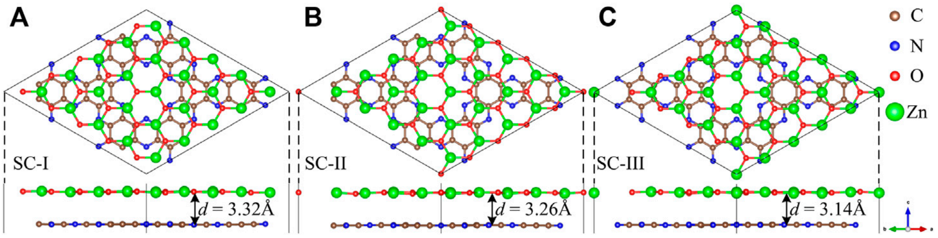

FIGURE 1
Optimized geometric structures of the **(A)** SC-I, **(B)** SC-II, **(C)** SC-III ZnO/C_2N heterostructure.

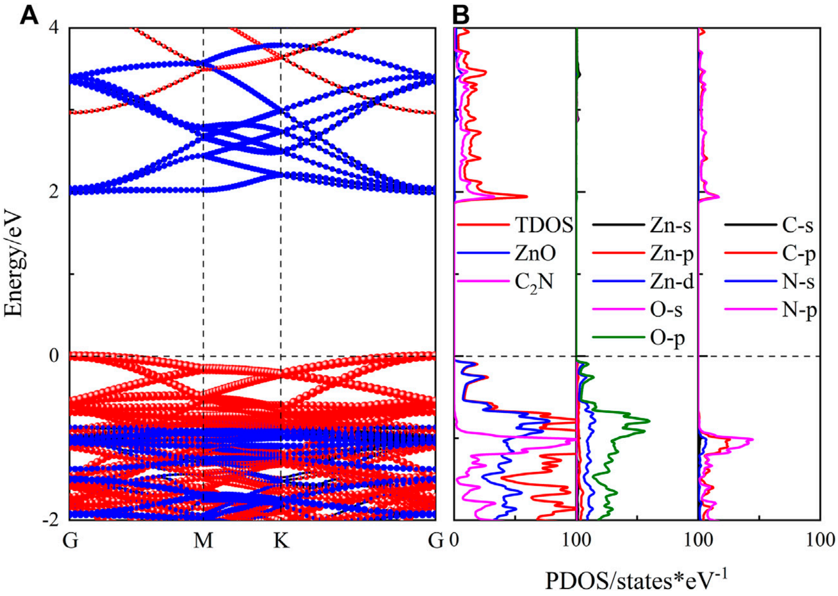

FIGURE 2
(A) Projected band structure and **(B)** PDOS of the ZnO/C_2N heterostructure.

Supplementary Figures S1B–D. The band gap values of ZnO and C_2N determined by HSE06 are 3.28 eV and 2.47 eV, which are close to the reported results (Mahmood et al., 2015; Lee et al., 2016).

In order to minimize the strain effect, a 5 × 5 ZnO supercell and a 2 × 2 C_2N supercell are used to make up the ZnO/C_2N heterostructure. The ZnO/C_2N heterostructure is constructed by fixing the C_2N layer and shifting the ZnO layer to a high symmetry location. According to the location of the ZnO layer in the lattice, three kinds of stacking configurations (SCs) for the ZnO/C_2N heterostructure are formed, as shown in Figure 1. In the interests of thermodynamic stability and for determining the most stable SC of the ZnO/C_2N heterostructure, the binding energy E_b and the formation energy E_f are calculated using the Supplementary Equations S1, S2. According to the results in Supplementary Table S1, E_f and E_b are close to those of typical vdW heterostructures (Guo et al., 2017; Fan et al., 2019; Bafekry et al., 2020; Guo et al., 2020). The negative values confirm that all ZnO/C_2N heterostructures can be prepared experimentally, as their stabilities are slightly different. The ZnO/C_2N heterostructure in SC-Ⅲ, with an interlayer distance *d* of 3.14 Å, is provided with the most beneficial stability. Therefore, the ZnO/C_2N heterostructure in SC-Ⅲ is the focus of the following research. Moreover, the *ab initio* molecular dynamic (AIMD) simulation is performed at 300 K to check the thermodynamic stability of the ZnO/C_2N heterostructure. As the snapshot for the last frame shows in Supplementary Figure S3A, the ZnO/C_2N heterostructure maintains good structural integrity within 6 ps, demonstrating its stability at room temperature. The time-dependent evolution of total potential

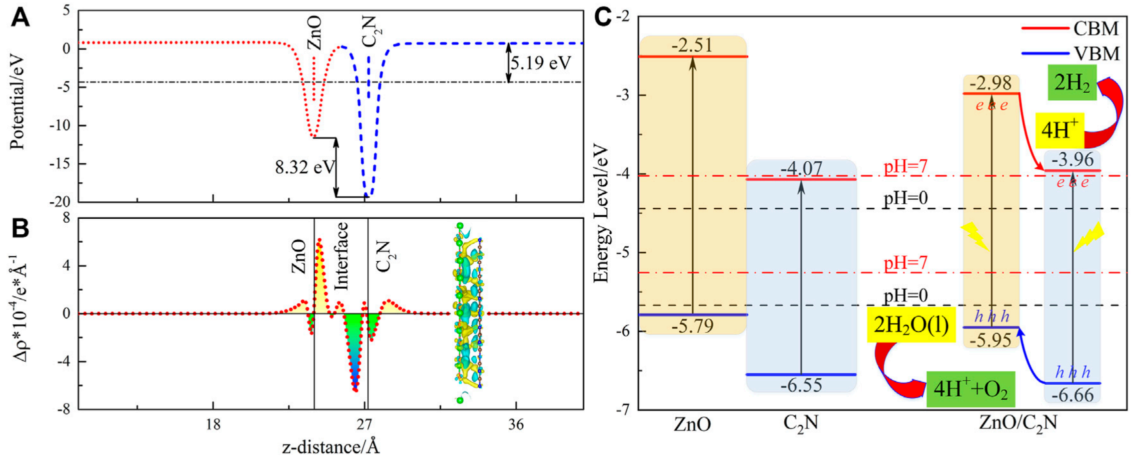

FIGURE 3
(A) Electrostatic potential, **(B)** planar-average and visual charge density difference $\Delta\rho$, and **(C)** band alignment for the ZnO/C_2N heterostructure.

energies, exhibited in Supplementary Figure S3B, also proves its thermal stability.

The band structures of the ZnO/C_2N heterostructure within the three SCs are calculated, together with the projected density of states (PDOS). As shown in Figure 2A, the ZnO/C_2N heterostructure is a direct band gap semiconductor, as both the VBM and CBM emerge at the *G*-point. Results of band structures also indicate that the SC has a negligible impact on electronic property. ZnO/C_2N heterostructures in three SCs possess the same band gap of 0.77 eV and 1.99 eV, based on the PBE functional and the HSE06 functional, respectively. The band gaps are smaller than those of pristine monolayers, meaning that forming a heterostructure can evidently reduce the band gap and widen the range of absorption. Moreover, both the Figures 2A,B demonstrate that a type-II heterostructure is formed when ZnO comes into contact with C_2N.

Figure 3 shows the electron transfer between two component layers. Work function (W_f) is a serious parameter defining the ability of a catalyst surface to attract electrons (Vayenas et al., 1990). The values of W_f for ZnO and C_2N are calculated as 4.82 eV and 5.78 eV, portending that electron flow from the ZnO layer to the C_2N layer at the interface. Electron migration from ZnO to C_2N is also observed from the planar-averaged charge density difference $\Delta\rho$ in Figure 3B, which ceases until the Fermi level is aligned, producing the positively charged ZnO layer and the negatively charged C_2N layer. The visual charge density difference is also exhibited in Figure 3B, in which the yellow and cyan marked areas represent electron accumulation and electron depletion, respectively. Therefore, a potential drop of 8.32 eV is formed in Figure 3A. Finally, a built-in electric field, pointing from ZnO to C_2N, is generated at the interface. The Bader charge calculation (Tang et al., 2009) also demonstrates the result of 0.203 electrons transferred from ZnO to C_2N. It is worth noting that the prominent potential drop in the ZnO/C_2N heterostructure can also offer a critical promotion for the separation of the photogenerated electron and hole, thereby reducing the recombination of carriers.

Suitable band edge positions (E_{VBM} and E_{CBM}) and decent band alignment are crucial for photocatalysis (Zheng et al., 2018; Tang et al., 2020). The method proposed by Toroker et al. (2011) has been employed to evaluate the E_{VBM} and E_{CBM} of the ZnO/C_2N heterostructure so as to explore its potential as a photocatalyst. It is obvious from Figure 3C that both the E_{VBM} and E_{CBM} of the two monolayers (Wang et al., 2018; Zhang X. et al., 2019) and the ZnO/C_2N heterostructure, meet the redox potential requirements for a photocatalyst in an acidic environment (pH = 0). The ZnO/C_2N heterostructure still has the talent of photocatalysis for water splitting in a neutral environment with pH = 7. Furthermore, a higher CBM and VBM of ZnO than those of C_2N can be observed. It is thus suggested that hydrogen evolution reaction (HER) occurs on the C_2N layer, while an oxygen evolution reaction (OER) happens on the ZnO layer. We then expand the type-II mechanism in the ZnO/C_2N heterostructure to boost HER and OER for water splitting. The conduction band offset (CBO) and valence band offset (VBO) are calculated as 0.98 eV and 0.69 eV, respectively. When the heterostructure is irradiated, the CBO promotes the transfer of photogenerated electrons in the CB of the ZnO layer to the CB of the C_2N layer. The photogenerated holes in the C_2N layer are driven by the VBO to the VB of the ZnO layer. Finally, the photogenerated electrons and holes remain in the C_2N and ZnO monolayers, respectively, bringing about carrier separation spatially. Naturally, the type-II band alignment of the ZnO/C_2N heterostructure is instrumental in overcoming the recombination of carriers to achieve better photocatalytic performance.

TABLE 1 Carrier mobilities of the ZnO/C_2N heterostructure and two monolayers.

Carrier	System	m^*_x (m_0)	m^*_y (m_0)	E_{1x} (eV)	E_{1y} (eV)	C_{2D_x} (N/m)	C_{2D_y} (N/m)	μ_x (cm^2/V/s)	μ_y (cm^2/V/s)
e	ZnO	0.21	0.25	5.91	5.38	51.76	51.65	477.8	406.1
	C_2N	0.46	0.42	1.59	2.58	160.45	160.57	4265.2	1944.5
	ZnO/C_2N	0.14	0.14	7.36	5.85	205.78	205.66	2756.0	4359.9
h	ZnO	0.58	0.49	5.42	5.15	51.76	51.65	74.5	115.3
	C_2N	10.64	6.05	3.41	3.29	160.45	160.57	1.7	5.7
	ZnO/C_2N	0.62	0.60	3.79	4.53	205.78	205.66	529.9	395.9

High carrier mobility μ is essential for superior photocatalysts (Guo et al., 2020; Ren et al., 2022b). The carrier mobility μ, defined as

$$\mu = \frac{2e\hbar^3 C_{2D}}{3k_B T m^{*2} E_1^2}, \tag{1}$$

has been evaluated based on the deformation potential theory (Bardeen and Shockley, 1950) for both the ZnO/C_2N heterostructure and the two monolayers. The methods and details are mentioned in Supplementary Section S1. As for the results of the ZnO monolayer listed in Table 1, the electron mobilities in the x- and y-directions are superior to those of the hole, conforming to previous theoretical (Ren et al., 2020) and experimental (Gonzalez-Valls and Lira-Cantu, 2009; Anta et al., 2012) results. It can be observed from Table 1 that the excellent electron mobilities of the C_2N monolayer are 4265 and 1944 cm^2/V/s in the x- and y-directions, mainly due to the small carrier effective mass (m^*) and deformation potential constant (E_1). However, the hole m^* of the C_2N monolayer is several times that of the electron, resulting in low hole mobility (Kumar et al., 2018; Zhang X. et al., 2019).

The hole m^*s of the ZnO/C_2N heterostructure in the x- and y-directions are close to those of the ZnO monolayer, while the values of E_1 in the aforementioned directions are comparable to those of the C_2N monolayer. The in-plane stiffness (C_{2D}) of the ZnO/C_2N heterostructure increases and is about equal to the sum of two component layers. Consequently, the hole mobilities of the heterostructure in the x- and y-directions are 529.9 and 395.9 cm^2/V/s, respectively, where pronounced improvements are due to the abovementioned changes of m^*, E_1, and C_{2D}. It can be deduced that higher carrier mobility will induce enhanced carrier separation and migration in the ZnO/C_2N heterostructure, which should illuminate its photocatalytic prospects for application in water splitting.

In order to explore the kinetic behavior of water splitting, the Gibbs free energy difference ΔG of HER and OER on the ZnO/C_2N heterostructure is calculated using the method developed by Nørskov et al. (2005). The calculation details and favor absorption sites are present in the Supplementary Material. The HER is divided into the following two reactions:

$$^* + H^+ + e^- \rightarrow H^*, \tag{2}$$

$$H^* + H^+ + e^- \rightarrow H_2 + ^*. \tag{3}$$

H^* is the only intermediate of HER, and it is obvious in Figure 4A that ΔG is a function of H coverage θ. When the θ equals 2/6, ΔG can be as low as 0.14 eV, which is comparable to the value of the C_2N/WS_2 heterostructure (Kumar et al., 2018). Therefore, the ZnO/C_2N heterostructure can be used as a potential photocatalyst for HER due to the small value of ΔG (Hinnemann et al., 2005).

The OER involves the following four steps:

$$^* + H_2O \rightarrow OH^* + H^+ + e^-, \tag{4}$$

$$OH^* \rightarrow O^* + H + +e^-, \tag{5}$$

$$O^* + H_2O \rightarrow OOH^* + H + +e^-, \tag{6}$$

$$OOH^* \rightarrow * + O_2 + H + +e^-. \tag{7}$$

Figure 4B shows the first step, with an overpotential of 2.19 V, is the limiting step when no external potential is applied. Under the action of 1.23 V external potential, the overpotential reduces to 0.96 V. As the value of the extra potential increases to 2.19 V, all the OER steps are downhill, suggesting that these reaction steps are exothermic.

The performance of absorption is an important function of a photocatalyst, as it is the first step in water splitting to produce electron–hole pairs. Superior absorption with a wide range and a high coefficient is essential for a photocatalyst's effective solar energy utilization. The optical coefficients $\alpha(\omega)$ of the ZnO/C_2N heterostructure and two components are calculated with the following equation (Gajdoš et al., 2006):

$$\alpha(\omega) = \sqrt{2}\omega\left[\sqrt{\varepsilon_1(\omega)^2 + \varepsilon_2(\omega)^2} - \varepsilon_1(\omega)\right]^{1/2}. \tag{8}$$

In this equation, ω_1 and ω_2 represent the real and imaginary parts of the dielectric function, respectively. The result, displayed in

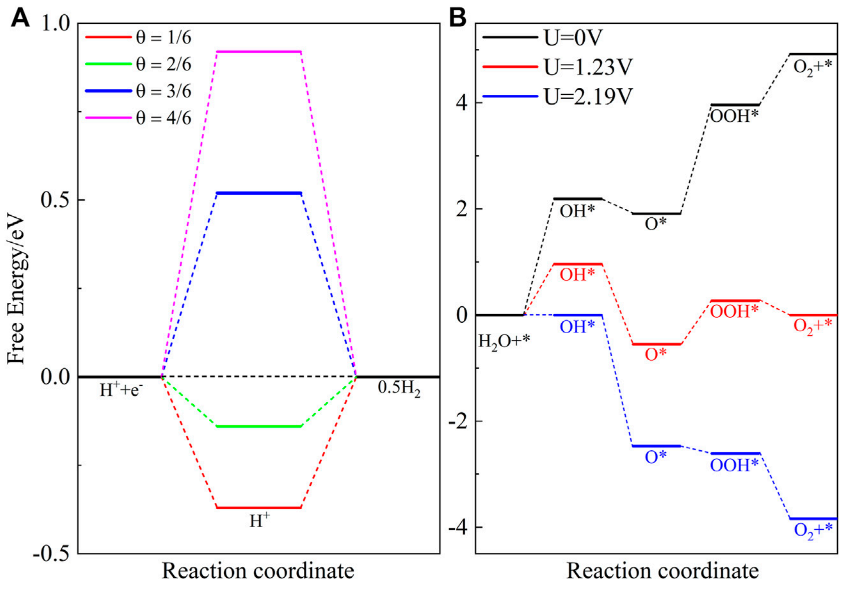

FIGURE 4
Free energy differences of **(A)** HER and **(B)** OER steps.

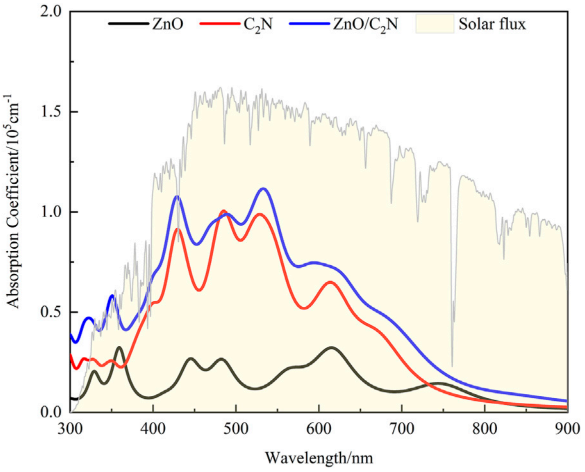

FIGURE 5
Absorption spectrum of the ZnO/C_2N heterostructure compared with ZnO and C_2N.

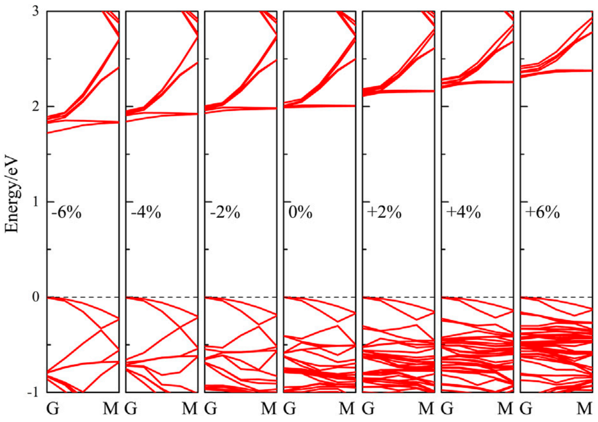

FIGURE 6
Calculated band structures of strained ZnO/C_2N heterostructures.

Figure 5, demonstrates the advantage of the heterostructure in absorption over ZnO and C_2N. The heterostructure not only possesses a higher absorption coefficient (~$10^5 cm^{-1}$) than ZnO and C_2N but also has a wider absorption range from visible to ultraviolet light. The improvement in absorption performance can be attributed to its reduced band gap and significantly improved carrier mobility. The excellent absorption ability can generate more electron–hole pairs in the first step of water splitting, which is beneficial for the ZnO/C_2N heterostructure in realizing its efficient photocatalytic performance.

The lateral strain is a common effect in heterostructures, as well as being a proven effective means of improving the photocatalytic performance of 2D material (Feng et al., 2012; Zhang J.-R. et al., 2019). We thus undertook a full investigation of the electronic and optical properties of the ZnO/C_2N heterostructure with biaxial lateral strain to explore the

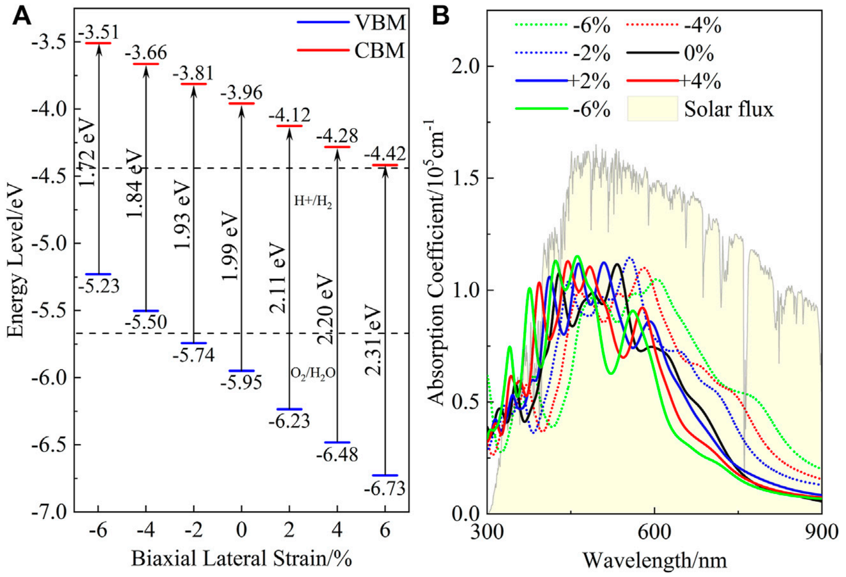

FIGURE 7
(A) Band alignment and **(B)** absorption spectrum of ZnO/C_2N heterostructure under different strain conditions.

regulatory effect of strain on photocatalytic performance. Strain ranging from −6% to +6% was applied to the ZnO/C_2N heterostructure, and the band structures calculated with the HSE06 functional in Figure 6 clearly announce the structure's identity as a direct band gap semiconductor.

Meanwhile, it can be seen from the PDOS exhibited in Supplementary Figure S13 that the strained heterostructures also belong to type-II heterostructures, as both the VBM and CBM of the ZnO are higher than those of C_2N. Moreover, it is clear in Figure 7A that compressive strain reduces the band gap, while tensile strain increases the gap. When the lattice is compressed by 6%, the band gap decreases to 1.72 eV, while the gap value increases to 2.31 eV when the heterostructure it is expanded by 6%. Within the strain range of −2% to +6%, we can also see that the band edge positions of the heterostructure still meet the requirements of photocatalysis for water splitting at the condition of pH = 0. It is very important for heterostructures to maintain their photocatalytic ability across a wide pH range (Ren et al., 2019). The band alignment shown in Supplementary Figure S15 indicates that the strained heterostructures still possess potential application for water splitting across a wide pH range. Figure 7B shows the effect of the strain on the absorption performance of the ZnO/C_2N heterostructure. Compared with the freestanding ZnO/C_2N heterostructure, the compressed heterostructures have higher absorption intensity and a wider absorption range, while the lattice expansion leads to improvement in the absorption performance of the heterostructures in the ultraviolet range. The significant modification of absorption is mainly a benefit of the regulation of the band gap. All the results directly confirm that the ZnO/C_2N heterostructure is a promising candidate for use in the field of water splitting.

Conclusion

In this study, the electronic and absorption properties of the ZnO/C_2N heterostructure are explored to reveal its potential for water splitting. The stabilized heterostructure is given a reduced band gap of 1.99 eV, while its band edge positions also meet the water-splitting requirements. The band alignment of the heterostructure belongs to type-II, which leads to the generation of a built-in electrical field between the two layers that promote carrier separation and migration. The more significant change is that the carrier mobility of the ZnO/C_2N heterostructure is several times improved. The results of the Gibbs free energy calculation clearly indicate the promising catalytic ability of the ZnO/C_2N heterostructure. As for the optical absorption performance, the reduced band gap and excellent carrier mobility endow the ZnO/C_2N heterostructure with considerable absorption intensity and a wider absorption range. Moreover, the electronic and absorption properties of the ZnO/C_2N heterostructure can be substantially tuned with biaxial lateral strain. All the results confirm that the ZnO/C_2N heterostructure has potential use as a superior photocatalyst for water splitting.

Data availability statement

The original contributions presented in the study are included in the article/Supplementary Material, and further inquiries can be directed to the corresponding author.

Author contributions

All authors listed have made a substantial, direct, and intellectual contribution to the work and approved it for publication.

Funding

This work was financially supported by the National Natural Science Foundation of China (Grant No. 11875284), the Program for Science and Technology Innovation Talents in Universities of Henan Province (No. 21HASTIT020), and the Key Scientific Research Project of Colleges and Universities in Henan Province (No. 22A140023).

Conflict of interest

The authors declare that the research was conducted in the absence of any commercial or financial relationships that could be construed as a potential conflict of interest.

Publisher's note

Supplementary material

The Supplementary Material for this article can be found online at: https://www.frontiersin.org/articles/10.3389/fchem.2022.1048437/full#supplementary-material

References

Anta, J., Guillén, E., and Tena-Zaera, R. (2012). ZnO-based dye-sensitized solar cells. *J. Phys. Chem. C* 116 (21), 11413–11425. doi:10.1021/jp3010025

Ashwin Kishore, M., and Ravindran, P. (2017). Tailoring the electronic band gap and band edge positions in the C_2N monolayer by P and as substitution for photocatalytic water splitting. *J. Phys. Chem. C* 121 (40), 22216–22224. doi:10.1021/acs.jpcc.7b07776

Bafekry, A., Akgenc, B., Shayesteh, S., and Mortazavi, B. (2020). Tunable electronic and magnetic properties of graphene/carbon-nitride van der Waals heterostructures. *Appl. Surf. Sci.* 505, 144450. doi:10.1016/j.apsusc.2019.144450

Bardeen, J., and Shockley, W. (1950). Deformation potentials and mobilities in non-polar crystals. *Phys. Rev.* 80 (1), 72. doi:10.1103/PhysRev.80.72

Cheng, L., Li, X., Zhang, H., and Xiang, Q. (2019). Two-dimensional transition metal MXene-based photocatalysts for solar fuel generation. *J. Phys. Chem. Lett.* 10 (12), 3488–3494. doi:10.1021/acs.jpclett.9b00736

Deng, D., Novoselov, K., Fu, Q., Zheng, N., Tian, Z., and Bao, X. (2016). Catalysis with two-dimensional materials and their heterostructures. *Nat. Nanotechnol.* 11 (3), 218–230. doi:10.1038/nnano.2015.340

Du, J., Xia, C., Wang, T., Xiong, W., and Li, J. (2016). Modulation of the band structures and optical properties of holey C_2N nanosheets by alloying with group IV and V elements. *J. Mat. Chem. C* 4 (39), 9294–9302. doi:10.1039/C6TC02469F

Fan, F., Wang, R., Zhang, H., and Wu, W. (2021). Emerging beyond-graphene elemental 2D materials for energy and catalysis applications. *Chem. Soc. Rev.* 50 (19), 10983–11031. doi:10.1039/C9CS00821G

Fan, Y., Wang, J., and Zhao, M. (2019). Spontaneous full photocatalytic water splitting on 2D $MoSe_2/SnSe_2$ and $WSe_2/SnSe_2$ vdW heterostructures. *Nanoscale* 11 (31), 14836–14843. doi:10.1039/C9NR03469B

Feng, J., Qian, X., Huang, C., and Li, J. (2012). Strain-engineered artificial atom as a broad-spectrum solar energy funnel. *Nat. Photonics* 6 (12), 866–872. doi:10.1038/nphoton.2012.285

Fujishima, A., and Honda, K. (1972). Electrochemical photolysis of water at a semiconductor electrode. *Nature* 238 (5358), 37–38. doi:10.1038/238037a0

Gajdoš, M., Hummer, K., Kresse, G., Furthmüller, J., and Bechstedt, F. (2006). Linear optical properties in the projector-augmented wave methodology. *Phys. Rev. B* 73 (4), 045112. doi:10.1103/PhysRevB.73.045112

Ganguly, P., Harb, M., Cao, Z., Cavallo, L., Breen, A., Dervin, S., et al. (2019). 2D nanomaterials for photocatalytic hydrogen production. *ACS Energy Lett.* 4 (7), 1687–1709. doi:10.1021/acsenergylett.9b00940

Gonzalez-Valls, I., and Lira-Cantu, M. (2009). Vertically-aligned nanostructures of ZnO for excitonic solar cells: A review. *Energy Environ. Sci.* 2 (1), 19–34. doi:10.1039/B811536B

Grimme, S., Antony, J., Ehrlich, S., and Krieg, H. (2010). A consistent and accurate *ab initio* parametrization of density functional dispersion correction (DFT-D) for the 94 elements H-Pu. *J. Chem. Phys.* 132 (15), 154104. doi:10.1063/1.3382344

Guan, S., Cheng, Y., Liu, C., Han, J., Lu, Y., Yang, S., et al. (2015). Effects of strain on electronic and optic properties of holey two-dimensional C_2N crystals. *Appl. Phys. Lett.* 107 (23), 231904. doi:10.1063/1.4937269

Guo, H., Zhang, Z., Huang, B., Wang, X., Niu, H., Guo, Y., et al. (2020). Theoretical study on the photocatalytic properties of 2D InX (X= S, Se)/transition metal disulfide (MoS_2 and WS_2) van der Waals heterostructures. *Nanoscale* 12 (38), 20025–20032. doi:10.1039/D0NR04725B

Guo, Z., Miao, N., Zhou, J., Sa, B., and Sun, Z. (2017). Strain-mediated type-I/type-II transition in MXene/Blue phosphorene van der Waals heterostructures for flexible optical/electronic devices. *J. Mat. Chem. C* 5 (4), 978–984. doi:10.1039/C6TC04349F

Heyd, J., Scuseria, G., and Ernzerhof, M. (2003). Hybrid functionals based on a screened Coulomb potential. *J. Chem. Phys.* 118 (18), 8207–8215. doi:10.1063/1.1564060

Hinnemann, B., Moses, P., Bonde, J., Jørgensen, K., Nielsen, J., Horch, S., et al. (2005). Biomimetic hydrogen evolution: MoS_2 nanoparticles as catalyst for hydrogen evolution. *J. Am. Chem. Soc.* 127 (15), 5308–5309. doi:10.1021/ja0504690

Kishore, M., Sjastad, A., and Ravindran, P. (2019). Influence of hydrogen and halogen adsorption on the photocatalytic water splitting activity of C_2N monolayer: A first-principles study. *Carbon* 141, 50–58. doi:10.1016/j.carbon.2018.08.072

Kresse, G., and Furthmüller, J. (1996a). Efficiency of *ab-initio* total energy calculations for metals and semiconductors using a plane-wave basis set. *Comput. Mat. Sci.* 6 (1), 15–50. doi:10.1016/0927-0256(96)00008-0

Kresse, G., and Furthmüller, J. (1996b). Efficient iterative schemes for *ab initio* total-energy calculations using a plane-wave basis set. *Phys. Rev. B* 54 (16), 11169–11186. doi:10.1103/PhysRevB.54.11169

Kumar, R., Das, D., and Singh, A. (2018). C_2N/WS_2 van der Waals type-II heterostructure as a promising water splitting photocatalyst. *J. Catal.* 359, 143–150. doi:10.1016/j.jcat.2018.01.005

Lee, J., Sorescu, D., and Deng, X. (2016). Tunable lattice constant and band gap of single-and few-layer ZnO. *J. Phys. Chem. Lett.* 7 (7), 1335–1340. doi:10.1021/acs.jpclett.6b00432

Li, X., Yu, J., and Jaroniec, M. (2016). Hierarchical photocatalysts. *Chem. Soc. Rev.* 45 (9), 2603–2636. doi:10.1039/C5CS00838G

Luo, X., Wang, G., Huang, Y., Wang, B., Yuan, H., and Chen, H. (2017). A two-dimensional layered CdS/C_2N heterostructure for visible-light-driven photocatalysis. *Phys. Chem. Chem. Phys.* 19 (41), 28216–28224. doi:10.1039/C7CP04108J

Ma, Z., Wang, S., Li, C., and Wang, F. (2021). Strain engineering for C_2N/Janus monochalcogenides van der Waals heterostructures: Potential applications for photocatalytic water splitting. *Appl. Surf. Sci.* 536, 147845. doi:10.1016/j.apsusc.2020.147845

Mahmood, J., Lee, E., Jung, M., Shin, D., Jeon, I., Jung, S., et al. (2015). Nitrogenated holey two-dimensional structures. *Nat. Commun.* 6 (1), 6486–6487. doi:10.1038/ncomms7486

Momma, K., and Izumi, F. (2011). VESTA3 for three-dimensional visualization of crystal, volumetric and morphology data. *J. Appl. Crystallogr.* 44 (6), 1272–1276. doi:10.1107/S0021889811038970

Monkhorst, H., and Pack, J. (1976). Special points for Brillouin-zone integrations. *Phys. Rev. B* 13 (12), 5188–5192. doi:10.1103/PhysRevB.13.5188

Nørskov, J., Bligaard, T., Logadottir, A., Kitchin, J., Chen, J., Pandelov, S., et al. (2005). Trends in the exchange current for hydrogen evolution. *J. Electrochem. Soc.* 152 (3), J23. doi:10.1149/1.1856988

Novoselov, K., Mishchenko, A., Carvalho, A., and Castro Neto, A. (2016). 2D materials and van der Waals heterostructures. *Science* 353 (6298), aac9439. doi:10.1126/science.aac9439

Perdew, J., Burke, K., and Ernzerhof, M. (1996). Generalized gradient approximation made simple. *Phys. Rev. Lett.* 77 (18), 3865–3868. doi:10.1103/PhysRevLett.77.3865

Qin, H., Ren, K., Zhang, G., Dai, Y., and Zhang, G. (2022). Lattice thermal conductivity of Janus MoSSe and WSSe monolayers. *Phys. Chem. Chem. Phys.* 24 (34), 20437–20444. doi:10.1039/D2CP01692C

Ren, K., Chen, Y., Qin, H., Feng, W., and Zhang, G. (2022a). Graphene/biphenylene heterostructure: Interfacial thermal conduction and thermal rectification. *Appl. Phys. Lett.* 121 (8), 082203. doi:10.1063/5.0100391

Ren, K., Ren, C., Luo, Y., Xu, Y., Yu, J., Tang, W., et al. (2019). Using van der Waals heterostructures based on two-dimensional blue phosphorus and XC (X= Ge, Si) for water-splitting photocatalysis: A first-principles study. *Phys. Chem. Chem. Phys.* 21 (19), 9949–9956. doi:10.1039/C8CP07680D

Ren, K., Yan, Y., Zhang, Z., Sun, M., and Schwingenschlögl, U. (2022b). A family of Li_xB_y monolayers with a wide spectrum of potential applications. *Appl. Surf. Sci.* 604, 154317. doi:10.1016/j.apsusc.2022.154317

Ren, K., Yu, J., and Tang, W. (2020). Two-dimensional ZnO/BSe van der waals heterostructure used as a promising photocatalyst for water splitting: A dft study. *J. Alloys Compd.* 812, 152049. doi:10.1016/j.jallcom.2019.152049

Roger, I., Shipman, M., and Symes, M. (2017). Earth-abundant catalysts for electrochemical and photoelectrochemical water splitting. *Nat. Rev. Chem.* 1 (1), 0003–0013. doi:10.1038/s41570-016-0003

Sahin, H. (2015). Structural and phononic characteristics of nitrogenated holey graphene. *Phys. Rev. B* 92 (8), 085421. doi:10.1103/PhysRevB.92.085421

Song, J., Zheng, H., Liu, M., Zhang, G., Ling, D., and Wei, D. (2021). A first-principles study on the electronic and optical properties of a type-II C_2N/g-ZnO van der Waals heterostructure. *Phys. Chem. Chem. Phys.* 23 (6), 3963–3973. doi:10.1039/D1CP00122A

Tang, W., Sanville, E., and Henkelman, G. (2009). A grid-based Bader analysis algorithm without lattice bias. *J. Phys. Condens. Matter* 21 (8), 084204. doi:10.1088/0953-8984/21/8/084204

Tang, Y., Liu, M., Zhou, Y., Ren, C., Zhong, X., and Wang, J. (2020). First-principles predication of facet-dependent electronic and optical properties in InSe/GaAs heterostructure with potential in solar energy utilization. *J. Alloys Compd.* 842, 155901. doi:10.1016/j.jallcom.2020.155901

Toroker, M., Kanan, D., Alidoust, N., Isseroff, L., Liao, P., and Carter, E. (2011). First principles scheme to evaluate band edge positions in potential transition metal oxide photocatalysts and photoelectrodes. *Phys. Chem. Chem. Phys.* 13 (37), 16644–16654. doi:10.1039/C1CP22128K

Vayenas, C., Bebelis, S., and Ladas, S. (1990). Dependence of catalytic rates on catalyst work function. *Nature* 343 (6259), 625–627. doi:10.1038/343625a0

Voiry, D., Yang, J., and Chhowalla, M. (2016). Recent strategies for improving the catalytic activity of 2D TMD nanosheets toward the hydrogen evolution reaction. *Adv. Mat.* 28 (29), 6197–6206. doi:10.1002/adma.201505597

Wang, B., Yuan, H., Chang, J., Chen, X., and Chen, H. (2019). Two dimensional $InSe/C_2N$ van der Waals heterojunction as enhanced visible-light-responsible photocatalyst for water splitting. *Appl. Surf. Sci.* 485, 375–380. doi:10.1016/j.apsusc.2019.03.344

Wang, G., Chang, J., Tang, W., Xie, W., and Ang, Y. S. (2022). 2D materials and heterostructures for photocatalytic water-splitting: A theoretical perspective. *J. Phys. D. Appl. Phys.* 55 (29), 293002. doi:10.1088/1361-6463/ac5771

Wang, G., Li, Z., Wu, W., Guo, H., Chen, C., Yuan, H., et al. (2020a). A two-dimensional h-BN/C_2N heterostructure as a promising metal-free photocatalyst for overall water-splitting. *Phys. Chem. Chem. Phys.* 22 (42), 24446–24454. doi:10.1039/D0CP03925J

Wang, S., Ren, C., Tian, H., Yu, J., and Sun, M. (2018). MoS_2/ZnO van der Waals heterostructure as a high-efficiency water splitting photocatalyst: A first-principles study. *Phys. Chem. Chem. Phys.* 20 (19), 13394–13399. doi:10.1039/C8CP00808F

Wang, V., Xu, N., Liu, J., Tang, G., and Geng, W. (2021). Vaspkit: A user-friendly interface facilitating high-throughput computing and analysis using VASP code. *Comput. Phys. Commun.* 267, 108033. doi:10.1016/j.cpc.2021.108033

Wang, X., Maeda, K., Thomas, A., Takanabe, K., Xin, G., Carlsson, J., et al. (2009). A metal-free polymeric photocatalyst for hydrogen production from water under visible light. *Nat. Mat.* 8 (1), 76–80. doi:10.1038/nmat2317

Wang, X., Wang, Y., Quhe, R., Tang, Y., Dai, X., and Tang, W. (2020b). Designing strained C_2N/GaTe (InTe) heterostructures for photovoltaic and photocatalytic application. *J. Alloys Compd.* 816, 152559. doi:10.1016/j.jallcom.2019.152559

Xu, B., Xiang, H., Wei, Q., Liu, J., Xia, Y., Yin, J., et al. (2015). Two-dimensional graphene-like C_2N: An experimentally available porous membrane for hydrogen purification. *Phys. Chem. Chem. Phys.* 17 (23), 15115–15118. doi:10.1039/C5CP01789K

Ye, K., Li, H., Huang, D., Xiao, S., Qiu, W., Li, M., et al. (2019). Enhancing photoelectrochemical water splitting by combining work function tuning and heterojunction engineering. *Nat. Commun.* 10 (1), 3687–3689. doi:10.1038/s41467-019-11586-y

Zhang, H., Zhang, X., Yang, G., and Zhou, X. (2018). Point defect effects on photoelectronic properties of the potential metal-free C_2N photocatalysts: Insight from first-principles computations. *J. Phys. Chem. C* 122 (10), 5291–5302. doi:10.1021/acs.jpcc.7b12428

Zhang, J.-R., Deng, X., Gao, B., Chen, L., Au, C., Li, K., et al. (2019a). Theoretical study on the intrinsic properties of In_2Se_3/MoS_2 as a photocatalyst driven by near-infrared, visible and ultraviolet light. *Catal. Sci. Technol.* 9 (17), 4659–4667. doi:10.1039/C9CY00997C

Zhang, J., Zhang, C., Ren, K., Lin, X., and Cui, Z. (2022). Tunable electronic and magnetic properties of $Cr_2Ge_2Te_6$ monolayer by organic molecular adsorption. *Nanotechnology* 33 (34), 345705. doi:10.1088/1361-6528/ac715d

Zhang, X., Chen, A., Zhang, Z., Jiao, M., and Zhou, Z. (2019b). Rational design of C_2N-based type-II heterojunctions for overall photocatalytic water splitting. *Nanoscale Adv.* 1 (1), 154–161. doi:10.1039/C8NA00084K

Zhao, D., Wang, Y., Dong, C., Huang, Y., Chen, J., Xue, F., et al. (2021). Boron-doped nitrogen-deficient carbon nitride-based Z-scheme heterostructures for photocatalytic overall water splitting. *Nat. Energy* 6 (4), 388–397. doi:10.1038/s41560-021-00795-9

Zheng, B., Ma, C., Li, D., Lan, J., Zhang, Z., Sun, X., et al. (2018). Band alignment engineering in two-dimensional lateral heterostructures. *J. Am. Chem. Soc.* 140 (36), 11193–11197. doi:10.1021/jacs.8b07401

frontiers | Frontiers in Chemistry

TYPE Mini Review
PUBLISHED 25 October 2022
DOI 10.3389/fchem.2022.1048504

Graphitic carbon nitride ($g-C_3N_4$)-based photocatalytic materials for hydrogen evolution

Rui-Han Gao[1,2], Qingmei Ge[1], Nan Jiang[1], Hang Cong[1]*, Mao Liu[1] and Yun-Qian Zhang[1,2]*

[1]Enterprise Technology Center of Guizhou Province, Guizhou University, Guiyang, China, [2]Key Laboratory of Macrocyclic and Supramolecular Chemistry of Guizhou Province, Guizhou University, Guiyang, China

OPEN ACCESS

EDITED BY
Kezhen Qi,
Shenyang Normal University, China

REVIEWED BY
Xin Ying Kong,
Nanyang Technological University, Singapore
Feng Guo,
Jiangsu University of Science and Technology, China

*CORRESPONDENCE
Hang Cong,
ecnuc@163.com
Yun-Qian Zhang,
sci.yqzhang@gzu.edu.cn

SPECIALTY SECTION
This article was submitted to Photocatalysis and Photochemistry, a section of the journal Frontiers in Chemistry

RECEIVED 19 September 2022
ACCEPTED 14 October 2022
PUBLISHED 25 October 2022

CITATION
Gao R-H, Ge Q, Jiang N, Cong H, Liu M and Zhang Y-Q (2022), Graphitic carbon nitride ($g-C_3N_4$)-based photocatalytic materials for hydrogen evolution.
Front. Chem. 10:1048504.
doi: 10.3389/fchem.2022.1048504

The semiconductors, such as TiO_2, CdS, ZnO, $BiVO_4$, graphene, produce good applications in photocatalytic water splitting for hydrogen production, and great progress have been made in the synthesis and modification of the materials. As a two-dimensional layered structure material, graphitic carbon nitride ($g-C_3N_4$), with the unique properties of high thermostability and chemical inertness, excellent semiconductive ability, affords good potential in photocatalytic hydrogen evolution. However, the related low efficiency of $g-C_3N_4$ with fast recombination rate of photogenerated charge carriers, limited visible-light absorption, and low surface area of prepared bulk $g-C_3N_4$, has called out the challenge issues to synthesize and modify novel $g-C_3N_4$-block photocatalyst. In this review, we have summarized several strategies to improve the photocatalytic performance of pristine $g-C_3N_4$ such as pH, morphology control, doping with metal or non-metal elements, metal deposition, constructing a heterojunction or homojunction, dye-sensitization, and so forth. The performances for photocatalytic hydrogen evolution and possible development of $g-C_3N_4$ materials are shared with the researchers interested in the relevant fields hereinto.

KEYWORDS

g-C3N4, photocatalysis, hydrogen evolution, energy materials, semiconductor

1 Introduction

With the development and progress of human society, environmental pollution and energy shortage have become two major problems that plague human beings. Hydrogen is considered as one of the best candidates for storing solar energy meeting the growing clean energy demand (Chen et al., 2016; Shen et al., 2016; Wang et al., 2016; Wu et al., 2017; Wang et al., 2018; Liu et al., 2019). Since Fujishima and Honda discovered the hydrogen evolution reaction activates by TiO_2 under irradiation in 1972, photocatalytic water splitting is one of the promising means for hydrogen production (Fujishima and Honda., 1972). Without relying on fossil reserves, the photocatalytic hydrogen evolution from water with highly efficient utilization of solar irradiation is a desirable exploration for the solution of the energy issues (Maeda et al., 2006; Qi et al., 2022). Although great process in photocatalysts of water splitting have been made for H_2 evolution under visible light, there are still challenging and concerns with semiconductors to promise hydrogen energy development methods (Zhong et al., 2015; Wang et al., 2016; Zhang et al., 2018; Qi et al., 2020).

Graphitic carbon nitride (g-C_3N_4) is considered as an ideal 2D material with the conjugated skeleton for photocatalytic water splitting with the activity of photoelectronic chemistry and high stability in the photochemical reaction (Ong et al., 2016). Compounds in rich carbon and nitrogen elements such as melamine, urea, cyanamide, dicyandiamide, cyanuric acid, etc. are usually subjected as the precursors. Graphitic carbon nitride materials were synthesized by methods including electrochemical deposition, thermal shrinkage polymerization, solid phase synthesis, gas phase synthesis, solvothermal synthesis and electrochemical deposition (Thomas et al., 2008). Under light irradiation, electron-hole pairs were generated on the surface of g-C_3N_4 photocatalyst to provide the reaction sites. The water molecules adsorbed on the surface of g-C_3N_4 undergo the photocatalytic reduction for H_2 evolution and oxidation for O_2 release, respectively, with the efficacious charge carriers by the reactions (1–3):

Oxidation:

$$H_2O + 2h^+ \rightarrow 2H^+ + 1/2O_2 \tag{1}$$

Reduction:

$$2H^+ + 2e \rightarrow H_2 \tag{2}$$

Overall reaction:

$$H_2O \rightarrow H_2 + 1/2O_2 \tag{3}$$

The first case of g-C_3N_4 as a polymeric photocatalyst for water splitting to produce H_2 under visible-light irradiation was reported by Wang et al. (Wang et al., 2009) Figure 1 schematically described the photogeneration of H_2 and O_2 in water splitting reaction with the pristine g-C_3N_4. The obtained bulk form of g-C_3N_4 exhibited some drawbacks including limited visible light utilization efficiency, fast recombination rate of photogenerated electron-hole pairs, and low specific surface areas (<10 m^2g^{-1}), which still limited the photocatalytic performance of on its practical applications (Reza et al., 2015; Fu et al., 2018), and modification of g-C_3N_4 has been recognized to be the effective way to improve the photocatalytic performance of pristine g-C_3N_4.

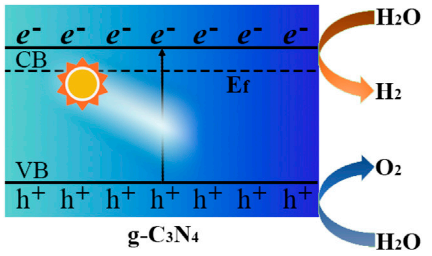

FIGURE 1
Schematic of generation of H_2 and O_2 from water with the catalysis of pristine g-C_3N_4 under light irradiation.

2 Modification of graphitic carbon nitride materials

Recently, the application of g-C_3N_4 with improved photocatalytic performance by developed several strategies, involving adjusting pH value, morphology control, doping by heteroatoms or metals, participation of co-catalyst, dye-sensitization, and construction of heterojunction. The hydrogen evolution performance of the modified g-C_3N_4-based materials are summarized in Table 1 to provide the development of the co-catalysts in the photolysis system.

2.1 pH

The pH value of solution was an important factor affecting the activity of g-C_3N_4, that is, Zeta potential values suggested the surface charge of g-C_3N_4 could be changes at different pH value for the diversity of functional groups on the surface (Wang et al., 2016). Wu et al. demonstrated that the alkaline environment was beneficial to the photocatalytic hydrogen evolution efficiency of g-C_3N_4 material as shown in Figure 2A (Wu et al., 2014). The experimental results show that pH and methanol have certain effects on the photocurrent amplification on g-C_3N_4 films. In the presence of methanol, the photoelectronic efficiency was improved to provide an increased photocurrent from 0.6 to 1.2 μA cm^{-2}, which was further enhanced to offer a 4.2 μA cm^{-2} current upon adding base to bring the pH to 12.8. The results implied the transfer of photogenerated holes into solution was enhanced by the addition of methanol and alkali, which could root in the additive-induced decrease of the energy gap of the flat band and band-edge of g-C_3N_4 as description in Figure 2B, that is, methanol oxidation occurred in alkaline solution, but restrained in acidic condition with the amine-terminated g-C_3N_4 surface.

2.2 Morphology control

The activity of g-C_3N_4 for H_2 production *via* water splitting under visible-light irradiation could be determined by morphology of the material surface (Niu et al., 2012; Zhang et al., 2012; Han et al., 2015). The targets of controllable morphologies in preparation of well-defined g-C_3N_4 nanostructures to get larger specific surface area and more

TABLE 1 Hydrogen evolution performance of the modified g-C_3N_4-based materials.

Methods	Co-catalysts	Hydrogen evolution rate (μmol $h^{-1}g^{-1}$)	Ref.
0D	Quantum dots	2,199.2	Wang et al. (2014)
1D	Nanotubes	11,850	Mo et al. (2018)
2D	Nanosheets	3,140	Zhao et al. (2018)
3D	Nanovesicles	10,300	Sun et al. (2022a)
Non-metal doping	P dopant	1,596	Ran et al. (2015)
Metal doping	Co dopant	560	Chen et al. (2017)
Metal deposition	Pt co-catalyst	947.64	Zhu et al. (2019)
Dye sensitization	Protoporphyrin	1,153.8	Liu et al. (2020)
Heterogeneous	CeO_2	1,240.9	Zhao et al. (2021)
Homojunction	High-crystalline g-C_3N_4	5,534	Sun et al. (2022b)

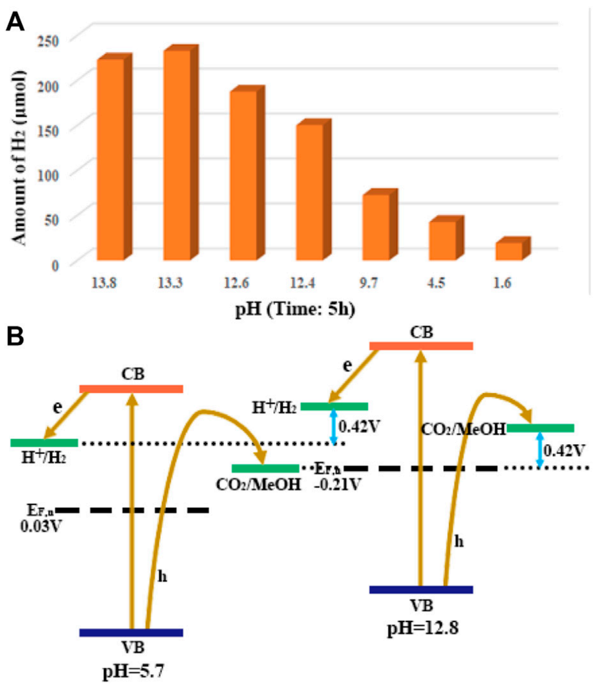

FIGURE 2
(A) the relationship of pH values to the efficiencies of H_2 evolution with g-C_3N_4 photolysis; **(B)** energy diagrams of g-C_3N_4 in solution at pH 5.7 and 12.8.

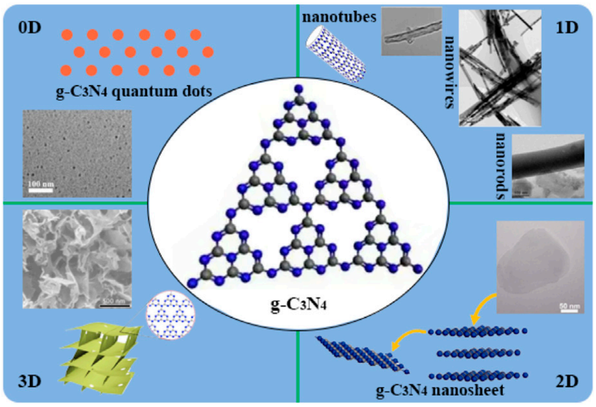

FIGURE 3
Schematic illustration of 0D, 1D, 2D and 3D g-C_3N_4.

abundant reactive sites, reduced the recombination rate of photogenerated charge carriers. There were different nanostructures of g-C_3N_4 have been described in pioneering reports involving zero-dimensional (Wang et al., 2014) (0D), one-dimensional (Bai et al., 2013; Zhang et al., 2013; Wang et al., 2015; Mo et al., 2018; Bashir et al., 2019; Zhang et al., 2020) (1D), two-dimensional (Li et al., 2015; Zhao et al., 2018; Qi et al., 2019; Shi et al., 2022) (2D), three-dimensional (Li et al., 2016; Di et al., 2018; Chen et al., 2019) (3D) as shown in Figure 3, which built an ideal platform for collectively advanced photoredox processes for the enormous advantages in terms of physical and chemical characterization in following details.

The photocatalytic performance of 0D nanostructured materials are dependence on the natures including quantum size effect, small size effect, surface effect, macroscopic quantum effect and so on. Prof. Yu and co-workers prepared graphitic carbon nitride quantum dot structures directly from g-C_3N_4 with a thermochemical etching process, which produced unique upconversion properties and higher hydrogen production efficiency than original g-C_3N_4 in 2.87 times (Wang et al., 2014).

There was more explosion of active sites on the surface of 1D g-C_3N_4, which was reported as nanotubes (Mo et al., 2018; Guo et al., 2021), nanowires (Zhang et al., 2013; Wang et al., 2015), nanorods (Bai et al., 2013; Bashir et al., 2019) and so on, and efficient transfer of photogenerated electrons could be realized along one-dimensional paths with enhancement of visible light absorption and fast short-distance electron transport. Mo et al. developed g-C_3N_4 nanotubes with large number of nitrogen defects by a green-, acid- and base-free synthesis method, and the hydrogen production of 118.5 μmol h^{-1} was far superior to pristine g-C_3N_4 (Mo et al., 2018).

Compared with 1D structures, 2D photocatalysts have greater potential because of their larger specific surface area and thinner thickness, exposing more active sites and shortening the transport path of photogenerated carriers. Prof. Zhu's group successfully fabricated g-C_3N_4 nanosheets with a single atomic layer structure of only 0.4 nm thickness, with a simple chemical exfoliation method. The single-atom-layer nanosheets offered better separation and transfer rates of photogenerated carriers, and exhibited higher performance than bulk g-C_3N_4 in photocatalytic splitting of water for hydrogen production and photocurrent generation. Chen's group proposed that the precursors assembled into nanorods at low power level, while grew into nanoplates at high power level, which implied that the morphology of g-C_3N_4 was dependance upon on a kinetically driven process (Li et al., 2015). Zhao et al. treated supramolecular precursors under the action of glycerol and ethanol to obtain porous few-layer g-C_3N_4 (Zhao et al., 2018). The hydrogen evolution rate of thin-layer g-C_3N_4 was evaluated to be 159.8 μmol h^{-1}, as the results of its large specific surface area, more active sites, and the abundant nitrogen vacancies in the framework, to accelerate the transfer of photogenerated electrons.

Compared with 2D g-C_3N_4 nanosheets, the porous 3D g-C_3N_4 material can provide a larger specific surface area. It also maximizes the use of incident photons through multiple reflections within the interconnected open frame (Di et al., 2018). In addition, the porous 3D g-C_3N_4 material acted as a support to prevent the agglomeration of ultrathin nanosheets and provided a pathway for electron transfer, thereby greatly enhancing the photocatalytic activity (Li et al., 2016). Zhang et al. utilized a simple bottom-up supramolecular self-assembly route to assemble a porous 3D g-C_3N_4 with high crystallinity and applied it to photocatalytic water splitting (Chen et al., 2019). In 2022, Guo et al. reported a facile template-free self-assembly method to synthesize three-dimensional porous g-C_3N_4 nanovesicles for achieving efficient and durable photocatalytic generation of H_2, and the large-size vesicles exhibited the high H_2 production rate of 10.3 mmol h^{-1} g^{-1} (Sun et al., 2022). And 3D onion-ring-like g-C_3N_4 was made from silica microsphere as a hard-template, which afforded excellent properties such as large specific surface area, strong optical absorption, high dispersion, for the efficient water splitting with 5-fold higher than that of pristine g-C_3N_4 (Cui et al., 2018; Shi et al., 2022).

2.3 Doping

Graphitic carbon nitride, as a conjugated polymeric material with a band gap of about 2.7 eV, has a relatively narrow response to visible-light. Numerous research results suggested that the optical properties and some other physical properties of g-C_3N_4 could be well regulated by doping foreign elements (Chen et al., 2017; Zeng et al., 2018; Fang et al., 2019; Sun H.,R. et al., 2022a). Therefore, the photocatalytic activity of pure g-C_3N_4 could be improved by hybridization with a small amounts of non-metals or metals into the framework.

2.3.1 Non-Metal doping

Hybridization of non-metallic dopants such as B, S, O, P and I to realize the ingenious design of the electronic structure, was considered as an important method for the improvement of g-C_3N_4 performance (Qi et al., 2021). Non-metal doping refers to doping of some non-metal elements into the structural framework, which not only modified the electronic and textural properties of g-C_3N_4 photocatalyst, but also improved the separation efficiency of photogenerated charge carriers and finally boosted the photocatalytic activity. Fang and coworkers (Fang et al., 2019) reported P-doped g-C_3N_4 for photocatalytic water splitting, and 4-(diphenylphosphino)benzoic acid (4-DPPBA) was employed as the precursor of phosphorous. The combination of P-doping and thermal exfoliation was applied for the preparation of porous g-C_3N_4 with P hybridization, which afford excellent photocatalysis for hydrogen evolution high to 1,596 μmol h^{-1} g^{-1} under irradiation of visible light (Ran et al., 2015). As demonstrated by DFT and experimental studies, the empty intermediate bandgap state enhanced the photo sensitivity with P hybridization, and the mass transfer process and light trapping were improved on the macroporous structure. The intrinsic energy gap of g-C_3N_4 was decrease from 2.98 to 2.66 eV in the attendance of P dopant. On the other hand, Lin and co-workers discovered the B,F-doped g-C_3N_4 porous nanosheets were achieved by the self-polymerization of urea in the presence of ionic liquid [Bmim][BF_4], which yielded photocatalytic hydrogen in 3.9 times higher than pristine g-C_3N_4 (Lin and Wang., 2014) (Zhang et al., 2014). successfully obtained iodine-doped carbon nitride (CN-I) with calcining dicyandiamide to significantly improve the hydrogen production performance (Zhang et al., 2014). The photocatalytic activity of iodine-doped g-C_3N_4 was occurred at the wavelength of 600 nm, while pristine g-C_3N_4 provided inactive catalysis at 500 nm. Guo et al. (Guo et al., 2016) prepared a phosphorus-doped hexagonal hollow tubular structure g-C_3N_4 by hydrothermal method and the special structure greatly increased the specific surface area of the catalyst, thereby increasing the number of active sites for hydrogen production. Carbon doping is also an important part of non-metal dopants. In 2021, Liu et al. reported the synthesis of C-doped g-C_3N_4 by one-step copolymerization using melamine and chitosan as the raw materials (Liu et al., 2021). The N atom in g-C_3N_4 matrix was replaced by C to form the delocalized big Π bonds. The prepared C-doped g-C_3N_4 exhibited an excellent photocatalytic H_2 evolution activity of 1,224 mmol h^{-1} g^{-1}, which was 4.5 times than the free g-C_3N_4.

2.3.2 Metal doping

In addition to the doping of non-metallic elements, the g-C_3N_4 framework was also doped with metallic elements to modify the electronic energy band structure, thereby improving the visible-light absorption, and enhancing the migration and separation of photogenerated carriers in the g-C_3N_4 photocatalyst (Chen et al., 2016). reported the Co-doped g-C_3N_4 synthesized by one-step thermal polymerization of cobalt phthalocyanine (CoPc) and melamine as the precursors (Chen et al., 2017). Yue et al. used a simple chemical method to dope metallic Zn into g-C_3N_4 (Yue et al., 2011). When the content of Zn was 10%, the visible-light-generated hydrogen production activity was 10 times higher than the pure g-C_3N_4. The proposed mechanism implied that doping of Zn increased the light absorption, improved the separation efficiency of electron-hole pairs, and enabled more electrons for water splitting. However, it is still a challenge to obtain nanoparticles with uniform size, regular shape, and high stability with common precursors such as polymers, carbon supports, ionic liquids, surfactants and microemulsions. In the recent report of our group, the coordination complex of cucurbit [6]uril and Co^{2+} was developed as the precursor, to produce cobalt nanoparticles with themolysis, for photocatalytic electrolysis of water by deposition on the surface of the g-C_3N_4 film. (Dai et al., 2022). The formed semiconductor-metal interface provided more reaction sites and electron transport channels for effective charge carriers to capture photons and excite electrons, thereby, promoting the photoelectrocatalytic reaction process. The discovery provided a new strategy for exploring macrocyclic/g-C_3N_4 materials with excellent photocatalytic activities.

2.4 Metal deposition (co-catalyst)

Various studies suggested that metal deposition on pure g-C_3N_4 was also one of the promising methods to enhance the photocatalytic activity. In theory, when metal nanoparticles are in contact with g-C_3N_4, a Schottky junction is formed at the interface of metal and g-C_3N_4 semiconductor due to the different work function, which changes the electron distribution on the semiconductor surface (Naseri et al., 2017; Caux et al., 2019; Qi et al., 2020; Zhao et al., 2021). The main function of metal is to accept the photogenerated electrons from the CB of g-C_3N_4 during the photocatalytic H_2 production process. Various metals such as Pt (Ou et al., 2017; Zhu et al., 2019), Au (Samanta et al., 2014; Caux et al., 2019), Pd (Xiao et al., 2019), Ag (Nagajyothi et al., 2017; Deeksha et al., 2021) and Ni (Indra et al., 2016; Kong et al., 2016) were employed as co-catalyst for the efficient sensitization for photocatalysis with the surface plasmon resonance (SPR) effect, which improved the light absorption capacity of the catalyst. With an *in situ* photoreduction, Pt/g-C_3N_4 was subjected to be a visible light photocatalyst by Wang's group, and the results indicated that the photocatalytic hydrogen evolution capability was gradually enhanced as the size decrease of the Pt co-catalyst (Zhu et al., 2019). The participation of Pt provided more active sites on the surface for reduction, which was favorable for accepting electrons from CB of g-C_3N_4, due to the formation of Schottky junctions at the interface of Pt and g-C_3N_4. The PL spectra and UV-vis/DRS spectra of g-C_3N_4 and Pt_x-CN with different Pt content, demonstrated that Pt loading greatly improved charge separation and transfer in g-C_3N_4 photocatalysts, thereby reduced charge recombination, and enhanced photocatalytic activity, as well as provided the maximum utilization efficiency photocatalytic performance for H_2 production. The $Pt_{0.1}$-CN (with 0.1wt% Pt loading amount) sample displayed the highest photocatalytic activity with H_2 evolution of 473.82 μmol mg^{-1} under visible-light irradiation.

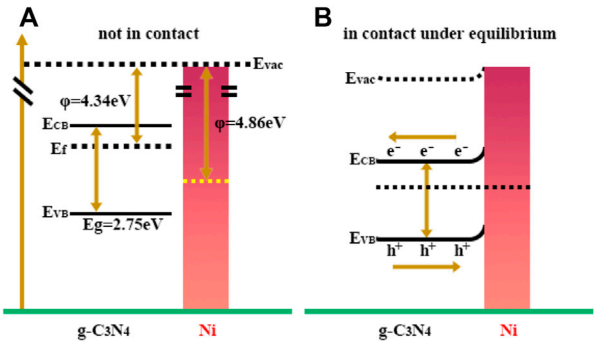

FIGURE 4
Schematic graph shows **(A)** the energy level diagram of g-C_3N_4 and Ni; **(B)** the interfacial electron transfer between g-C_3N_4 and Ni under irradiation.

Furthermore, Bi et al. reported a Ni cocatalyst for the enhancement of photocatalytic performance of g-C_3N_4 (Bi et al., 2015). A higher separation efficiency of photogenerated charge carriers was obtained as a result of a deeper band bending of g-C_3N_4 contacting with Ni, which contributed to enhanced photocatalytic H_2 production performance. In addition, the heterojunction formed between the Ni nanoparticles and g-C_3N_4 acted as an electron collector, and impeded the recombination rate of photogenerated electron and holes as illumination in Figure 4. Ni/g-C_3N_4 catalyst exhibited high photocatalytic H_2 evolution rate (8.314 μmol h^{-1}) compared with pristine g-C_3N_4, in which rapid recombination between conduction band (CB) and valence band (VB) holes and the quick reversible reaction occurred.

2.5 Dye sensitization

To overcome the g-C_3N_4 absorption edge of a band gap of 2.7 eV, organic dyes were employed as a driver to improve the visible-light photoactivity (Bard and Fax., 1995; Kudo and Miseki., 2009; Kim et al., 2015), which were considered to dramatically extend the visible-light region of the band-gap of semiconductor (Zhuang et al., 2019). However, the researches about H_2 production based on dye-sensitized carbon nitride were still insufficient, only few organic dyes such as metal-porphyrins (Yu et al., 2014; Chen et al., 2015; Zhang et al., 2015; Zhuang et al., 2019; Liu et al., 2020), poly (3-hexylthiophene) (Zhang et al., 2015), eosin Y (EY) (Min and Liu., 2012; Wang et al., 2018; Qi et al., 2019; Xu et al., 2019; Nagaraja et al., 2020; Zhao et al., 2021) and erythrosin B (ErB) (Wang et al., 2013; Zhang et al., 2017; Zhang et al., 2017) have been successfully applied to enhance the photocatalytic activity with improvement of the utilization efficiency of visible-light. In the process of H_2 generation, the organic dyes were damaged in oxidation reactions, and its stabilization could be realized with a porous support, which accelerates the transfer of electrons from the excited dye molecule to the active site in definition of a cocatalyst, in general use of noble metals (especially Pt). The hybridization of Ag with g-C_3N_4 was applied for hydrogen evolution, and the photocatalysis was improved with the dye-sensitization under visible-light irradiation (Schwinghanmmer et al., 2013). Min et al. reported that g-C_3N_4 with modification of Eosin Y performed the light-drove H_2 generation at about 600 nm, while the reaction occurred at less than 460 nm on the pristine g-C_3N_4 surface (Min and Liu., 2012).

2.6 Heterogeneous structure

The photocatalytic efficiency and application of pristine g-C_3N_4 were limited for high recombination rate of photogenerated charge carriers and narrow range of visible light response in a solar spectrum. Recently, g-C_3N_4-based heterojunctions were developed by enhancement of carrier separation efficiency and demonstrated excellent photocatalytic performance. Semiconductors were induced to form heterojunctions with g-C_3N_4 including carbon materials (graphene (Xiang et al., 2011), carbon nanotubes (Ge and Han., 2012), fullerenes (Chai et al., 2014)), metal oxides (TiO_2(Chen and Liu, 2016), SnO_2(Zada et al., 2019), ZnO(Sun et al., 2012), $NiFe_2O_4$(Liu et al., 2022), Fe_2O_3(Theerthagiri et al., 2014)), metal sulfides (CdS(Chen et al., 2016), ZnS(Shi et al., 2014), MoS_2(Li et al., 2014)), bismuth-based compounds ($BiPO_4$(Zou et al., 2015), $BiVO_4$(Li et al., 2014), Bi_2WO_6(Li et al., 2018)), silver-based compounds (Ag_2O(Liang et al., 2019), Ag_3PO_4(Liu et al., 2016), Ag_3VO_4(Zhu et al., 2015)), multi-element rare Earth oxides (Zn_2GeO_4(Sun et al., 2014), $SrTiO_3$(Xu et al., 2011)), etc. The principle was executed in design of the heterojunction, that is, the recombination of g-C_3N_4 and the band-matched semiconductor promoted the transfer of charge carriers and suppressed the recombination of charges.

Based on different photogenerated carrier transfer mechanisms, the heterojunctions were formed when g-C_3N_4 coupled with other materials (Reza et al., 2015; Patnaik et al., 2016; Fu et al., 2018). In the heterojunction structures, Type-I constructure refers to that the position of CB of semiconductor-1 is higher than that of semiconductor-2, while the VB position of semiconductor-1 is lower than that of semiconductor-2, as shown in Figure 5A. Under the excitation of visible light, electrons and holes of the Type-I heterojunction photocatalyst are more inclined to migrate to the semiconductor-2 with a smaller band gap and undergo a redox reaction, and the separation efficiency of carriers is not significantly improved, resulting in the low rate of photocatalytic redox reaction. In the Type-II structure, the positions of both CB and VB of semiconductor-2 are lower than those of semiconductor-1, and therefore the photogenerated electrons and holes transferr into different sides of the heterostructure, as shown in Figure 5B. The carrier transport mode of the Type-II heterojunction greatly improve the photocatalytic activity of the composite photocatalyst. In 2021, Roy's team reported the TiO_2/ultrathin g-C_3N_4 (U-g-CN) heterostructure photocatalyst using a unique *in situ* thermal exfoliation process, and the presence of U-g-CN produced a redshift (~0.13eV) in the absorption edge of heterostructures compared to that of bare TiO_2, which extended the light absorption capability. Combined with the morphological characteristics of g-C_3N_4, Chen et al. prepared a novel 3D hierarchical hollow tubular g-C_3N_4/$ZnIn_2S_4$ nanosheets as the type-II heterojunction photocatalyst (Chen et al., 2022). The optimum photocatalyst offered the H_2 evolution rate up to 20,738 μmol h^{-1} g^{-1}. In the case of the Type-III heterojunction (Figure 5C), there are no any energy band intersection of semiconductor-1 and semiconductor-2, resulting in the inability of transport of photogenerated carriers between the semiconductors to greatly improve the photocatalytic efficiency.

Thus, a suitable semiconductor heterojunction is able to both enhance the ability to capture sunlight and significantly accelerate the separation and migration of photogenerated electron-hole pairs as description in Type II structure, but it is still insufficient in terms of photocatalytic oxidation ability. The Z-scheme heterojunction (Xu et al., 2022) was explored to overcome this disadvantage to a certain extent, which was mainly divided into binary and ternary structures, as shown in the Figure 6 (Maeda, 2013). The CB and VB potentials of

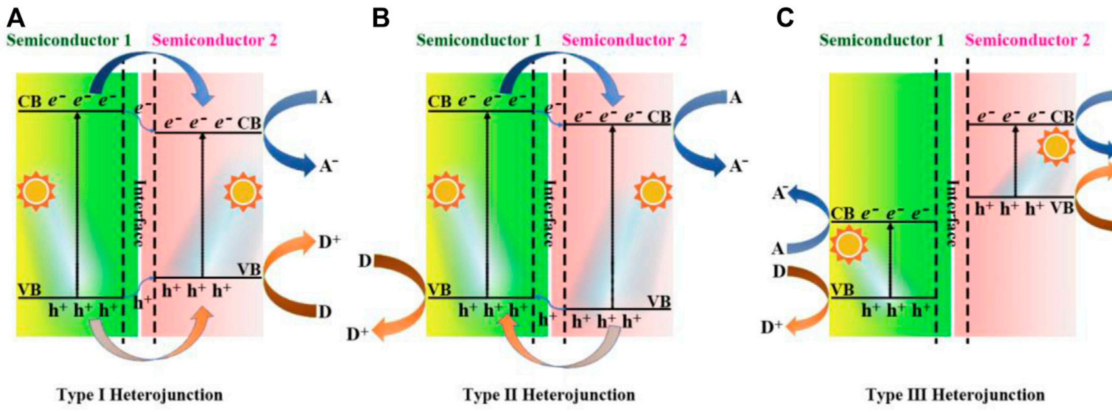

FIGURE 5
Schematic representation band structure of different heterojunctions: **(A)** Type I heterojunction; **(B)** Type II heterojunction; **(C)** Type III heterojunction. A and D represent electron acceptor and electron donor, respectively.

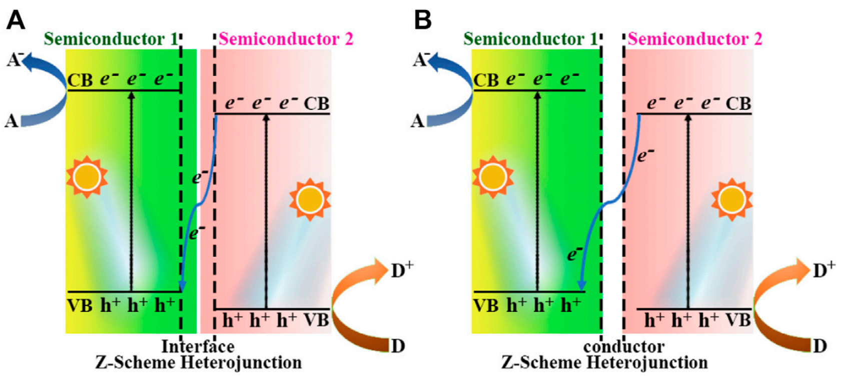

FIGURE 6
Schematic energy band diagram of two different types of Z-scheme heterojunction: **(A)** binary Z-scheme heterojunction, **(B)** ternary Z-scheme heterojunction. A and D denote electron acceptor and electron donor, respectively.

semiconductor-2 were more positive than those of semiconductor-1 in binary Z-scheme (Figure 6A), thereby enhancing the reduction and oxidation capacity of e^- and h^+. Zhao et al. prepared the $CeO_2/g\text{-}C_3N_4$ heterojunction photocatalysts, through a one-step *in situ* pyrolysis formation of 3D hollow CeO_2 mesoporous nanospheres and 2D $g\text{-}C_3N_4$ nanosheets. The hydrogen evolution from water splitting experiment of the $CeO_2/g\text{-}C_3N_4$-6 gave a maximum yield of 1,240.9 μmol g^{-1} h^{-1}, which was about 5.2 times higher than that of CeO_2 (Zhao et al., 2021). Figure 6B pictured out a conductor was employed as a charge bridge between the VB of semiconductor-1 and the CB of semiconductor-2 in the ternary Z-scheme heterojunction, which was played by metal particles, such as Cu, Au, Ag, etc. Hieu et al. synthesized the $TiO_2/Ti_3C_2/g\text{-}C_3N_4$ (TTC) photocatalyst from $g\text{-}C_3N_4$ and Ti_3C_2 MXene *via* a calicination technique, and a high H_2 production of 2,592 μmol g^{-1} was achieved (Hieu et al., 2021).

2.7 Homojunction structure

The $g\text{-}C_3N_4$ homojunctions are also recognized as the efficient photocatalysts. However, the type II structures and *Z*-schemes in the pioneering reports require deep optimization of the electron transport path in $g\text{-}C_3N_4$ homojunctions, since the redox potentials were depressed to inhibit the improvement of photocatalytic performance. The barrier could be overcome by the inspiration of *S*-scheme heterojunction proposed by Yu's group (Xu et al., 2020), Guo et al. fabricated the *S*-scheme homojunctions with high-crystalline/amorphous $g\text{-}C_3N_4$

(HCCN/ACN) with solvothermal method, which was applied in photocatalytic H_2 production with the evolution rates of 5.534 mmol h^{-1} g^{-1} in water and 3.147 mmol h^{-1} g^{-1} in seawater (Sun et al., 2022).

3 Conclusion

The excessive use and combustion of fossil fuels will inevitably bring some environmental problems. The value of hydrogen energy has been fully recognized, but its preparation technology still needs to be further explored. Photocatalytic technology is expected to realize sustainable energy production under the premise of making full use of solar energy, and has great potential in terms of energy and environment. The main factor limiting the photocatalytic activity of pristine g-C_3N_4 is its bulk structure, resulting in its small specific surface area and few active sites, which prolongs the transfer path of photogenerated electrons, thus accelerates the photogenerated charge carriers compound odds. The ability of photocatalytic hydrogen production performance of g-C_3N_4 could be improved by adjusting pH of the environment to induce the change of the surface charge of g-C_3N_4, controlling the morphology of g-C_3N_4 to increase active sites and shorten the transport path of carriers, and compositing co-catalysts or narrow-band semiconductors or dyes to enhance light absorption and reduce the recombination of photogenerated electrons and holes. So far, the strategies for exploration of stable hybridization structures to boost the photocatalytic efficiency could be the main concern in this filed, and more cases should be discovered to realize the dependence of the morphologies, structures, and species of dopants on the activities. This review is aimed at summarization of the recent progress of preparation and performance of g-C_3N_4-block photocatalysts to induce new ideas for the structural design with further improved efficiency by interdisciplinary researches across chemistry, physics, and material science.

Author contributions

R-HG, HC, and Y-QZ contributed to conception and design of the study. ML, QG, and NJ organized the database. R-HG wrote the first draft of the manuscript. All authors contributed to manuscript revision, read, and approved the submitted version.

Funding

This work was supported by Natural Science Foundation of Guizhou Province [No. ZK(2022)049], and National Natural Science Foundation of China (No. 22161011).

Conflict of interest

The authors declare that the research was conducted in the absence of any commercial or financial relationships that could be construed as a potential conflict of interest.

Publisher's note

Supplementary material

The Supplementary Material for this article can be found online at: https://www.frontiersin.org/articles/10.3389/fchem.2022.1048504/full#supplementary-material

References

Bai, X. J., Wang, L., Zong, R. L., and Zhu, Y. (2013). Photocatalytic activity enhanced via g-C_3N_4 nanoplates to nanorods. *J. Phys. Chem. C* 117 (19), 9952–9961. doi:10.1021/jp402062d

Bard, A. J., and Fox, M. A. (1995). Artificial photosynthesis: Solar splitting of water to hydrogen and oxygen. *Acc. Chem. Res.* 28 (3), 141–145. doi:10.1021/ar00051a007

Bashir, H., Yi, X. Y., Yuan, J. L., Yin, K., and Luo, S. (2019). Highly ordered TiO_2 nanotube arrays embedded with g-C_3N_4 nanorods for enhanced photocatalytic activity. *J. Photochem. Photobiol. A Chem.* 382, 111930. doi:10.1016/j.jphotochem.2019.111930

Bi, L., Xu, D., Zhang, L., Lin, Y., Wang, D., and Xie, T. (2015). Metal Ni-loaded g-C_3N_4 for enhanced photocatalytic H_2 evolution activity: The change in surface band bending. *Phys. Chem. Chem. Phys.* 17 (44), 29899–29905. doi:10.1039/c5cp05158d

Caux, M., Menard, H., AlSalik, Y. M., Irvine, J. T. S., and Idriss, H. (2019). Photo-catalytic hydrogen production over Au/g-C_3N_4: Effect of Gold Particle dispersion and morphology. *Phys. Chem. Chem. Phys.* 21 (29), 15974–15987. doi:10.1039/c9cp02241d

Chai, B., Liao, X., Song, F., and Zhou, H. (2014). Fullerene modified C_3N_4 composites with enhanced photocatalytic activity under visible light irradiation. *Dalton Trans.* 43 (3), 982–989. doi:10.1039/c3dt52454j

Chen, D., Wang, K., Hong, W., Zong, R., Yao, W., and Zhu, Y. (2015). Visible light photoactivity enhancement via CuTCPP hybridized g-C_3N_4 nanocomposite. *Appl. Catal. B Environ.* 166, 366–373. doi:10.1016/j.apcatb.2014.11.050

Chen, D., Wang, Z., Yue, D., Yang, G., Ren, T., and Ding, H. (2016). Synthesis and visible photodegradation enhancement of CdS/mpg-C_3N_4 photocatalyst. *J. Nanosci. Nanotechnol.* 16 (1), 471–479. doi:10.1166/jnn.2016.10661

Chen, H. B., and Liu, W. X. (2016). Cellulose-based photocatalytic paper with Ag_2O nanoparticles loaded on graphite fibers. *J. Bioresour. Bioprod.* 1 (4), 192–198. doi:10.21967/jbb.v1i4.63

Chen, P. W., Li, K., Yu, Y. X., and Zhang, W. De. (2017). Cobalt-doped graphitic carbon nitride photocatalysts with high activity for hydrogen evolution. *Appl. Surf. Sci.* 392, 608–615. doi:10.1016/j.apsusc.2016.09.086

Chen, X., Shi, R., Chen, Q., Zhang, Z., Jiang, W., Zhu, Y., et al. (2019). Three-dimensional porous g-C3N4 for highly efficient photocatalytic overall water splitting. *Nano Energy* 59, 644–650. doi:10.1016/j.nanoen.2019.03.010

Chen, X., Wei, J., Hou, R., Liang, Y., Xie, Z., Zhu, Y., et al. (2016). Growth of g-C_3N_4 on mesoporous TiO_2 spheres with high photocatalytic activity under visible light irradiation. *Appl. Catal. B Environ.* 188, 342–350. doi:10.1016/j.apcatb.2016.02.012

Chen, Z. H., Guo, F., Sun, H., Shi, Y. X., and Shi, W. L. (2022). Well-designed three-dimensional hierarchical hollow tubular g-C_3N_4/$ZnIn_2S_4$ nanosheets heterostructure for achieving efficient visible-light photocatalytic hydrogen evolution. *J. Colloid Interface Sci.* 607, 1391–1401. doi:10.1016/j.jcis.2021.09.095

Cui, L., Song, J., McGuire, A. F., Kang, S., Fang, X., Wang, J., et al. (2018). Constructing highly uniform onion-ring-like graphitic carbon nitride for efficient visible-light-driven photocatalytic hydrogen evolution. *ACS Nano* 12, 5551–5558. doi:10.1021/acsnano.8b01271

Dai, X., Jin, X. Y., Gao, R. H., Ge, Q., Chen, K., Jiang, N., et al. (2022). Controllable synthesis of Co nanoparticles with the assistance of cucurbit[6]uril and its efficient photoelectrochemical catalysis in water splitting on a g-C_3N_4 photoanode. *New J. Chem.* 46, 6738–6746. doi:10.1039/d2nj00036a

Deeksha, B., Sadanand, V., Hariram, N., and Rajulu, A. V. (2021). Preparation and properties of cellulose nanocomposite fabrics with *in situ* generated silver nanoparticles by bioreduction method. *J. Bioresour. Bioprod.* 6 (1), 75–81. doi:10.1016/j.jobab.2021.01.003

Di, J., Xiong, J., Li, H., and Liu, Z. (2018). Ultrathin 2D photocatalysts: Electronic-structure tailoring, hybridization, and applications. *Adv. Mat.* 30 (1), 1704548. doi:10.1002/adma.201704548

Fang, X. X., Ma, L. B., Liang, K., Zhao, S. J., Jiang, Y. F., Ling, C., et al. (2019). The Doping of phosphorus atoms into graphitic carbon nitride for highly enhanced photocatalytic hydrogen evolution. *J. Mat. Chem. A Mat.* 7 (18), 11506–11512. doi:10.1039/c9ta01646e

Fu, J., Yu, J., Jiang, C., and Cheng, B. (2018). g-C_3N_4-based heterostructured photocatalysts. *Adv. Energy Mat.* 8 (3), 1701503–1701531. doi:10.1002/aenm.201701503

Fujishima, A., and Honda, K. (1972). Electrochemical photolysis of water at a semiconductor electrode. *Nature* 238 (5358), 37–38. doi:10.1038/238037a0

Ge, L., and Han, C. (2012). Synthesis of MWNTs/g-C_3N_4 composite photocatalysts with efficient visible light photocatalytic hydrogen evolution activity. *Appl. Catal. B Environ.* 117, 268–274. doi:10.1016/j.apcatb.2012.01.021

Guo, F., Chen, Z., Huang, X., Cao, L., Cheng, X., Shi, W., et al. (2021). Cu_3P nanoparticles decorated hollow tubular carbon nitride as a superior photocatalyst for photodegradation of tetracycline under visible light. *Sep. Purif. Technol.* 275 (15), 119223. doi:10.1016/j.seppur.2021.119223

Guo, S., Deng, Z., Li, M., Jiang, B., Tian, C., Pan, Q., et al. (2016). Phosphorus-doped carbon nitride tubes with a layered micro-nanostructure for enhanced visible-light photocatalytic hydrogen evolution. *Angew. Chem. Int. Ed.* 55 (5), 1830–1834. doi:10.1002/anie.201508505

Han, Q., Wang, B., Zhao, Y., Hu, C., and Qu, L. (2015). A graphitic-C_3N_4 "seaweed" architecture for enhanced hydrogen evolution. *Angew. Chem. Int. Ed.* 54 (39), 11433–11437. doi:10.1002/anie.201504985

Hieu, V. Q., Lam, T. C., Khan, A., Thi Vo, T., Nguyen, T. Q., Doan, V. D., et al. (2021). TiO_2/Ti_3C_2/g-C_3N_4 ternary heterojunction for photocatalytic hydrogen evolution. *Chemosphere* 285, 131429. doi:10.1016/j.chemosphere.2021.131429

Indra, A., Menezes, P. W., Kailasam, K., Hollmann, D., Schroder, M., Thomas, A., et al. (2016). Nickel as a Co-catalyst for photocatalytic hydrogen evolution on graphitic-carbon nitride (sg-CN): What is the nature of the active species? *Chem. Commun.* 52 (1), 104–107. doi:10.1039/c5cc07936e

Kim, D., Sakimoto, K. K., Hong, D., and Yang, P. D. (2015). Artificial photosynthesis for sustainable fuel and chemical production. *Angew. Chem. Int. Ed.* 54 (11), 3259–3266. doi:10.1002/anie.201409116

Kong, L., Dong, Y., Jiang, P., Wang, G., Zhang, H., and Zhao, N. (2016). Light-assisted rapid preparation of a Ni/g-C_3N_4 magnetic composite for robust photocatalytic H_2 evolution from water. *J. Mat. Chem. A* 4 (25), 9998–10007. doi:10.1039/c6ta03178a

Kudo, A., and Miseki, Y. (2009). Heterogeneous photocatalyst materials for water splitting. *Chem. Soc. Rev.* 38 (1), 253–278. doi:10.1039/b800489g

Li, C., Wang, S., Wang, T., Wei, Y., Zhang, P., and Gong, J. (2014). Monoclinic porous $BiVO_4$ networks decorated by discrete g-C_3N_4 nano-islands with tunable coverage for highly efficient photocatalysis. *Small* 10 (14), 2783–2790. doi:10.1002/smll.201400506

Li, H. J., Qian, D. J., and Chen, M. (2015). Templateles infrared heating process for fabricating carbon nitride nanorods with efficient photocatalytic H_2 evolution. *ACS Appl. Mat. Interfaces* 7 (45), 25162–25170. doi:10.1021/acsami.5b06627

Li, H., Li, N., Wang, M., Zhao, B., and Long, F. (2018). Synthesis of novel and stable g-C_3N_4-Bi_2WO_6 hybrid nanocomposites and their enhanced photocatalytic activity under visible light irradiation. *R. Soc. open Sci.* 5 (3), 171419. doi:10.1098/rsos.171419

Li, Q., Zhang, N., Yang, Y., Wang, G., and Ng, D. H. L. (2014). High efficiency photocatalysis for pollutant degradation with MoS_2/C_3N_4 heterostructures. *Langmuir* 30 (29), 8965–8972. doi:10.1021/la502033t

Li, X., Yu, J., and Jaroniec, M. (2016). Hierarchical photocatalysts. *Chem. Soc. Rev.* 45 (9), 2603–2636. doi:10.1039/c5cs00838g

Liang, S., Zhang, D., Pu, X., Yao, X., Han, R., Yin, J., et al. (2019). A novel Ag_2O/g-C_3N_4 p-n heterojunction photocatalysts with enhanced visible and near-infrared light activity. *Sep. Purif. Technol.* 210, 786–797. doi:10.1016/j.seppur.2018.09.008

Lin, Z., and Wang, X. (2014). Ionic liquid promoted synthesis of conjugated carbon nitride photocatalysts from urea. *ChemSusChem* 7 (6), 1547–1550. doi:10.1002/cssc.201400016

Liu, E., Lin, X., Hong, Y., Yang, L., Luo, B., Shi, W., et al. (2021). Rational copolymerization strategy engineered C self-doped g-C_3N_4 for efficient and robust solar photocatalytic H_2 evolution. *Renew. Energy* 178, 757–765. doi:10.1016/j.renene.2021.06.066

Liu, L., Qi, Y., Lu, J., Lin, S., An, W., Liang, Y., et al. (2016). A stable Ag_3PO_4@g-C_3N_4 hybrid core@shell composite with enhanced visible light photocatalytic degradation. *Appl. Catal. B Environ.* 183, 133–141. doi:10.1016/j.apcatb.2015.10.035

Liu, Q., Li, N., Qiao, Z., Li, W., Wang, L., Zhu, S., et al. (2019). The multiple promotion effects of ammonium phosphate-modified Ag_3PO_4 on photocatalytic performance. *Front. Chem.* 7, 866. doi:10.3389/fchem.2019.00866

Liu, S., Zada, A., Yu, X., Liu, F., and Jin, G. (2022). $NiFe_2O_4$/g-C_3N_4 heterostructure with an enhanced ability for photocatalytic degradation of tetracycline hydrochloride and antibacterial performance. *Chemosphere* 307, 135717. doi:10.1016/j.chemosphere.2022.135717

Liu, Y., Kang, S., Cui, L., and Ma, Z. (2020). Boosting near-infrared-driven photocatalytic H_2 evolution using protoporphyrin-sensitized g-C_3N_4. *J. Photochem. Photobiol. A Chem.* 396, 112517–112526. doi:10.1016/j.jphotochem.2020.112517

Maeda, K., Teramura, K., Lu, D., Takata, T., Saito, N., Inoue, Y., et al. (2006). Photocatalyst releasing hydrogen from water. *Nature* 440 (7082), 295. doi:10.1038/440295a

Maeda, K. (2013). Z-scheme water splitting using two different semiconductor photocatalysts. *ACS Catal.* 3 (7), 1486–1503. doi:10.1021/cs4002089

Min, S., and Lu, G. (2012). Enhanced electron transfer from the excited eosin Y to mpg-C_3N_4 for highly efficient hydrogen evolution under 550 nm irradiation. *J. Phys. Chem. C* 116 (37), 19644–19652. doi:10.1021/jp304022f

Mo, Z., Xu, H., Chen, Z. G., She, X., Song, Y., Wu, J., et al. (2018). Self-assembled synthesis of defect-engineered graphitic carbon nitride nanotubes for efficient conversion of solar energy. *Appl. Catal. B Environ.* 225, 154–161. doi:10.1016/j.apcatb.2017.11.041

Nagajyothi, P. C., Pandurangan, M., Vattikuti, S. V. P., Tettey, C. O., Sreekanth, T. V. M., and Shim, J. (2017). Enhanced photocatalytic activity of Ag/g-C_3N_4 composite. *Sep. Purif. Technol.* 188, 228–237. doi:10.1016/j.seppur.2017.07.026

Nagaraja, C. M., Kaur, M., and Dhingra, S. (2020). Enhanced visible-light-assisted photocatalytic hydrogen generation by MoS_2/g-C_3N_4 nanocomposites. *Int. J. Hydrogen Energy* 45 (15), 8497–8506. doi:10.1016/j.ijhydene.2020.01.042

Naseri, A., Samadi, M., Pourjavadi, A., Moshfegh, A. Z., and Ramakrishma, S. (2017). Graphitic carbon nitride (g-C_3N_4)-based photocatalysts for solar hydrogen generation: Recent advances and future development directions. *J. Mat. Chem. A Mat.* 5 (45), 23406–23433. doi:10.1039/c7ta05131j

Niu, P., Zhang, L., Liu, G., and Cheng, H. M. (2012). Graphene-like carbon nitride nanosheets for improved photocatalytic activities. *Adv. Funct. Mat.* 22 (22), 4763–4770. doi:10.1002/adfm.201200922

Ong, W. J., Tan, L. L., Ng, Y. H., Yong, S. T., and Chai, S. P. (2016). Graphitic carbon nitride (g-C3N4)-based photocatalysts for artificial photosynthesis and environmental remediation: Are we a step closer to achieving sustainability? *Chem. Rev.* 116 (12), 7159–7329. doi:10.1021/acs.chemrev.6b00075

Ou, M., Wan, S., Zhong, Q., Zhang, S., and Wang, Y. (2017). Single Pt atoms deposition on g-C_3N_4 nanosheets for photocatalytic H_2 evolution or NO oxidation under visible light. *Int. J. Hydrogen Energy* 42 (44), 27043–27054. doi:10.1016/j.ijhydene.2017.09.047

Patnaik, S., Martha, S., and Parida, K. M. (2016). An overview of the structural, textural and morphological modulations of g-C_3N_4 towards photocatalytic hydrogen production. *RSC Adv.* 6 (52), 46929–46951. doi:10.1039/c5ra26702a

Qi, K., Cui, N., Zhang, M., Ma, Y., Wang, G., Zhao, Z., et al. (2021). Ionic liquid-assisted synthesis of porous boron-doped graphitic carbon nitride for photocatalytic hydrogen production. *Chemosphere* 272, 129953. doi:10.1016/j.chemosphere.2021.129953

Qi, K., Li, Y., Xie, Y., Liu, S., Zheng, K., Chen, Z., et al. (2019). Ag loading enhanced photocatalytic activity of g-C_3N_4 porous nanosheets for decomposition of organic pollutants. *Front. Chem.* 7, 91. doi:10.3389/fchem.2019.00091

Qi, K., Liu, S., and Zada, A. (2020). Graphitic carbon nitride, a polymer photocatalyst. *J. Taiwan Inst. Chem. Eng.* 109, 111–123. doi:10.1016/j.jtice.2020.02.012

Qi, K., Lv, W., Khan, I., and Liu, S. (2020). Photocatalytic H_2 generation via CoP quantum-dot-modified g-C_3N_4 synthesized by electroless plating. *Chin. J. Catal.* 41 (1), 114–121. doi:10.1016/s1872-2067(19)63459-5

Qi, K., Zhang, C., Zhang, M., Gholami, P., and Khataee, A. (2022). Sonochemical synthesis of photocatalysts and their applications. *J. Mat. Sci. Technol.* 123, 243–256. doi:10.1016/j.jmst.2022.02.019

Qi, Y., Xu, J., Zhang, M., Lin, H., and Wang, L. (2019). *In situ* metal-organic framework-derived C-doped Ni_3S_4/Ni_2P hybrid co-catalysts for photocatalytic H_2 production over g-C_3N_4 via dye sensitization. *Int. J. Hydrogen Energy* 44 (31), 16336–16347. doi:10.1016/j.ijhydene.2019.04.276

Ran, J., Ma, T. Y., Gao, G., Du, X. W., and Qiao, S. Z. (2015). Porous P-doped graphitic carbon nitride nanosheets for synergistically enhanced visible-light photocatalytic H_2 production. *Energy Environ. Sci.* 8 (12), 3708–3717. doi:10.1039/c5ee02650d

Reza, G. M., Dinh, C. T., Beland, F., and Do, T. O. (2015). Nanocomposite heterojunctions as sunlight-driven photocatalysts for hydrogen production from water splitting. *Nanoscale* 7 (18), 8187–8208. doi:10.1039/c4nr07224c

Samanta, S., Martha, S., and Parida, K. (2014). Facile synthesis of Au/g-C_3N_4 nanocomposites: An inorganic/organic hybrid plasmonic photocatalyst with enhanced hydrogen gas evolution under visible-light irradiation. *ChemCatChem* 6 (5), 1453–1462. doi:10.1002/cctc.201300949

Schwinghanmmer, K., Tuffy, B., Mesch, M. B., Wirnhier, E., Martineau, C., Taulelle, F., et al. (2013). Triazine-based carbon nitrides for visible-light-driven hydrogen evolution. *Angew. Chem. Int. Ed.* 52 (9), 2435–2439. doi:10.1002/anie.201206817

Shen, X. C., Tang, Y. J., Zhou, D. D., Zhang, J. H., Guo, D. L., and Friederichs, G. (2016). Improving the electroconductivity and mechanical properties of cellulosic paper with multi-walled carbon nanotube/polyaniline nanocomposites. *J. Bioresour. Bioprod.* 1 (1), 48–54. doi:10.21967/jbb.v1i1.40

Shi, W. L., Sun, W., Liu, Y., Li, X. Y., Lin, X., Guo, F., et al. (2022). Onion -ring-like g-C_3N_4 modified with Bi_3TaO_7 quantum dots: A novel 0D/3D S-scheme heterojunction for enhanced photocatalytic hydrogen production under visible light irradiation. *Renew. Energy* 182, 958–968. doi:10.1016/j.renene.2021.11.030

Shi, Y., Jiang, S., Zhou, K., Wang, B., Wang, B., Gui, Z., et al. (2014). Facile Preparation of ZnS/g-C_3N_4 nanohybrids for enhanced optical properties. *RSC Adv.* 4 (6), 2609–2613. doi:10.1039/c3ra44256j

Shi, Y. X., Li, L. L., Sun, H. R., Xu, Z., Cai, Y., Shi, W. L., et al. (2022). Engineering ultrathin oxygen-doped g-C_3N_4 nanosheet for boosted photoredox catalytic activity based on a facile thermal gas-shocking exfoliation effect. *Sep. Purif. Technol.* 292, 121038. doi:10.1016/j.seppur.2022.121038

Sun, H., R., Wang, L. J., Guo, F., Shi, Y. X., Li, L. L., Xu, Z., et al. (2022a). Fe-doped g-C_3N_4 derived from biowaste material with Fe-N bonds for enhanced synergistic effect between photocatalysis and Fenton degradation activity in a broad pH range. *J. Alloys Compd.* 900, 163410. doi:10.1016/j.jallcom.2021.163410

Sun, H. R., Shi, Y. X., Shi, W. L., and Guo, F. (2022b). High-crystalline/amorphous g-C_3N_4 S-scheme homojunction for boosted photocatalytic H_2 production in water/simulated seawater: Interfacial charge transfer and mechanism insight. *Appl. Surf. Sci.* 593, 153281. doi:10.1016/j.apsusc.2022.153281

Sun, J. X., Yuan, Y. P., Qiu, L. G., Jiang, X., Xie, A. J., Shen, Y. H., et al. (2012). Fabrication of composite photocatalyst g-C_3N_4-ZnO and enhancement of photocatalytic activity under visible light. *Dalton Trans.* 41 (22), 6756–6763. doi:10.1039/c2dt12474b

Sun, L., Qi, Y., Jia, C. J., Jin, Z., and Fan, W. (2014). Enhanced visible-light photocatalytic activity of g-C_3N_4/Zn_2GeO_4 heterojunctions with effective interfaces based on band match. *Nanoscale* 6 (5), 2649–2659. doi:10.1039/c3nr06104c

Sun, X. H., Shi, Y. X., Lu, J. L., Shi, W. L., and Guo, F. (2022). Template-free self-assembly of three-dimensional porous graphitic carbon nitride nanovesicles with size-dependent photocatalytic activity for hydrogen evolution. *Appl. Surf. Sci.* 606, 154841. doi:10.1016/j.apsusc.2022.154841

Theerthagiri, J., Senthil, R. A., Priya, A., Madhavan, J., Michael, R. J. V., and Ashokkumar, M. (2014). Photocatalytic and photoelectrochemical studies of visible-light active alpha-Fe_2O_3-g-C_3N_4 nanocomposites. *RSC Adv.* 4 (72), 38222–38229. doi:10.1039/c4ra04266b

Thomas, A., Fischer, A., Goettmann, F., Antonietti, M., Muller, J. O., Schlogl, R., et al. (2008). Graphitic carbon nitride materials: Variation of structure and morphology and their use as metal-free catalysts. *J. Mat. Chem.* 18 (41), 4893–4908. doi:10.1039/b800274f

Wang, B., Wang, Y., Lei, Y., Wu, N., Gou, Y., Han, C., et al. (2016). Mesoporous silicon carbide nanofibers with *in situ* embedded carbon for Co-catalyst free photocatalytic hydrogen production. *Nano Res.* 9 (3), 886–898. doi:10.1007/s12274-015-0971-z

Wang, L. X., Zhao, F., Han, Q., Hu, C., Lv, L., Chen, N., et al. (2015). Spontaneous formation of Cu_2O-g-C_3N_4 core-shell nanowires for photocurrent and humidity responses. *Nanoscale* 7 (21), 9694–9702. doi:10.1039/c5nr01521a

Wang, P., Guan, Z., Li, Q., and Yang, J. (2018). Efficient visible-light-driven photocatalytic hydrogen production from water by using Eosin Y-sensitized novel g-C_3N_4/Pt/GO composites. *J. Mat. Sci.* 53 (1), 774–786. doi:10.1007/s10853-017-1540-5

Wang, Q., Hisatomi, T., Jia, Q., Tokudome, H., Zhao, M., Wang, C., et al. (2016). Scalable water splitting on particulate photocatalyst sheets with a solar-to-hydrogen energy conversion efficiency exceeding 1%. *Nat. Mat.* 15 (6), 611–615. doi:10.1038/nmat4589

Wang, W., Yu, J. C., Shen, Z., Chan, D. K. L., and Gu, T. (2014). g-C_3N_4 quantum dots: direct synthesis, upconversion properties and photocatalytic application. *Chem. Commun.* 50 (70), 10148–10150. doi:10.1039/c4cc02543a

Wang, X., Maeda, K., Thomas, A., Takanabe, K., Xin, G., Carlsson, J. M., et al. (2009). A metal-free polymeric photocatalyst for hydrogen production from water under visible light. *Nat. Mat.* 8 (1), 76–80. doi:10.1038/nmat2317

Wang, Y., Hong, J., Zhang, W., and Xu, R. (2013). Carbon nitride nanosheets for photocatalytic hydrogen evolution: Remarkably enhanced activity by dye sensitization. *Catal. Sci. Technol.* 3 (7), 1703–1711. doi:10.1039/c3cy20836b

Wang, Z., Xu, X., Si, Z., Liu, L., He, Y., Ran, R., et al. (2018). *In situ* synthesized MoS_2/Ag dots/Ag_3PO_4 Z-scheme photocatalysts with ultrahigh activity for oxygen evolution under visible light irradiation. *Appl. Surf. Sci.* 450, 441–450. doi:10.1016/j.apsusc.2018.04.149

Wu, P., Wang, J., Zhao, J., Guo, L., and Osterloh, F. E. (2014). High alkalinity boosts visible light driven H_2 evolution activity of g-C_3N_4 in aqueous methanol. *Chem. Commun.* 50 (98), 15521–15524. doi:10.1039/c4cc08063g

Wu, X., Zhu, C., Wang, L., Guo, S., Zhang, Y., Li, H., et al. (2017). Control strategy on two-/four-electron pathway of water splitting by multidoped carbon based catalysts. *ACS Catal.* 7 (3), 1637–1645. doi:10.1021/acscatal.6b03244

Xiang, Q., Yu, J., and Jaroniec, M. (2011). Preparation and enhanced visible-light photocatalytic H_2 production activity of graphene/C_3N_4 composites. *J. Phys. Chem. C* 115 (15), 7355–7363. doi:10.1021/jp200953k

Xiao, N., Li, Y., Li, X., Gao, Y., Ge, L., Lu, G., et al. (2019). *In-situ* synthesis of PdAg/g-C_3N_4 composite photocatalyst for highly efficient photocatalytic H_2 generation under visible light irradiation. *Int. J. Hydrogen Energy* 44 (36), 19929–19941. doi:10.1016/j.ijhydene.2019.05.236

Xu, J., Qi, Y., Wang, W., and Wang, L. (2019). Montmorillonite-hybridized g-C_3N_4 composite modified by NiCoP cocatalyst for efficient visible-light-driven photocatalytic hydrogen evolution by dye-sensitization. *Int. J. Hydrogen Energy* 44 (8), 4114–4122. doi:10.1016/j.ijhydene.2018.12.167

Xu, Q., Zhang, L., Cheng, B., Fan, J., and Yu, J. (2020). S-scheme heterojunction photocatalyst. *Chem* 6 (7), 1543–1559. doi:10.1016/j.chempr.2020.06.010

Xu, X., Liu, G., Randorn, C., and Irvine, J. T. S. (2011). g-C_3N_4 coated $SrTiO_3$ as an efficient photocatalyst for H_2 production in aqueous solution under visible light irradiation. *Int. J. Hydrogen Energy* 36 (21), 13501–13507. doi:10.1016/j.ijhydene.2011.08.052

Xu, Z., Shi, Y. X., Li, L. L., Sun, H., R., Amin, M. D. S., Guo, F., et al. (2022). Fabrication of 2D/2D Z-scheme highly crystalline carbon nitride/δ-Bi_2O_3 heterojunction photocatalyst with enhanced photocatalytic degradation of tetracycline. *J. Alloys Compd.* 895, 162667. doi:10.1016/j.jallcom.2021.162667

Yu, L., Zhang, X., Zhuang, C., Lin, L., Li, R., and Peng, T. (2014). Syntheses of asymmetric zinc phthalocyanines as sensitizer of Pt-loaded graphitic carbon nitride for efficient visible/near-IR-light-driven H_2 production. *Phys. Chem. Chem. Phys.* 16 (9), 4106–4114. doi:10.1039/c3cp54316a

Yue, B., Li, Q., Iwai, H., Kako, T., and Ye, J. (2011). Hydrogen production using zinc-doped carbon nitride catalyst irradiated with visible light. *Sci. Technol. Adv. Mat.* 12 (3), 034401034401–034401/7. doi:10.1088/1468-6996/12/3/034401

Zada, A., Khan, M., Qureshi, M. N., Liu, S. Y., and Wang, R. D. (2019). Accelerating photocatalytic hydrogen production and pollutant degradation by functionalizing g-C_3N_4 with SnO_2. *Front. Chem.* 7, 941. doi:10.3389/fchem.2019.00941

Zeng, Y., Liu, X., Liu, C., Wang, L., Xia, Y., Zhang, S., et al. (2018). Scalable one-step production of porous oxygen-doped g-C_3N_4 nanorods with effective electron separation for excellent visible-light photocatalytic activity. *Appl. Catal. B Environ.* 224, 1–9. doi:10.1016/j.apcatb.2017.10.042

Zhang, G., Zhang, M., Ye, X., Qiu, X., Lin, S., and Wang, X. (2014). Iodine modified carbon nitride semiconductors as visible light photocatalysts for hydrogen evolution. *Adv. Mat.* 26 (5), 805–809. doi:10.1002/adma.201303611

Zhang, J. Y., Wang, Y. H., Jin, J., Lin, Z., Huang, F., Yu, J. G., et al. (2013). Efficient visible-light photocatalytic hydrogen evolution and enhanced photostability of core/shell CdS/g-C_3N_4 nanowires. *ACS Appl. Mat. Interfaces* 5 (20), 10317–10324. doi:10.1021/am403327g

Zhang, P., Song, T., Wang, T., and Zeng, H. (2017). Effectively extending visible light absorption with a broad spectrum sensitizer for improving the H_2 evolution of *in-situ* Gu/g-C_3N_4 nanocomponents. *Int. J. Hydrogen Energy* 42 (21), 14511–14521. doi:10.1016/j.ijhydene.2017.04.234

Zhang, P., Wang, T., and Zeng, H. (2017). Design of Cu-Cu_2O/g-C_3N_4 nanocomponent photocatalysts for hydrogen evolution under visible light irradiation using water-soluble Erythrosin B dye sensitization. *Appl. Surf. Sci.* 391, 404–414. doi:10.1016/j.apsusc.2016.05.162

Zhang, S., Khan, I., Qin, X., Qi, K., Liu, Y., and Bai, S. (2020). Construction of 1D Ag-AgBr/AlOOH plasmonic photocatalyst for degradation of tetracycline hydrochloride. *Front. Chem.* 8, 117. doi:10.3389/fchem.2020.00117

Zhang, X., Peng, B., Zhang, S., and Peng, T. (2015). Robust wide visible-light-responsive photoactivity for H_2 production over a polymer/polymer heterojunction photocatalyst: The significance of sacrificial reagent. *ACS Sustain. Chem. Eng.* 3 (7), 1501–1509. doi:10.1021/acssuschemeng.5b00211

Zhang, X., Peng, T., Yu, L., Li, R., Li, Q., and Li, Z. (2015). Visible/near-infrared-light-induced H_2 production over g-C_3N_4 Co-sensitized by organic dye and zinc phthalocyanine derivative. *ACS Catal.* 5 (2), 504–510. doi:10.1021/cs5016468

Zhang, X. W., Zhu, Y. F., Chen, X. Q., Shen, W. H., and Lutes, R. (2018). How does binuclear zinc amidohydrolase FwdA work in the initial step of methanogenesis: From formate to formyl-methanofuran. *J. Inorg. Biochem.* 3 (2), 71–79. doi:10.1016/j.jinorgbio.2018.05.004

Zhang, X., Yu, L., Zhuang, C., Peng, T., Li, R., and Li, X. (2014). Highly asymmetric phthalocyanine as a sensitizer of graphitic carbon nitride for extremely efficient photocatalytic H_2 production under near-infrared light. *ACS Catal.* 4 (1), 162–170. doi:10.1021/cs400863c

Zhang, Y., Liu, J., Wu, G., and Chen, W. (2012). Porous graphitic carbon nitride synthesized via direct polymerization of urea for efficient sunlight-driven photocatalytic hydrogen production. *Nanoscale* 4 (17), 5300–5303. doi:10.1039/c2nr30948c

Zhao, S., Xu, J., Mao, M., Li, L., and Li, X. (2021). Protonated g-C_3N_4 cooperated with Co-MOF doped with Sm to construct 2D/2D heterojunction for integrated dye-sensitized photocatalytic H_2 evolution. *J. Colloid Interface Sci.* 583, 435–447. doi:10.1016/j.jcis.2020.09.063

Zhao, S., Zhang, Y. W., Zhou, Y. M., Wang, Y., Qiu, K., Zhang, C., et al. (2018). Facile one-step synthesis of hollow mesoporous g-C_3N_4 spheres with ultrathin nanosheets for photoredox water splitting. *Carbon* 126, 247–256. doi:10.1016/j.carbon.2017.10.033

Zhao, W., She, T., Zhang, J., Wang, G., Zhang, S., Wei, W., et al. (2021). A novel z-scheme CeO_2/g-C_3N_4 heterojunction photocatalyst for degradation of bisphenol A and hydrogen evolution and insight of the photocatalysis mechanism. *J. Mater. Sci. Technol.* 85, 18–29. doi:10.1016/j.jmst.2020.12.064

Zhao, Y., Zada, A., Yang, Y., Pan, J., Wang, Y., Yan, Z., et al. (2021). Photocatalytic removal of antibiotics on g-C_3N_4 using amorphous CuO as cocatalysts. *Front. Chem.* 9, 797738. doi:10.3389/fchem.2021.797738

Zhong, X., Wang, G., Papandrea, B., Li, M., Xu, Y., Chen, Y., et al. (2015). Reduced graphene oxide/silicon nanowire heterostructures with enhanced photoactivity and superior photoelectrochemical stability. *Nano Res.* 8 (9), 2850–2858. doi:10.1007/s12274-015-0790-2

Zhu, T., Song, Y., Ji, H., Xu, Y., Song, Y., Xia, J., et al. (2015). Synthesis of g-C_3N_4/Ag_3VO_4 composites with enhanced photocatalytic activity under visible light irradiation. *Chem. Eng. J.* 271, 96–105. doi:10.1016/j.cej.2015.02.018

Zhu, Y., Wang, T., Xu, T., Li, Y., and Wang, C. (2019). Size effect of Pt co-catalyst on photocatalytic efficiency of g-C_3N_4 for hydrogen evolution. *Appl. Surf. Sci.* 464, 36–42. doi:10.1016/j.apsusc.2018.09.061

Zhuang, J., Zhang, J., Pang, J., Wang, A., Wang, X., and Zhu, W. (2019). Fabrication of pyrimidine/g-C_3N_4 nanocomposites for efficient photocatalytic activity under visible-light illumination. *Dyes Pigments* 163, 634–640. doi:10.1016/j.dyepig.2018.12.046

Zou, X., Dong, Y., Li, X., Zhao, Q., Cui, Y., and Lu, G. (2015). Inorganic-organic photocatalyst $BiPO_4$/g-C_3N_4 for efficient removal of gaseous toluene under visible light irradiation. *Catal. Commun.* 69, 109–113. doi:10.1016/j.catcom.2015.04.035

Frontiers in Chemistry

TYPE Original Research
PUBLISHED 14 November 2022
DOI 10.3389/fchem.2022.1069816

EDITED BY
Guangzhao Wang,
Yangtze Normal University, China

REVIEWED BY
Kai Wang,
Hubei Normal University, China
Xibao Li,
Nanchang Hangkong University, China

*CORRESPONDENCE
Shu-Yuan Liu,
liushuyuan@symc.edu.cn
Ying Liu,
yingliusd@163.com
Iltaf Khan,
doctoriltafkhan@just.edu.cn

SPECIALTY SECTION
This article was submitted to Photocatalysis and Photochemistry, a section of the journal Frontiers in Chemistry

RECEIVED 17 October 2022
ACCEPTED 28 October 2022
PUBLISHED 14 November 2022

CITATION
Song J, Zhao K, Yin X, Liu Y, Khan I and Liu S-Y (2022), Photocatalytic degradation of tetracycline hydrochloride with g-C_3N_4/Ag/AgBr composites.
Front. Chem. 10:1069816.
doi: 10.3389/fchem.2022.1069816

Photocatalytic degradation of tetracycline hydrochloride with g-C_3N_4/Ag/AgBr composites

Jiahe Song[1], Kun Zhao[1], Xiangbin Yin[1], Ying Liu[1]*, Iltaf Khan[2]* and Shu-Yuan Liu[3]*

[1]Institute of Catalysis for Energy and Environment, College of Chemistry and Chemical Engineering, Shenyang Normal University, Shenyang, China, [2]School of Environmental and Chemical Engineering, Jiangsu University of Science and Technology, Zhenjiang, China, [3]Department of Pharmacology, Shenyang Medical College, Shenyang, China

Graphite carbon nitride (g-C_3N_4), as a polymer semiconductor photocatalyst, is widely used in the treatment of photocatalytic environmental pollution. In this work, a Z-scheme g-C_3N_4/Ag/AgBr heterojunction photocatalyst was prepared based on the preparation of a g-C_3N_4-based heterojunction *via in-situ* loading through photoreduction method. The g-C_3N_4/Ag/AgBr composite showed an excellent photocatalytic performance in the degradation of tetracycline hydrochloride pollutants. Among the prepared samples, g-C_3N_4/Ag/AgBr-8% showed the best photocatalytic ability for the degradation of tetracycline hydrochloride, whose photocatalytic degradation kinetic constant was 0.02764 min^{-1}, which was 9.8 times that of g-C_3N_4, 2.4 times that of AgBr, and 1.9 times that of Ag/AgBr. In the photocatalytic process, $^{\bullet}O^{2-}$ and $^{\bullet}OH$ are main active oxygen species involved in the degradation of organic pollutants. The photocatalytic mechanism of g-C_3N_4/Ag/AgBr is mainly through the formation of Z-scheme heterojunctions, which not only effectively improves the separation efficiency of photogenerated electron-hole pairs, but also maintains the oxidation and reduction capability of AgBr and g-C_3N_4, respectively.

KEYWORDS

G-C_3N_4, Ag/AgBr, Z-scheme heterojunction, photocatalytic degradation, tetracycline hydrochloride

Introduction

With the rapid development of social economy and the chemical industry, all kinds of pollutants, such as heavy metal ions, organic pesticides, chemical dyes, medical residues and other pollutants, are discharged into water bodies in large quantities and participate in water cycle, leading to the deterioration of water environment, which has posed a huge threat to human life and health as well as the survival of various aquatic organisms. In the pharmaceutical industry, with an increasing demand for drugs, especially antibiotics, antibiotics have begun to be widely used worldwide. Antibiotics cannot be completely absorbed after entering human or animal bodies, leading the unabsorbed antibiotics to be discharged into the water environment as metabolites, which are even in their original state with metabolic activities. Antibiotics of low doses discharged into the environment for a long time will lead to an enhanced drug resistance for sensitive bacteria. Moreover, drug-resistance genes can expand and evolve in the environment, posing a potential threat to the ecological environment and human health. In addition to causing bacterial resistance, antibiotics may also produce certain toxicity to other organisms. Therefore, as new micro-pollutants, antibiotics have characteristics including a low concentration, a high toxicity and a difficult treatment in the environment.

Traditional water treatment technologies mainly include physical, chemical and biological methods. Physical methods refer to enriching and treating pollutants in turn by physical means, which have characteristics including relatively simple operation and a low cost, but they are easy to cause secondary pollution (Qi et al., 2022). Chemical methods refer to water treatment methods through which organic pollutants are oxidized by adding strong oxidizing chemicals. However, in practical application, a high use of oxidants is required, which may cause secondary pollution very easily due to incomplete reactions. Biological methods refer to further transforming organic matters in water into nutrients or other small molecular substances required by microorganisms through the metabolism of microorganisms. The process of microbial methods is simple, through which secondary pollution can be avoided. However, a microbial treatment cycle is long and the microbial activity is greatly affected by the outside world, which is not conducive to the treatment of organic wastewater that is difficult to be biodegraded due to the changeable environment. Therefore, it is urgent to find a new water pollution treatment technology with a high efficiency, a low cost and less secondary pollution.

In photocatalysis technology, solar energy is used to drive and excite light catalysts to produce a variety of strong-oxidizing active substances, destroy the molecular structure of pollutants, and finally convert organic pollutants into CO_2, H_2O or other pollution-free small molecules, which can be directly discharged into the environment (Wang et al., 2019; Li et al., 2020b; Li et al., 2022b; Wang L. et al., 2022). Compared with traditional water pollution treatment methods, the photocatalytic degradation method has advantages including a high efficiency, simplicity, a good reproducibility and an easy treatment, which is often used to degrade organic pollutants (Li et al., 2022a; Tao et al., 2022; Wang W. et al., 2022). The core of photocatalysis technology is the development of new photocatalysts (Yang et al., 2021; Wang et al., 2022c; Wang et al., 2022e). At present, traditional semiconductor photocatalyst materials are mainly inorganic compounds, but their large-scale application has been restricted due to limited resources.

Graphite like carbon nitride (g-C_3N_4) is a polymeric semiconductor photocatalyst material. Compared with traditional photocatalysts such as metal oxides, metal sulfides and metal halides, g-C_3N_4 is a non-metallic semiconductor material with a narrow band gap of ~2.7 eV, which has attracted extensive attention due to its unique optical and electronic properties, a high controllability, a good chemical stability, non-toxicity and other characteristics. A large number of studies have shown that g-C_3N_4 is an ideal photocatalyst material in terms of the photocatalytic treatment of water and air pollution as well as hydrogen production, etc (Li et al., 2020a; Xiong et al., 2020; Li et al., 2021; Wang et al., 2022b). However, g-C_3N_4 itself has some shortcomings, especially its small specific surface area and high photogenerated electron-hole recombination rate, which reduce its photocatalytic efficiency and utilization meanwhile limiting its industrial application (Wang et al., 2022a; Li et al., 2022c; Wang et al., 2022d). Therefore, the research on g-C_3N_4 to improve its photocatalytic activity has become a research hotspot.

To improve the photocatalytic activity of g-C_3N_4, researchers usually modify existing photocatalysts. Nowadays, there are several ways to modify them, including element doping, noble metal modification, semiconductor recombination or improving the photocatalytic performance of materials by changing their microstructure. Therefore, the structure and physicochemical properties of g-C_3N_4 can be changed through defect regulation, surface noble metal modification and semiconductor material recombination, so that it can have a wider visible light absorption range, its electron-hole recombination efficiency is reduced and its photocatalytic activity is improved.

In this study, silver (Ag), a noble metal matching the Fermi level of g-C_3N_4, was selected to modify g-C_3N_4, change its energy band structure and form a plasma effect. At the same time, semiconductor materials AgBr and g-C_3N_4 were compounded to form a Z-type heterostructure, whose purpose was to enhance the light absorption capacity of photocatalysts, improve the separation efficiency of photogenerated carriers and enhance the redox capacity as well as activity of photocatalysts. The photocatalytic activity of the photocatalysts obtained was investigated through the simulated solar light degradation of tetracycline hydrochloride with the g-C_3N_4/Ag/AgBr composites prepared. The charge separation and migration behavior of the samples prepared were studied through different characterization and analysis methods. The possible enhancement mechanism of photocatalysis was reasonably described in combination with the results of a free radical capture experiment based on the semiconductor energy band theory.

Experimental section

Preparation

The g-C_3N_4 catalyst is prepared by placing melamine in a crucible and firing it in a muffle furnace at 550°C for 4 h, then the samples obtained are grinded and collected after cooling. To load different amounts of Ag/AgBr on the surface of g-C_3N_4 and produce g-C_3N_4/Ag/AgBr composites, g-C_3N_4-Ag/AgBr photocatalyst was prepared through simple *in-situ* coprecipitation method and photo-reduction-assisted method. The specific steps are as follows: 0.2 g of g-C_3N_4 is dispersed in 60 ml of deionized water to obtain Solution A. Then $AgNO_3$ (0.1 mol/L) solutions of different volumes are added to Solution A respectively, which are continuously stirred for 30 min. Then, drop KBr (0.1 mol/L) solution into the above solutions respectively, and continue stirring in a dark condition for 3 h. After this step is completed, irradiate the solution under a xenon lamp for 1 h, and finally naturally cool the whole system to room temperature. After centrifugation, wash the solution with anhydrous ethanol and deionized water for three times alternately. Dry the collected samples in an oven at 70°C for 12 h, and finally grind and collect them. By changing the volume of $AgNO_3$ solution added, g-C_3N_4/Ag/AgBr composites loaded with 4 wt%, 6 wt%, 8 wt%, and 10 wt% of Ag can be obtained, which are labeled as g-C_3N_4/Ag/AgBr-4%, g-C_3N_4/Ag/AgBr-6%, g-C_3N_4/Ag/AgBr-8%, and g-C_3N_4/Ag/AgBr-10% respectively. AgBr and Ag/AgBr monomers are prepared through the same preparation process as above without adding g-C_3N_4.

Characterization

The crystal structure of the samples was obtained *via* an XRD diffractometer produced by Bruker D8, Germany, with a scanning range of 10°–80°. TEM and HRTEM photos were obtained through transmission electron microscopy (JEOL 2100). For a Fourier transform infrared (FTIR) analysis, a Nicolet Magna 560 spectrophotometer (US) was used. An ESCALAB MKII X-ray photoelectron spectrometer (UK) and Mg-K α were used. The binding energy and element state of composite materials were measured through radiation. The ultraviolet-visible absorption spectrum (UV-vis DRS) of the samples at the wavelength of 200–800 nm was measured by a spectrophotometer with an integrating sphere (Hitachi, U-4100), with $BaSO_4$ as the reference.

Photocatalytic activity test

The photocatalytic activity of g-C_3N_4/Ag/AgBr composite in the degradation of tetracycline hydrochloride is measured at room temperature. The specific experimental steps are as follows: before the photochemical reaction, 50 ml of tetracycline hydrochloride solution (20 mg/L) and 32 mg of g-C_3N_4/Ag/AgBr composite photocatalyst were added and stirred in the dark for 1 h to achieve an adsorption-desorption equilibrium. Then the reaction mixture was irradiated with an iodine tungsten lamp to induce the occurrence of photocatalytic reaction. During the reaction, 3 ml of reaction solution was extracted from the reaction system every 20 min, which was added to the UV cuvette after centrifugation and filtration. The absorbance was measured by a UV-visible spectrophotometer. The concentration of tetracycline hydrochloride was determined at its maximum absorption wavelength of 356 nm by an ultraviolet spectrophotometer.

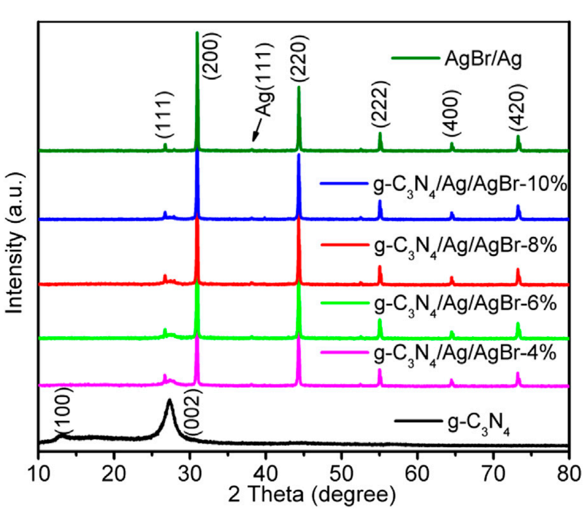

FIGURE 1
XRD pattern of g-C_3N_4, Ag/AgBr, and g-C_3N_4/Ag/AgBr.

Results and discussion

XRD

The composition and crystal phase of the g-C_3N_4/Ag/AgBr composite are analyzed through XRD measurement. The XRD diffraction spectra of each sample are shown in Figure 1. Among them, the diffraction peak at 13.1° corresponds to crystal plane (100) of g-C_3N_4, representing a regular arrangement of 3-s-triazine ring units on the g-C_3N_4 plane; the diffraction peak at about 27.5° belongs to crystal plane (002) of g-C_3N_4, representing the layer spacing among g-C_3N_4 layers (Qi et al., 2020a). The main XRD diffraction peaks of Ag/AgBr appear at 26.7°, 31.0°, 44.3°, 55.0°, 64.5°, and 73.3°, whose corresponding crystal planes are plane (111), (200), (220), (222), (400), and (420) of AgBr (JCPDS: 06-0438) (Chen et al., 2020). In addition, a weak diffraction peak can also be observed at 38.1°, which corresponds to plane 111) of Ag (JCPDS: 04-0783) (Li S. et al., 2020). The characteristic peaks of g-C_3N_4 and AgBr can be observed in the XRD diffraction pattern of the g-C_3N_4/Ag/AgBr composite, indicating the existence of g-C_3N_4 and AgBr in the composite. In addition, the peaks of Ag can also be observed. However, due to the low content and uniform dispersion of Ag in the system, the diffraction peak intensity is weak.

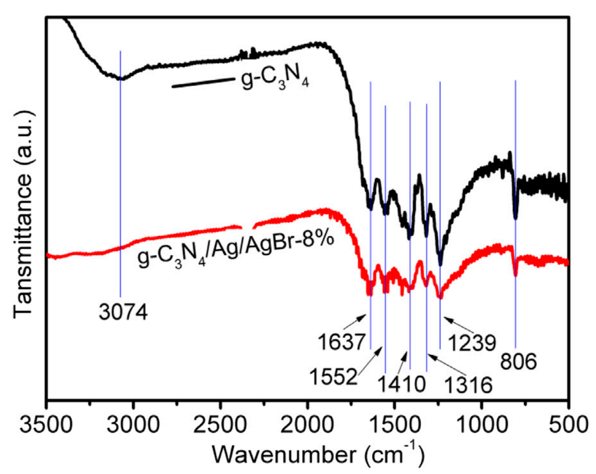

FIGURE 2
FTIR spectrum of g-C_3N_4 and g-C_3N_4/Ag/AgBr-8%.

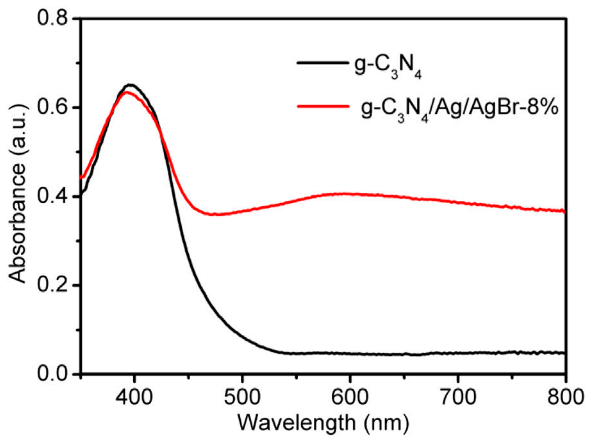

FIGURE 3
UV–vis DRS spectrum of g-C_3N_4 and g-C_3N_4/Ag/AgBr-8%.

Fourier transform infrared

The chemical bonds and functional group composition of g-C_3N_4/Ag/AgBr-8% and g-C_3N_4 were studied *via* FTIR measurement, as is shown in Figure 2. The absorption peak between 1239 and 1637 cm^{-1} in the g-C_3N_4 spectrum corresponds to the typical C (sp^2) = N and C (sp^2)-N stretching vibration (Qi et al., 2020b). The wider absorption peak at 3,074 cm^{-1} is attributed to the N-H stretching vibration of g-C_3N_4 or the O-H stretching vibration of adsorbed water (Qi et al., 2021). In addition, the peak at 806 cm^{-1} corresponds to the vibration mode absorption band of triazine (Zhao et al., 2020). It can be seen from the spectrum that the absorption peak of g-C_3N_4/Ag/AgBr-8% is similar to the characteristic absorption peak of g-C_3N_4. When Ag/AgBr is compounded with g-C_3N_4, the intensity of the absorption peak of the g-C_3N_4/Ag/AgBr sample becomes weak, indicating the successful preparation of the composite photocatalyst.

Ultraviolet-visible diffuse reflectance spectroscopy

The optical absorption property of samples was analyzed *via* ultraviolet-visible diffuse reflectance spectroscopy (UV-DRS). The UV-DRS spectrum of g-C_3N_4 and g-C_3N_4/Ag/AgBr-8% is shown in Figure 3, whose light absorption edge is located at about 456 nm and 480 nm. Compared with g-C_3N_4, the absorption band of the g-C_3N_4/Ag/AgBr-8% composite is red shifted, its visible light absorption range is increased, and the energy required for its transition is reduced, which is due to the introduction of Ag/AgBr. A stronger absorption is also shown in the whole wavelength range of visible light, which is also attributed to the surface adsorption of Ag/AgBr nanoparticles.

TEM

To further identify the microstructure of the g-C_3N_4/Ag/AgBr-8% composite in detail, the material was characterized through TEM measurement. Figure 4A shows the images of the local sheet structure of g-C_3N_4/Ag/AgBr-8%, where Ag/AgBr can be observed on the surface of the sheet. In addition, the nanoparticles formed by the accumulation of reduced Ag can also be observed. EDS technology was used to study the composition and spatial distribution of elements in the sample. Figure 4B shows the distribution of elements C, N, Ag, and Br, which are uniformly distributed on the whole composite, indicating that AgBr is successfully and uniformly loaded on the surface of g-C_3N_4. The above TEM results show that g-C_3N_4, Ag, and AgBr are in close contact with each other, and a heterojunction structure is formed between each two components, which is conducive to the separation and transfer of photogenerated charges, and is also one of the main reasons for the enhanced photocatalytic activity.

XPS

The chemical composition and element valence changes in g-C_3N_4/Ag/AgBr-8% composite were analyzed *via* XPS measurement, as is shown in Figure 5. Figure 5A shows that the high-resolution XPS spectrum of C 1s can be divided into four peaks with a binding energy of 284.75, 285.50, 288.15, and 288.70 eV. The peak is located at 284.75 eV, which corresponds to the adventitious surface carbon (Qi et al., 2019a). The peak at 285.50 eV is a C-C bond group (Qi et al., 2020c). The peaks at

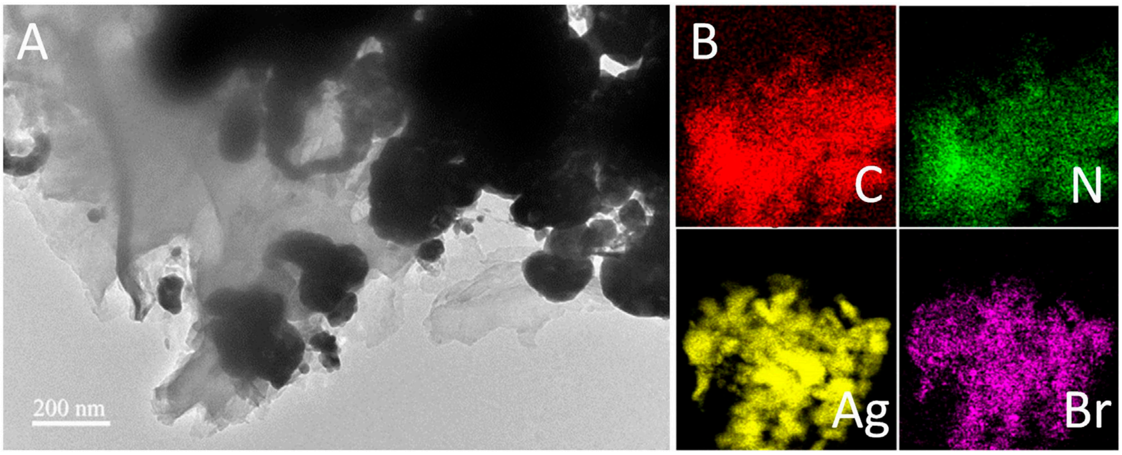

FIGURE 4
(A) TEM image of g-C_3N_4/Ag/AgBr-8% and **(B)** corresponding elemental mapping of C, N, Ag, and Br.

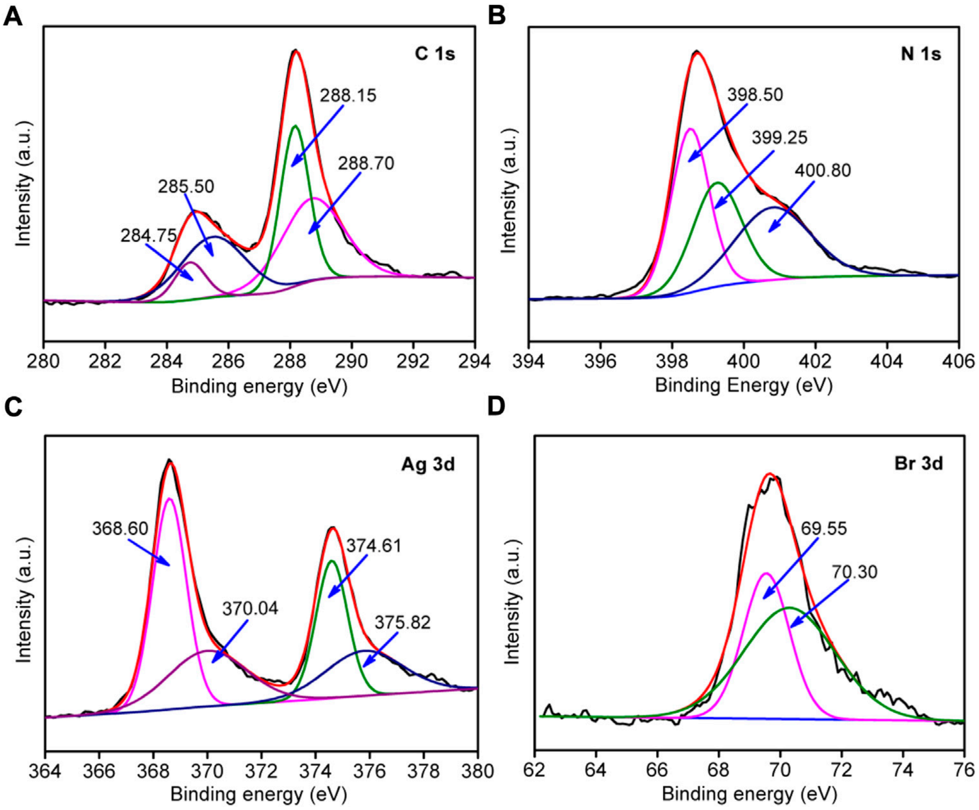

FIGURE 5
High-resolution XPS spectra of g-C_3N_4/Ag/AgBr-8% for C 2p **(A)**, N2p **(B)**, Br 1s **(C)**, and Ag 3d **(D)**.

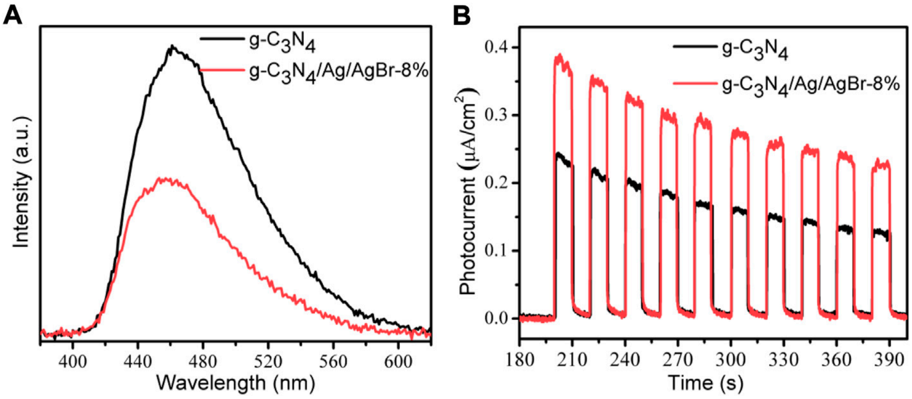

FIGURE 6
PL spectrum **(A)** and photocurrent response **(B)** of g-C_3N_4 and g-C_3N_4/Ag/AgBr-8%.

288.15 and 288.70 eV are an assigned N-C=N bond and C-$(N)_3$ respectively (Liu et al., 2022). Figure 5B shows that the N1s spectrum can be divided into three peaks with a binding energy of 398.50, 399.25, and 400.80 eV respectively. The peak with a binding energy of 398.50 eV corresponds to the C-N=C bond of the 3-s-triazine ring, and the peaks at 399.25 as well as 400.80 eV belong to the C-$(N)_3$ and N-H structure respectively (Zhao et al., 2021). Figure 5C shows the high-resolution energy spectrum of Ag 3d, and four peaks with different positions can be obtained through further fitting. The peaks with a binding energy of 368.60 eV and 374.61 eV belong to Ag^+ $3d_{5/2}$ and Ag^+ $3d_{3/2}$ in AgBr. The peaks with a binding energy of 370.04 eV and 375.82 eV belong to Ag^0 $3d_{5/2}$ and Ag^0 $3d_{3/2}$, indicating the existence of Ag simple substances (Qi et al., 2019b). As is shown in Figure 5D, there are peaks of Br $3d_{5/2}$ and Br $3d_{3/2}$ at 69.55 and 70.30 eV in the binding energy of Br 3d, indicating that Br element exists in the system with a negative valence (Zhang et al., 2020).

Photoluminescence and photocurrent analysis

Photoluminescence spectra (PL) can reflect the transport efficiency of a carrier to some extent. Generally, the higher the recombination rate of photogenerated carriers is, the stronger the corresponding fluorescence intensity will be. The fluorescence spectrum of g-C_3N_4 and g-C_3N_4/Ag/AgBr-8% composite was characterized, whose results were obtained, as is shown in Figure 6A. Compared with g-C_3N_4, the PL intensity of g-C_3N_4/Ag/AgBr-8% is weaker, which indicates that the loading of Ag/AgBr on g-C_3N_4 is conducive to the separation of photogenerated carriers, which will help to improve the photocatalytic activity.

Photocurrent density is an effective means to reveal the separation and transmission characteristics of photogenerated electrons in semiconductor materials. The higher the photocurrent density is, the higher the separation efficiency of photogenerated carriers is. Through the electrode preparation method, g-C_3N_4 and g-C_3N_4/Ag/AgBr-8% composite was prepared into corresponding working electrodes, and a transient photocurrent cycle test was carried out in light and dark conditions. The photocurrent results are shown in Figure 6B. Both the two materials can generate photocurrent under simulated solar light irradiation, indicating that they can be excited to generate photogenerated carriers under simulated solar light irradiation. The photocurrent intensity produced by g-C_3N_4/Ag/AgBr-8% (~0.28 μA/cm^2) is higher than that produced by g-C_3N_4 (~0.16 μA/cm^2), indicating that the separation effect of photogenerated electron-hole pairs is enhanced by constructing heterojunctions between g-C_3N_4 and Ag/AgBr.

Photocatalytic activity

To explore the effect of g-C_3N_4/Ag/AgBr composite on improving the photocatalytic activity under simulated solar light irradiation, the g-C_3N_4/Ag/AgBr composite prepared was used to conduct a degradation experiment on tetracycline hydrochloride solution under simulated sunlight irradiation. Figure 7A shows the photodegradation efficiency of tetracycline hydrochloride using g-C_3N_4, AgBr, Ag/AgBr, and g-C_3N_4/Ag/AgBr as photocatalysts in 30 min, within which tetracycline hydrochloride has degraded by 57.5% with g-C_3N_4/Ag/AgBr-8% as the photocatalyst. Compared with AgBr (30.0%), Ag/AgBr (35.0%), and g-C_3N_4 (8.9%), it can be seen that the photocatalytic activity of g-C_3N_4/Ag/AgBr sample has been significantly improved after constructing

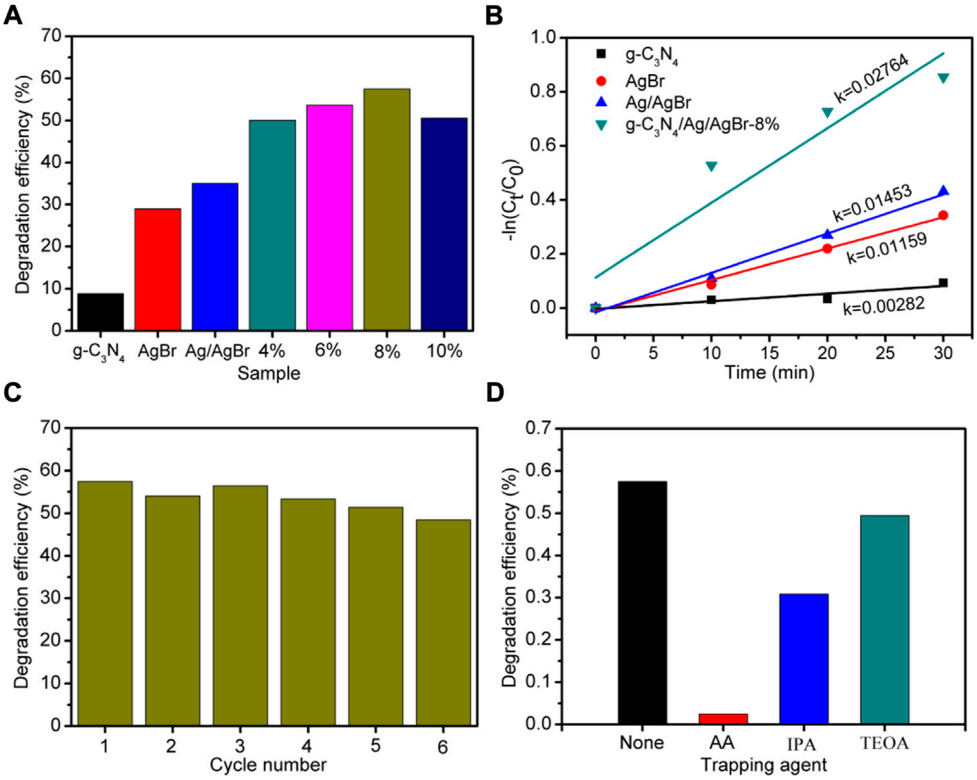

FIGURE 7
(A) Photodegradation efficiency of tetracycline hydrochloride using g-C_3N_4, AgBr, Ag/AgBr, and g-C_3N_4/Ag/AgBr as photocatalysts in 30 min. Here x% represents the sample of g-C_3N_4/Ag/AgBr-x%. **(B)** Reaction rate curve, **(C)** recycling test and **(D)** free radical capture experiment on g-C_3N_4/Ag/AgBr-8%.

heterojunctions between g-C_3N_4 and Ag/AgBr. Figure 7B shows that g-C_3N_4 has the lowest photocatalytic degradation rate, followed by AgBr, and Ag/AgBr has the lowest photocatalytic activity. The kinetic constant of the sample is as high as 0.02764 min^{-1}, which is 9.8 times that of g-C_3N_4, 2.4 times that of AgBr and 1.9 times that of Ag/AgBr. The photocatalytic activity of the g-C_3N_4/Ag/AgBr composite is higher than that of g-C_3N_4, AgBr, and Ag/AgBr. Among them, the g-C_3N_4/Ag/AgBr-8% sample has the best photocatalytic activity, which also maintains a good stability within six cycles (Figure 7C).

In order to determine the formation and effect of different reactive oxygen species in the photocatalytic process, g-C_3N_4/Ag/AgBr-8% is used as the photocatalyst to conduct capture agent experiments, and the results are shown in Figure 7D. In these experiments, ascorbic acid (AA), triethanolamine (TEOA) and isopropanol (IPA) were introduced into the reaction mixture respectively, corresponding to the capture of superoxide radicals ($^\bullet O^{2-}$), holes (h^+) and hydroxyl radicals ($^\bullet OH$) respectively. It can be seen that although TEOA was added, the decomposition of antibiotics was not significantly hindered. However, in the presence of AA and IPA, the photocatalytic efficiency decreased significantly, especially in the condition where AA was added. This shows that $^\bullet OH$ and $^\bullet O^{2-}$ are two main reactive oxygen species for the decomposition of tetracycline antibiotics.

Photocatalytic mechanism

According to the energy band positions of AgBr and g-C_3N_4, a traditional type-II heterojunction mechanism may be possibly formed between AgBr and g-C_3N_4, as is shown in Figure 8A. Under simulated solar light irradiation, both AgBr and g-C_3N_4 can be excited to generate electrons and holes. The holes on the VB of AgBr will migrate to that of g-C_3N_4, and the electrons on the CB of g-C_3N_4 will transfer to AgBr, which is conducive to further participating in the photocatalytic degradation reaction. However, since the conduction band potential of AgBr (0.057 V vs NHE) is lower than the $O_2/^\bullet O^{2-}$ potential (−0.046 V vs NHE) (Ye et al., 2012) and the valence band potential of g-C_3N_4 (1.58 V vs NHE) is lower than the $H_2O/^\bullet OH$ potential (2.40 V vs NHE) (Tian et al., 2015), the electrons accumulated in the AgBr conduction band and the h^+ accumulated in the g-C_3N_4

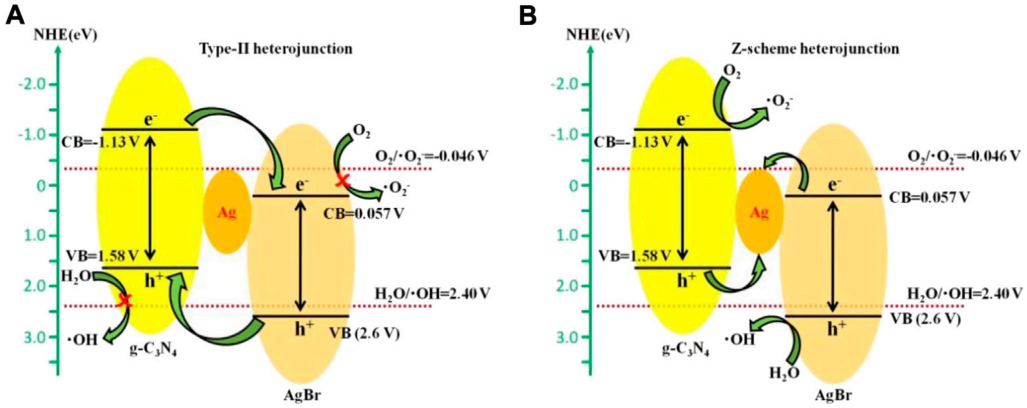

FIGURE 8
Photocatalytic mechanism of g-C_3N_4/Ag/AgBr based on **(A)** type-II heterojunction **(A)** and Z-type heterojunction **(B)**.

valence band cannot further generate $^{\bullet}O^{2-}$ or $^{\bullet}OH$. Therefore, AgBr and g-C_3N_4 contact through traditional type-II heterojunctions, $^{\bullet}O^{2-}$ and $^{\bullet}OH$ cannot be formed in the system, and type-II heterojunctions between AgBr and g-C_3N_4 are not reasonable. On the contrary, the free radical capture experiment results show that $^{\bullet}O^{2-}$ and $^{\bullet}OH$ are main free radicals involved in the photocatalytic degradation process. Therefore, it can be inferred that photogenerated electrons and holes in the g-C_3N_4/Ag/AgBr composite are not transferred through the traditional type-II heterojunction mode. A Z-type heterojunction with silver nanoparticles as bonds is more suitable for explaining the mechanism of the g-C_3N_4/Ag/AgBr photocatalysis system. As is shown in Figure 8B, the electrons on the AgBr CB will flow to the Ag nanoparticles under simulated solar light irradiation, which then recombine with the holes from the g-C_3N_4 VB, and the photogenerated carriers are effectively separated from the system. The electrons gathering on g-C_3N_4 conduction band can fully react with O_2 to form $^{\bullet}O^{2-}$; the holes on the valence band of AgBr can effectively oxidize H_2O molecules to generate $^{\bullet}OH$ or directly oxidize organic pollutants. Therefore, it can be inferred that a possible photodegradation enhancement mechanism of g-C_3N_4/Ag/AgBr composite is the Z-type heterojunction mechanism.

Conclusion

Based on the development of new g-C_3N_4 heterojunction composite photocatalyst materials, a Z-scheme g-C_3N_4/Ag/AgBr photocatalyst was prepared in this work by loading AgBr on g-C_3N_4, and then AgBr was reduced to Ag through the photoreduction process. The composite material g-C_3N_4/Ag/AgBr shows a good ability in the photocatalysis and degradation of tetracycline hydrochloride under simulated solar light irradiation. Among them, g-C_3N_4/Ag/AgBr-8% shows the best photocatalytic degradation ability for tetracycline hydrochloride, and its photocatalytic degradation kinetic constant is as high as 0.02764 min^{-1}. The photocatalytic activity of g-C_3N_4/Ag/AgBr-8% is 9.8 times that of g-C_3N_4 and 1.48 times that of AgBr. The photocurrent response and PL spectra indicate that g-C_3N_4/Ag/AgBr composite has a high photo-induced charge separation efficiency. The main active species are $^{\bullet}O^{2-}$ and $^{\bullet}OH$, which are involved in the photodegradation of organic pollutants. The enhanced photocatalysis mechanism of g-C_3N_4/Ag/AgBr composite is mainly attributed to the establishment of a Z-type heterojunction system with silver nanoparticles as the composite center, which makes the energy bands of g-C_3N_4 and AgBr match, meanwhile the electrons and holes can shift between their conduction bands and valence bands, effectively reducing the electron hole recombination rate.

Data availability statement

The original contributions presented in the study are included in the article/supplementary material, further inquiries can be directed to the corresponding authors.

Author contributions

JS and KZ conducted catalysts synthesis and activity test. XY carried out the characterization. YL and IK contributed to data analysis and discussed the photocatalytic mechanism. S-YL conceived the project and wrote the manuscript.

Funding

This work was supported by National Natural Science Foundation of China (22202138).

Conflict of interest

The authors declare that the research was conducted in the absence of any commercial or financial relationships that could be construed as a potential conflict of interest.

The handling editor declared a past co-authorship with the author SL.

Publisher's note

References

Chen, M., Guo, C., Hou, S., Lv, J., Zhang, Y., Zhang, H., et al. (2020). A novel Z-scheme AgBr/P-g-C_3N_4 heterojunction photocatalyst: Excellent photocatalytic performance and photocatalytic mechanism for ephedrine degradation. *Appl. Catal. B Environ.* 266, 118614. doi:10.1016/j.apcatb.2020.118614

Li, S., Zhang, M., Qu, Z., Cui, X., Liu, Z., Piao, C., et al. (2020). Fabrication of highly active Z-scheme Ag/g-C_3N_4-Ag-Ag_3PO_4 (110) photocatalyst photocatalyst for visible light photocatalytic degradation of levofloxacin with simultaneous hydrogen production. *Chem. Eng. J.* 382, 122394. doi:10.1016/j.cej.2019.122394

Li, X., Kang, B., Dong, F., Deng, F., Han, L., Gao, X., et al. (2022a). BiOBr with oxygen vacancies capture 0D black phosphorus quantum dots for high efficient photocatalytic ofloxacin degradation. *Appl. Surf. Sci.* 593, 153422. doi:10.1016/j.apsusc.2022.153422

Li, X., Kang, B., Dong, F., Zhang, Z., Luo, X., Han, L., et al. (2021). Enhanced photocatalytic degradation and H_2/H_2O_2 production performance of S-pCN/$WO_{2.72}$ S-scheme heterojunction with appropriate surface oxygen vacancies. *Nano Energy* 81, 105671. doi:10.1016/j.nanoen.2020.105671

Li, X., Liu, J., Huang, J., Feng, Z., He, C., Chen, Z., et al. (2020a). All organic S-scheme heterojunction PDI-ala/S-C_3N_4 photocatalyst with enhanced photocatalytic performance. *Acta Phys. Chim. Sin.* 37, 2010030. doi:10.3866/pku.whxb202010030

Li, X., Liu, Q., Deng, F., Huang, J., Han, L., He, C., et al. (2022b). Double-defect-induced polarization enhanced OV-BiOBr/$Cu_{2-x}S$ high-low junction for boosted photoelectrochemical hydrogen evolution. *Appl. Catal. B Environ.* 314, 121502. doi:10.1016/j.apcatb.2022.121502

Li, X., Luo, Q., Han, L., Deng, F., Yang, Y., and Dong, F. (2022c). Enhanced photocatalytic degradation and H_2 evolution performance of N CDs/S-C_3N_4 S-scheme heterojunction constructed by π-π conjugate self-assembly. *J. Mater. Sci. Technol.* 114, 222–232. doi:10.1016/j.jmst.2021.10.030

Li, X., Xiong, J., Gao, X., Ma, J., Chen, Z., Kang, B., et al. (2020b). Novel BP/BiOBr S-scheme nano-heterojunction for enhanced visible-light photocatalytic tetracycline removal and oxygen evolution activity. *J. Hazard. Mater.* 387, 121690. doi:10.1016/j.jhazmat.2019.121690

Liu, S., Zada, A., Yu, X., Liu, F., and Jin, G. (2022). $NiFe_2O_4$/g-C_3N_4 heterostructure with an enhanced ability for photocatalytic degradation of tetracycline hydrochloride and antibacterial performance. *Chemosphere* 307, 135717. doi:10.1016/j.chemosphere.2022.135717

Qi, K., Cui, N., Zhang, M., Ma, Y., Wang, G., Zhao, Z., et al. (2021). Ionic liquid-assisted synthesis of porous boron-doped graphitic carbon nitride for photocatalytic hydrogen production. *Chemosphere* 272, 129953. doi:10.1016/j.chemosphere.2021.129953

Qi, K., Li, Y., Xie, Y., Liu, S. y., Zheng, K., Chen, Z., et al. (2019a). Ag loading enhanced photocatalytic activity of g-C_3N_4 porous nanosheets for decomposition of organic pollutants. *Front. Chem.* 7, 91. doi:10.3389/fchem.2019.00091

Qi, K., Liu, S. y., Selvaraj, R., Wang, W., and Yan, Z. (2019b). Comparison of Pt and Ag as co-catalyst on g-C_3N_4 for improving photocatalytic activity: Experimental and DFT studies. *Desalination Water Treat.* 153, 244–252. doi:10.5004/dwt.2019.24079

Qi, K., Liu, S. y., and Zada, A. (2020a). Graphitic carbon nitride, a polymer photocatalyst. *J. Taiwan Inst. Chem. Eng.* 109, 111–123. doi:10.1016/j.jtice.2020.02.012

Qi, K., Lv, W., Khan, I., and Liu, S. y. (2020b). Photocatalytic H_2 generation via CoP quantum-dot-modified g-C_3N_4 synthesized by electroless plating. *Chin. J. Catal.* 41, 114–121. doi:10.1016/s1872-2067(19)63459-5

Qi, K., Zada, A., Yang, Y., Chen, Q., and Khataee, A. (2020c). Design of 2D–2D NiO/g-C_3N_4 heterojunction photocatalysts for degradation of an emerging pollutant. *Res. Chem. Intermed.* 46, 5281–5295. doi:10.1007/s11164-020-04262-0

Qi, K., Zhuang, C., Zhang, M., Gholami, P., and Khataee, A. (2022). Sonochemical synthesis of photocatalysts and their applications. *J. Mater. Sci. Technol.* 123, 243–256. doi:10.1016/j.jmst.2022.02.019

Tao, S., Wan, S., Huang, Q., Li, C., Yu, J., and Cao, S. (2022). Molecular engineering of g-C_3N_4 with dibenzothiophene groups as electron donor for enhanced photocatalytic H_2-production. *Chin. J. Struct. Chem.* 41. doi:10.14102/j.cnki.10254-15861.12022-10068

Tian, N., Huang, H., He, Y., Guo, Y., Zhang, T., and Zhang, Y. (2015). Mediator-free direct Z-scheme photocatalytic system: $BiVO_4$/g-C_3N_4 organic–inorganic hybrid photocatalyst with highly efficient visible-light-induced photocatalytic activity. *Dalton Trans.* 44, 4297–4307. doi:10.1039/c4dt03905j

Wang, G., Long, X., Qi, K., Dang, S., Zhong, M., Xiao, S., et al. (2019). Two-dimensional CdS/g-C_6N_6 heterostructure used for visible light photocatalysis. *Appl. Surf. Sci.* 471, 162–167. doi:10.1016/j.apsusc.2018.12.015

Wang, K., Jiang, L., Xin, T., Li, Y., Wu, X., and Zhang, G. (2022a). Single-atom V-N charge-transfer bridge on ultrathin carbon nitride for efficient photocatalytic H_2 production and formaldehyde oxidation under visible light. *Chem. Eng. J.* 429, 132229. doi:10.1016/j.cej.2021.132229

Wang, K., Peng, L., Shao, X., Cheng, Q., Wang, J., Li, K., et al. (2022b). Nb–O–C charge transfer bridge in 2D/2D Nb_2O_5/g-C_3N_4 S-scheme heterojunction for boosting solar-driven CO_2 reduction: *In situ* illuminated X-ray photoelectron spectroscopy investigation and mechanism insight. *Sol. RRL* 6, 2200434. doi:10.1002/solr.202200434

Wang, K., Shao, X., Zhang, K., Wang, J., Wu, X., and Wang, H. (2022c). 0D/3D $Bi_3TaO_7/ZnIn_2S_4$ heterojunction photocatalyst towards degradation of antibiotics coupled with simultaneous H_2 evolution: *In situ* irradiated XPS investigation and S-scheme mechanism insight. *Appl. Surf. Sci.* 596, 153444. doi:10.1016/j.apsusc.2022.153444

Wang, K., Wang, H., Cheng, Q., Gao, C., Wang, G., and Wu, X. (2022d). Molecular-functionalized engineering of porous carbon nitride nanosheets for wide-spectrum responsive solar fuel generation. *J. Colloid Interface Sci.* 607, 1061–1070. doi:10.1016/j.jcis.2021.09.034

Wang, K., Wang, Q., Zhang, K., Wang, G., and Wang, H. (2022e). Selective solar-driven CO_2 reduction mediated by 2D/2D $Bi_2O_2SiO_3$/MXene nanosheets heterojunction. *J. Mater. Sci. Technol.* 124, 202–208. doi:10.1016/j.jmst.2021.10.059

Wang, L., Fei, X., Zhang, L., Yu, J., Cheng, B., and Ma, Y. (2022). Solar fuel generation over nature-inspired recyclable TiO_2/g-C_3N_4 S-scheme hierarchical thin-film photocatalyst. *J. Mater. Sci. Technol.* 112, 1–10. doi:10.1016/j.jmst.2021.10.016

Wang, W., Li, X., Deng, F., Liu, J., Gao, X., Huang, J., et al. (2022). Novel organic/inorganic PDI-Urea/BiOBr S-scheme heterojunction for improved photocatalytic antibiotic degradation and H_2O_2 production. *Chin. Chem. Lett.* 33, 5200–5207. doi:10.1016/j.cclet.2022.01.058

Xiong, J., Li, X., Huang, J., Gao, X., Chen, Z., Liu, J., et al. (2020). CN/rGO@ BPQDs high-low junctions with stretching spatial charge separation ability for photocatalytic degradation and H_2O_2 production. *Appl. Catal. B Environ.* 266, 118602. doi:10.1016/j.apcatb.2020.118602

Yang, Y., Tan, H., Cheng, B., Fan, J., Yu, J., and Ho, W. (2021). Near-infrared-Responsive photocatalysts. *Small Methods* 5, 2001042. doi:10.1002/smtd.202001042

Ye, L., Liu, J., Gong, C., Tian, L., Peng, T., and Zan, L. (2012). Two different roles of metallic Ag on Ag/AgX/BiO_X (X = Cl, Br) visible light photocatalysts: Surface plasmon resonance and Z-scheme bridge. *ACS Catal.* 2, 1677–1683. doi:10.1021/cs300213m

Zhang, S., Khan, I., Qin, X., Qi, K., Liu, Y., and Bai, S. (2020). Construction of 1D Ag-AgBr/AlOOH plasmonic photocatalyst for degradation of tetracycline hydrochloride. *Front. Chem.* 8, 117. doi:10.3389/fchem.2020.00117

Zhao, K., Khan, I., Qi, K., Liu, Y., and Khataee, A. (2020). Ionic liquid assisted preparation of phosphorus-doped g-C_3N_4 photocatalyst for decomposition of emerging water pollutants. *Mater. Chem. Phys.* 253, 123322. doi:10.1016/j.matchemphys.2020.123322

Zhao, Y., Zada, A., Yang, Y., Pan, J., Wang, Y., Yan, Z., et al. (2021). Photocatalytic removal of antibiotics on g-C_3N_4 using amorphous CuO as cocatalysts. *Front. Chem.* 9, 797738. doi:10.3389/fchem.2021.797738

frontiers | Frontiers in Chemistry

TYPE Original Research
PUBLISHED 30 November 2022
DOI 10.3389/fchem.2022.1069824

OPEN ACCESS

EDITED BY
Guangzhao Wang,
Yangtze Normal University, China

REVIEWED BY
Weiji Dai,
Jiangsu University of Science and Technology, China
Longfei Yang,
Nanjing University of Science and Technology, China

*CORRESPONDENCE
Hongling Ye,
yhl@bbc.edu.cn
Kai Ren,
kairen@njfu.edu.cn

SPECIALTY SECTION
This article was submitted to Electrochemistry, a section of the journal *Frontiers in Chemistry*

RECEIVED 14 October 2022
ACCEPTED 07 November 2022
PUBLISHED 30 November 2022

CITATION
Ye H, Ren K, Wang P and Wang L (2022), The investigation of the NH_3-SCR performance of a copper-based AEI-CHA intergrown zeolite catalyst.
Front. Chem. 10:1069824.
doi: 10.3389/fchem.2022.1069824

The investigation of the NH_3-SCR performance of a copper-based AEI-CHA intergrown zeolite catalyst

Hongling Ye[1]*, Kai Ren[2]*, Pengfei Wang[1] and Lin Wang[1]

[1]School of Mechanical and Vehicle Engineering, Bengbu University, Bengbu, Anhui, China, [2]School of Mechanical and Electronic Engineering, Nanjing Forestry University, Nanjing, China

This work prepared an ISAPO-34/SAPO-18 intergrown zeolite using phosphate organoamine as the structure guiding agent. Physical-chemical characterizations by XRD, SEM, TG, and BET showed that the SAPO-34/SAPO-18 presents a cross-stacked cubic block-like microscopic morphology, with characteristic diffusive diffraction peaks at $2\theta = 16–18°$ and 30–33° and a specific surface area of $557\,m^2\,g^{-1}$. The series of copper-based catalysts prepared from SAPO-34/SAPO-18 showed a shift of the active temperature window to a lower temperature with increasing copper content. Moreover, the Brønsted acid site decreased significantly due to copper ion exchange and zeolite structure framework damage. Among them, the 1.2 wt% sample showed the widest active temperature window, with a T_{90} range of 175–435°C. After low-temperature hydrothermal aging treatment, the zeolite structure was eroded and the catalyst activity deteriorated significantly.

KEYWORDS

intergrown structure, copper-based zeolite catalyst, selective catalytic reduction, nitrogen oxides, low-temperature hydrothermal deactivation

Introduction

Due to the recent increasing seriousness of environmental pollution, theoretical studies have explored methods to relieve this phenomenon based on two-dimensional catalysts (Ren et al., 2022a; Ren et al., 2022b; Ren et al., 2022c; Ren et al., 2022d; Zhang et al., 2022). The gas emissions of internal combustion engines have produced considerable levels of pollution. China steadily ranks first worldwide in the production and sales of internal combustion engines, with domestic sales reaching 46.813 million in 2020. Among these, diesel internal combustion engines comprised 6.341 m units, accounting for 13.5% of the total internal combustion engine sales and showing a steady growth trend. Given this trend, the challenge of exhaust pollutant emission is increasingly prominent and seriously threatens the sustainable development of atmospheric ecological environments. The diesel vehicle emission standards in China mainly follow European emission regulations, for which selective catalytic reduction (SCR) technology provides a necessary way for diesel vehicles to meet VI emission standards (Han et al., 2019). The core catalyst required by ammonia selective catalytic reduction (NH_3-SCR) technology, an internationally recognized efficient technology for nitrogen oxides (NO_X), is shifted from a vanadium, tungsten, and titanium system (Yang et al., 2014) to a zeolite catalyst system (Chen et al., 2022). The latter is usually composed of zeolite as a carrier of active metal elements (Zheng et al., 2020; Jin et al., 2022; Yuan et al., 2022). The common zeolite skeleton configurations include MFI (Yuan et al., 2016), AEI (Wu et al., 2022), BEA (Lin et al., 2018), LTA (Lin et al., 2021), CHA (Wang et al., 2015; Bergmana et al., 2020; Sun et al., 2020; Zhang et al., 2021a; Bello et al., 2022), AFX (Li et al., 2022a), etc. The zeolite SCR catalyst (Tsukamoto et al., 2019) represented by CHA has advantages including good low-temperature activity, a wide active temperature window, high nitrogen selectivity, green environmental protection due to its unique micropore structure, and suitable surface acidity (Xu et al., 2020; Wang et al., 2021; Zhang et al., 2022a). In recent years, in-depth studies have evaluated the formula, performance, and mechanism of an SCR catalyst with single-structure zeolite. The corresponding intellectual property rights are owned by foreign companies. Polycrystalline/mixed crystal/intergrown zeolite SCR catalysts also show excellent catalytic activity and durability. Zhang et al. (2021b) reported greater catalytic activity, hydrothermal stability, and sulfur aging resistance for a Cu/SAPO-18/34 intergrown zeolite catalyst compared to those for Cu/SAPO-18 and Cu/SAPO-34. As a typical representative, SAPO-18/34 zeolite is a new type of zeolite (Boruntea et al., 2019; Tsuchiya et al., 2020; Li et al., 2022b) composed of AEI and CHA skeleton structure units in stacking faults. It has both the pore canals and acidity of the two crystal phase structures, which usually show better catalytic performance than a single zeolite. Zhao et al. (2016) used triethylamine and N, N-diisopropyl ethylamine as double templates to prepare AEI/CHA intergrown SAPO zeolite and its catalyst, which not only increased the catalytic activity but also significantly reduced the carbon deposition rate. This dual template method is the most common way to prepare symbiotic molecular sieves. However, compared to single templates, it is more difficult to prepare molecular sieves with double templates, and the effects of the proportion, distribution, and chemical state of the templates on the synthesis are more complex. Therefore, the efficient preparation of AEI/CHA symbiotic molecular sieves requires a template.

The present study used phosphate organic amine (Li et al., 2022c) as a template and phosphorus source in a synthesis environment at a pH of 6–7. A SAPO-34/SAPO-18 intergrown zeolite with a hydrogen API-CHA structure was directly prepared and its physicochemical properties and catalytic activity were analyzed by characterization methods including XRD, SEM, and BET. The effects of factors such as active component content and low-temperature hydrothermal inactivation on the performance were studied to provide a reference for the performance research and application of intergrown zeolite SCR catalysts.

Experimental methods

Reagents

The reagents included SAPO-18/SAPO-34 zeolite (self-made, $SiO_2:P_2O_5:Al_2O_3 = 1:3.74:3.81$); copper nitrate (analytically pure, Shanghai McLean Biochemical Technology Co., Ltd.); nitric acid (analytically pure, Tianjin Kemio Chemical Reagent Co., Ltd.); deionized water (self-made).

Preparation of the zeolite catalyst

A 0.1N copper nitrate solution was prepared, 200 g of which was weighed and placed in a 500 ml beaker. Next, 10 g of SAPO-18/SAPO-34 zeolite was added to the solution. Nitric acid was then added until pH = 3, stirred, and reacted in a water bath at 80°C. A series of copper-based catalysts were prepared. Those with copper contents of 0.3wt%, 0.8wt%, and 1.2wt% were labeled as 0.3, 0.8, and 1.2, respectively.

Characterization of the zeolite catalysts

XRD characterization was performed using a SmartLab SE X-ray diffractometer (Rigaku Corporation) to analyze the crystal structures of the samples. SEM characterization was performed using an Apero-Lowvac high-resolution field emission scanning electron microscope (Thermo Fisher) to observe the sample microstructure. BET characterization was performed using an ASAP 2460 specific surface area and porosity analyzer (Micrometrics) to analyze the specific surface area, pore volume, and pore size of the test samples. NH_3-TPD characterization was performed using an AutoChem II 2920 chemical adsorption instrument (Micrometrics) to analyze the surface acidity characteristics of the samples. TG-DSC characterization was performed using a STA449F5 Jupiter-type synchronous thermal analyzer (NETZSCH) to assess the mass and heat changes of the samples at increasing temperatures.

Evaluation of the catalyst activities

The catalytic performance was tested in a miniature fixed-bed activity evaluation device, as shown in Figure 1. For these tests, 5 g catalyst powder was fully ground to prepare a 40–60 mesh sample and placed in a quartz reaction tube with a 15 mm inner diameter. Both ends were sealed with quartz cotton to form a catalyst bed. The evaluation device comprised a simulation gas distribution system, a programmed heating device, and a gas analyzer. The simulated tail gas composition was as follows: $[NO] = 500$ PPM, $[NH_3] = 500$ PPM, $[H_2O] = 10$ vol.%, $[O_2] = 10$ vol.%, with N_2 as the equilibrium gas, and an

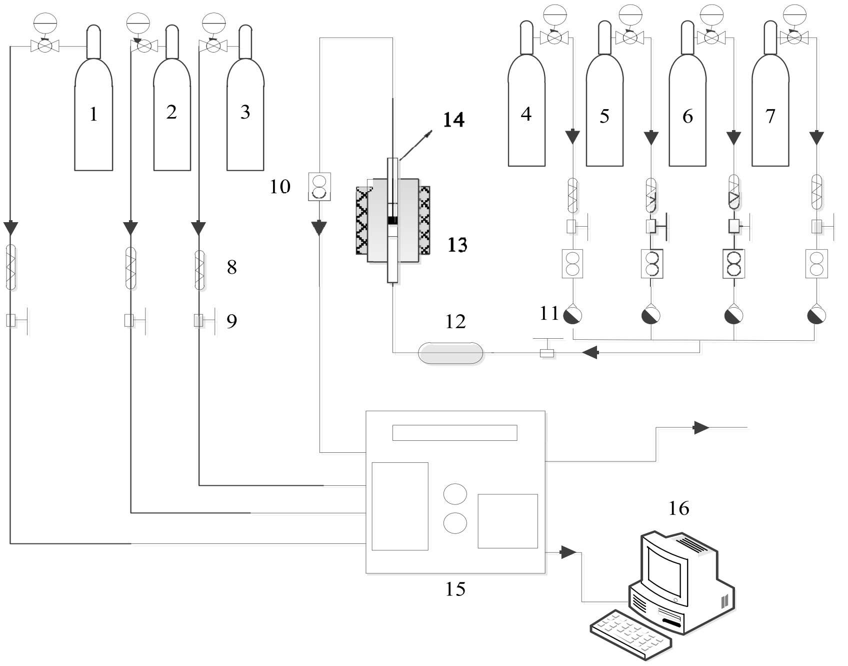

FIGURE 1
Equipment diagram for the evaluation of the activity of the NH_3-SCR catalyst. 1. Nitric oxide. 2. Ammonia. 3. Nitrogen. 4. Oxygen. 5. Propane. 7. Other Gases. 8. Filter. 9. Globe valve. 10. Mass flowmeter. 11. One-way valve. 12. Mixer. 13. Heating furnace. 14. Reactor. 15. Gas analyzer. 16. Computer.

airspeed of 30,000 h^{-1} (default conditions). The NO conversion rate, NH_3 conversion rate, N_2O content, and N_2 selectivity were calculated according to the following formula:

$$x_{NO} = \frac{n_{NO_{in}} - n_{NO_{out}}}{n_{NO_{in}}} \times 100\% \tag{1}$$

$$s_{N_2} = \frac{n_{NH3in} - n_{NH3out} + n_{NO_{in}} - n_{NO_{out}} - n_{NO2out} - 2n_{N_2O_{out}}}{n_{NH3in} + n_{NO_{in}} - n_{NO_{out}}} \times 100\% \tag{2}$$

where NO $_{(out)}$, NO_2 $_{(out)}$, N_2O $_{(out)}$, and NH_3 $_{(out)}$ are the outlet concentrations of NO, NO_2, N_2O, and NH_3 and NO $_{(in)}$ and NH_3 $_{(in)}$ are the inlet concentrations of NO and NH_3.

The formula for the heating program T was as follows:

$$T = \frac{1}{12} \times t + 25 \tag{3}$$

where the unit of the T is °C; t represents the time with the unit of second.

Low-temperature hydrothermal aging treatment

To investigate the hydrothermal stability of the SAPO-18/SAPO-34 zeolite at low temperature, an SCR catalyst with 1.2% copper content was aged for 100 h at 90°C under 10% water vapor at a space speed of 30,000 h^{-1}. The age and fully dried samples were labeled as 1.2-a. The NH_3-SCR catalytic activity of the aged samples was investigated in a micro fixed-bed reactor.

Results and discussion

Catalytic performance

Figure 2A shows the NO conversion curves of the series copper-based SAPO-18/SAPO-34 catalyst in the standard NH_3-SCR reaction. With increasing copper content, the ion exchange sites on which copper ions bonded to the molecular sieve as well as the formed active species are generally believed to change, with the temperature window shifting from higher to lower temperatures. The common copper active species in Cu-based zeolite SCR catalysts include Cu^{2+}, $[Cu(OH)]^+$, Cu-O-Cu, CuOx, etc. (Borfecchia et al., 2015; Shan et al., 2019; Liu et al., 2020; Khurana et al., 2022). Figure 2A shows that when the copper content increased from 0.3wt% to 0.8wt%, the range of the active temperature window T_{90} (the temperature at which the NO conversion rate is 90%) widened from 325–525°C to 170–425°C. Accordingly, the NO ignition

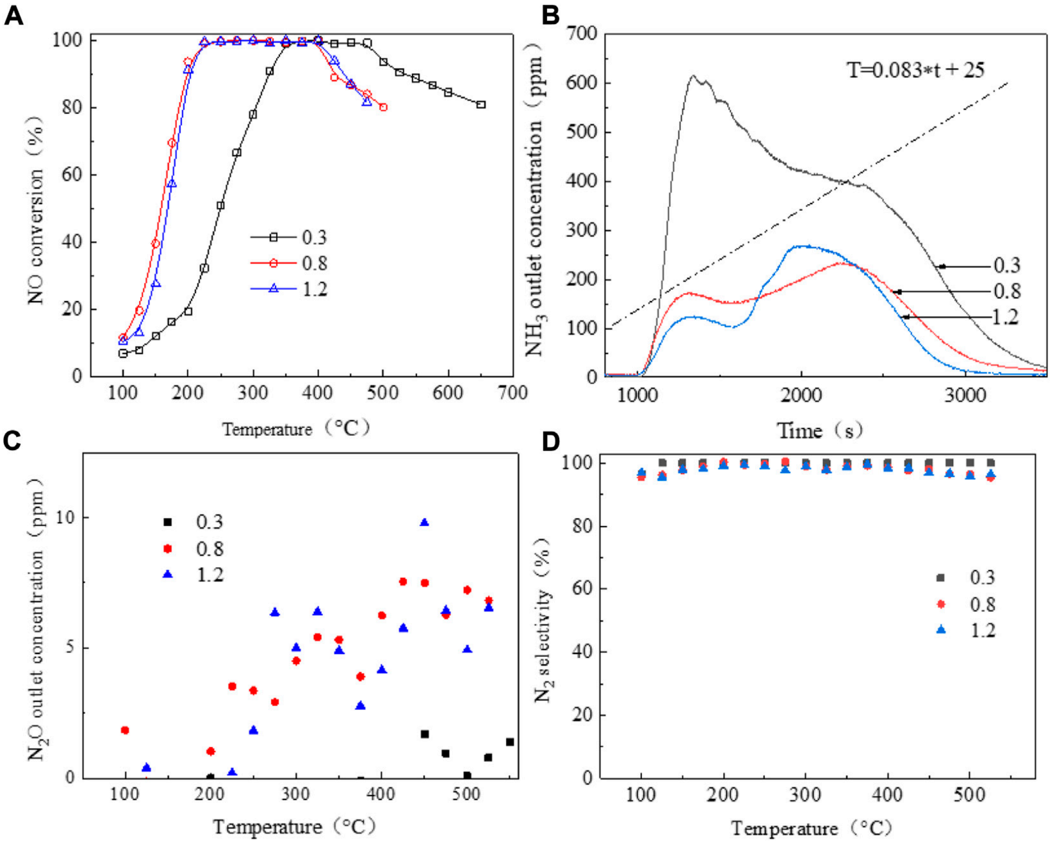

FIGURE 2
NH_3-SCR performance of a series of copper-based SCR catalysts. **(A)** No conversion; **(B)** NH_3 outlet concentration; **(C)** N_2O outlet concentration; **(D)** N_2 selectivity.

temperature T_{50} (the temperature at which the NO conversion rate is 50%) decreased from 250°C to 160°C. Kwak et al. (2012) reported that at low copper content, the active component copper preferentially occupied the sites in the D6R cage, while some copper ions migrated to the CHA cage when the copper content increased. At a copper content of 1.2wt%, the low-temperature performance of the catalyst decreased slightly and the T_{50} temperature increased to about 165°C compared to 0.8wt%, and the high-temperature activity increased slightly, with the temperature window widening to 175–435°C. All Cu-based SAPO-18/SAPO-34 catalysts showed excellent nitrogen selectivity of close to 100%, as shown in Figure 2D.

Figure 2B shows the outlet ammonia concentrations of the series of copper-based SAPO-18/SAPO-34 catalysts during the activity test. In general, the SAPO-18/SAPO-34 intergrown zeolite showed poor ammonia storage performance, with ammonia escape concentrated at 100°C–300°C. At temperatures above 100°C, the adsorbed NH_3 showed excessive desorption. Due to the lower temperature and the poor catalyst activity, NH_3 could not fully participate in the selective catalytic reduction reaction, resulting in a sharp increase in its desorption capacity. When the number of catalytic active centers was small, this situation was particularly prominent. The amount of NH_3 escape ranked from high to low was as follows: under 0.3wt%> 0.8wt%> 1.2wt%. N_2O production showed the opposite trends as those for ammonia escape, as shown in Figure 2C. At lower copper content, less secondary pollutant N_2O was generated (Isapour et al., 2022), which may be related to the species of CuOX crystal cluster; however, the overall production was <10 PPM, which met the relevant limit requirements for national emission standards.

Physicochemical properties of the intergrown zeolite

Figure 3A shows the XRD pattern of the SAPO-34/SAPO-18 intergrown zeolite. The characteristic diffraction peaks are attributed to 2θ = 9.79°, 13.22°, 16.41°, 18.18°, 19.51°, 21.05°, 23.56°, 24.47°, 25.47°, 26.45°, 31.27°, and 31.61°, respectively. By comparison to the standard spectrum diagram in Figure 3A, the

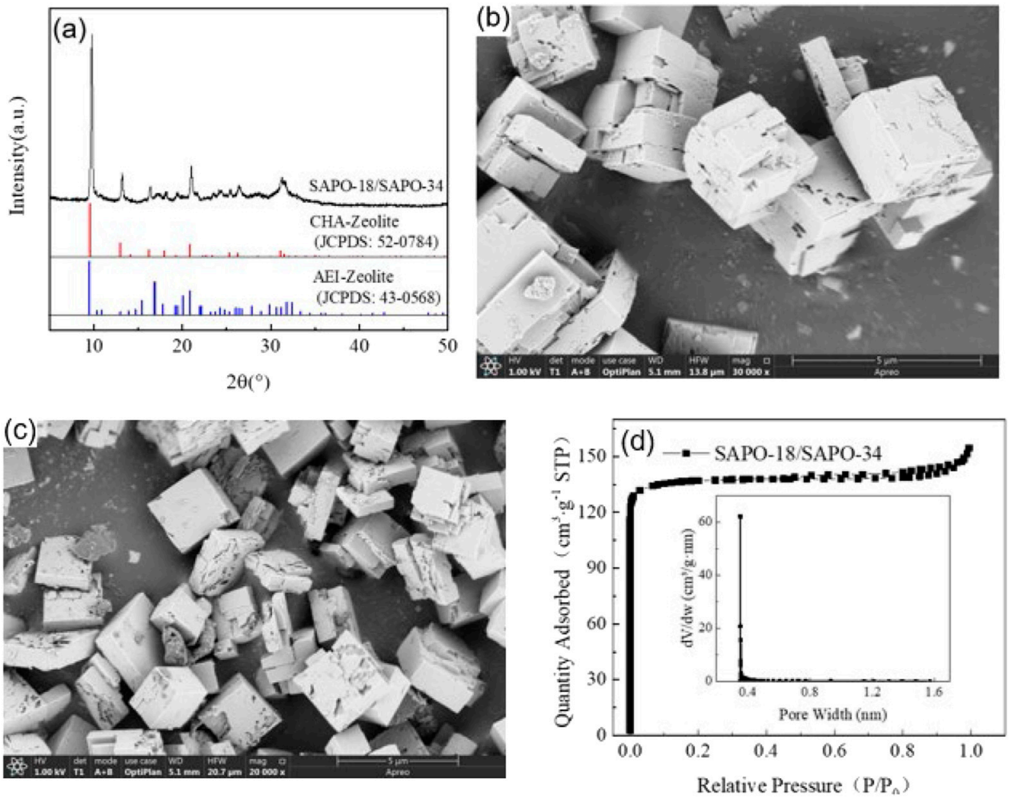

FIGURE 3
(A) XRD patterns; SEM photo of a SAPO-34/SAPO-18 intergrown zeolite: **(B)** fresh sample (30,000x) and **(C)** aged sample (20,000x). **(D)** N_2 adsorption-desorption isotherms and porosity distribution curve of a SAPO-34/SAPO-18 intergrown zeolite.

characteristic diffraction peaks of the SAPO-34 zeolite were attributed to 2θ = 9.64°, 13.08°, 14.20°, 16.28°, 18.05°, 19.35°, 20.94°, while the characteristic diffraction peaks of SAPO-18 zeolite were attributed to 2θ = 9.60°, 13.08°, 14.78°, 15.48°, 16.97°, 19.28°, 19.49°, 20.12°, 24.85°, and 26.11°. In contrast, the characteristic diffraction peaks of the SAPO-34/SAPO-18 intergrown zeolite were wide and weak in the range of 2θ = 16–18° and 30–33°, which were not observed in the above two single crystal zeolites. The ellipsoidal CHA structure and the pear-shaped AEI structure have similar skeleton topologies and the hexagonal prism cage (D6R) is key to the connection of the two lattices (Zhao et al., 2017). Where the D6R cage of CHA structural zeolite is straight and parallel, AEI structural zeolite shows a cross-oblique and parallel distribution. Therefore, the SAPO-34/SAPO-18 intergrown zeolite was more inclined to cross-stack on the cubic bulk crystal, with the microstructure shown in Figures 3B,C.

Figure 3B shows the microstructure photos of the SAPO-34/SAPO-18 intergrown zeolite, displaying generally irregular cross-stacked cube blocks. The crystal size is 3–5 μm, and the morphology obviously differs from those of SAPO-34 and SAPO-18 zeolites, which intuitively confirmed the formation of a eutectic structure. The intergrown crystal surface of SAPO-34/SAPO-18 was not smooth, but rather showed defects and damage, possibly because the use of the concentrated sol-gel system to prepare the intergrown zeolite affected the nucleation and growth process. The industrial pure-grade silicon and aluminum sources may have also contributed to the irregular morphology. After low-temperature hydrothermal aging, the defects on the SAPO-34/SAPO-18 crystal surface expanded and showed a tendency for fragmentation, indicating that its structure was damaged, as shown in Figure 3C.

Figure 3D presents the nitrogen physical adsorption test results of the SAPO-34/SAPO-18 intergrown zeolite. The nitrogen isotherm absorption/desorption curve of the intergrown zeolite showed type I isotherm characteristics, as defined by IUPAC, and had a type H4 hysteresis loop. That is, in the interval 0 < P/P0 < 0.01, the adsorption curve rose sharply with increasing relative pressure, indicating that the intergrown zeolite had structural characteristics of microporous materials (Lu et al., 2022). According to the gap width distribution curve, the median pore size was approximately 0.36 nm (Horvath-Kawazoe method); the narrow and sharp distribution reflected

TABLE 1 XRF and BET results of SAPO-34/SAPO-18 zeolite and its catalysts.

Sample number	Fraction mole ratio	Copper content (wt%)	Specific surface area ($m^2 \cdot g^{-1}$)	Median pore diameter (Å)
SAPO-18/SAPO-34	SiO_2:P_2O_5: Al_2O_3 = 1:3.74:3.81	0	557	3.60
0.3	—	0.3	523	3.60
0.8	—	0.8	508	3.61
1.2	—	1.2	487	3.61

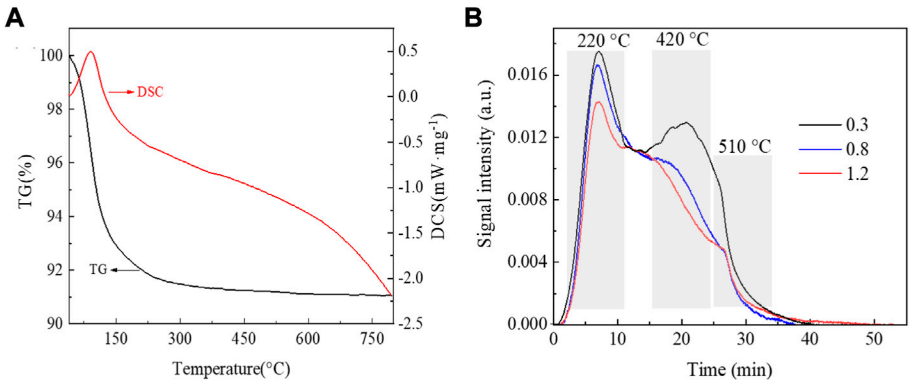

FIGURE 4
(A) TG-DSC curve of a SAPO-34/SAPO-18 intergrown zeolite. **(B)** NH_3-TPD curves of the series of copper-based SCR catalysts.

the regular lattice and orderly pore distribution of the intergrown zeolite. Moreover, the two-phase symbiosis did not significantly change the skeleton types of the CHA and AEI structural zeolites.

The XRF test results in Table 1 show an elemental composition of SAPO-34/SAPO-18 intergrown zeolite of SiO_2:P_2O_5: Al_2O_3 = 1:3.74:3.81, which is related to the use of phosphoric acid-organic amine as template agent. The intergrown zeolite had low copper ion exchange efficiency and the copper content was only 0.3wt% after constant exchange at 80°C for 8 h. The copper content increased to 0.8wt% after two more exchanges. After three exchanges, the copper content loading rate was only 1.2 wt%. However, with increasing rounds of ion exchange, the specific surface area of the corresponding zeolite catalyst decreased significantly. The specific surface area of the SAPO-34/SAPO-18 intergrown zeolite was as high as 557 $m^2 g^{-1}$ and decreased to 487 $m^2 g^{-1}$ after three rounds of copper ion exchange. This may occur due to damage to the SAPO-34/SAPO-18 intergrown zeolite structure in the hot water environment used in ion exchange.

Figure 4A shows the test results of the synchronous thermal analysis of the SAPO-34/SAPO-18 intergrown zeolite. The weight loss curve (TG) shows two main weight loss intervals at 40–150°C and 150–300°C and a weight loss rate of about 9 wt%. Below 150°C, the weight loss is obvious (up to 7 wt%), which is related to the rapid evaporation of excessive free water adsorbed by the zeolite. The heat curve (DSC) also reflects the water evaporation and heat absorption at this stage. With increasing temperature, the remaining water bound in the zeolite begins to volatilize and the organic amine template agent undergoes thermal decomposition with heating. The significant slowing of mass and heat changes at 150–300°C were attributed to the new phosphoric acid-organic amine template used in the SAPO-34/SAPO-18 synthesis process effectively avoiding the excessive use of template agent compared to the traditional method. The use of phosphoric acid-organic amine as a structure-diverting agent allowed the accurate and efficient use of organic amine molecules, thus improving environmental protection and economic benefits.

Ammonia adsorption characteristics

The surface acidity of zeolite catalysts is generally believed to have an important influence on NH_3-SCR performance. The surface acidity and amount of acid in zeolite SCR catalysts are usually characterized by NH_3-TPD. Figure 4B shows the temperature-programmed ammonia desorption curves of the

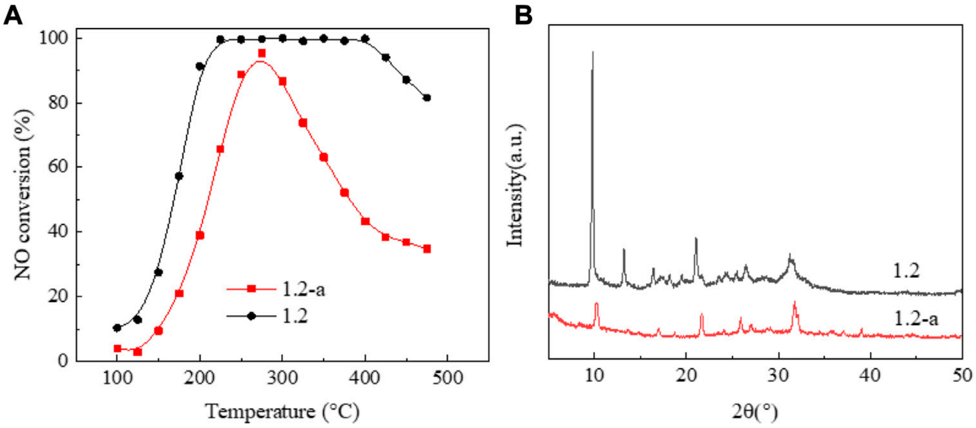

FIGURE 5
Performance changes of the 1.2 wt% copper content catalyst before and after low-temperature hydrothermal aging. **(A)** NO conversion. **(B)** XRD patterns.

series of copper-based SAPO-34/SAPO-18 zeolite catalysts. The three main characteristic peaks were attributed to weak, medium-strong, and strong acid sites, respectively (Pérez-Uriarte et al., 2016; Xu et al., 2017; Shin et al., 2018). The weak acid site at low temperatures corresponded to a weak Lewis acid (T = 220°C), the medium strong acid site at middle temperatures corresponds to strong Lewis acids and some active copper species sites (T = 420°C), and the strong acid adsorption site at high temperatures corresponded to a Brønsted acid (T = 510°C). As shown in Figure 4B, increasing copper content was associated with a decreased acid content of the zeolite catalyst and acid peak intensity to varying degrees. The Brønsted acid position was particularly obvious. Regarding the main factors affecting Brønsted acid sites, 1) during the ion exchange, Cu occupies the hydroxyl site of Si-OH-Al in the six-member ring of zeolite to form Cu^{2+}, with Brønsted acid sites decreasing accordingly (Villamaina et al., 2019). 2) During ion exchange reactions, the high-temperature water environment damages the structure of the SAPO-34/SAPO-18 zeolite, leading to a significant reduction of Brønsted acid sites (Liu et al., 2022). 3) The copper loading amount in the zeolite is exceeded and the active components mainly exist as $[Cu(OH)]^+$ and CuOx clusters (Lee et al., 2021). The generation of CuO may lead to the dealuminization of the zeolite skeleton; that is, the destruction of zeolite Brønsted acid (Si-OH-Al) (Di Iorio et al., 2015; Millan et al., 2021; Negri et al., 2021). Based on the above factors, we further investigated the effect of low-temperature hydrothermal aging treatment on the performance of the NH_3-SCR catalyst.

Low-temperature hydrothermal stability

Figure 5A shows the NO conversion curve of a 1.2 wt% sample before and after low-temperature hydrothermal aging. Figure 5A shows significantly decreased catalyst activity with aging. Moreover, the temperature window basically disappears, and the NO ignition temperature exceeds 200°C. The results of crystal phase structure characterization Figure 5B demonstrated that, after aging, the catalyst presents an amorphous state and the characteristic diffraction peak of SAPO-34/SAPO-18 zeolite almost completely disappears. The above results suggest that the crystal phase structure of the copper-based SAPO-34/SAPO-18 zeolite catalyst was destroyed after low-temperature hydrothermal aging treatment, leading to irreversible inactivation (Woo et al., 2018) (Figure 6).

Ma et al. (2020) reported that the Si-O(H)-Al bond of SAPO-34 zeolite was prone to hydrolysis in low-temperature hydrothermal environments. Woo et al. (2020) believed that the hydrolysis first formed Si (2Al) (2OH) and Si (3Al) (OH), which were finally transformed into silicon clusters. Gao et al. (2013) reported that SAPO-34 zeolite structures with more Si-O(H)-Al bonds showed more serious hydrolysis damage. Wang et al. (2019) studied the effect of SAPO-34 zeolite hydrolysis on active species, in which $Cu(OH)^+$ was transformed into spinel-structured $CuAl_2O_4$, with significantly decreased catalytic activity. Leistner et al. (2015) confirmed the loss of the active Cu^{2+} species lost after the water vapor treatment of Cu-SAPO-34. Zhang et al. (2022b) proposed that the hydrolysis of the Si-O(H)-Al bond and the loss of active copper species jointly induced Cu/SAPO-34 inactivation, with inactivation the easier under a larger proportion of the two.

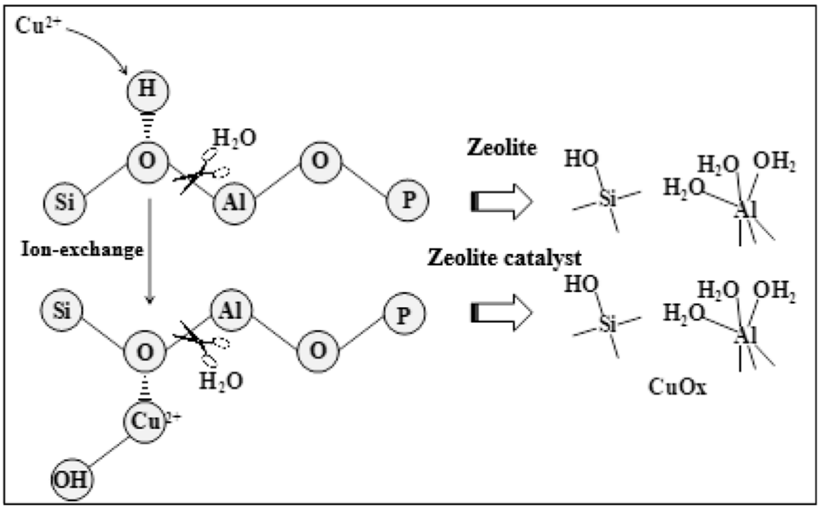

FIGURE 6
Schematic diagram of the destruction of zeolite and its catalyst by low-temperature hydrothermal aging treatment.

Conclusion

First, SAPO-18/SAPO-34 intergrown zeolite was prepared using phosphoric acid-organic amine, which has a unique crystal phase structure and microstructure, displaying the typical adsorption characteristics of zeolite microporous materials. Phosphoric acid-organic amines act as both a phosphorus source and a structure-diverting agent. The excessive use of structure-diverting agents can be avoided by use of a synthetic stoichiometric ratio. TG-DSC test results did not show an obvious thermal decomposition phenomenon of organic amines. Secondly, with increasing active component content, the state of copper species changed due to migration, and the active temperature window of the Cu-based SAPO-18/SAPO-34 catalyst shifted toward low temperatures. At copper contents <0.8wt%, the T_{50} was 160°C, and the T_{90} range was 170–425°C, showing the optimal performance. Finally, the SAPO-18/SAPO-34 intergrown zeolite showed three main ammonia adsorption sites, and the Brønsted acid sites of the zeolite carrier were lost due to copper occupying the exchange sites during the ion exchange. However, a more important incentive is the structural damage of SAPO zeolite in the low-temperature hydrothermal process. After low-temperature hydrothermal aging treatment, the temperature window of the 1.2wt% Cu content sample almost disappeared, with the crystal phase structure seriously damaged.

Data availability statement

The raw data supporting the conclusion of this article will be made available by the authors without undue reservation.

Author contributions

Conceptualization, HY; experimental methods, HY, KR and PW; validation, KR and LW; investigation, HY and PW; writing—original draft preparation, HY, PW and LW; writing—review and editing, KR; funding acquisition, HY. All authors have read and agreed to the published version of the manuscript.

Acknowledgments

The authors thank the Natural Science Foundation of Jiangsu for support (No. BK20220407).

Conflict of interest

The authors declare that the research was conducted in the absence of any commercial or financial relationships that could be construed as a potential conflict of interest.

Publisher's note

References

Bello, E., Ferri, P., Nero, M., Willhammar, T., Millet, I., Schutze, F. W., et al. (2022). NH_3-SCR catalysts for heavy-duty diesel vehicles: Preparation of CHA-type zeolites with low-cost templates. *Appl. Catal. B Environ.* 303, 120928. doi:10.1016/j.apcatb.2021.120928

Bergmana, S. L., Dahlin, S., Mesilov, V. V., Xiao, Y., Englund, J., Xi, S., et al. (2020). *In-situ* studies of oxidation/reduction of copper in Cu-CHA SCR catalysts: Comparison of fresh and SO_2-poisoned catalysts. *Appl. Catal. B Environ.* 269, 118722. doi:10.1016/j.apcatb.2020.118722

Borfecchia, E., Lomachenko, K. A., Giordanino, F., Falsig, H., Beato, P., Soldatov, A. V., et al. (2015). Revisiting the nature of Cu sites in the activated Cu-SSZ-13 catalyst for SCR reaction. *Chem. Sci.* 6, 548–563. doi:10.1039/c4sc02907k

Boruntea, C. R., Lundegaard, L. F., Corma, A., and Vennestrom, P. N. (2019). Crystallization of AEI and AFX zeolites through zeolite-to-zeolite transformations. *Microporous Mesoporous Mater.* 278, 105–114. doi:10.1016/j.micromeso.2018.11.002

Chen, L., Ren, S., Liu, L., Su, B., Yang, J., Chen, Z., et al. (2022). Catalytic performance over Mn-Ce catalysts for NH_3-SCR of NO at low temperature: Different zeolite supports[J]. *J. Environ. Chem. Eng.* 10, 107167. doi:10.1016/j.jece.2022.107167

Di Iorio, J. R., Bates, S. A., Verma, A. A., Delgass, W. N., Ribeiro, F. H., Miller, J. T., et al. (2015). The dynamic nature of brønsted acid sites in Cu–zeolites during NOx selective catalytic reduction: Quantification by gas-phase Ammonia titration. *Top. Catal.* 58 (7), 424–434. doi:10.1007/s11244-015-0387-8Topics in Catalysis

Gao, F., Walter, E. D., Washton, N. M., Szanyi, J., and Peden, C. H. F. (2013). Synthesis and evaluation of Cu-SAPO-34 catalysts for ammonia selective catalytic reduction. 1. Aqueous solution ion exchange. *ACS Catal.* 3, 2083–2093. doi:10.1021/cs4004672

Han, L. P., Cai, S. X., Gao, M., Hasegawa, J. y., Wang, P., Zhang, J., et al. (2019). Selective catalytic reduction of NO_x with NH_3 by using novel catalysts: State of the art and future prospects. *Chem. Rev.* 119 (19), 10916–10976. doi:10.1021/acs.chemrev.9b00202

Isapour, G., Wang, A. Y., Han, J., Feng, Y., Gronbeck, H., Creaser, D., et al. (2022). *In situ* DRIFT studies on N_2O formation over Cu-functionalized zeolites during ammonia-SCR. *Catal. Sci. Technol.* 12, 3921–3936. doi:10.1039/d2cy00247g

Jin, Q. Q., Fang, D., Ye, Y. L., Hou, S., He, F., and Xie, J. (2022). Cu, Co, or Ni species in exchanged Y zeolite catalysts and their denitration performance for selective catalytic reduction by ammonia. *Appl. Surf. Sci.* 600, 154075. doi:10.1016/j.apsusc.2022.154075

Khurana, I., Albarracin-Caballero, J. D., and Shih, A. J. (2022). Identification and quantification of multinuclear Cu active sites derived from monomeric Cu moieties for dry NO oxidation over Cu-SSZ-13. *J. Catal.* 413, 1111–1122. doi:10.1016/j.jcat.2022.08.005

Kwak, J. H., Zhu, H. Y., Lee, J. H., Peden, C. H. F., and Szanyi, J. (2012). Two different cationic positions in Cu-SSZ-13. *Chem. Commun.* 48 (39), 4758–4760. doi:10.1039/c2cc31184d

Lee, H., Song, I., Jeon, S. W., and Kim, D. H. (2021). Mobility of Cu ions in Cu-SSZ-13 determines the reactivity of selective catalytic reduction of NOx with NH_3. *J. Phys. Chem. Lett.* 12 (12), 3210–3216. doi:10.1021/acs.jpclett.1c00181

Leistner, K., and Olsson, L. (2015). Deactivation of Cu/SAPO-34 during low-temperature NH_3-SCR[J]. *Appl. Catal. B Environ.* 165, 192–199. doi:10.1016/j.apcatb.2014.09.067

Li, K. X., Li, Z. G., Ren, X. N., Shao, Y. K., Wang, J. H., Zhang, L., et al. (2022). *AEI-CHA symbiotic molecular sieve and catalyst thereof.* China. 202210002965.9 [P].

Li, R., Jiang, X. Q., Lin, J. C., Zhang, Z., Huang, Q., Fu, G., et al. (2022). Understanding the influence of hydrothermal treatment on NH_3-SCR of NOx activity over Cux-SSZ-16. *Chem. Eng. J.* 441, 136021. doi:10.1016/j.cej.2022.136021

Li, Z. H., Liu, Y. S., Dou, T., Li, X., Di, C., and Chen, S. L. (2022). Sustainable synthesis of AEI/CHA intergrowth zeolites for methanol-to-olefins conversion. *Microporous Mesoporous Mater.* 344, 112201. doi:10.1016/j.micromeso.2022.112201

Lin, J. H., Lee, K. H., and Hong, S. B. (2021). Effect of preparation method on NH_3-SCR activity of Cu-LTA catalysts. *Catal. Today* 376, 41–46. doi:10.1016/j.cattod.2020.08.030

Lin, Q. J., Feng, X., Zhang, H. L., Lin, C., Liu, S., Xu, H., et al. (2018). Hydrothermal deactivation over CuFe/BEA for NH_3-SCR. *J. Industrial Eng. Chem.* 65, 40–50. doi:10.1016/j.jiec.2018.04.009

Liu, C., Yasumura, S., Toyao, Ta, Maeno, Z., and Shimizu, K. i. (2022). Mechanism of standard NH_3–SCR over Cu-CHA via NO^+ and HONO intermediates. *J. Phys. Chem. C* 126 (28), 11594–11601. doi:10.1021/acs.jpcc.2c03432

Liu, K., Yan, Z. D., Shan, W. P., Shan, Y., Shi, X., and He, H. (2020). Quantitative determination of the Cu species, acid sites and NH_3-SCR mechanism on Cu-SSZ-13 and H-SSZ-13 at low temperatures. *Catal. Sci. Technol.* 10, 1135–1150. doi:10.1039/c9cy02352f

Lu, X. M., Ren, T. S., Cao, P. Z., Wang, Z., Liu, L., He, J., et al. (2022). Construction of high performance binder-free zeolite monolith. *Chem. Eng. J.* 447, 137558. doi:10.1016/j.cej.2022.137558

Ma, Y., Wu, X. D., Liu, L. P., Cao, L., Ran, R., Si, Z., et al. (2020). Critical roles of $Cu(OH)_2$ in low-temperature moisture-induced degradation of Cu-SAPO-34 SCR catalyst: Correlating reversible and irreversible deactivation. *Appl. Catal. B Environ.* 278, 119306. doi:10.1016/j.apcatb.2020.119306

Millan, R., Cnudde, P., Speybroeck, V. V., and Boronat, M. (2021). Mobility and reactivity of Cu^+ species in Cu-CHA catalysts under NH_3-SCR-NOx reaction conditions: Insights from AIMD simulations. *JACS Au* 1 (10), 1778–1787. doi:10.1021/jacsau.1c00337

Negri, Chiara, Martini, A., Deplano, G., Lomachenko, K. A., Janssens, T. V. W., Borfecchia, E., et al. (2021). Investigating the role of Cu-oxo species in Cu-nitrate formation over Cu-CHA catalysts. *Phys. Chem. Chem. Phys.* 23, 18322–18337. doi:10.1039/d1cp01754c

Pérez-Uriarte, P., Ateka, A., Aguayo, A. T., and Bilbao, J. (2016). Comparison of HZSM-5 zeolite and SAPO (-18 and -34) based catalysts for the production of light olefins from DME. *Catal. Lett.* 146, 1892–1902.doi:10.1007/s10562-016-1829-z

Ren, K., Chen, Y., Qin, H., Feng, W., and Zhang, G. (2022). Graphene/biphenylene heterostructure: Interfacial thermal conduction and thermal rectification. *Appl. Phys. Lett.* 121, 082203. doi:10.1063/5.0100391

Ren, K., Qin, H., Liu, H., Chen, Y., Liu, X., and Zhang, G. Manipulating interfacial thermal conduction of 2D janus heterostructure via a thermo-mechanical coupling[J]. *Adv. Funct. Mat.*, 2022, 32: 2110846, doi:10.1002/adfm.202110846

Ren, K., Wang, K., and Zhang, G. (2022). Atomic adsorption-controlled magnetic properties of a two-dimensional (2D) janus monolayer. *ACS Appl. Electron. Mat.* 4, 4507–4513. doi:10.1021/acsaelm.2c00740

Ren, K., Yan, Y., Zhang, Z., Sun, M., and Schwingenschlögl, U. (2022). A family of Li_xB_y monolayers with a wide spectrum of potential applications. *Appl. Surf. Sci.* 604, 154317. doi:10.1016/j.apsusc.2022.154317

Shan, Y. L., Shi, X. Y., Du, J. P., Yu, Y., and He, H. (2019). Cu-Exchanged RTH-type zeolites for NH_3-selective catalytic reduction of NO_x: Cu distribution and hydrothermal stability. *Catal. Sci. Technol.* 9, 106–115. doi:10.1039/c8cy01933a

Shin, Y. H., Kweon, S., Park, M. B., and Chae, H. J. (2018). Comparative study of CHA- and AEI-type zeolytic catalysts for the conversion of chloromethane into light olefins. *Korean J. Chem. Eng.* 35 (7), 1433–1440. doi:10.1007/s11814-018-0050-8

Sun, L. J., Yang, M., Cao, L., Cao, Y., Xu, S., Zhu, D., et al. (2020). Fabrication of Cu-CHA composites with enhanced NH_3-SCR catalytic performances and hydrothermal stabilities. *Microporous Mesoporous Mater.* 309, 110585. doi:10.1016/j.micromeso.2020.110585

Tsuchiya, K., Tsunoji, N., Sasaki, Y., Uemura, M., Onishi, M., Sadakane, M., et al. (2020). Triple-template system for phosphorus-modified AFX/CHA intergrowth zeolite. *Microporous Mesoporous Mater.* 309, 110540. doi:10.1016/j.micromeso.2020.110540

Tsukamoto, Y., Fukuma, T., and Kusaka, J. (2019). Analysis and modeling of NOx reduction based on the reactivity of Cu active sites and brønsted acid sites in a Cu-chabazite SCR catalyst. *SAE Tech. Pap.* 24, 0150.

Villamaina, R., Liu, S. J., Nova, I., Tronconi, E., Ruggeri, M. P., Collier, J., et al. (2019). Speciation of Cu cations in Cu-CHA catalysts for NH_3-SCR: Effects of SiO2/Al2O3 ratio and Cu-loading investigated by transient response methods. *ACS Catal.* 9, 8916–8927. doi:10.1021/acscatal.9b02578

Wang, A. Y., Chen, Y., Walter, E. D., Washton, N. M., Mei, D., Varga, T., et al. (2019). Unraveling the mysterious failure of Cu/SAPO-34 selective catalytic reduction catalysts. *Nat. Commun.* 10, 1137. doi:10.1038/s41467-019-09021-3

Wang, B., Ma, L. J., Han, L. N., Feng, Y., Hu, J., Xie, W., et al. (2021). Assembly-reassembly of coal fly ash into Cu-SSZ-13 zeolite for NH_3-SCR of NO via interzeolite transformations. *Chem. Eng. Sci. X* 10, 100089. doi:10.1016/j.cesx.2021.100089

Wang, D., Jangjou, Y., Liu, Y., Sharma, M. K., Luo, J., Li, J., et al. (2015). A comparison of hydrothermal aging effects on NH_3-SCR of NO_x over Cu-SSZ-13 and Cu-SAPO-34 catalysts. *Appl. Catal. B Environ.* 165, 438–445. doi:10.1016/j.apcatb.2014.10.020

Woo, J., Bernin, D., Ahari, H., Shost, M., Zammit, M., and Olsson, L. (2020). Regeneration of Cu/SAPO-34(MO) with H_2O only: Too good to be true. *Catal. Sci. Technol.* 10, 1529–1538. doi:10.1039/c9cy01981b

Woo, J. W., Leistner, K., Bernin, D., Ahari, H., Shost, M., Zammit, M., et al. (2018). Effect of various structure directing agents (SDAs) on low-temperature deactivation of Cu/SAPO-34 during NH_3-SCR reaction. *Catal. Sci. Technol.* 8, 3090–3106. doi:10.1039/c8cy00147b

Wu, Q., Fan, C., Wang, Y., Chen, X., Wang, G., Qin, Z., et al. (2022). Direct incorporating small amount of Ce (III) in Cu-SAPO-18 catalysts for enhanced low-temperature NH3-SCR activity: Influence on Cu distribution and Si coordination. *Chem. Eng. J.* 435, 134890. doi:10.1016/j.cej.2022.134890

Xu, H. D., Lin, C. L., Lin, Q. J., Feng, X., Zhang, Z., Wang, Y., et al. (2020). Grain size effect on the high-temperature hydrothermal stability of Cu/SAPO-34 catalysts for NH_3-SCR. *J. Environ. Chem. Eng.* 8, 104559. doi:10.1016/j.jece.2020.104559

Xu, Z. Q., Li, J. W., Qian, W. X., Ma, H., Zhang, H., and Ying, W. (2017). Synthesis of core–shell SAPO-34@SAPO-18 composites by the epitaxial growth method and their catalytic properties for the MTO reaction. *RSC Adv.* 7, 54866–54875. doi:10.1039/c7ra11395a

Yang, J., Lei, S., Yu and Xu, G. (2014). Low-cost V−W−Ti SCR catalyst from titanium-bearing blast furnace slag. *J. Environ. Chem. Eng.* 2, 1007–1010. doi:10.1016/j.jece.2014.03.022

Yuan, E. H., Li, M., Yang, M. H., Huang, X., Zhang, K., Han, W., et al. (2022). Encapsulation of ultra-small Cu–Fe into ZSM-5 zeolites for NH3-SCR with broad reaction-temperature ranges. *Microporous Mesoporous Mater.* 331, 111675. doi:10.1016/j.micromeso.2021.111675

Yuan, E. H., Zhang, K., Lu, G. X., Mo, Z., and Tang, Z. (2016). Synthesis and application of metal-containing ZSM-5 for the selective catalytic reduction of NOX with NH_3. *J. Industrial Eng. Chem.* 42, 142–148. doi:10.1016/j.jiec.2016.07.030

Zhang, J. Y., Liang, J., Peng, H. G., Mi, Y., Luo, P., Xu, H., et al. (2021). Cost-effective fast-synthesis of chabazite zeolites for the reduction of NO_x. *Appl. Catal. B Environ.* 292, 120163. doi:10.1016/j.apcatb.2021.120163

Zhang, L., Ren, K., Li, J., Cui, Z., and Cheng, H. (2022). The first-principles study of external strain tuning the electronic and optical properties of the 2D $MoTe_2/PtS_2$ van der Waals heterostructure. *Front. Chem.* 10, 934048. doi:10.3389/fchem.2022.934048

Zhang, S. T., Chen, J. W., Meng, Y., Pang, L., Guo, Y., Luo, Z., et al. (2022). Insight into solid-state ion-exchanged Cu-based zeolite (SSZ-13, SAPO-18, and SAPO-34) catalysts for the NH_3-SCR reaction: The promoting role of NH4-form zeolite substrates. *Appl. Surf. Sci.* 571, 151328. doi:10.1016/j.apsusc.2021.151328

Zhang, S. T., Meng, Y., Pang, L., Ding, Q., Chen, Z., Guo, Y., et al. (2022). Understanding the direct relationship between various structure-directing agents and low-temperature hydrothermal durability over CuSAPO-34 during the NH_3-SCR reaction. *Catal. Sci. Technol.* 12, 579–595. doi:10.1039/d1cy02046c

Zhang, S. T., Ming, S. J., Guo, L., Bian, C., Meng, Y., Liu, Q., et al. (2021). Controlled synthesis of Cu-based SAPO-18/34 intergrowth zeolites for selective catalytic reduction of NOx by ammonia. *J. Hazard. Mater.* 414, 125543. doi:10.1016/j.jhazmat.2021.125543

Zhao, D. P., Zhang, Y., Li, Z., Wang, Y., and Yu, J. (2017). Synthesis of SAPO-18/34 intergrowth zeolites and their enhanced stability for dimethyl ether to olefins. *RSC Adv.* 7, 939–946. doi:10.1039/c6ra25080g

Zhao, D. P., Zhao, Q. S., Zhang, Y., Shi, T., Yao, H. G., and Yu, J. Q. (2016). Synthesis and characterization of intergrowth structured SAPO-18/SAPO-34. *Chem. J. Chin. Univ.* 2 (37), 342–348. doi:10.7503/cjcu20150527

Zheng, W., Chen, J. L., Guo, L., Zhang, W. B., Zhao, H. R., and Wu, X. Q. (2020). Research progress of hydrothermal stability of metal-based zeolite catalysts in NH_3-SCR reaction. *J. Fuel Chem. Technol.* 48 (10), 1193–1210. doi:10.1016/s1872-5813(20)30081-5

Frontiers in Chemistry

Explores all fields of chemical science across the periodic table

Advances our understanding of how atoms, ions, and molecules come together and come apart. It explores the role of chemistry in our everyday lives - from electronic devices to health and wellbeing.

Discover the latest Research Topics

See more →

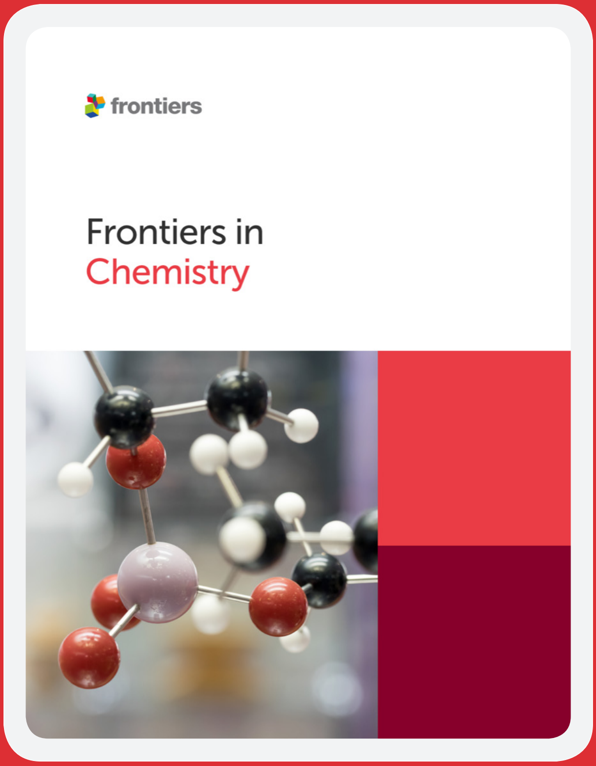

frontiers

Frontiers in
Chemistry

Frontiers

Avenue du Tribunal-Fédéral 34
1005 Lausanne, Switzerland
frontiersin.org

Contact us

+41 (0)21 510 17 00
frontiersin.org/about/contact